Design Expressions and Dynamic Evaluation of CFST Bridges Subjected to Seismic Hazards

Max Taylor Stephens

A dissertation
submitted in partial fulfillment of the
requirements for the degree of

Doctor of Philosophy

University of Washington

2016

Reading Committee:

Dawn E. Lehman, Chair

Charles W. Roeder, Chair

Jeffrey W. Berman

Program Authorized to Offer Degree:
Civil and Environmental Engineering

University of Washington

Abstract

Design Expressions and Dynamic Evaluation of CFST Bridges Subjected to Seismic Hazards

Max Taylor Stephens

Co-Chairs of the Supervisory Committee:
Dawn E. Lehman
Civil and Environmental Engineering
Charles W. Roeder
Civil and Environmental Engineering

Concrete filled steel tubes (CFSTs) consist of a steel tube with concrete infill. CFST columns offer an efficient and economical alternative to conventional reinforced concrete bridge columns, in that CFST columns can offer larger strength and stiffness and facilitate rapid construction.

The first phase of this research project uses numerical and experimental methods to develop design procedures for various CFST column-to-cap beam connections. Three connections were studied, namely: (1) an embedded flange connection in which the CFST is embedded in the cap beam, (2) a welded dowel connection in which a series of headed dowels is welded inside the tube and embedded into the cap beam (both fully bonded and partially deboned conditions were studied), and (3) a dowel connection in which an independent cage of headed dowels and transverse reinforcing is developed into the CFST and embedded into the cap beam. All specimens were constructed using precast cap-beam components to demonstrate the feasibility of using these connections for accelerated bridge construction (ABC). The experimental program included specimens that simulated either the transverse or longitudinal direction of the bridge. Results showed that the three connection types provide excellent ductility under reversed-cyclic loading while all super-structure elements remained

essentially elastic. The document provides design expressions, design examples and proposed codified language to facilitate immediate implementation of the research results into practice.

In the second phase, performance based earthquake engineering (PBEE) tools were used to evaluate and compare the response of a reinforced concrete (RC) bridge with a CFST bridge designed using the design expressions developed in phase 1. The PBEE tool set included fragility functions that express the likelihood of damage and reparability, nonlinear analysis methods that capture the full cyclic response of the structural system, and incremental dynamic analyses (IDAs) to evaluate collapse potential. The analysis process was as follows: (1) the selected bridge was designed using RC and CFST components, with the objective of having the same strength and stiffness, (2) the structures were subjected to a suite of ground motions scaled to represent servicability (10% probability of exceedance in 50 years), design (7% probability of exceedance in 75 years), and maximum considered (2% probability of exceedance in 50 years) seismic hazard levels, (3) fragility curves were used to compare the performance of the bridge including damage state as well as maximum and residual drift, and (4) IDAs were conducted to compare the collapse probability. Results indicate that the CFST structure is more resilient than the RC structure by all measures.

TABLE OF CONTENTS

LIST OF FIGURES

LIST OF TABLES

Table Number Page

ACKNOWLEDGMENTS

This research was primarily sponsored by the California Department of Transportation under Agreement Number 65A0446. I would like to specifically acknowledge the advice and assistance provided by Ron Bromenschenkel, Michael Cullen, and Peter Lee of the California Department of Transportation. Input provided by members of the Washington Department of Transportation is also greatly appreciated.

I also wish to express sincere appreciation to the Co-Chairs of my committee, Dr. Dawn E. Lehman and Dr. Charles W. Roeder, for their support throughout this process. Their experience and insight helped me grow as a researcher and educator.

Input provided by my peers also proved invaluable. I would like to extend specific thanks to Travis Thonstad for being a great friend throughout this process and providing valuable advice related to all facets of my research. I would also like to acknowledge all members of More 236 including Olafur Haraldsson, Hung Viettran, Jonathan Weigand, Bo-shiuan Wang, Andrew Sen, and Ramona Barber.

Finally, I would like to thank Vince Chaijaroen. None of this work would have been possible without his input or assistance in the lab.

DEDICATION

To Kathy and Jerry Stephens.

Chapter 1

INTRODUCTION

1.1 Research Motivation/Impetus

Accelerated bridge construction (ABC) has become a major focus of many departments of transportation to decrease construction cost and limit economic loss due to disruptions in the transportation network. However, current ABC technologies developed for use nationwide do not necessarily translate to resilient lateral load resisting systems for use in high seismic areas. Thus there is an interest in developing ABC technologies which limit earthquake damage, provide stable cyclic response, and meet engineering and construction constraints. Circular concrete filled steel tubes (CFST) which consist of steel tubes filled with concrete are practical structural elements which fulfill these objectives, and offer an efficient and economical alternative to conventional reinforced concrete and steel construction.

As illustrated in the construction sequence in Fig. 1.1, CFSTs facilitate accelerated construction. The steel tube eliminates the need for temporary shoring and formwork which is necessary for reinforced concrete (RC) construction, and acts as reinforcing to the concrete fill which eliminates the need for reinforcing cages. The placement of the concrete fill may be further enhanced using self consolidating concrete (SCC) so that vibration is not required.

In addition, CFSTs optimize the mechanical contributions of the the concrete fill and steel tube. The steel tube is placed at the optimal location to resist bending, thereby maximizing strength and stiffness while minimizing weight and material requirements. In addition, the steel tube provides optimal confinement to the concrete and greater shear strength than spiral reinforcement typically used for circular reinforced concrete columns. The concrete fill, in turn, restrains local tube buckling, supports compressive stress demands, and offers large stiffness to meet functionality performance objectives. Shear stress transfer must occur between the steel tube and concrete fill to ensure full composite action which increases efficiency, resistance, and ductility. Because CFSTs provide large axial load carrying capacity, they are suitable for bridge piers, piles, and drilled shaft foundations.

The current American Association of State Highway and Transportation Officials (AASHTO) LRFD specifications permit the use of CFST construction [AASHTOa, 2015]. However, CFSTs are not extensively used in highway bridges in the United States due to inconsistent design requirements specified by different code writing agencies [AASHTOa, 2015; ACI, 2011; AISC, 2011] as well as a lack of standard design expression for connections to RC components. Furthermore, the performance of CFST bridges subjected to natural hazards has never been evaluated at a system-level to demonstrate resiliency and provide a direct comparison to the performance of traditional RC bridge systems.

1.2 Research Objectives

The primary objectives of this research are to overcome the aforementioned deficiencies by:

1. Developing design expressions for CFST column-to-precast concrete connections capable of sustaining cyclic lateral load demands while mitigating damage and degradation and

2. Developing numerical models for a system level evaluation and comparison of CFST and RC bridges subjected to natural hazards.

1.2.1 Proposed Connections

Recent research has evaluated several variations of CFST column-to-foundation and column-to-cap beam connections. The connection types range from embedded connections in which the steel tube is embedded in the foundation or cap beam concrete [Hsu and Mo, 2010; Hitaka et al., 2003; Lehman and Roeder, 2012b,a; Kappes et al., 2013; Stephens et al., 2015] to supplemental dowel connections in which external or internal dowels extend from the CFST into the foundation or cap beam [Kadoya et al., 2004; Morino et al., 2003;

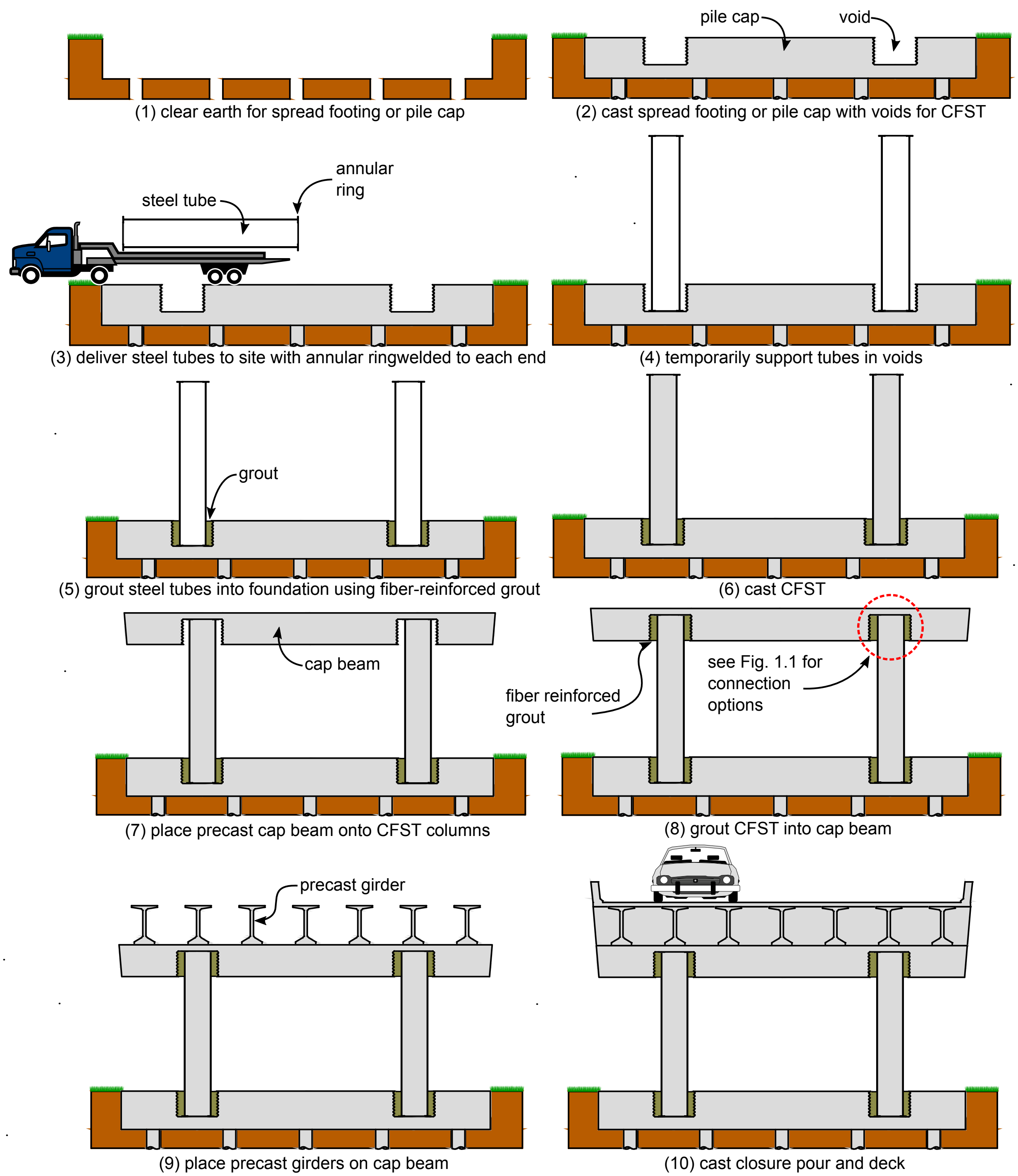

Figure 1.1: Accelerated Bridge Construction Sequence Using CFST Columns

Montejo et al., 2009, 2013]. However, few studies have resulted in implementable design expressions for the connection, and only limited research has focused on connections to precast components to achieve ABC objectives. The first phase of this research focused on developing a range of CFST column-to-cap beam connections that facilitate ABC and provide superior seismic performance. The proposed CFST column-to-cap beam connections are illustrated in Fig. 1.2. There are three connection types: (1) embedded ring (ER) connections (Fig. 1.2a), (2) welded dowel (WD) connections (Fig. 1.2b), and (3) reinforced concrete (RC) connections (Fig. 1.2c). This provides a suite of connections for designers, each option offering advantages as the bridge may require.

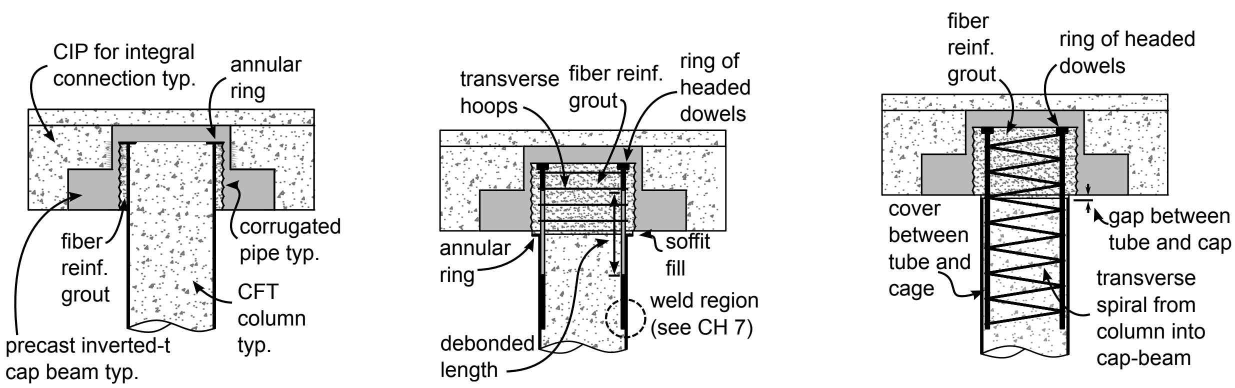

(a) Embedded Ring (ER) Connection

(b) Welded Dowel (WD) Connection

(c) Reinforced Concrete (RC) Connection

Figure 1.2: Proposed CFST column-to-cap beam connections

The ER connection is similar to the embedded flange column-to-foundation connection that was developed in prior research [Lehman and Roeder, 2012b,a]. It uses a grouted connection detail, with a void cast into a precast cap beam (shown as cast into an inverted-t beam in Fig. 1.2a; note an RC cap beam can also be utilized). A circular ring is welded to the steel tube to provide anchorage and transfer stress to the concrete and reinforcing in the cap beam. The precast cap beam is placed onto the column after the column is set, and the recess between the tube and corrugated pipe is filled with high strength fiber reinforced grout.

The connections illustrated in Fig. 1.2b and Fig. 1.2c utilize T-headed reinforcing dowels that extend from the CFST column into the cap beam to provide axial, moment, and shear transfer. These connections can be used in traditional cast-in-place construction, or can be integrated into precast elements using a void similar to that described from grouted CFST connection as shown in Fig. 1.2b and Fig. 1.2c, or individual ducts.

The WD connection utilizes headed dowels to resist the flexural demand. The dowels are welded to the steel to to facilitate transfer of moment from the pier cap to the composite CFST column, and are developed into the cap beam using a high-strength, fiber-reinforced grout. Welding the dowel directly to the tube, as opposed to embedding the dowel directly into the connection maximizes the moment capacity of the dowel connection. A soffit is included between the steel tube and cap beam. A flange is welded to the exterior of the steel tube to increase compressive bearing area on the soffit. The longitudinal bars are de-bonded in the column-to-cap beam interface to reduce damage to the pier cap during inelastic deformation and increase the ductility of the connection, and transverse reinforcing is included in the joint region to provide confinement to the fiber-reinforced grout.

Fig. 1.2c shows an RC connection in which a short independent cage for both transverse and longitudinal reinforcing extends from the CFST column into the cap beam, and cover is provided between the reinforcing cage and steel tube within the column. A soffit is left between the steel tube and cap beam to help focus the plastic hinging location between the CFST component and the cap beam [Montejo et al., 2009].

1.3 Document Overview

This document discusses a large scale experimental and numerical program to facilitate the implementation of CFST bridges into practice. The components of the program were as follows:

1. Conduct a comprehensive review of past literature and research related to the development of CFST and precast concrete connections.

2. Identify and select connections for study.

3. Develop high-resolution finite element models to evaluate the behavior of each connection type.

4. Utilize results from the finite element analyses to select specimens for experimental investigation.

5. Use successful experimental results to develop practical design expressions for the proposed CFST column-to-cap beam connections.

6. Use the proposed design expressions to re-design a reinforced concrete (RC) bridge using CFST.

7. Compare the response of the CFST and RC structure subjected to natural hazards to evaluate performance and resiliency.

8. Present proposals for efficient CFST connections for rapid and economical construction of highway bridges.

Chapter 2 outlines current design provisions for CFST members available in the AASHTO LRFD Bridge Design Specifications [AASHTOa, 2015] (herein referred to as the AASHTO LRFD) as well as the 14th Edition of the American Institute for Steel Construction (AISC) Steel Design Manual [AISC, 2011]. Joint detailing requirements from the AASHTO Guide Specifications for LRFD Seismic Bridge Design [AASHTOb, 2011] (herein referred to as the AASHTO Seismic Specificaitons) as well as the California Department of Transportation (Caltrans) Seismic Design Criteria (SDC)Version 1.6 [Caltrans, 2010] are introduced.

Chapter 3 reviews extensive research which was previously conducted on CFST and precast concrete connections, while Chapter 4 discusses a limited numerical study which was used to develop the experimental matrix. Chapters 5 and 6 describe the experimental program to evaluate the ER and dowel type connections respectively; proposed design expressions for the connections are also introduced. Reinforcing details for the large-scale specimens have been included in Appendix B. The design recommendations presented in Chapters 5 and 6 provide a comprehensive review of the design requirements for a range of CFST column-to-cap beam connections, and provide a solid basis for moving forward with CFST bridge piers in practice. Several service load design examples have been included in Appendix A to demonstrate the use of the proposed expressions, and proposed specification language has been included in Appendix C.

Chapter 7 provides an in-depth comparison of the proposed connections in terms of seismic response and accelerated construction. Prototype-level design and material cost comparisons between traditional RC structures and CFST structures which utilize the ER and WD connections are also included.

Chapter 8 discusses nonlinear fiber element modeling of RC and CFST columns using the open source structural analysis software OpenSees. Numerical results for RC and CFST columns are validated using experimental data.

Chapter 9 extends the validated component modeling into a full scale bridge model. A series of dynamic analysis are performed on the bridge using RC and CFST columns to evaluate and compare the performance of the two structural systems for a range of seismic hazards. An incremental dynamic analysis (IDA) is also introduced.

Chapter 10 concludes with a summary of results presented herein as well as several recommendations for future research of CFST bridge systems.

Chapter 2

DESIGN PROVISIONS

This chapter summarizes design provisions for CFST components specified in AASHTOa [2015] as well as joint detailing requirements for RC bridges in seismic regions specified in Caltrans [2010] and AASHTOb [2011]. These provisions are reviewed because they are relevant to the design of CFST components and RC dowel-type cap beam connections for use in seismic regions and were referenced heavily in this research.

2.1 Design Provisions for CFST Components

The AASHTO LRFD [AASHTOa, 2015] provides design rules for CFST construction. These AASHTO provisions are primarily in Articles 6.9.6 and 6.12.2. The local stability of the steel tube is provided using a limit of the diameter to thickness ($\frac{D}{t}$) ratio. The limiting value is defined in AASHTO Eq. 6.9.6.2-1 as:

$$\frac{D}{t} \leq 0.15 \frac{E_s}{F_{y,st}} \tag{2.1}$$

where E and $F_{y,st}$ are the elastic modulus and nominal yield stress of steel respectively.

The effective flexural stiffness of a CFST member , EI_{eff}, is defined in AASHTO Eq. 6.9.6.3.2-6 as:

$$EI_{eff} = E_s I_s + C' E_c I_c \tag{2.2a}$$

$$C' = 0.15 + \frac{P}{P_o} + 2 \frac{A_{st}}{A_{st} + A_c} < 0.9 \tag{2.2b}$$

where the subscripts c and st refer to the properties of the concrete and steel tube sections, respectively, I and A are the moment of inertia of the area of the respective material sections, P is the applied axial load.

The maximum compressive resistance, P_o, of a CFST member is the crushing capacity of the CFsT as defined in AASHTO Eq. 6.9.6.3.2-4 as:

$$P_o = 0.95 f'_{cf} A_c + F_y A_s \tag{2.3}$$

where f'_{cf} is the compressive strength of concrete and other variables have been define previously. The member buckling capacity P_{cr}, is based on conventional steel buckling equations as defined in AASHTO Eqs. 6.9.6.3-2 and 6.9.6.3-3 as:

$$P_{cr} = 0.658^{\frac{P_o}{P_e}} P_o \quad \text{if} \quad \frac{KL}{r} \leq 4.71\sqrt{\frac{E}{F_y}} \tag{2.4a}$$

$$P_{cr} = 0.877 P_e \quad \text{if} \quad \frac{KL}{r} > 4.71\sqrt{\frac{E}{F_y}} \tag{2.4b}$$

where P_e is the elastic buckling load. Note that the above equations look slightly different than the equations appearing in the LRFD specification, because internal reinforcement is not included, and some terms have been combined.

Combined loading is an important design consideration as CFSTs are commonly used as columns with full moment-resisting connections. The current AASHTO LRFD provisions permit the use of plastic stress distribution (PSDM) or strain-compatibility methods (SCM) to calculate combined axial-flexural resistance of CFSTs along with a stability based interaction curve to incorporate global buckling. The PSDM and SCM methods are discussed in AASHTOa [2015] 6.12.2.3.3. The PSDM assumes that the section develops the full yield stress of the steel in tension and compression and a uniform compressive stress of $0.95f'_c$ for concrete over the compression region in circular CFST as illustrated in Fig. 2.1a. The 0.95 coefficient on f'_c for circular CFST is larger than the 0.85 typically used for a Whitney's stress block calculation in recognition of the concrete confinement provided by circular tubes. For each neutral axis depth, pairs of axial and bending resistances are determined by satisfying equilibrium over the cross section for the given stress distribution as illustrated in Fig. 2.1a. This calculation results in a material-based, closed-form axial load-bending moment (P-M)curve.

Strain compatibility methods are typically used to compute the resistance of reinforced concrete members. For reinforced concrete components, a maximum concrete compression strain of 0.003 is assumed. The strain profile is constructed for each neutral axis depth, and pairs of axial and bending resistances are determined by satisfying equilibrium, as is illustrated in Fig. 2.1b.

Recent research evaluated the PSDM and SCM methods for calculating the combined capacity of CFST components[Bishop, 2009]. In general, it was found that the PSDM method was easier to use and had a mean value closer to 1 and a lower coefficient of variation than the SCM when compared to experimental data. To illustrate and amplify this conclusion, Fig. 2.2 provides comparisons between the measured moment resistance and the computed moment resistance with the plastic stress distribution method (Fig. 2.2a) and the strain compatibility method (Fig. 2.2b). Fig. 2.2 shows that PSDM is more reliable and somewhat conservative. The strain compatibility method had a much larger average and standard deviation values indicating less reliability and greater conservatism in the method.

The stability based P-M interaction curve for CFSTs is described in AASHTOa [2015] 6.9.6.3.4 and is constructed by joining points A', A'', D, and B as illustrated in 2.3. This curve accounts for global buckling as a nominal failure mode. Point A corresponds to the nominal crushing load of the CFST column as calculated using Equation 2.3, while point A' corresponds to the axial compression resistance with moment as calculated in Equation 2.4. Point A'' is the intersection of the material-based interaction curve as calculated using the PSDM or SCM. Point B corresponds to the composite plastic moment resistance without axial load, and point C corresponds to the axial force on the material based interaction curve as calculated using the PSDM or SCM which corresponds to the composite plastic moment

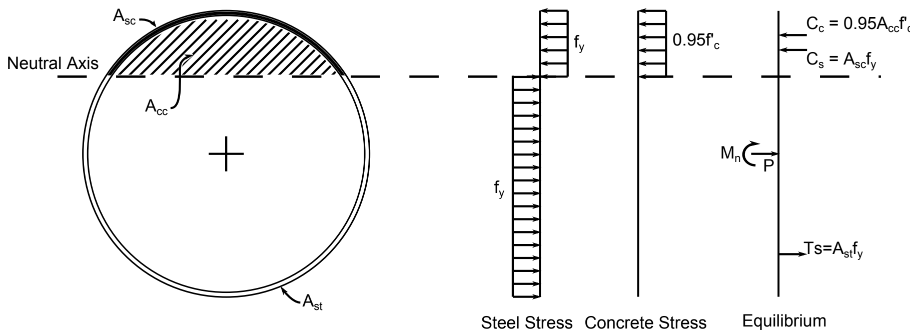

(a) Plastic Stress Distribution Method

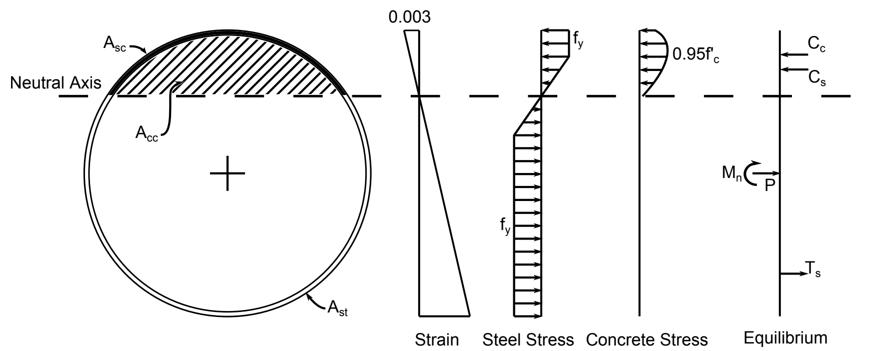

(b) Strain Compatability Method

Figure 2.1: AISC model for prediction of CFST resistance.

resistance without axial load. Point D is located on the material-based interaction curve as calculated using the PSDM or SCM, and is taken at an axial of load $P_D = 0.5P_c(P_n/P_O)$.

2.2 *Superstructure Joint Design Provisions for Reinforced Concrete Bridges*

The AASHTO Seismic Specifications [AASHTOb, 2011] as well as the Caltrans SDC [Caltrans, 2010] provide detailing requirements for reinforcement in the joint regions of RC bridges. These requirements are intended to capacity protect elements of the superstructure such that they remain essentially elastic when plastic hinges form in adjacent substructure elements [AASHTOb, 2011]. The AASHTO provisions are primarily in Section 8.13, while provisions in the Caltrans SDC are in Section 7.4. As many of the requirements in the AASHTO Specifications were taken directly from the Caltrans SDC, only specifications from

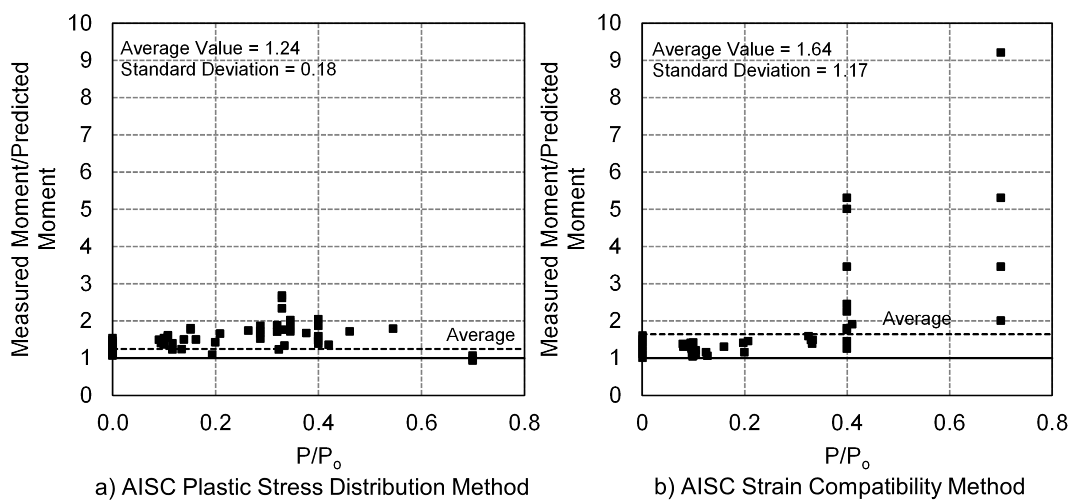

Figure 2.2: Comparison of PSDM and SCM Methods for Predicting the Combined P-M Capacity of CFST Components

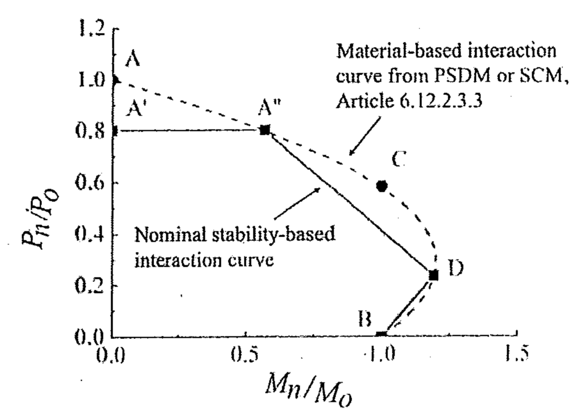

Figure 2.3: Construction of the Normalized Stability-Based P-M Interaction Curve [?]

the Caltrans SDC will be presented here. Furthermore, because this research is primarily concentrated on the behavior of interior joints in non-skewed multi-column bents, only requirements for joints of this type are discussed.

2.2.1 Joint Capacity

Moment resisting connections between the superstructure and column are designed to resist the maximum overstrength moment and corresponding shear generated by the column, denoted as M_o^{col} and V_o^{col} respectively. M_o^{col} is defined in Eq. 4.4 of the SDC as $1.2M_p^{col}$ where M_p^{col} is the idealized plastic moment strength of the column. The procedure to calculate M_p^{col} is described in Section 3.3 of the Caltrans SDC [Caltrans, 2010].

2.2.2 Joint Stresses

Requirements for proportioning superstructure-to-column joints as well as requirements for reinforcing details in the joint region are based on the principal tension and compression stresses in the joint. The equations for calculating these stresses are defined in Eqns. 7.11 and 7.12 in the Caltrans SDC as:

$$p_t = \frac{(f_h + f_v)}{2} - \sqrt{\left(\frac{(f_h + f_v)}{2}\right)^2 + v_{jv}^2} \tag{2.5a}$$

$$p_c = \frac{(f_h + f_v)}{2} + \sqrt{\left(\frac{(f_h + f_v)}{2}\right)^2 + v_{jv}^2} \tag{2.5b}$$

where f_h and f_v are the horizontal and vertical normal stresses at the center of the joint respectively, and v_{jv} is the vertical shear stress. The equations for calculating these stresses are defined in Eqns. 7.13, 7.15, and 7.17 of the Caltrans SDC. The loads which result in these stresses as well as the location of the stresses in the joint are shown in Fig. 2.4a, however the equations have not been included here for brevity.

2.2.3 Joint Proportioning

The proportions of superstructure-to-column joints must be selected such that the principal stresses do not exceed $0.25f'_c$ in compression ($p_c \leq 0.25f'_c$ (psi)) and $12\sqrt{f'_c}$ in tension ($p_t \leq 12\sqrt{f'_c}$ (psi)). Larger widths may be required to develop a compression strut outside the joint for large diameter columns [Caltrans, 2010].

2.2.4 Joint Reinforcing

Joint shear reinforcing is required based on the value of the principal tension stress in the joint, p_t. For $p_t < 3.5\sqrt{f'_c}$(psi), a minimum joint shear reinforcing ratio of $\rho_{s,min} = \frac{3.5\sqrt{f'_c}}{f_{yh}}$ is required and may be provided in the form of column transverse steel continued into the cap beam.

For $p_t \geq 3.5\sqrt{f'_c}$(psi), additional joint reinforcing is required in the form of vertical stirrups, horizontal stirrups, and horizontal side reinforcing. The required area of vertical and horizontal stirrups extending a distance of the column diameter, D_c, from either side of the column center line are defined in Eqns. 7.19 and 7.20 of the Caltrans SDC as:

$$A_s^{jv} = 0.2A_{st} \tag{2.6}$$

$$A_s^{jh} = 0.1A_{st} \tag{2.7}$$

where A_s^{jv} is the required vertical stirrup area, A_s^{jh} is the horizontal stirrup area, and A_{st} is the total area of column steel extending from the column into the bent cap. The horizontal stirrups are required to be placed around the vertical stirrups in two or more layers spaced vertically at a maximum distance of 18-in. The exact locations where transverse vertical and horizontal reinforcing are required for multi-column interior t-type joints are denoted by areas 1-4 in Fig. 2.4b. Steel located in overlapping areas is counted towards meeting the requirements for both areas [Caltrans, 2010]. The area of longitudinal side reinforcing is

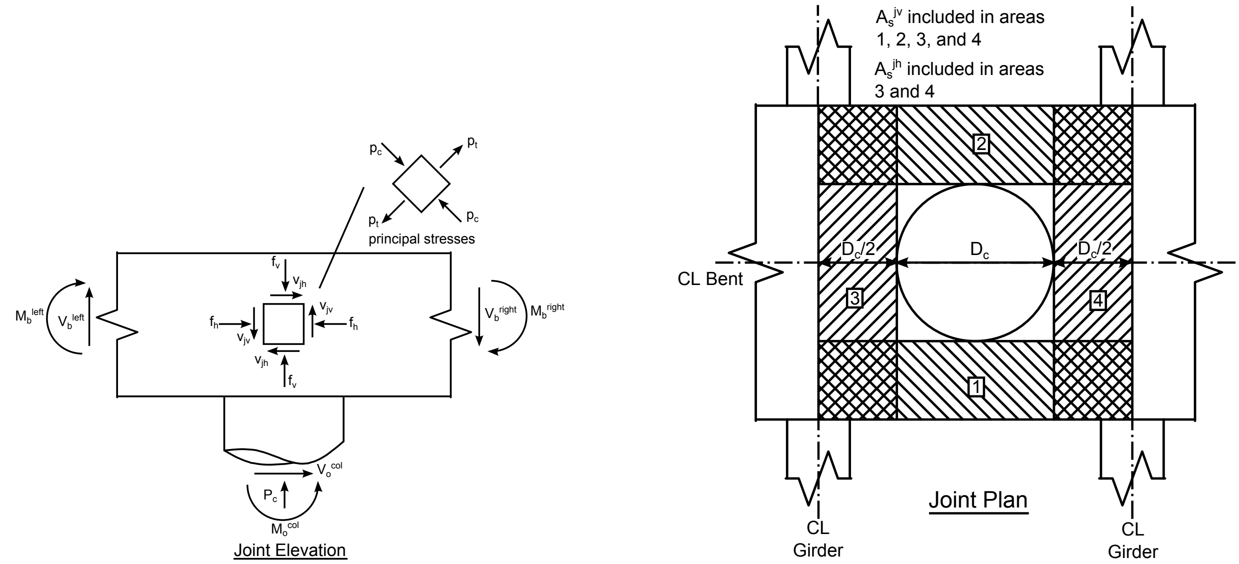

(a) Joint Shear Stresses in T-Joints

(b) Required Location of Transverse Joint Reinforcing

Figure 2.4: Caltrans SDC joint shear definition and transverse reinforcing requirements [Caltrans, 2010].

specified in Equation 7.21 of the Caltrans SDC as:

$$A_s^{sf} \geq \begin{cases} 0.1A_{cap}^{top} \\ 0.1A_{cap}^{bot} \end{cases} \tag{2.8}$$

where A_s^{sf} is the required area of side reinforcing, and A_{cap}^{top} and A_{cap}^{bot} are the areas of the primary top and bottom flexural steel in the bent cap respectively.

Chapter 3

LITERATURE REVIEW

This chapter reviews research that was conducted and provided the basis of the connections studied here. First, CFST to RC component connections are studied; CFST to precast components were not found in the literature search. Numerical procedures for modeling CFST components and connections are also briefly addressed. Second, because some of the proposed connections emulate standard connection details for precast components, various RC column-to-precast cap beam connections are reviewed. As such, this chapter reviews previous work in two primary categories: (1) CFST connections and (2) connection details for precast RC components. Connections developed with an emphasis on ABC are further identified based on the connection type as: (1) individual duct connections, (2) partial height pocket connections, or (3) full height pocket connections. The three connection types are illustrated in Fig. 3.1. An individual duct connection which utilizes dowels grouted into individual ducts cast through the full depth of the precast component is shown in Fig. 3.1a. Two variations of a partial height pocket connection are illustrated in Fig. 3.1b. Finally a full height pocket connection is shown in Fig. 3.1c.

3.1 CFST Connections

Research that has been conducted on two primary types of CFST connections: (1) fully restrained connection intended to transfer the full moment strength of the CFST component, and (2) partial strength connections in which the strength emulates RC construction and is less than that of the CFST component. This chapter reviews experimental and numerical research conducted on both connection types.

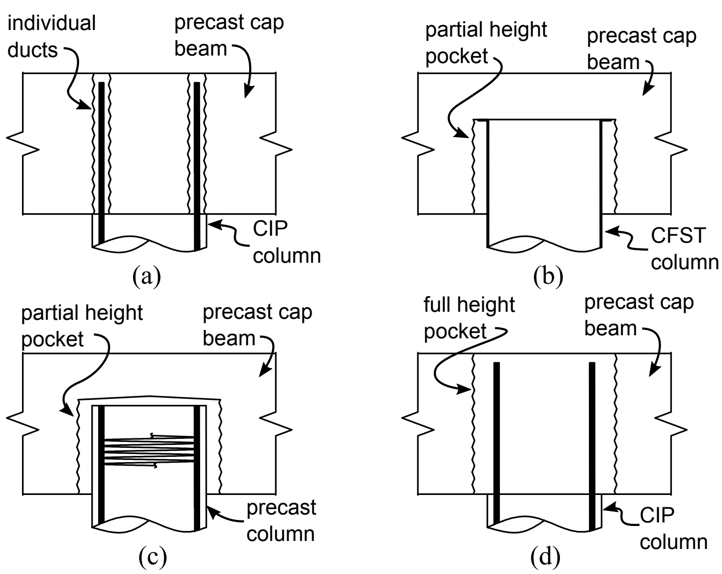

Figure 3.1: Connections with Emphasis on ABC (a) Individual Duct with CIP Column[Pang et al., 2010; Stueck et al., 2009; Restrepo et al., 2011], (b) Partial Height Pocket with Embedded CFST [Lehman and Roeder, 2012b,a], (c) Partial Height Pocket with Embedded Precast Column [A. Mehrsoroush, 2014], and (d) Full Height Pocket with CIP Column [Restrepo et al., 2011]

3.1.1 Partial Strength Connections

The following section provides a summary of relevant research programs that studied partial strength connections with a focus on connections utilizing reinforced concrete in the transition region. These connections have been labeled as "Partial Strength" because the strength of the connection is controlled by reinforcing dowels or bars which extend from the CFST into foundation or cap beam concrete. Studies using either circular or rectangular CFSTs were included because the research is so limited. Kawaguchi and Morino [2006] developed a CFST-to-foundation connection consisting of an exposed base plate with multiple anchor bolts as well as internal reinforcing bars as shown in Fig. 3.2. The central reinforcing bars are included to increase the stiffness and strength of the exposed base plate, as this connection type has been shown to provide limited rotational stiffness. These bars are cast into the foundation prior to placement of the CFST, and extend through holes in the base plate into the CFST column.

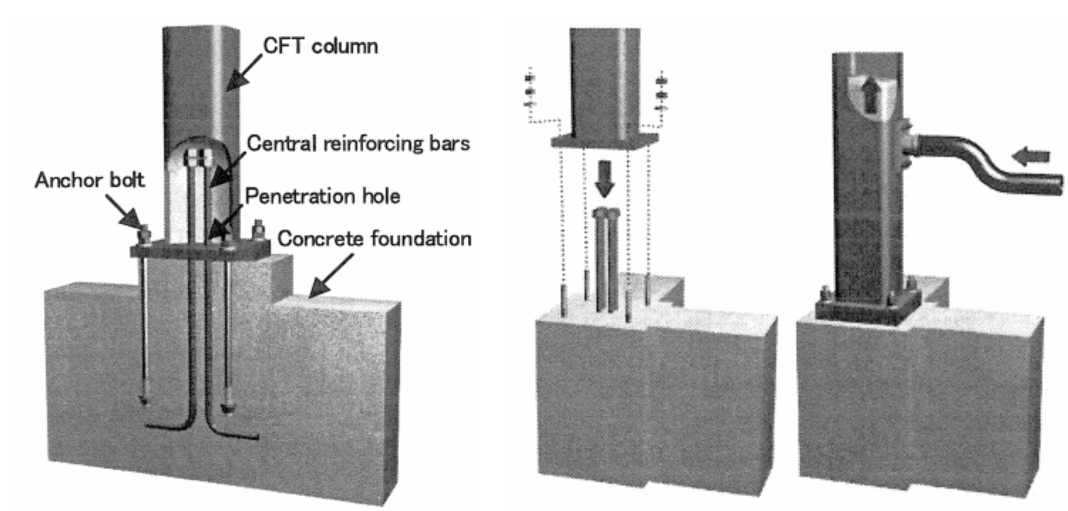

(a) Schematic of Foundation Connection (b) Procedure of Construction

Figure 3.2: CFST-to-Foundation Connection Developed by Kawaguchi and Morino [2006]

Ten specimens were constructed to evaluate the performance of the connection. The specimen geometry consisted of a 62-in. high column anchored into 40x27.5-in. foundation with an 82-in. length. Two different types of tubes were evaluated: (1) 12x12-in. square steel tubes with 0.75-in. wall thickness and (2) 16-in. diameter circular tubes with 0.5-in. wall thickness. The shape and size of the base plate and the size and number of anchor bolts were identical for all specimens. The primary parameters were: (1) axial force: zero, constant tension, constant compression, and reversed cyclic (2) type of connection; base plate or internally reinforced CFST, and (3) strength of the CFST column. Results from the experiments showed that the internally reinforced CFST connection exhibited larger stiffness and strength compared to base plate connections. Specifically, the connections with internal bars showed increases in stiffness and yield strengths of 1.2 and 1.8 respectively compared to the traditionally detailed connections. However, all specimens exhibited fairly low drift capacities (approximately 5%) when subjected to reversed cyclic loading, and the failure mode was generally characterized by extreme damage in the foundation which is not ideal for seismic design.

Montejo et al. [2009, 2013] evaluated the behavior of a jacketed RC column which utilized a traditional RC column-to-foundation connection. Jacketed reinforced concrete columns utilize a conventional steel cage placed within the steel tube as is illustrated in Fig. 3.2. This reinforcing steel is also used to transfer the moment, shear and axial forces to the adjacent RC component and vise versa. To ensure the tube does not contribute to the strength or in the transfer mechanism, a soffit is left between the tube and adjacent members. As such, this member and connection does not respond as a CFST but instead responds as a jacketed RC component and connection with much lower stiffness and strength than the CFST component.

In the study by Montejo et al. [2009, 2013], a total of six connections were tested experimentally; two flexure dominated RC columns with an 18-in. diameter and 65-in. height and four flexure dominated jacketed RC columns with an 18-in. diameter tube that had a 1/4-in. wall thickness (D/t=72), and 65-in. height. The primary parameters were: (1)

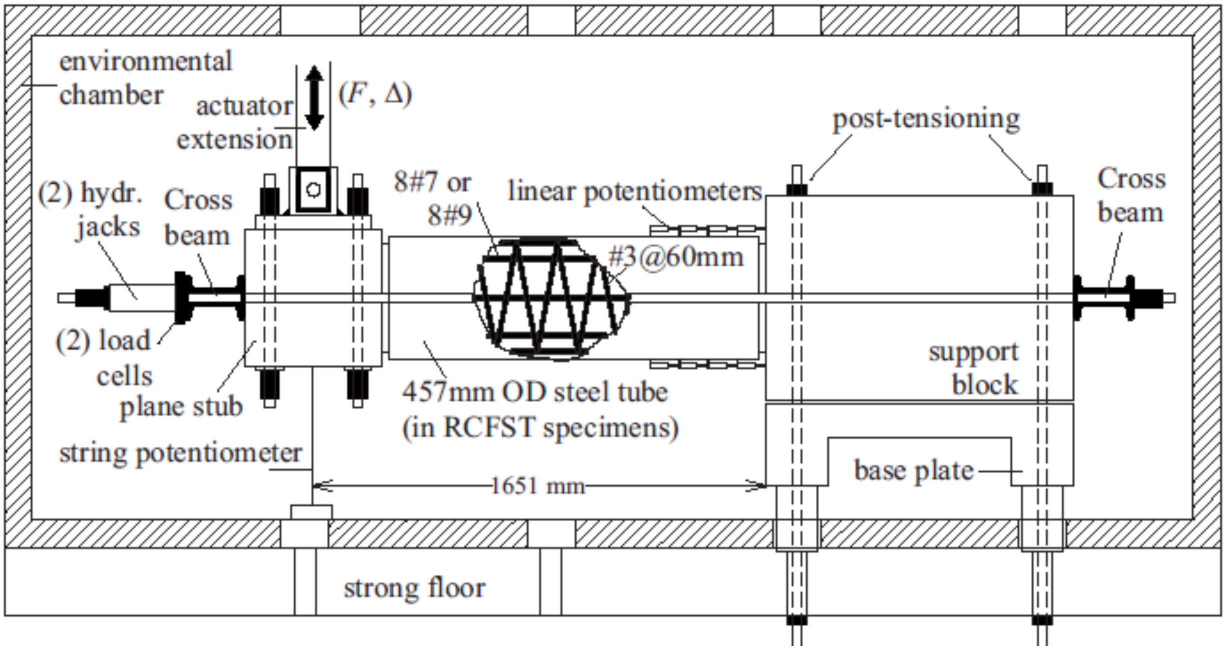

Figure 3.3: Schematic of Test Setup and Specimen Tested by Montejo et al. [2009, 2013][Montejo et al., 2009, 2013]

axial load ratio (ranging from 3.3% - 6.4%), (2) longitudinal reinforcing ratio (ranging from 2.1% to 3.1%), and (3) ambient temperature (ranging from −33°F - 72°F). An overview of the specimen geometry and test setup is shown in Fig. 3.3.

Results from the experiments showed that the jacked RC column connection performed largely similar to the RC connection. Differences were noted in the length of the damaged region of the two different components. The RCFST components exhibited significant strain concentrations in the longitudinal reinforcing at the column-to-foundation interface, which resulted in lower ductility capacities than the comparable RC specimens. This observation highlights the importance of mitigating strain concentrations in this region to fully realize the advantages of using CFST columns.

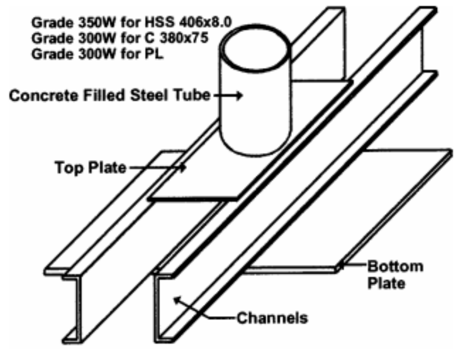

Figure 3.4: Schematic of Connection Tested by Marson and Bruneau [2004]

3.1.2 Full Strength Connections

The following section provides a summary of relevant research programs that full strength connections in which the connection transfers the full capacity of the CFST component. A full strength structural steel connection was developed by Marson and Bruneau (2004). The connection was constructed by welding the steel tube to structural steel members and encasing the built-up base into a concrete foundation, as shown in Fig. 3.4. The steel members act both to fully develop the moment capacity of the CFST, and as flexure reinforcement in the foundation. Four specimens were constructed with D/t ratios of 34, 51, 42, and 64 and diameters of 12.75-in. 12.75-in., 16.16-in., and 16.16-in. respectively to experimentally evaluate the performance of the structural steel connection, and axial load ratio was the primary parameter.

The embedded structural steel connection was able to develop the full plastic moment capacity of the CFST with failure modes characterized by local buckling of the steel tube. All columns exhibited large energy dissipation, and exceeded 7% drift without significant strength loss or foundation damage. Strain gage data from the embedded structural steel suggested that the CFST was primarily anchored by the foundation concrete as opposed to the built up base.

While this connection performed well when subjected to reversed cyclic loading, the details are not economical and do not facilitate accelerated construction. Utilizing rolled structural steel as the primary flexural reinforcing results in higher costs than traditional reinforcing steel. Further, concrete in the foundation or cap beam would have to be cast after the column has been set which requires shoring and formwork.

The strength of an embedded CFST column-to-pier cap connection (shown in Fig. 3.5) was evaluated by Kappes et al. [2013]. To simplify construction and transfer the moment at the pier cap connection, the tube was extended into the pier cap. Mechanical anchors were not included in the connection, thus there was only chemical bond between the tube and the concrete. This represented standard construction practice for CFST bridge bent connections in the state of Montana.

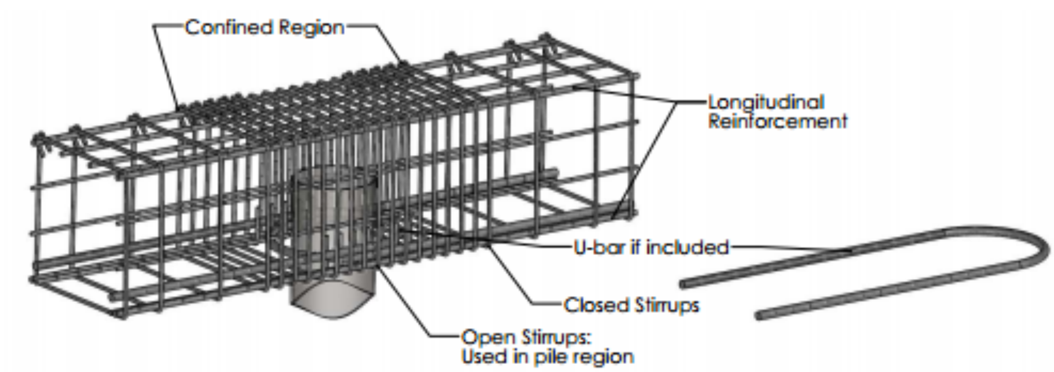

Figure 3.5: Overview of connection evaluated by Kappes et al. [2013].

Nine 50% scale specimens with D/t ratios varying from 18-28 were constructed to evaluate the strength of the connection. The primary parameter evaluated in the experiment was the reinforcing details in the pier cap; several specimens were constructed with standard practice detailing, and several were constructed using detailing intended to increase the strength of the connection. Results from the experiments showed that the pier cap could be detailed to achieve the plastic moment capacity of the CFST with limited damage to the pier for D/t ratios of 28. In this case, the failure of the connection was characterized by yielding of the CFST column as a plastic hinge developed in the column adjacent to the pier cap. Significant cap beam reinforcing beyond standard practice was included to achieve this failure mode. As it was the intent of the experiment to evaluate the capacity of the connection, larger steel tubes with a D/t ratio of 18 were introduced which resulted in the failure of the pier cap from prying effects. Note that this failure mode is not desirable nor permitted by most state DOT's in seismic regions.

3.1.2.1 Embedded CFST Column to Footing Tests as the University of Washington

Several research programs undertaken at the University of Washington studied a CFST foundation connection capable of developing the full plastic moment capacity of a CFST component [Kingsley, 2005; Williams, 2006; Lee, 2011; Lehman and Roeder, 2012b,a]. The latter research program was the prior phase to the program discussed in this document.

The embedded CFST connection studied was a fully restrained moment connection that employs a flanged annular ring that was welded to the base of the steel tube. This flange provides anchorage and efficient shear and moment transfer to the surrounding concrete and reinforcement, as illustrated by the compression struts in Fig. 3.6a. There are no reinforcing bars in the tube or dowels penetrating from the tube into the foundation; the force transfer is solely accomplished by the anchored portion of the tube and the flange. The foundation or pile cap is designed to normal geometric limits, design loads, and shear and flexural reinforcement.

Two variations of the embedded foundation connection have been developed, as shown in Fig. 3.6b and Fig. 3.6c, a CIP monolithic option and a partial height pocket option. For the monolithic option, the steel tube and annular ring are temporarily anchored within the foundation reinforcing, and the foundation and CFST-column are cast simultaneously, as shown in Fig. 3.6b. The grouted variation is a partial height pocket connection in that the footing is cast with a recess formed by a lightweight corrugated steel tube with an inner diameter slightly larger than the outside diameter of the annular ring, as shown in Fig. 3.6c.

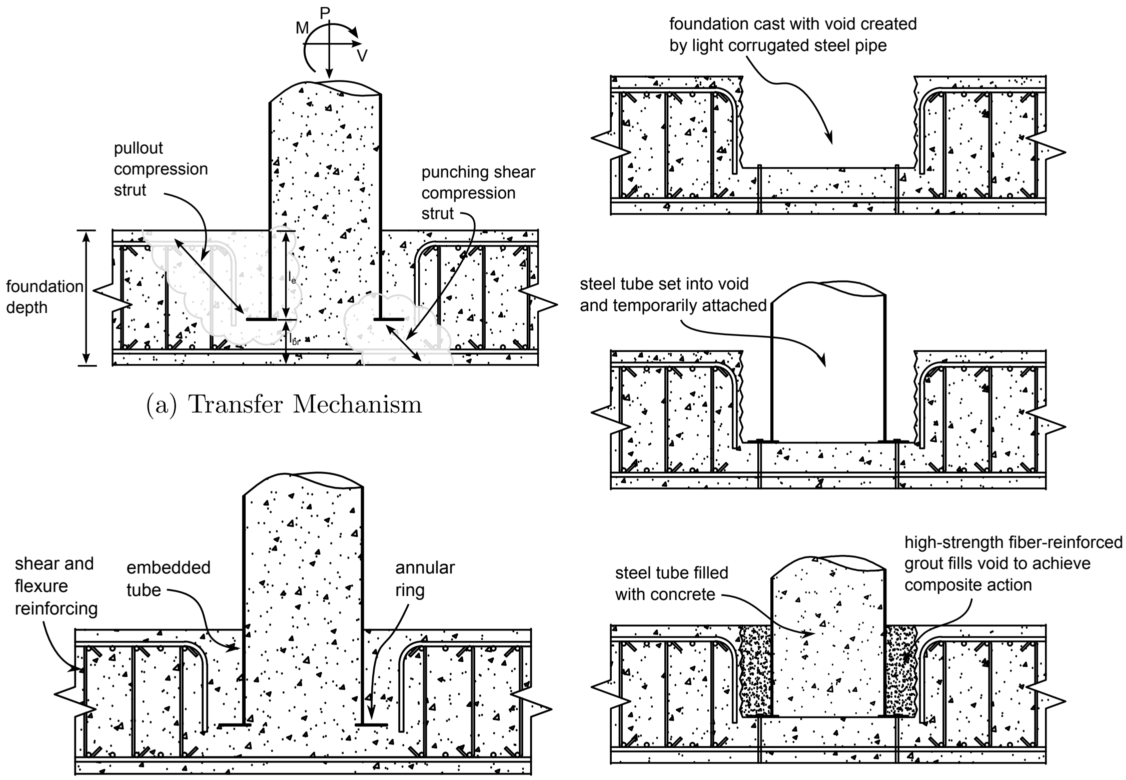

(a) Transfer Mechanism

(b) Monolithic Option

(c) Grouted Option

Figure 3.6: Foundation connection proposed at the University of Washington.

The tube and ring are placed into the void after the foundation is cast, and the recess between the tube and corrugated pipe is filled with high-strength, fiber-reinforced grout to anchor the column into the foundation. For both options, the steel tube is filled with low-shrinkage self-consolidating concrete to complete the CFST member, and no vibration is required [Lehman and Roeder, 2012b,a].

The compilation of the experimental programs to evaluate the CFST column-to-foundation connections consisted of a series of 19 large-scale specimens, which simulated approximately a half-scale bridge column [Kingsley, 2005; Williams, 2006; Lee, 2011; Lehman and Roeder, 2012b,a]. The details and geometry of a typical specimen are shown in Fig. 3.7, while specimen descriptions and nominal material strengths are summarized in Table 3.1.

The diameter and thickness of the steel tube in a majority of the specimens were 20-in. and 0.25-in. respectively, resulting in a diameter-to-thickness ratio D/t of 80. This meets the slenderness requirements in AASHTOa [2015]. The annular ring in all specimens extended 16t (4-in.) out from and 8t (2-in.) in to the steel tube respectively.

The dimensions of the footing as well as the primary flexure reinforcing were selected to provide adequate strength for the foundation to minimize the influence of footing size on the failure mode, resist Mp of the CFST without yielding, and to represent a scale model of a typical bridge footing. The imposed displacement history for a majority of the specimens was based on the ATC-24 protocol [ATC-24, 1992]. The majority of the specimens were subjected to approximately 10% of the gross compressive load capacity of the CFST column; however several additional axial load ratios were evaluated. A summary of the experimental results is included in Table 3.1, the moment-drift behaviors of several specimens are plotted in Fig. 4.6 and Fig.

As the testing program was so large, only the hysteretic performances of selected specimens are discussed here to highlight the influence of several different parameters on performance of the connection. These parameters include connection type, tube embedment depth, axial load ratio, and column diameter. In general, both the CIP and partial height pocket connections exhibited large strength and ductility so long as an adequate embedment depth was provided.

Specimens 13 and 14 (as summarized in Table 3.1) demonstrate the strength and ductility of the CIP and partial height pocket connection types respectively. As is illustrated by the hysteretic curves in Fig. 4.6, using a grouted connection type did not influence the performance of the embedded connection.

Specimens 1 and 3 demonstrate the strength and ductility as well as typical failure modes of adequately and inadequately embedded specimens. In summary, ductility of the inadequately embedded connections (Specimen 1) was ultimately limited by foundation damage as illustrated in Fig. 3.9a, while the failure mode of the adequately embedded

Table 3.1: Experimental Parameters and Material Properties

Spec.	$\frac{l_e}{D}$	Connection Type and Study Parameter	F_y (ksi)	F_u (ksi)	f'_c (ksi)	Tearing Drift	$\frac{M_{max}}{M_{P,PSDM}}$	Failure Mode
1	0.6	Monolithic connection, no vertical reinforcing	75	88	11	3.5%	0.88	Cone pullout
2	0.6	Monolithic connection, vertical reinforcing	75	88	11	4.2%	0.92	Cone pullout
3	0.9	Monolithic connection, embedment depth	75	88	10	8.0%	1.13	Cone pullout
4	0.6	Isolated connection, embedment depth	75	88	10	6.5%	0.98	Partial pullout
5	0.9	Isolated connection, flexible underlay	75	88	11.3	6.0%	1.15	Ductile tearing
6	0.75	Isolated connection, flexible underlay	75	88	11.9	6.0%	1.22	Ductile tearing
7	0.75	Monolithic axial load only, punching with 9-in. depth	75	88	9.3	NA	NA	Monotonic punching
8	0.75	Cyclic axial load only, punching with 9-in. depth	75	88	9.4	NA	NA	Cyclic punching
9	0.9	Isolated connection, galvanized tube	75	88	10	7.8%	1.27	Ductile tearing
10	0.9	Isolated connection - galvanized, near-fault load history	75	88	9.7	9.5%	1.30	Ductile tearing
11	0.9	Isolated connection, $0.15P_o$ axial load	75	88	9.3	9.2%	1.14	Ductile tearing
12	0.9	Isolated connection, $0.2P_o$ axial load	75	88	10	9.0%	1.23	Ductile tearing
13	0.8	Monolithic connection, straight seam tube	79	60	8.7	11.6%	1.17	Ductile tearing
14	0.77	Isolated connection, straight seam tube	79	60	9.4	10.4%	1.17	Ductile tearing
15	0.77	Isolated connection, spiral weld tube/evaluate l_e	51	78	7.8	10.2%	1.14	Ductile tearing
16	0.8	Monolithic connection, spiral weld tube/evaluate l_e	51	78	8.7	7.3%	1.07	Ductile tearing
17	0.7	Isolated connection, spiral weld tube/evaluate l_e	51	78	9.9	7.4%	1.31	Ductile tearing w/ cracking
18	0.6	Isolated connection, spiral weld tube/evaluate l_e	51	78	10.2	7.4%	1.22	Ductile tearing w/ cracking
19	0.62	Isolated connection Larger, 30-in. tube $0.05P_o$ axial load	51	78	11.2	7.0%	1.3	Ductile tearing w/ cracking

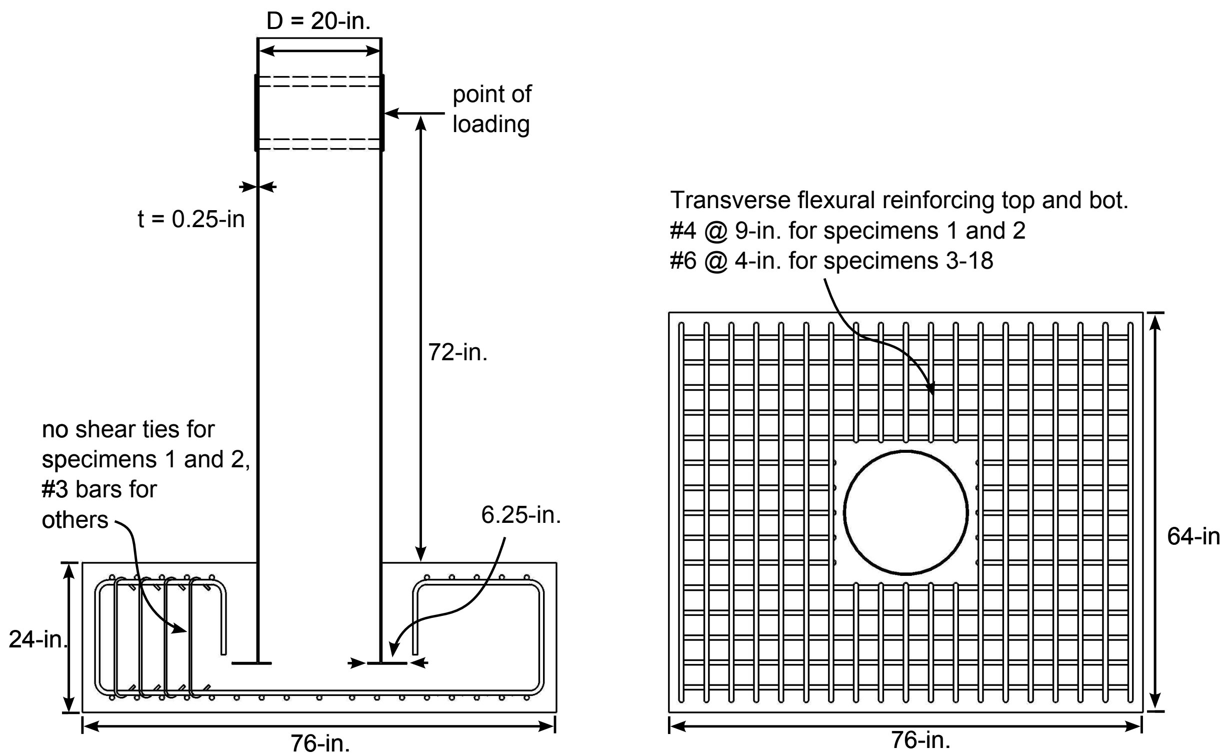

Figure 3.7: Typical specimen geometry and reinforcing.

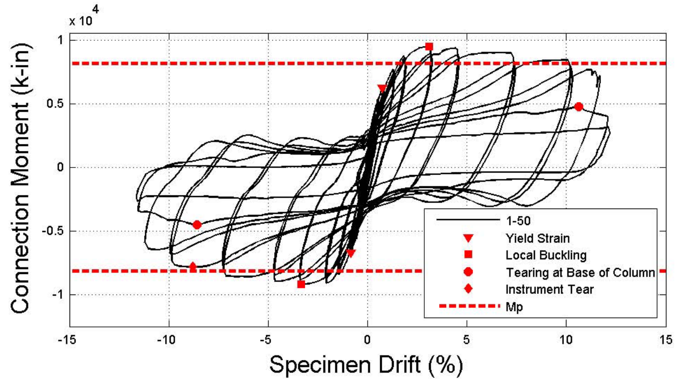

(a) Specimen 13 (CIP Connection)

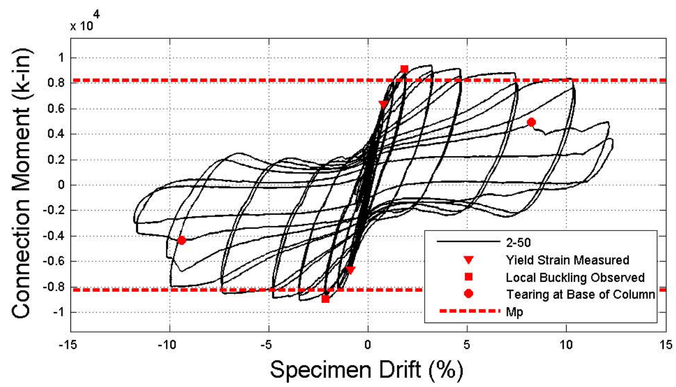

(b) Specimen 14 (Partial Height Pocket Connection)

Figure 3.8: Typical Moment-Drift Response for CIP and Partial Height Socket Connection Types [Lee, 2011]

connections (Specimen 3) was characterized by ductile tearing of the steel tube as shown in Fig. 3.9b, which occurred at the location of local buckling (see Fig. 3.10b).

Specimens 11, 12, and 19 evaluated the influence of the axial load ratio on the behavior of the embedded connections. These specimens were subjected to constant axial load ratios of 15%, 20%, and 5% respectively, and were subjected to an increased cyclic lateral loading. Specimen 19 was tested as part of the prior phase of the research discussed in this report. The axial load ratio did not greatly influence the behavior of the embedded connection as is illustrated by the hysteretic curves shown in Fig. 3.11.

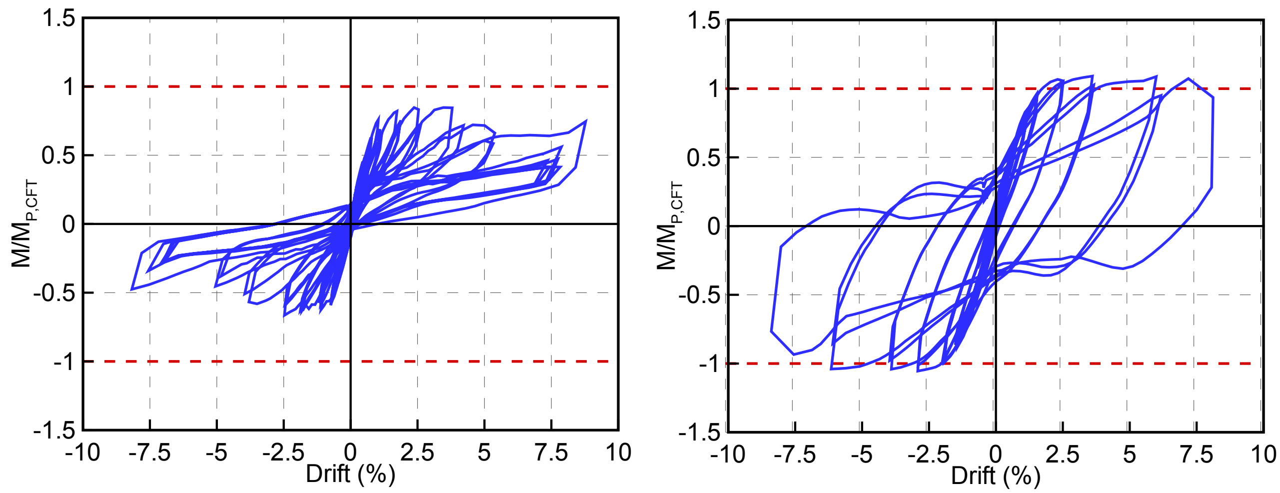

(a) Specimen 1(Inadequately Embedded) (b) Specimen 3(Adequately Embedded)

Figure 3.9: Typical Moment-Drift Response for Inadequately and Adequately Embedded Specimens [Kingsley, 2005]

In addition to evaluating the influence of varying axial load ratio on the embedded connection, the hysteretic curves shown in Fig. 3.11 illustrate that the embedded connection can develop the full plastic capacity of the CFST for fairly large connection diameters. Specimen 19 is the largest CFST ever tested, with a diameter of 30-in.

3.1.2.2 Design Expressions from the University of Washington Tests

Annular Ring

The annular ring is welded to tube using complete joint penetration welds or fillet welds on both the inside and outside of the column designed to transfer the full strength of the tube to provide anchorage and stress transfer. The ring is made of steel of the same thickness and similar yield stress as the steel tube. It was initially recommended that the ring extends into the tube 8 times the tube thickness and out of the tube 16 times the tube thickness to provide adequate anchorage.

EmbedmentDepth

(a) Foundation Failure (b) Tube Local Buckling (c) Ductile Tube Tearing

Figure 3.10: Photos of connection behavior [Kingsley, 2005].

The required embedment depth, le, of the CFST was determined using a conical pullout model discussed in detail in reference material [Lehman and Roeder, 2012b,a]. The required embedment depth to eliminate the potential for foundation failure is given in Equation 3.1 as:

$$L_e = \sqrt{\frac{D_o^2}{4} + \frac{DtF_u}{6\sqrt{f'_{cf}}}} - \frac{D}{2} \text{ (psi)} \tag{3.1}$$

where D_o is the outside diameter of the annular ring and corrugated pipe for the monolithic and grouted connections respectfully and $F_{u,st}$, D, and t are the diameter, thickness, and ultimate stress of the steel tube, and f'_{cf} is the compressive strength of the foundation concrete in psi.

Punching Shear

Adequate concrete depth must be provided below the tube to eliminate the potential for punching shear failure in the foundation. The ACI [2011] provisions for footings in single shear were used as a basis to develop an expression for the minimum foundation depth, df, to avoid this failure mode. This expression is given in Equation 4.1 as:

$$d_f = \sqrt{\frac{D^2}{4} + \frac{C_c + C_s}{4\sqrt{f'_{cf}}}} - \frac{D}{2} \text{ (psi)} \tag{3.2}$$

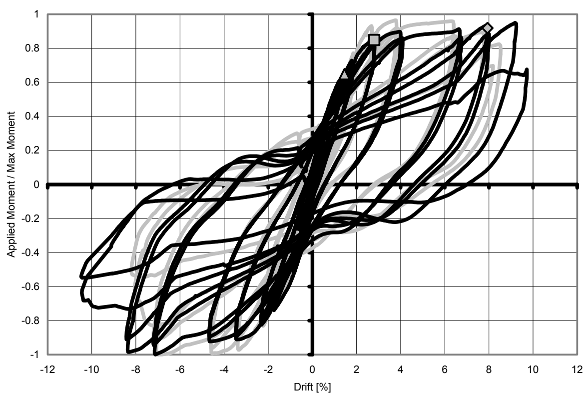

(a) Specimen 11

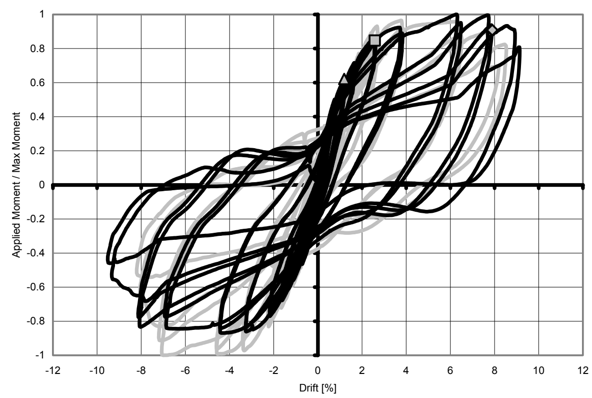

(b) Specimen 12

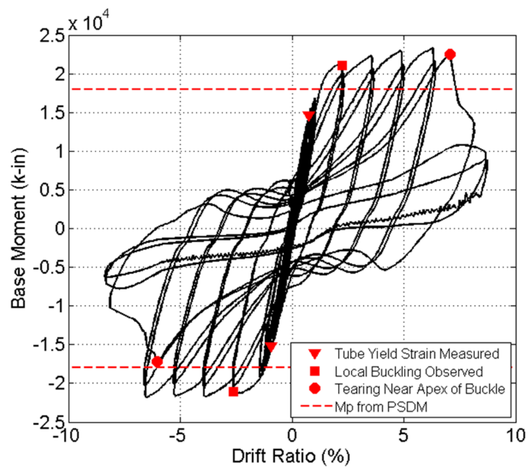

(c) Specimen 19

Figure 3.11: Typical Moment-Drift Response for Embedded Connection Specimens Subjected to Axial Load Ratios of (a) 15 (b) 20%, and (c) 5%

where C_c and C_s are the compressive forces in the concrete and steel due to the combined axial load and bending moment as computed using the PSDM.

3.1.3 Modeling CFST Components and Connections

3.1.3.1 Continuum Analysis of the Embedded Ring Foundation Connection

A comprehensive series of nonlinear continuum analyses were performed using the finite element analysis software ABAQUS to extend the experiments summarized in Table 3.1 to a wider range of the experimentally studied parameters and include unstudied parameters [Moon et al., 2013]. An overview of the numerical model is shown in Fig. 3.12. Model geometry included the embedded CFST column-to-foundation connection, the CFST column, and the reinforced concrete foundation. A half model was developed taking advantage of symmetry in the plane parallel to the direction of loading and the center of the specimen; this increased computational efficiency. The nodes at the base of the footing were fully restrained, and lateral loading was applied by assigning displacements δ_y along the y-axis to the top nodes of the concrete fill and steel tube. A distributed axial load was applied to the top of the concrete and steel tube using the pressure load option in ABAQUS. A constant axial load of $0.1P_o$ was applied in for most models unless the axial load ratio was being evaluated.

The 4-node shell element with reduced integration (S4R), 2-node truss element (T3D2), and 8-node solid element with reduced integration (C3D8R) were used to model steel tube, reinforcing steel, and concrete elements, respectively. Gap elements were used at every nodal point that was geometrically common to the steel tube and concrete fill elements to simulate bond stress between the concrete by combining the confining contact stress with a coefficient of friction to develop shear stresses at the interface; penetration of the concrete element by the steel element was prevented. The reinforcing steel and concrete components in the footing were spatially assembled, and interactive constraint relationships were defined using the ABAQUS Embedded constraint to perfectly embed the reinforcing bar in the concrete.

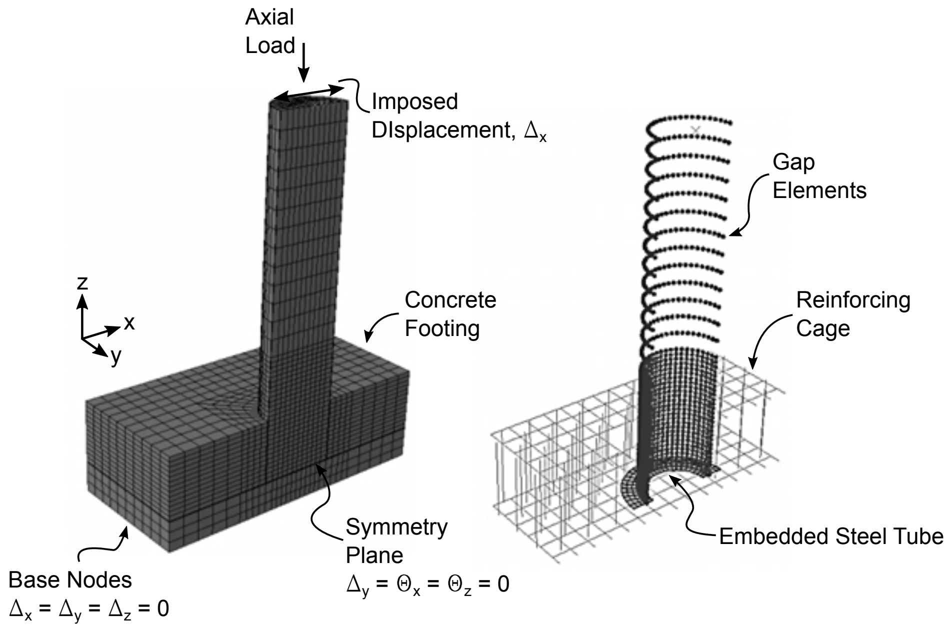

Figure 3.12: Overview of Finite Element Model of CFST Column-to-Foundation Connection

This constraint does not allow for relative slip between the reinforcing bar and concrete components.

Material nonlinearity was incorporated using the concrete damaged plasticity model for concrete and a trilinear stress strain relationship with isotropic hardening for steel. The numerical values to define the properties in these constitutive models were calibrated to numerical properties of past CFST column-to-foundation connection experiments. Mesh refinement in the CFST column-to-foundation model was primarily concentrated in the plastic hinge and embedded regions of the steel tube due to the load and deformation demands in these regions. Global mesh convergence of the concrete components in the foundation and the steel and concrete components in the CFST was conducted by analyzing the maximum numerical moment capacity of each specimen. The final mesh size in the critical region adjacent to the foundation was approximately 1-in.x1-in. for the shell elements in the steel tube, and 1-in.x1-in.x1-in. for the concrete block elements.

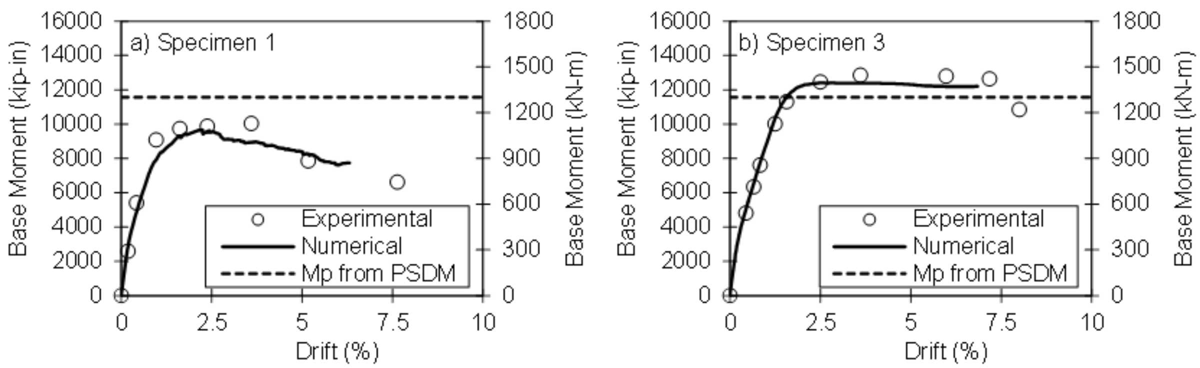

Figure 3.13: Comparison of Predicted and Measured Base Moment vs. Drift for (a) Specimen 1 and (b) Specimen 3

The experimental and numerical base moment-drift relationships from Specimens 1 and 3 (as defined in Table 3.1) are shown in Fig. 3.13. From this figure, it can be seen that the numerical results accurately predict the stiffness, strength, and post-peak behavior of the CFST and CFST column-to-foundation connection for adequate and inadequate embedment depths.

Furthermore, the experimental failure modes characterized by extensive cracking in the footing or local buckling in the tube for inadequate and adequate embedment depths respectively were accurately captured in the numerical results. As described above, Specimen 1 failed due to extensive footing damage. The numerical and experimental crack formation results for this specimen are compared in Fig. 3.14a. In both cases, cracks radiating diagonally from the column are observed. Note that cracking in the numerical results was predicted using the maximum principal plastic strain output variable. The direction of the vector normal to the crack plane is assumed to be parallel to the direction of the line of action of the maximum principal plastic strain tensor [Simulia, 2015]. Specimen 3 developed the full flexural capacity of the CFST and sustained large load and deformation demands with little or no damage to the footing. The failure mode of this specimen was characterized by local buckling and ductile tearing of the steel tube near the footing interface. The local buckling behavior was captured in the numerical results as is shown in Fig. 3.14b. Note that the essentially elastic behavior of the footing was also captured.

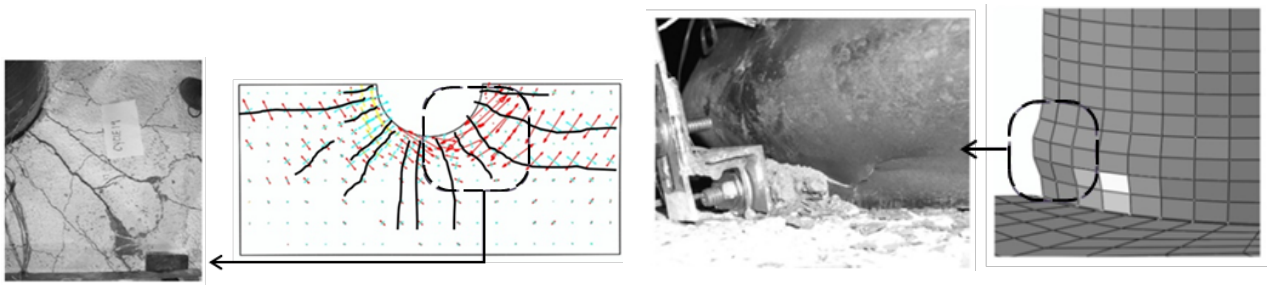

(a) Cracking Pattern of Specimen 1 at 5%

(b) Local Buckling of Specimen 3 at 6%

Figure 3.14: Simulated and Experimental Damage Patterns

3.1.3.2 Reduced Order Modeling of CFST Components

Reduced order line element modeling procedures for CFST have previously been proposed. M.D. Denavit [2010] provides recommendations for modeling CFST components using the open source finite element analysis software OpenSees. A wide range of numerical topics are discussed, however of specific interest to this research are the proposed constitutive models for the steel and concrete materials. Constitutive models which account for the salient properties of concrete and steel (i.e. concrete crushing and tube yielding and buckling) as well as interactions between the two (i.e. confinement) are essential to modeling the response of CFST.

Concrete confinement plays a large role in the response of CFST. M.D. Denavit [2010] utilized the confinement model of J.B. Mander [1988] (defined in Equation 3.3) in conjunction with a lateral confinement pressure (f_l) defined as a function of the hoop stress as well as the D/tratio of the steel tube as given in Equation 3.4. Note that the hoop stress is expressed as function of the yield stress ($\alpha_\theta F_y$) where α_θ is the ratio of hoop stress to yield stress.

$$f'_{cc} = f'_c \left(-1.254 + 2.254\sqrt{1 + \frac{7.94 f_l}{f'_c}} - 2\frac{f_l}{f'_c} \right) \tag{3.3}$$

$$f'_l = \alpha_\theta F_y \frac{2}{D/t - 2} \tag{3.4}$$

An expression for the hoop stress ratio (α_θ) was developed empirically using a least squares optimization which reduced the error between computed and experimental strengths as defined in Equation 3.5.

$$\alpha_\theta = 0.138 - 0.00174(D/t) \geq 0 \tag{3.5}$$

The strain at peak stress for unconfined concrete (ϵ_c) was calculated using recommendations from J.B. Mander [1988](Equation 3.6), and the increase in strain at peak stress due to confinement (ϵ_{cc}) was calculated using recommendations from F.E Richart [1929](Equation 3.7).

$$\epsilon_c = \frac{f'_c[MPa]^{(1/4)}}{28} \tag{3.6}$$

$$\epsilon'_{cc} = \epsilon_c(1 + 5(f'_{cc}/f'_c - 1)) \tag{3.7}$$

The post-peak descending branch was defined using an r factor which was calibrated such that the energy represented by the computed force-deformation response was equal to the corresponding energy obtained from experiments. Two r values are used; one in the pre-peak range, and one in the post peak range as defined in Equation 3.8 [M.D. Denavit, 2010].

$$r = \begin{cases} f'_c[MPa]/5.2 - 1.9 \rightarrow for \epsilon > \epsilon'_{cc} \\ 0.4 + 0.016(D/t)(f'_c/F_y) \rightarrow for \epsilon \leq \epsilon'_{cc} \end{cases} \tag{3.8}$$

Under compressive loading, the steel tube is susceptible to local buckling. The initiation of local buckling can be determined using strain limits in the steel tube as defined in Equation 3.9 where ϵ_{lb} is the strain at local buckling, ϵ_y is the yield strain, and R is a stiffness parameter defined in Equation 3.10 [M.D. Denavit, 2010]. Note if strain at local buckling is less than the yield strain, then the local buckling is considered elastic.

$$\epsilon'_{lb} = \epsilon_y(0.2139R^{-1.413}) \tag{3.9}$$

$$R = \frac{D}{t}\frac{F_y}{E_s} \tag{3.10}$$

3.2 Dowel Connections for Precast Concrete Components

Using precast concrete elements in highway bridge construction is a method to achieve ABC. These elements are fabricated in a controlled environment off site which improves material quality and product durability. Once on site, they can be rapidly assembled without the construction of temporary shoring or flexible reinforcing cages which decreases construction time and cost and minimizes traffic impacts.

A significant amount of research has been conducted to develop construction details for precast elements (including individual dowel, full height pocket, and partial height pocket connections), and they have successfully been implemented around the United States [Restrepo et al., 2011]. However, precast elements have limited use in regions of high seismicity is due to uncertainty of their strength and ductility of the connections. Column-to-bent cap connections are a concern because they transfer forces and moments and connection damage can lead to system failure. Considerable research has been conducted on precast connections which exhibit adequate performance during lateral loading events. Since this research is focused on ABC with CFST, precast pier caps are of interest, and a review of precast connections offers options for CFST to precast cap beam connections.

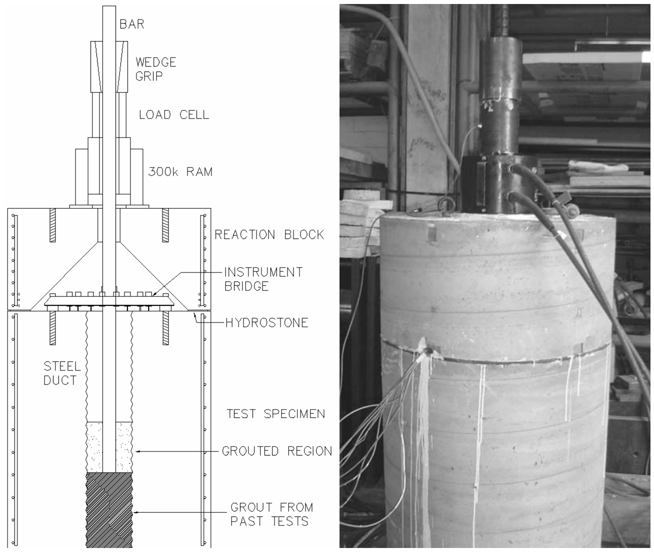

Figure 3.15: Grouted Large Bar Pullout Test Apparatus [Raynor et al., 2002; Stueck et al., 2007, 2009]

A research program was undertaken at the University of Washington to evaluate the feasibility of using large bars grouted into individual ducts [Raynor et al., 2002], and to develop and evaluate individual dowel type column-to-cap beam connections for ABC [Stueck et al., 2007, 2009; Pang et al., 2008, 2010].

Raynor et al. [2002] and Stueck et al. [2007, 2009] conducted full-scale pullout tests on No. 8, No. 10, and No. 18 bars grouted into ducts. An overview of the test setup is shown in Fig. 3.15 The experiments showed that yielding of the bars could be achieved in lengths as low as 6db, while the ultimate strength could be achieved in 14db. These tests demonstrated that grouted large bar connections could practically be used within the depth of common precast bent cap sections.

Pang et al. [2008] and Stueck et al. [2007] completed a survey of column-to-cap beam connections which evaluated fabrication and construction difficulties as well as the structural behavior of several RC connection types. Based on the results of the survey, a large bar connection type was selected for experimental investigation. The concept of this connection is the improvement of construction tolerances through use of a reduced number of large longitudinal column bars in the place of a large number of smaller longitudinal bars. Transitioning to larger bars, however, is challenging because of the increased development lengths.

Pang et al. [2008, 2010] and Stueck et al. [2007, 2009] conducted tests on four 42% scale columns to evaluate the performance of the large bar individual dowel type connection. One of the columns served as a base-line specimen with 16 No. 5 longitudinal bars constructed using typical CIP methods. The other three columns used 6 No. 8 bars with differing de-bonded lengths. The purpose of the de-bonding was to distribute plastic strain across a longer effective length to decrease stress concentrations at the column-to-cap interface. An overview of the large bar connection specimen is shown in Fig. 3.16.

The columns were subjected to a constant axial load and cyclic lateral loading protocol. Results from the experiments showed that the large bar connections perform similarly to comparative CIP connections. De-bonding the bars had a limited influence on the performance, as it was conjectured that the fully bonded specimens naturally de-bonded during testing. All specimens exhibited a stable hysteretic response through cycling from 5%-7%. Further, extreme concrete damage and bar fracture was observed at the end of each test.

The National Cooperative Highway Research Program Project 681 was conducted by Restrepo et al. [2011] with the objective of developing and validating design methodologies, specifications, design examples, and example connections details for precast bent systems for use in seismic areas in the United States. This project conducted a survey of existing practice precast bent cap systems, developed a series of connection details for experimental analysis, and ultimately provides recommendations to facilitate the implementation of precast bent cap systems. The connections evaluated in this report ranged from emulative (designed to emulate the behavior of typical CIP RC connections) to hybrid details which include self-centering post-tensioned concrete and concrete filled tube columns. The 681 document

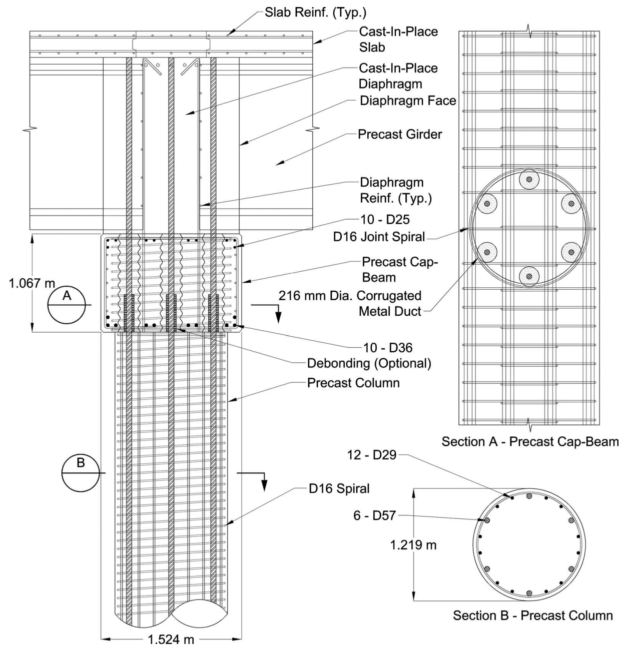

Figure 3.16: Typical Large Bar Connection Specimen [Pang et al., 2008; Stueck et al., 2009]

provides valuable information regarding state-of-practice and innovative connections for precast components.

As part of the NCHRP 12-74, tests were conducted on four 42% scale column to cap beam connections. The specimen geometry consisted of a 35-in high, 20-in. diameter column connected to a 12-ft long cap beam with a height and width of 25-in. The four connection types consisted of a typical CIP connection, a individual duct grouted bar connection (shown in Fig. 3.17a), and two full height pocket connections in which a void was created in the cap beam using a corrugated pipe as illustrated in Fig. 3.17b. Typical specimen geometry is illustrated in Fig. 3.18.

The columns were subjected to constant axial load and a cyclic lateral loading protocol. Results from the experiments showed that the emulative precast connections could develop the capacity of the RC columns. However, the grouted duct and full height pocket connections exhibited extremely low displacement capacities before resistance dropped below

(a) Duct Connection

(b) Pocket Connection

Figure 3.17: Grouted Duct and Pocket Cap Beam Connection Evaluated by Restrepo et al. [2011]

80% of the recorded maximum (5.5% drift and 4.5% for the grouted duct and full height connections respectively).

A research program was undertaken at the University of Washington to develop damage-resistant wharf pile connections [Jellen, 2008; Stringer, 2010]. The specimens consisted of a 24-in. diameter prestressed concrete pile embedded 3-in. into a CIP deck segment. The connections consisted of eight No. 10 T-headed dowel bars, which were grouted into the pile for a length of 16db. An overview of specimen geometry is shown in Fig. 3.19. The primary parameter of interest in these experiments was the inclusion of a bearing pad between the precast wharf-pile and CIP pile cap to limit damage at the interface. This research has been included here as the proposed WD connection utilized both headed dowels and de-bonding along the length of the dowels at the interface.

The specimens were subjected to a constant axial load ranging from 10% to 20% of the theoretical crushing load of the wharf pile, and an reversed cyclic lateral load was applied according to the ATC-24 protocol. In general, all of the connections exhibited largely stable

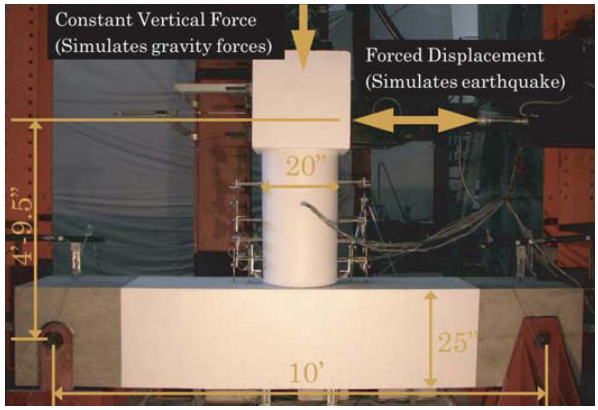

Figure 3.18: Typical Specimen Geometry from Restrepo et al. [2011]

hysteretic behaviors. Furthermore, all of the connections appeared to displace in near rigid body rotation. The inclusion of the bearing pad between the wharf pile and pile cap delayed the onset of pile cover spalling by up to 3.5% drift, and debonding the longitudinal reinforcing in the pile significantly decreased strain demands in the critical region adjacent to the wharf pile.

Figure 3.19: Specimen Geometry from Stringer [2010]

Chapter 4

ANALYTICAL INVESTIGATION TO INFORM REFERENCE SPECIMEN DESIGN

This chapter discusses a detailed numerical study used to evaluate and select the values of the key parameters for the test specimens. First, the geometry of the prototype structure is introduced and the study area is highlighted. The numerical model is introduced in Section 4.2, and numerical results are given in Sections 4.3 and 4.4. The primary study parameters included: (1) the type of connection (ER, WD, and RC), (2) limits on cap beam width with the ER connection, (3) limits on the annular ring diameter with the ER connection, (5) de-bonding the bars with the WD connection detail, and (6) direction of loading (transverse and longitudinal).

4.1 Prototype Structure

Specimens for the numerical and experimental programs were designed using the Laguna De Santa Rosa Bridge located outside of Santa Rosa, California as a prototype. An overview of the prototype bridge is shown in Fig. 4.1. The columns in this prototype bridge are reinforced concrete with 48-in. diameter, and are detailed using 32 bundled No. 11 longitudinal bars, and No. 8 hoops at 6-in. on-center in the transverse direction. These columns were redesigned using CFST columns with equivalent strength under combined axial-moment (P-M) loading as well as equivalent stiffness, which resulted in CFST members with a thickness and diameter of 0.5-in. and 42-in. respectfully and a diameter to thickness ratio (D/t) of 84. A detailed overview of the re-design is included Appendix A. The CFST connection specimens were scaled using the redesigned CFST column as a prototype column. The original RC column and redesigned CFST column are shown in Fig. 4.1.

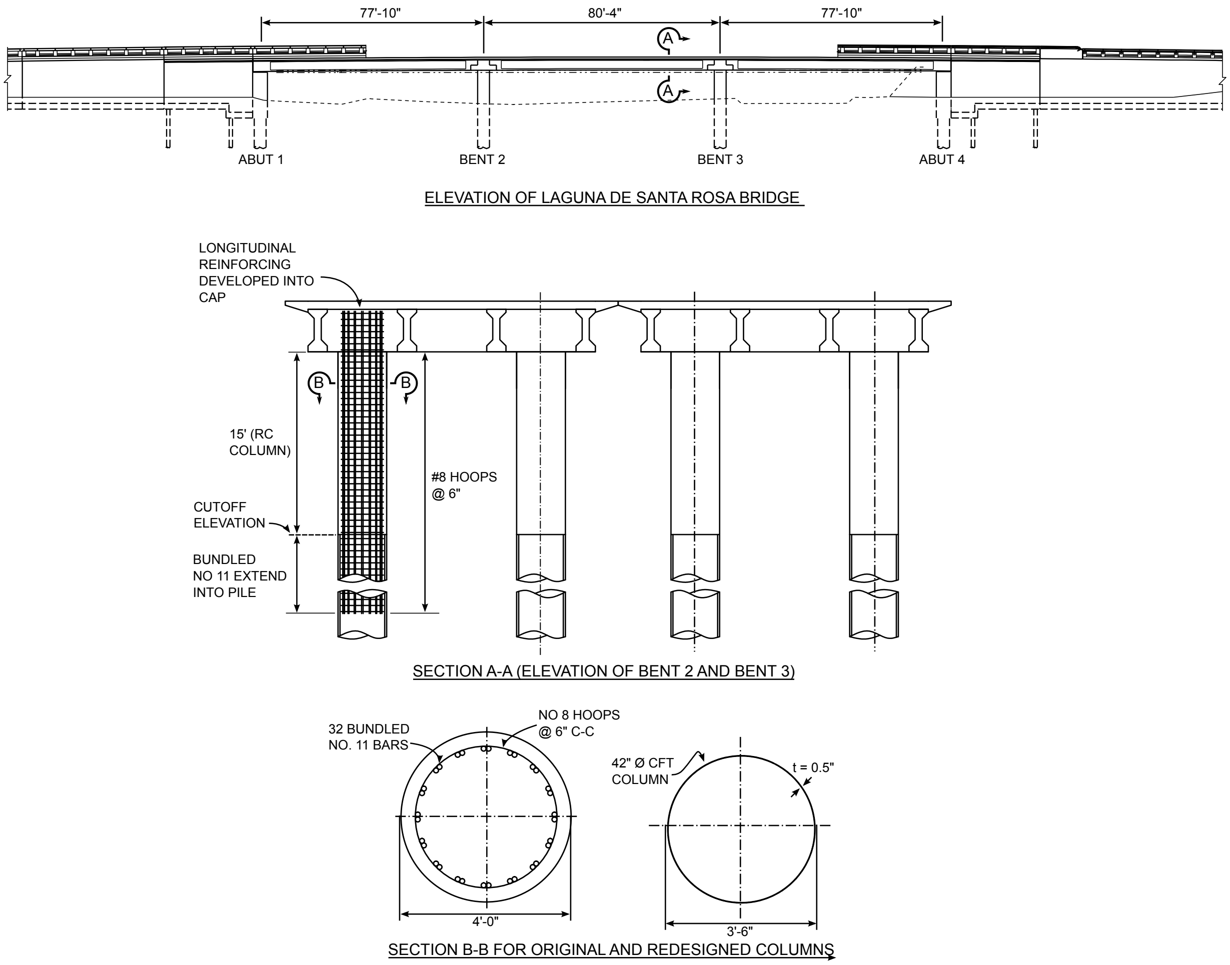

Figure 4.1: Prototype Bridge

The reference specimens were large-scale models of the prototype connections, and the scale was selected to adapt to the available test rig in University of Washington Structural Research Laboratory. Specimen geometries were selected to evaluate the response of the ER connection for two distinct loading scenarios: (1) loading in the tranverse direction of the bridge (illustrated in Fig. 4.2a) and (2) loading in the longitudinal direction of the bridge(illustrated in Fig. 4.2b). The longitudinal loading scenario was included due to a lack of information in literature regarding the response of bridge structures for loading in this direction.

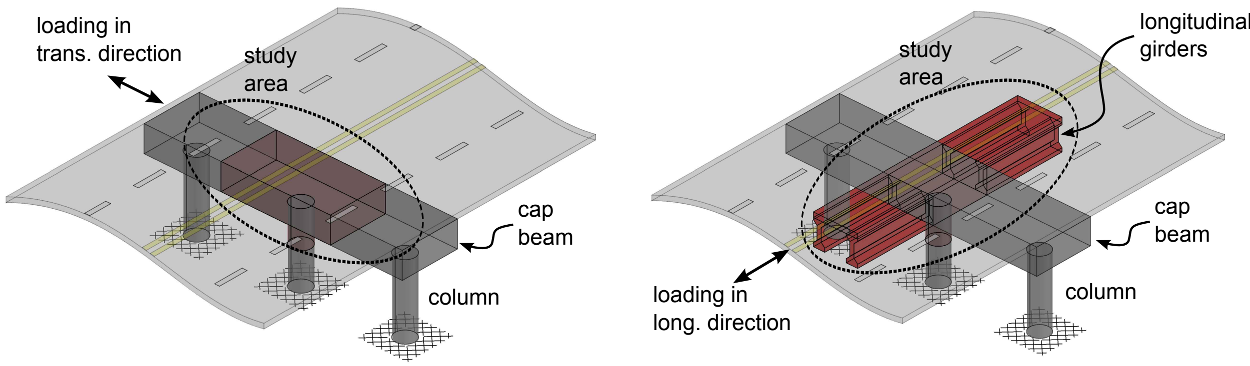

(a) Transverse Study Area

(b) Longitudinal Study Area

Figure 4.2: Overview of Study Area for Transverse and Longitudinal Loading

4.2 Overview of Numerical Analysis

A limited numerical study was conducted in both the transverse and longitudinal directions to evaluate the behavior of the proposed cap beam connections and inform the design of the experimental specimens.

The commercially available finite element analysis software ABAQUS was used to perform a preliminary series of nonlinear analyses on the ER, WD, and RC cap beam connections in the transverse direction, and the ER connection in the longitudinal direction. An overview of the numerical model for the transverse analyses is shown in Fig. 4.3, while the longitudinal model is summarized in Fig. 4.4.

Model geometry in the transverse direction included the CFST column-to-cap beam connection, the CFST column, and the reinforced concrete cap beam as illustrated in Fig 4.2a. Geometry in the longitudinal direction included the CFST column-to-cap beam connection, the CFST column, a precast inverted-T, a CIP diaphragm, dapped ended precast girders, and a deck as shown in Fig. 4.2b. A half model was developed taking advantage of symmetry in the plane parallel to the direction of loading and the center of the specimen; this increased computational efficiency. The CFST column was modeled using 3-dimensional elements for a length of 2 times the diameter of the column. The remainder of the length was modeled using the ABAQUS MPC constraint tied to a reference point. This approach models the remaining length of the column as a rigid beam to decrease computation time. The nodes at the top of the cap beam were restrained to simulate the boundary conditions of future experimental tests, and lateral loading was applied by assigning monotonic displacements δx along the x-axis to the reference point.

A distributed axial load was applied to the top of the concrete and steel tube using the pressure load option in ABAQUS. A constant axial load of 0.1Po was applied for most models unless the axial load ratio was being evaluated.

The 4-node shell element with reduced integration (ABAQUS element type S4R), 2-node truss element (ABAQUS element type T3D2), 2-node beam element (ABAQUS element type B31), and 8-node solid element with reduced integration (ABAQUS element type C3D8R) were used to model steel tube, cap beam reinforcing steel, connection reinforcing steel (for WD and RC), and concrete elements, respectively.

Gap elements were used at every nodal point that was geometrically common with the steel tube and concrete fill elements to simulate bond stress between the concrete by combining the confining contact stress with a coefficient of friction to develop shear stresses at the interface; penetration of the concrete element by the steel element was prevented.

The reinforcing steel and concrete components in the cap beam were spatially assembled, and interactive constraint relationships were defined using the ABAQUS Embedded constraint to perfectly embed the cap beam reinforcement in the cap beam concrete. This constraint does not allow for relative slip between the reinforcing bar and concrete components. The interaction between the connection reinforcing steel and the concrete is more complex and required a more robust interaction approach. Spring elements were used to connect every nodal point that was geometrically common between the concrete and connection reinforcing. These elements allowed for the definition of a bond-slip interaction, as well as de-bonding of the reinforcing in the cases when the longitudinal dowels were de-bonded in the WD connection.

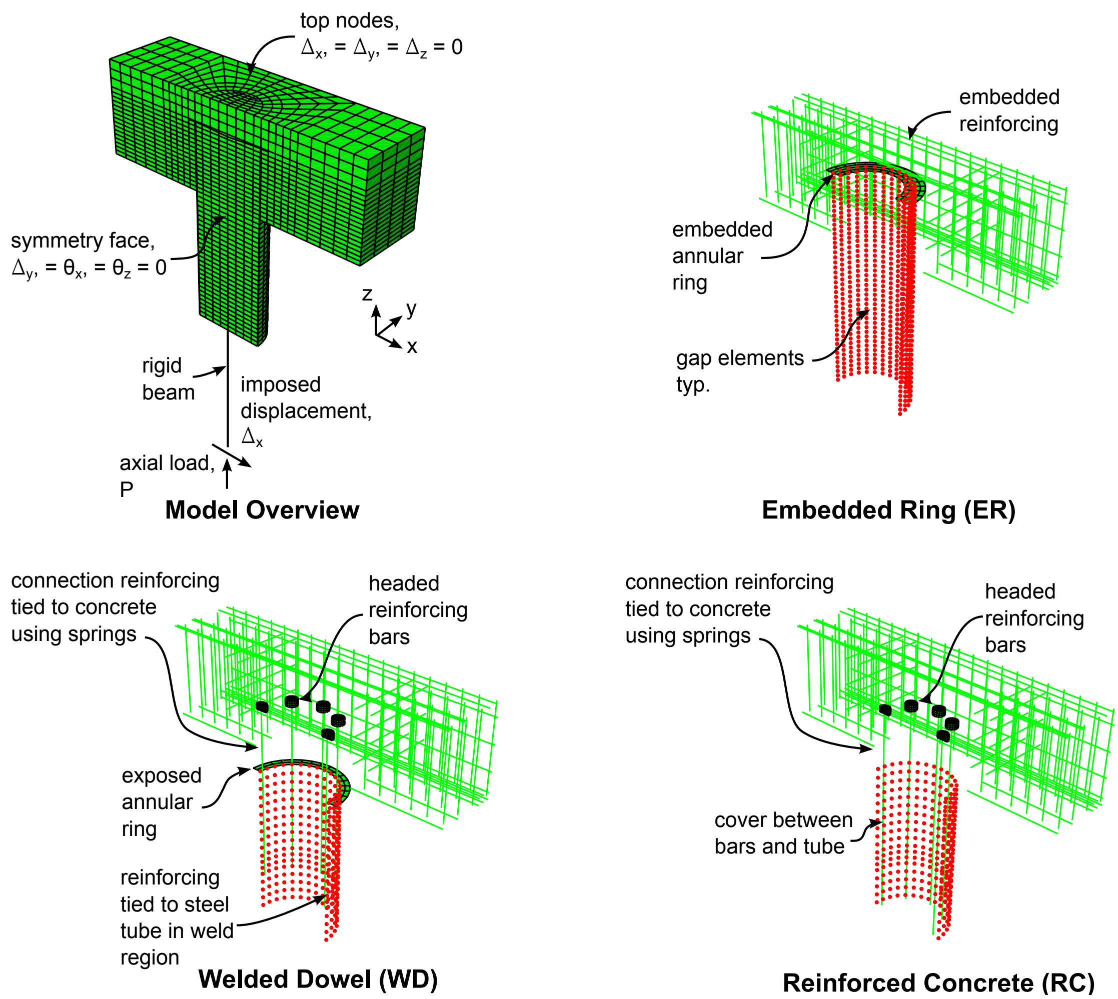

Figure 4.3: Transverse Model Overview

Mesh refinement in the CFST column-to-cap beam model was primarily concentrated in the plastic hinge and embedded regions of the steel tube due to the load and deformation demands in these regions. Global mesh convergence of the concrete components in the cap beam and the steel and concrete components in the CFST was conducted by analyzing the maximum numerical moment capacity of each specimen.

Material nonlinearity was incorporated using the concrete damaged plasticity model for concrete and isotropic hardening for steel. The concrete damaged plasticity model utilizes a non-associative flow rule and can capture the influence of tri-axially dependent

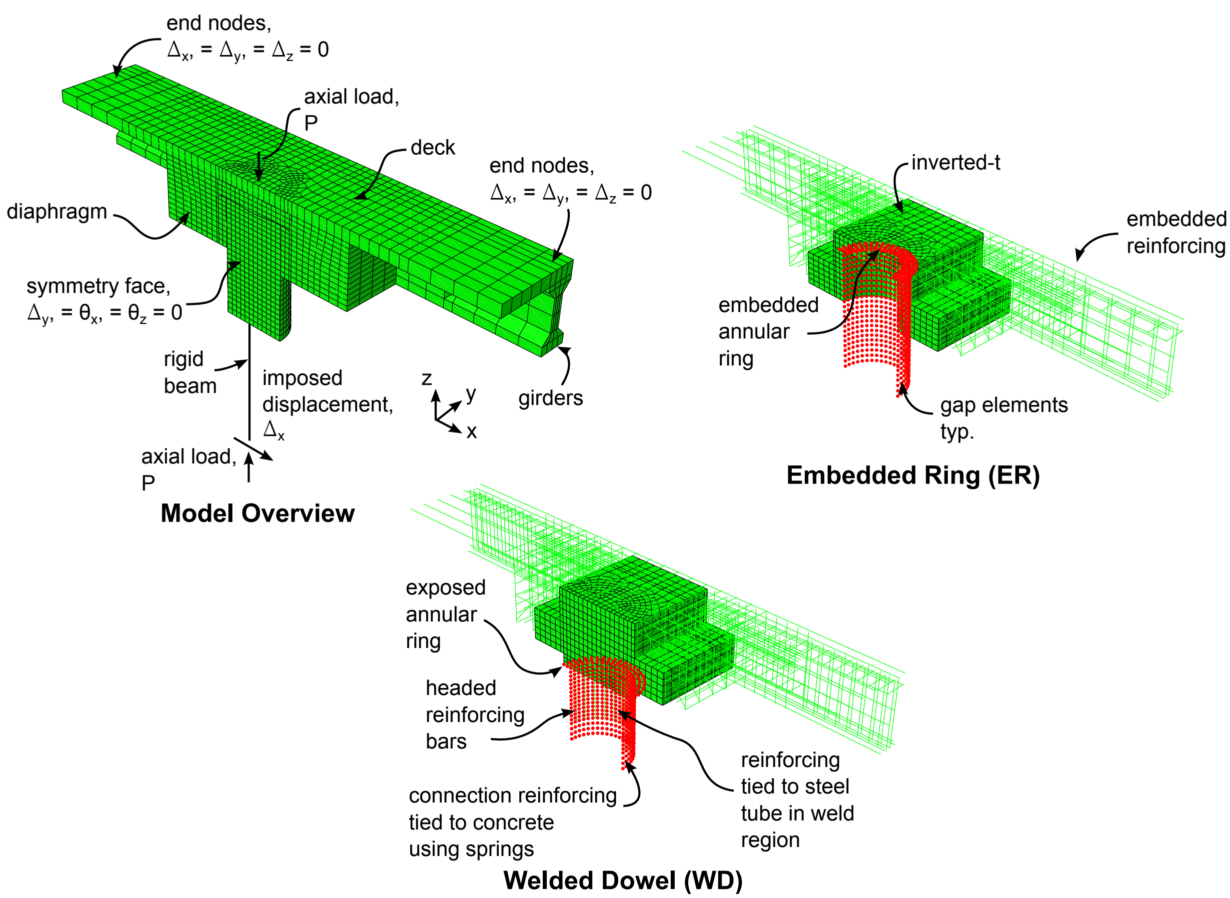

Figure 4.4: Longitudinal Model Overview

plastic hardening as well as a reduction in tensile and compressive stiffness in cyclic loading applications (Lee and Fenves, 1998). The compressive stress-strain behavior of the concrete was defined using a relationship proposed by Saenz (1964) in which linear elastic behavior is assumed up to a concrete stress of $0.5f'_c$ and a maximum compressive stress is achieved at a compressive strain of 0.003. The tensile stress strain behavior was modeled using a relationship developed by Hsu and Mo (2010) where linearity is assumed up to the cracking stress of the concrete, $f_{cr} = 7\sqrt{f'_c}$, and the softening relationship is defined as:

$$L_t = f_{cr}\left(\frac{\epsilon_{cr}}{\epsilon_c}\right)^{0.4} \tag{4.1}$$

where ϵ_{cr} is the cracking strain of concrete. The compressive and tensile stress-strain relationships used to define the concrete behavior are shown in Fig. 4.5a.

A tri-linear stress strain relationship with isotropic hardening was used to define the behavior of the tube steel and reinforcing bars. The plastic plateau was terminated when the strain in the steel, ϵ_s was 10 times the yield, and the ultimate stress, $F_{u,st}$, was assigned at an ultimate steel strain $\epsilon_{su} = 0.1$. The stress-strain relationship used to define the steel components is shown in Fig. 4.5b.

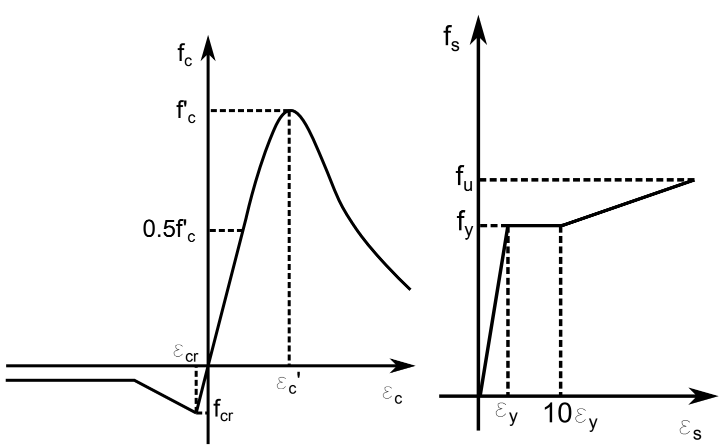

(a) Concrete (b) Steel

Figure 4.5: Material models.

The material models were calibrated for monotonic loading. Extending the concrete constitutive models available in ABAQUS to cyclic applications presents many problems with regards to crack closure in reversed cyclic tension-to-compression loading applications. Damage implementation in the model was investigated for the concrete damaged plasticity model. A smeared cracking formulation was also investigated, but ultimately not used in this research.

4.3 Numerical Studies for Loading in the Transverse Direction

A limited series of numerical studies were conducted to evaluate the influence of different parameters on the performance of the proposed CFST column-to-cap beam connections in the transverse direction. The parameters included: (1) the type of connection (ER, WD, and RC), (2) limits on cap beam width with the ER connection, (3) limits on the annular ring diameter with the ER connection, and (5) de-bonding the bars with the WD connection detail. The steel tube and reinforcement were assigned nominal yield strengths of 49-ksi and 60-ksi respectively, while the concrete was assigned a nominal compressive capacity of 6-ksi.

4.3.1 Type of Connection

Normalized moment-drift relationships, accumulated plastic concrete strain distributions, and stress distributions for the different connection types are plotted in Fig. 4.6, and the maximum stress recorded in the cap beam flexure and shear reinforcing are illustrated in Fig 4.7. The moments were normalized to $M_{P,PSDM}$ of the CFST.

For all connection types, the plastic strain was isolated to the connection region of the CFST with limited inelastic behavior in the cap beam, as illustrated in Fig. 4.6b. However, there is significant difference in the response of the concrete. The large stress and strains in the ER connection occur within the highly confined concrete in the CFST, while the WD and RC connections developed large concrete strains and stresses in areas of the connection and the cap beam, which have lesser confined strength and strain capacities than the interior of the CFST. The shear and flexure reinforcing in the cap beam remained well below the nominal yield stress of the reinforcing (f_y=60-ksi) through 10% drift for all connections as indicated in Fig. 4.7.

The dowels of the WD and RC connections yield within the column and joint region. The RC and WD connections did not achieve the plastic moment capacity of the CFST, but they did achieve the moment capacity of the RC section. However, these connections will be affected by size and yield stress of the reinforcing bars. De-bonding the dowel bars reduced inelastic strain demand in both the grout region of the cap beam and the extreme tension reinforcing bar (as illustrated in Fig. 4.8), and is expected to increase the drift capacity.

4.3.2 Embedded Ring Connection

A primary difference between the foundation and cap beam connection is the limitation on the cap beam width. This was studied analytically. The cap beam width varied from 2 to 3 times the column diameter (D). The cap width was evaluated using an annular ring outer diameter $D_o = D + 32t$ per design recommendations developed for the embedded ring footing connection [Lehman and Roeder, 2012b,a].

The accuracy of the model was verified by comparison of the force-deflection behavior (Fig. 4.9a) and cap beam cracking of the wider cap beam with prior connection tests. Fig. 4.9b shows the crack patterns for various cap beam widths. Cracking was very limited for all widths but increased somewhat for the narrower width, but cracking was very limited at large inelastic deformations for widths of $2D$ or greater. Although analyses were performed for narrower widths, convergence problems developed at larger inelastic deformations. Fig. 4.9a shows that the analysis predicted that cap beam width had no measurable effect on the moment resistance of the connection for widths $2D$ and greater.

The cap beam width was held constant at $2D$ for the annular ring study, and the outer diameter of the annular ring was varied from $D + 32t$ down to $D + 8t$ (that is the ring extended between $16t$ to $4t$ outside of the tube). An embedment depth of $0.8D$ was used to ensure a fully developed connection, and the inner radius of the ring was constant for all analyses as this dimension has been shown to be effective in the force transfer mechanism and did not impact the cap beam width [Lehman and Roeder, 2012b,a].

The moment-drift relationship (normalized by the plastic moment capacity of the CFST determined by the plastic stress distribution method, $M_{P,PSDM}$) for the cap beam annular ring diameter parameter study is plotted in Fig. 4.10a. The concrete strain distributions (maximum principal strains) are shown in Fig. 4.10b for several annular ring geometries, and concrete stress distributions are illustrated in Fig 4.10c. The figure shows that concrete strains in the cap beam were not sensitive to the flange projection, but concrete strains within the CFST were better controlled with the $8t$ projection. The maximum stress recorded in the cap beam shear and flexure reinforcing is plotted in Fig 4.11. Stress in the cap beam reinforcing was well below f_y of the reinforcing steel, however the stress was better controlled for the $8t$ projection.

The theoretical moment capacity of the CFST, $M_{P,PSDM}$, was exceeded for cap beam widths as low as $2D$, and an outer annular ring diameter of $D+8t$. Therefore, experimentally the cap beam width was set at $2D$ to minimize cracking patterns observed in the outer face, as illustrated in Fig. 4.9b. The annular ring diameter did not influence the distribution of plastic strain in the CFST or increase inelastic deformation in the cap beam, as shown in Fig. 4.10b. The intermediate diameter $(D + 16t)$ was used based on the maximum recorded stress in the cap beam reinforcing for this projection (as illustrated in Fig 4.11).

and therefore the intermediate diameter $(D + 16t)$ was used.

4.4 Numerical Studies for Loading in the Longitudinal Direction

Limited numerical studies were conducted on the ER connection and WD connection with debonded dowels in the longitudinal direction to ensure the connections could achieve strength and ductility requirements. The only parameter evaluated was the axial load ratio, P/P_o due to the computational cost of model construction and analysis. Note that a cap beam width of $2D$ was used in this analysis; the cap beam widths in the longitudinal experiments discussed in the next chapter were approximately $3D$ as scaled from the prototype structure. Thus the results presented here provide a conservative estimation of performance.

The moment drift relationships for the two connection types subjected to axial load ratios of 0.05, 0.10, and 0.15 are shown in Fig. 4.12a and Fig. 4.12b for drifts up to 5% for the ER and WD connections respectively, while the concrete stress distributions are shown in Fig. 4.13. Both connections exceeded the theoretical plastic moment capacity of the CFST column and the longitudinal connection reinforcing respectively, and concrete stress in the cap beam remained below the nominal compressive strength of the cap beam concrete (f_c'=6-ksi). Maximum stress recorded in the flexure and shear reinforcing in the superstructure are plotted in Fig. 4.14. Stress in the flexure reinforcing remained below the nominal yield strength up to 5% drift in both connections. Maximum stress in the shear reinforcing exceeded the nominal yield stress of the reinforcing steel at approximately 2% drift, however remained below the expected yield strength (68-ksi) which was used in the numerical model. These results indicated that the ER and WD connections could acheive strength and ductility requirements for loading in the longitudinal direction of the bridge.

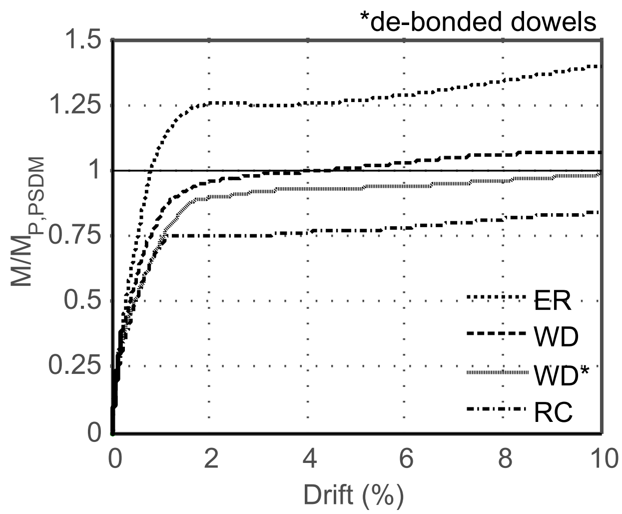

(a) Moment-Drift Behavior

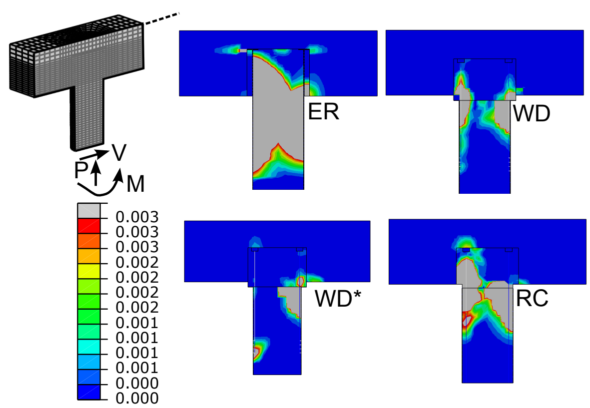

(b) Accumulated Plastic Concrete Strain at 10% Drift

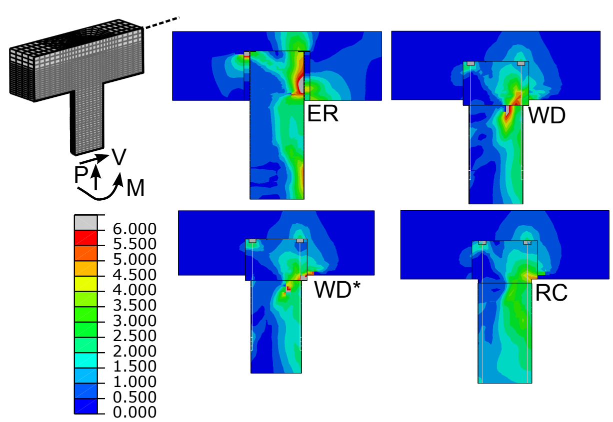

(c) Concrete Stress at 10% Drift

Figure 4.6: Moment-Drift and Inelastic Strains in the Proposed Connection Types

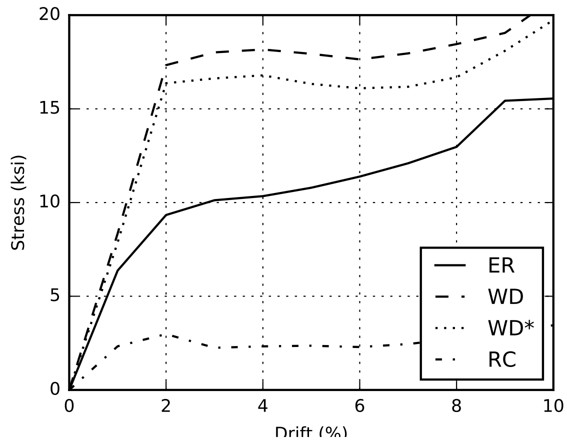

(a) Maximum Stress in Cap Beam Flexural Reinforcing

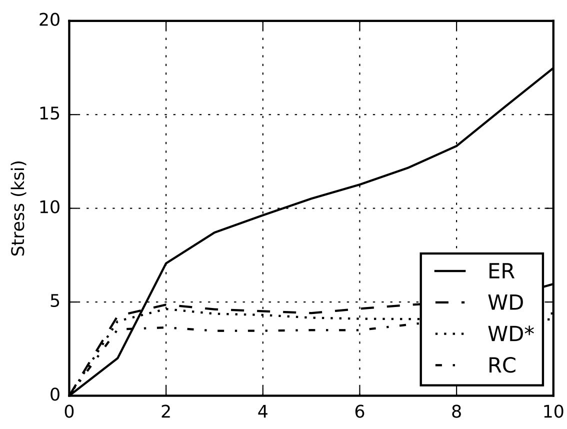

(b) Maximum Stress in Cap Beam Shear Reinforcing

Figure 4.7: Maximum Stress in Cap Beam Reinforcing. Note WD* uses debonded dowels.

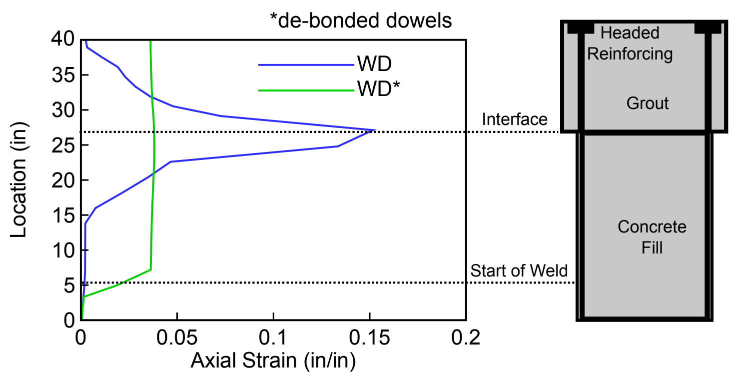

Figure 4.8: Welded Dowel Connection Dowel Strain at 10% Drift

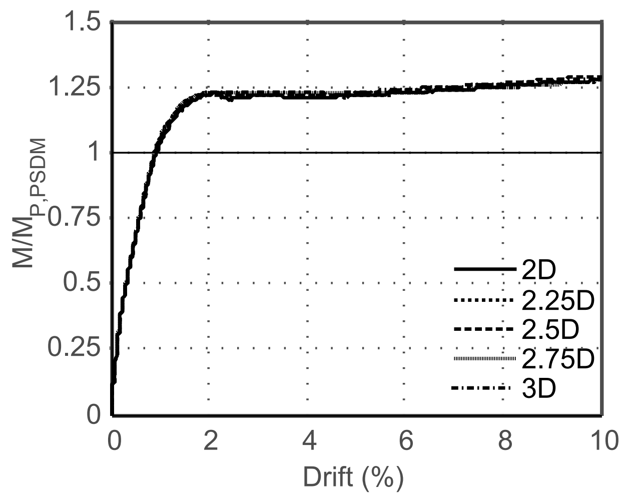

(a) Moment-Drift Behavior

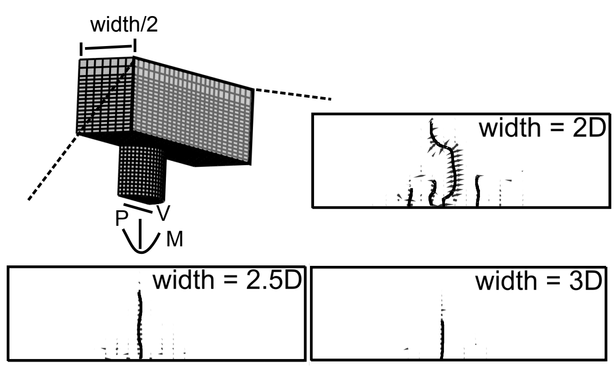

(b) Cap Beam Cracking at 10% Drift

Figure 4.9: ER Connection Cap Beam Width Parameter Study

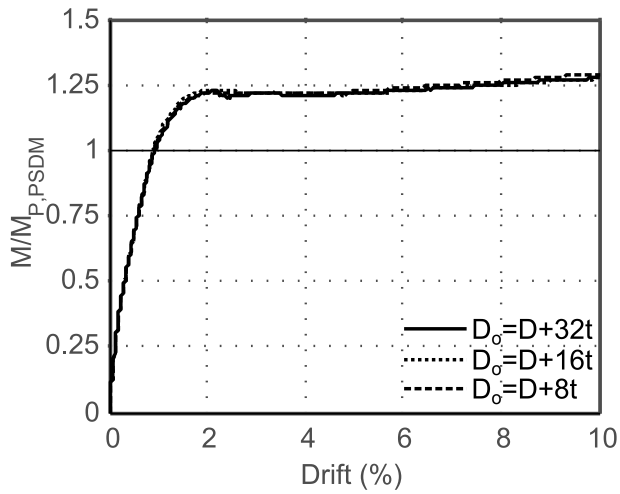

(a) Moment-Drift Behavior

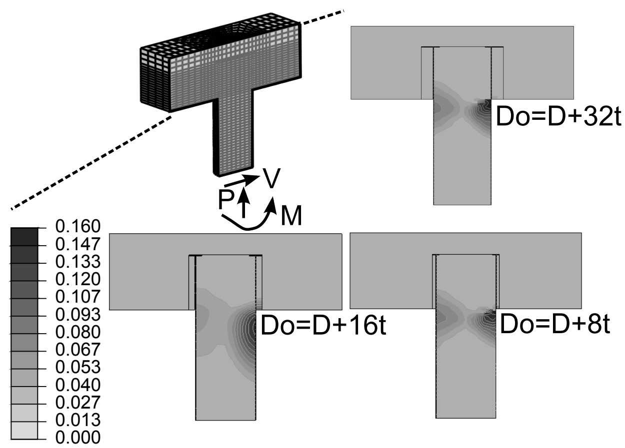

(b) Accumulated Plastic Concrete Strain at 10% Drift

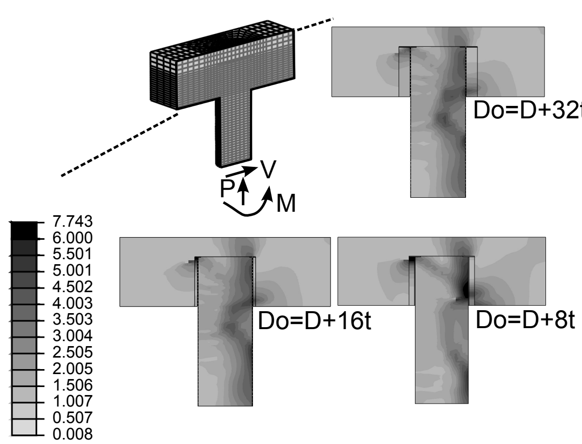

(c) Concrete Stress at 10% Drift

Figure 4.10: ER Connection Annular Ring Diameter Parameter Study

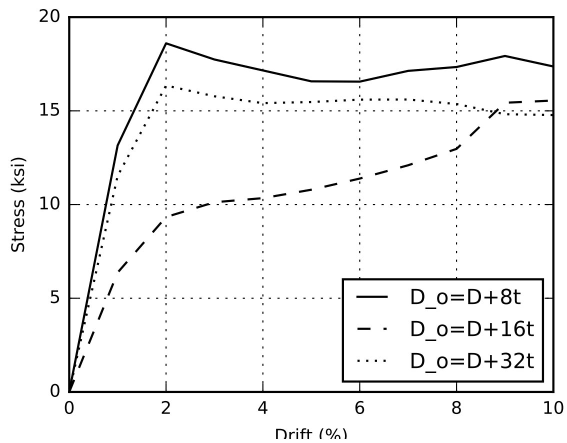

(a) Maximum Stress in Cap Beam Flexural Reinforcing

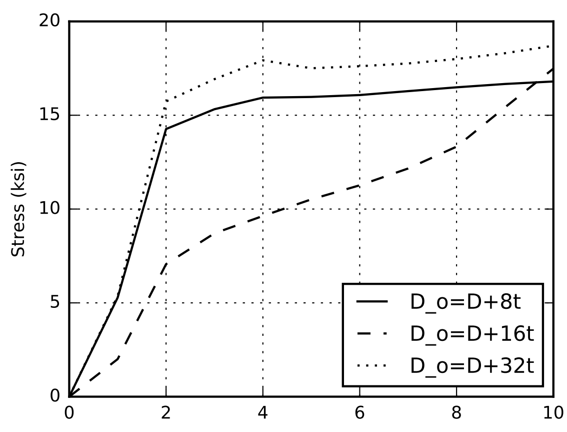

(b) Maximum Stress in Cap Beam Shear Reinforcing

Figure 4.11: Maximum Stress in Cap Beam Reinforcing

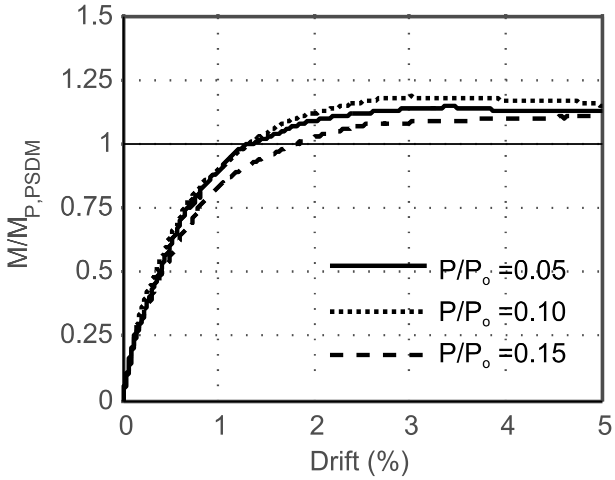

(a) Moment Drift Behavior of ER Connection

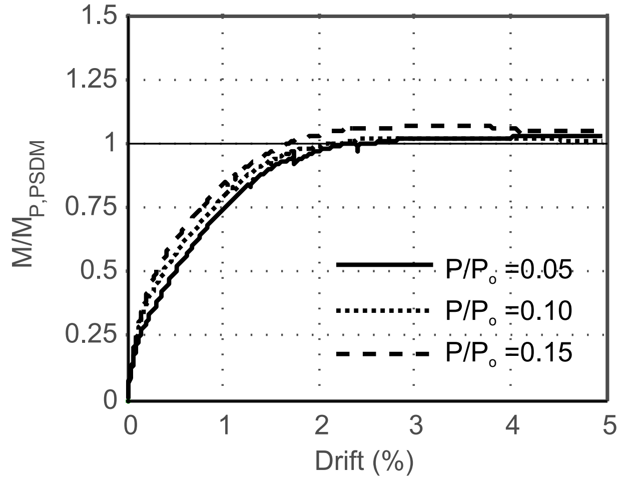

(b) Moment Drift Behavior of WD Connection

Figure 4.12: Moment Drift Relationships for Varying Axial Loads and Loading in the Longitudinal Direction

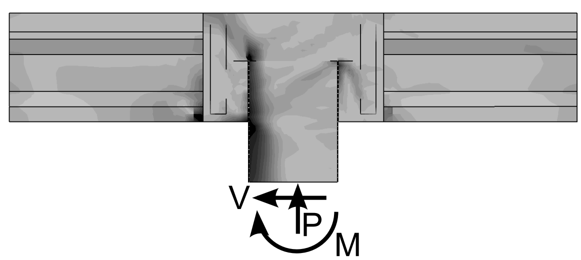

(a) ER Connection

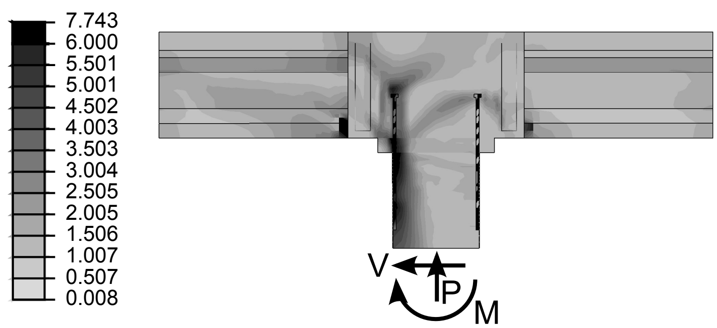

(b) WD Connection

Figure 4.13: Concrete Stress at 5% Drift for $P/P_o = 0.10$

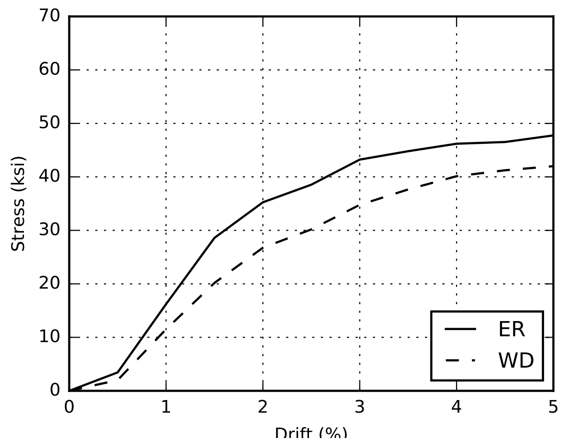

(a)
Maximum Stress in Longitudinal Flexural Reinforcing in Deck and Girders

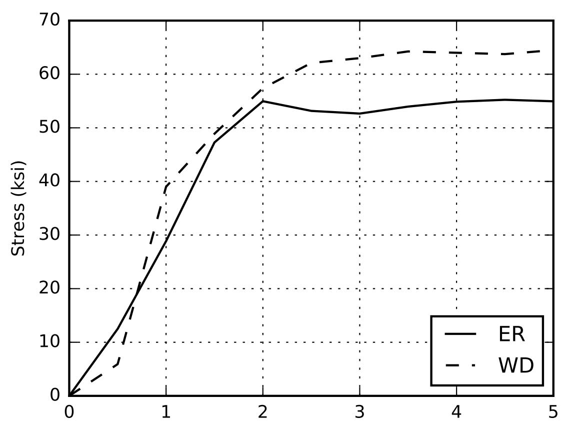

(b) Maximum Stress in Cap Beam Shear Reinforcing

Figure 4.14: Maximum Stress in Cap Beam Reinforcing for $P/P_o = 0.10$

Chapter 5

PARTIAL HEIGHT POCKET EMBEDDED RING (ER) CONNECTION

This chapter discusses large scale experiments and proposed design expressions for the ER connection. A detailed overview of the connection is provided in Section 5.1. The experimental program including specimen geometry, specimen construction, test apparatus, and instrumentation is described in Section 5.2. Experimental results are given in Section 5.3, and finally design expressions are proposed in Section 5.4.

5.1 Connection Overview

Fig. 5.1 shows a partial height pocket ER connection; this connection is similar to the embedded flange column-to-foundation connection that was developed in prior research [Lehman and Roeder, 2012b,a]. The partial height pocket ER connection uses a grouted connection detail, with a void cast into a precast cap beam (note a CIP RC cap beam can also be utilized). A circular ring is welded to the steel tube to provide anchorage and transfer stress to the concrete and reinforcing in the cap beam. The precast cap beam is placed onto the column after the column is set, and the recess between the tube and corrugated pipe is filled with high strength fiber reinforced grout.

5.2 Experimental Program

5.2.1 Reference Specimens

The non-linear numerical analysis formed the basis for the final design of the connection test specimens, and the test matrix is summarized in Table 5.1. All tubes had a nominal wall

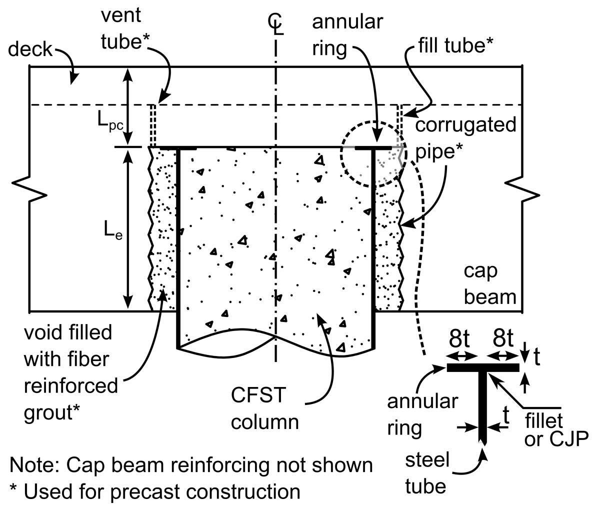

Figure 5.1: Embedded Ring Connection

thickness of 0.25-in., and specimens denoted with T and L were constructed to represent the transverse (normal to axis of the bridge) and longitudinal directions, respectively.

Four ER specimens were tested. An overview of the global transverse and longitudinal specimen geometries is included in Fig. 5.2, while connection details are illustrated in Fig. 5.3. Geometric variables in Fig. 5.2 are defined in Table 5.1. The number in the specimen designation indicated the D/t ratio of the steel tube. For specimens loaded in the transverse direction (denoted with a T in the specimen name) the cap beam had a width equal to twice the column diameter ($2D$). The width of the cap beam for specimens loaded in the longitudinal direction was scaled from the prototype bridge. In all ER specimens, an annular ring projected 2-in. inside and outside of the tube with an outer diameter of D+16t. Transverse and vertical shear reinforcing in the joint region of the cap beam was design according to recommendations by Lehman and Roeder [2012b,a]. Flexural reinforcement in the cap beam was designed to resist 1.25 times the theoretical flexural strength of the CFST component as calculated using the PSDM. Reinforcing details for the ER specimens are located in Appendix B. The four ER specimens were as follows:

- ER80T had an embedment depth of 18-in. (0.9D), and utilized a 61-ksi ASTM A1018 spiral welded steel tube.

- ER96T and ER96L had a D/t ratio of 96, with a diameter of 20-in. and were embedded 20-in. (0.83D) into the cap beam. Both utilized a 53-ksi API 5L X42 PSL1 grade straight seam tube. The larger D/t ratio compared to Specimen ER80T was expected to cause earlier buckling and increased deterioration of resistance. The D/t ratio of this specimen satisfies the D/t requirement for the current AASHTOa [2015] specification, but is within 7% of the limit.

- ER103L utilized a 25.75-in. diameter spiral welded tube with D/t = 103 and 69.3-ksi ASTM A1018 steel. The tube was embedded 20.25-in. (0.8D) into the cab beam. The CFST member exceeds the D/t limit permitted by the current AASHTO LRFD specification slenderness limits by approximately 18%.

Table 5.1: Experimental Matrix and Specimen Properties

Specimen	Steel Tube Type	D, in.	t, in.	D/t	L_e, in.	L_{pc}, in.	ρ, %	h_{col}, in.	L_{cap}, in.	h_{cap}, in.	b_{cap}, in.	Axial Load Ratio, %
ER80T	ASTM A1018-07	20	0.25	80	18	7	5	72	76	25	40	10
ER96T	API-5LX42	24	0.25	96	20	9.75	4	72	76	29.75	48	5
ER96L	API-5LX42	24	0.25	96	20	9.75	4	72	186	29.75	65	5
ER103L	ASTM A1018-07	25.75	0.25	103	20.25	9.5	4	108	186	29.75	65	10

5.2.2 Specimen Construction

The specimens were constructed in the Structural Testing Laboratory at the University of Washington. To eliminate the need for the construction of temporary shoring, all of the

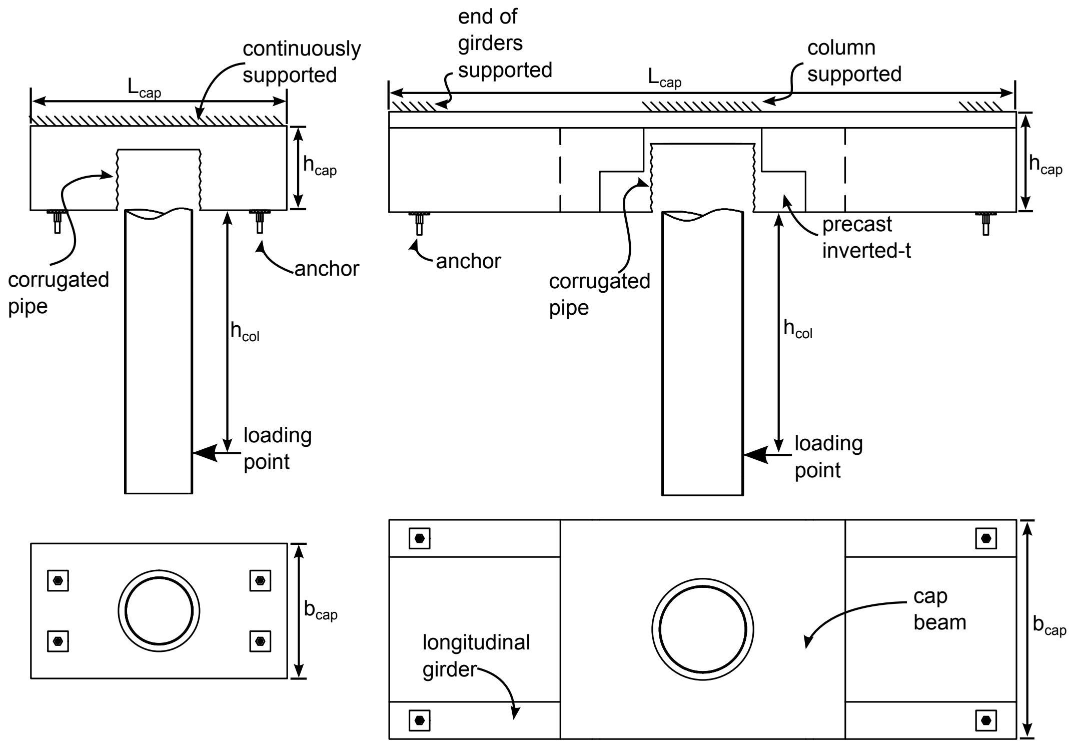

(a) Transverse Specimen Overview

(b) Longitudinal Specimen Overview

Figure 5.2: Overview of Specimen Geometry

specimens were constructed upside-down (i.e. the columns were cast into the cap-beams while the cap-beams rested on the floor). This resulted in construction sequences and practices which would not be used in the field. Construction of all specimens began with welding an annular ring to the end of the steel tube as illustrated in Fig. 5.4.

5.2.2.1 Transverse Specimens

An overview of the construction sequence for the transverse specimens is given in Fig. 5.5. The construction sequence was as follows:

1. The cap beam was precast with a void created using a corrugated pipe.

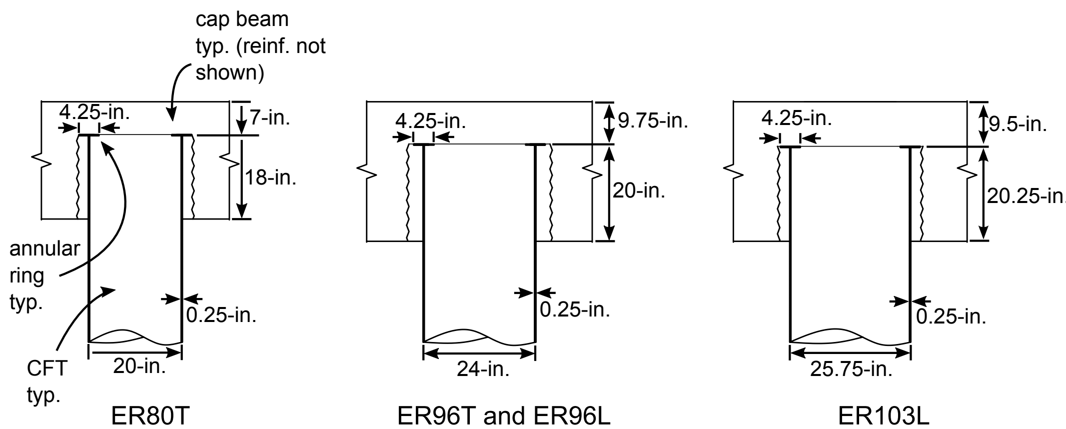

Figure 5.3: Connection Details for ER Specimens

Figure 5.4: Annular Ring Temporarily Supported and Welded to Steel Tube

2. The steel tube was leveled and grouted into the void.

3. The CFST column was cast using self-consolidating concrete with low shrinkage admixture.

Construction photos are shown in Fig. 5.6

5.2.2.2 Longitudinal Specimens

An overview of the construction sequence for the longitudinal specimens in given in Fig. 5.7. The construction sequence used for the longitudinal specimens was designed to demonstrate that the ER connection could be used in conjunction with precast inverted-t cap beams. Thus the superstructure of these specimens was constructed in 4 steps:

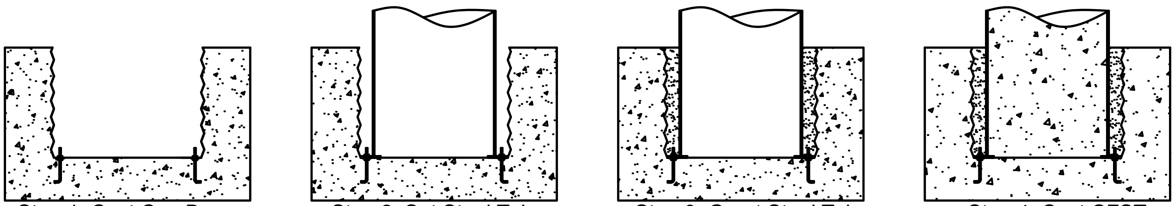

Figure 5.5: ER Transverse Construction Sequence

(a) Transverse Cap Beam Formwork

(b) Steel Tube Placed into Void

Figure 5.6: Transverse ER Construction Photos

1. The inverted-t cap beam was precast with a void created using a corrugated pipe.

2. The superstructure including diaphragm, deck, and longitudinal girders were cast around the inverted-t.

3. The steel tube was leveled and grouted into the void.

4. The CFST column was cast using self-consolidating concrete with low shrinkage admixture.

Typical construction photos of the precast inverted-t and diaphragm and girder reinforcing cages are provided in Fig. 5.8.

5.2.3 Test Setup

The specimens were tested using a self-reacting test frame with a horizontal actuator to apply lateral load, and a Baldwin Universal Testing Machine to apply a constant lateral load as shown in Fig. 5.9. The transverse specimens were fully supported on the reaction block, while the longitudinal specimens were supported under the column and at the ends of the longitudinal girders as illustrated in Fig. 5.9 and Fig. 5.10 respectfully. The fully supported condition in the transverse experiments represents a conservative estimation of connection performance in terms of ductility, as flexural deformation in the cap beam is neglected. The longitudinal specimens were supported under the column to allow flexural deformation of the superstructure, while eliminating a transfer of the column dead load into the longitudinal girders. The length of these girders was restricted by the geometric limitations of the cap beam; supporting the column dead load ensured shear failure would not develop at the longitudinal girder-to-cap beam interface, since the longitudinal beams-to-cap beam connections was not the focus of this research.

The self-reacting rig was centered under a Baldwin Universal Testing machine with a compressive capacity of 2400-kips. Each specimen was leveled, and grouted into place using

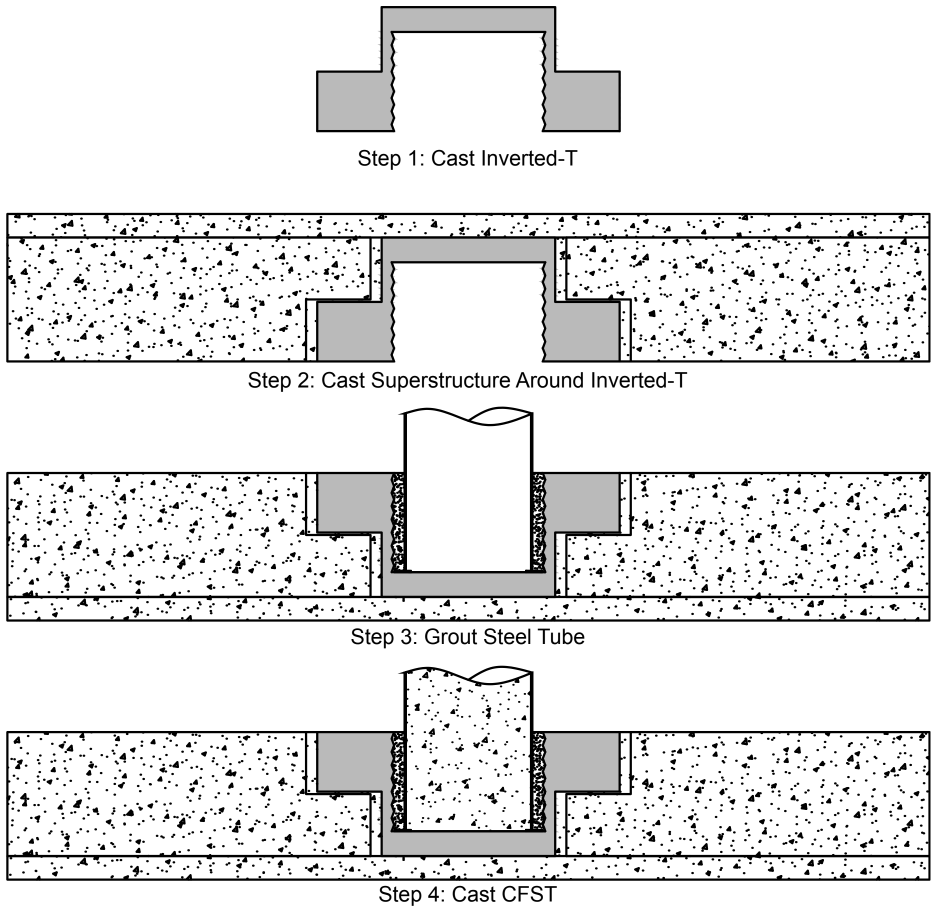

Figure 5.7: ER Longitudinal Construction Sequence

(a) Precast Inverted-T

(b) Superstructure Reinforcing Cage

Figure 5.8: Longitudinal ER Construction Photos

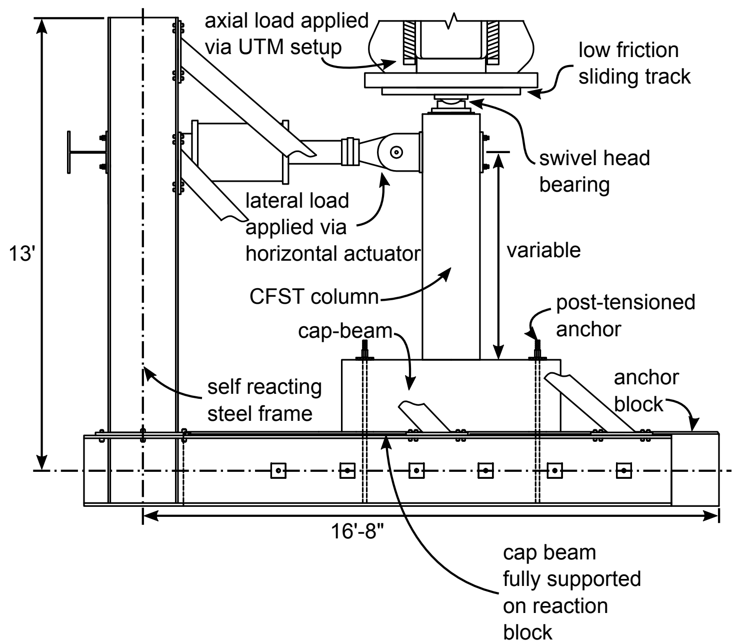

Figure 5.9: Test Apparatus with Transverse Specimen

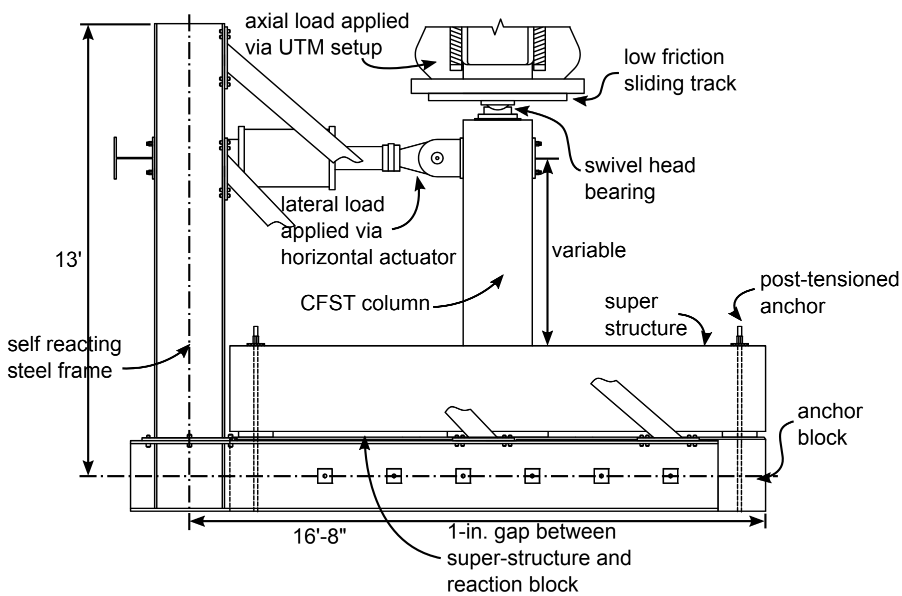

Figure 5.10: Test Apparatus with Longitudinal Specimen

Hydrostone, and the specimen was anchored and post-tensioned to the base of the test apparatus with four 1 1/4-in. Williams Form Engineering All-Thread high-strength steel bars post-tensioned to 120-kips. The anchor rods were placed at a position to minimize confinement of concrete and to avoid development of additional resistance to the foundation in the area where cone pullout failure of the foundation could occur.

The actuator was clamped to the CFST column by a pair of machined blocks, which conformed to the outside diameter of the tube, and were post-tensioned to the tube using four 1 1/4-in. Williams All Thread bars to prevent all slip and movement during loading. The actuator had a pin swivel connection at each end, to prevent development of moment in the actuator or specimen.

A spherical, swivel-head bearing was fixed to the top of the CFST column to allow for rotation while still maintaining a constant axial load. The bearing sat within a recessed steel plate, which was lined with a dimpled polytetrafluoroethylene (PTFE) sliding surface to permit lateral displacements, as shown in Fig. 5.11. Under lateral loading, the PTFE slid within a stainless steel-lined channel, which was fixed to the bottom of the Baldwin head to permit free in-plane movement and prevent out-of-plane movement. A silicone grease lubricant was applied between the PTFE and stainless steel to create a low-friction sliding surface. Research has shown that this arrangement results in friction less than one tenth of one percent of the applied load.

Each specimen was subjected to a constant axial load of either 10% or 5% of the gross crush capacity $P_o = (A_{st}F_{y,st} + 0.95A_c f'_{cf})$ of the column as indicated in Table 5.1, as well as a reversed cyclic lateral load with incrementally increasing displacements. The lateral load displacement protocol was adapted from that of previous University of Washington tests, and the ATC-24 [1992] guidelines, in which the imposed displacements are based on incremental multiples of the member's yield displacement. The target lateral load protocol for each specimen is illustrated in Fig. 5.12.

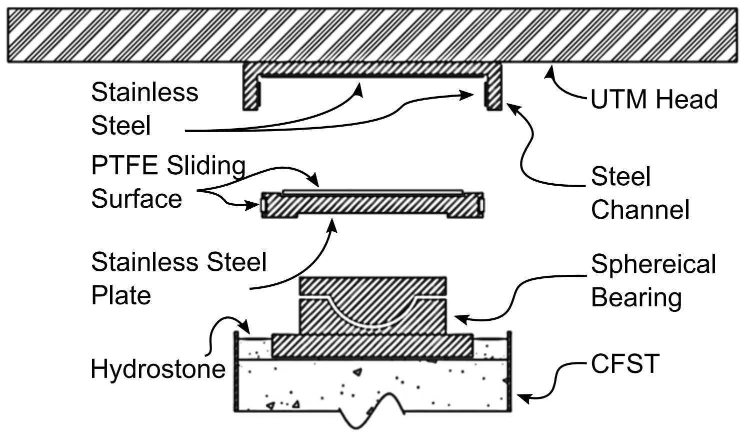

Figure 5.11: Sphereical Bearing with Low Friction Sliding Surface

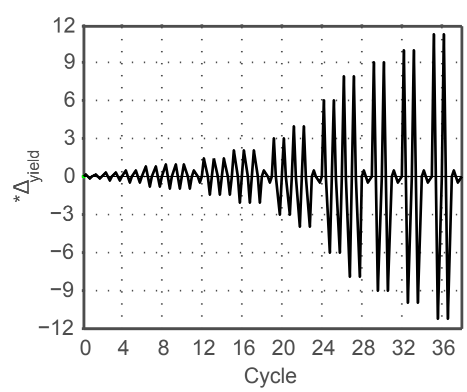

Figure 5.12: Typical Lateral Displacement Protocol used in Testing

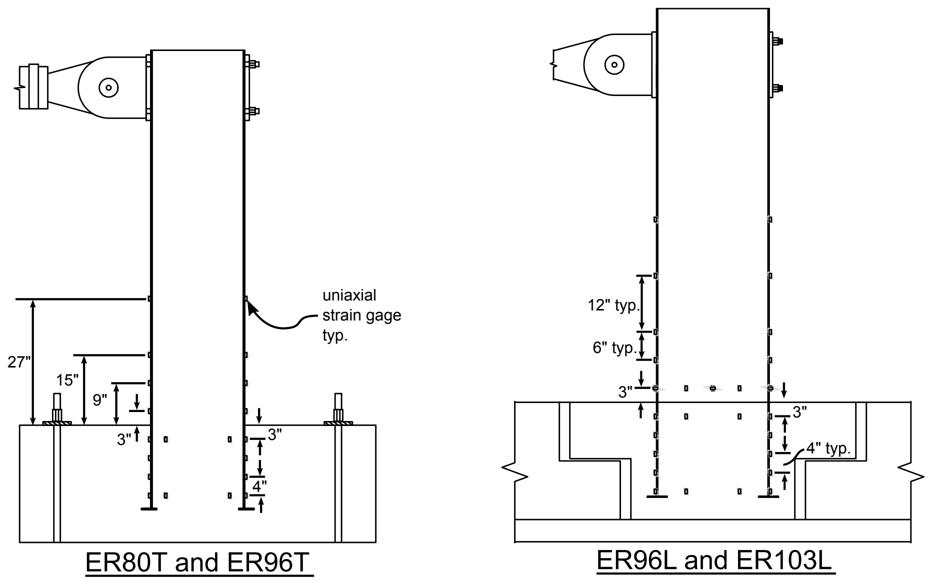

Figure 5.13: Strain Gage Schematic

5.2.4 Instrumentation

Strain gages, linear potentiometers, string potentiometers, and an Optotrak motion capture system were attached to each specimen. The instruments were electronically recorded using computer controlled data acquisition systems.

The applied gravity and lateral loads were directly measured using load cells, which were calibrated prior to testing for all tests. Strain gages were attached to the steel tube as illustrated in Fig. 5.13, and were used primarily to measure elastic strains in the steel tube for evaluation of elastic curvature, elastic bending moments, and the plastic strain distribution the critical regions of the connection.

Displacements were measured using string potentiometers and short stroke Duncan potentiometers. String potentiometers can measure a large range of displacement (typically 10 to 20-in.), and they were used to measure the actual top displacement of the tube as illustrated in Fig. 5.14. String potentiometers were additionally used to measure tube displacement at 3 additional locations along the height of the tube to allow for development of a displaced profile of the column, and track displacements within the plastic hinge region. Small stroke Duncan potentiometers were placed at locations where small displacements were expected as illustrated in Fig. 5.14. In particular, they measured slip or uplift of the specimen and the test rig. They were additionally used to monitor deformations along the length of the longitudinal girders in the longitudinal specimens as illustrated in Fig. 5.14.

An Optotrak Certus motion capture system was used to monitor the deformed shape of the columns during testing. The system consists of a 3-dimensional optical sensor and a series of LED markers, which were attached to the specimen using adhesive foam pads, and emit an electronic signal that is photographed by optical sensors. The optical sensors consist of 3 precision cameras, which locate the position of each LED marker in 3-dimensional space by triangulation of the relative positions noted by each camera. This system was used to capture the buckled shape of the tube as well as inelastic rotation, and relative displacement fields in the plastic hinge region of the columns. Measurements from the Optotrak system were compared to the string potentiometer and inclinometer data, and provided the most accurate and consistent measurements of the inelastic performance of the system. The placement of the LED targets is shown in Fig. 5.15.

5.3 Experimental Results

Key results from the experiments for the four ER specimens are summarized in Table 5.2, while test day material strengths are given in Table 5.3. The performance of each connection was assessed based on the secant stiffness to $0.8M_y$ of the CFST, maximum moment resistance, maximum drift, the drift where the resistance decreased to 80% of its maximum, accumulated energy dissipation, as well as damage state progression.

Secant stiffness was measured when the moment resistance achieved approximately 80% of the yield moment of the CFST. Specimen stiffness is expressed as the ratio of the measured stiffness to the theoretical stiffness of the CFST ($EI_{measured}/EI_{eff}$) as calculated using the stiffness expression in AASHTOa [2015]. Using this method, $EI_{measured}/EI_{eff}$ values greater than 1.0 would suggest a larger stiffness than the theoretical stiffness of the CFST component,

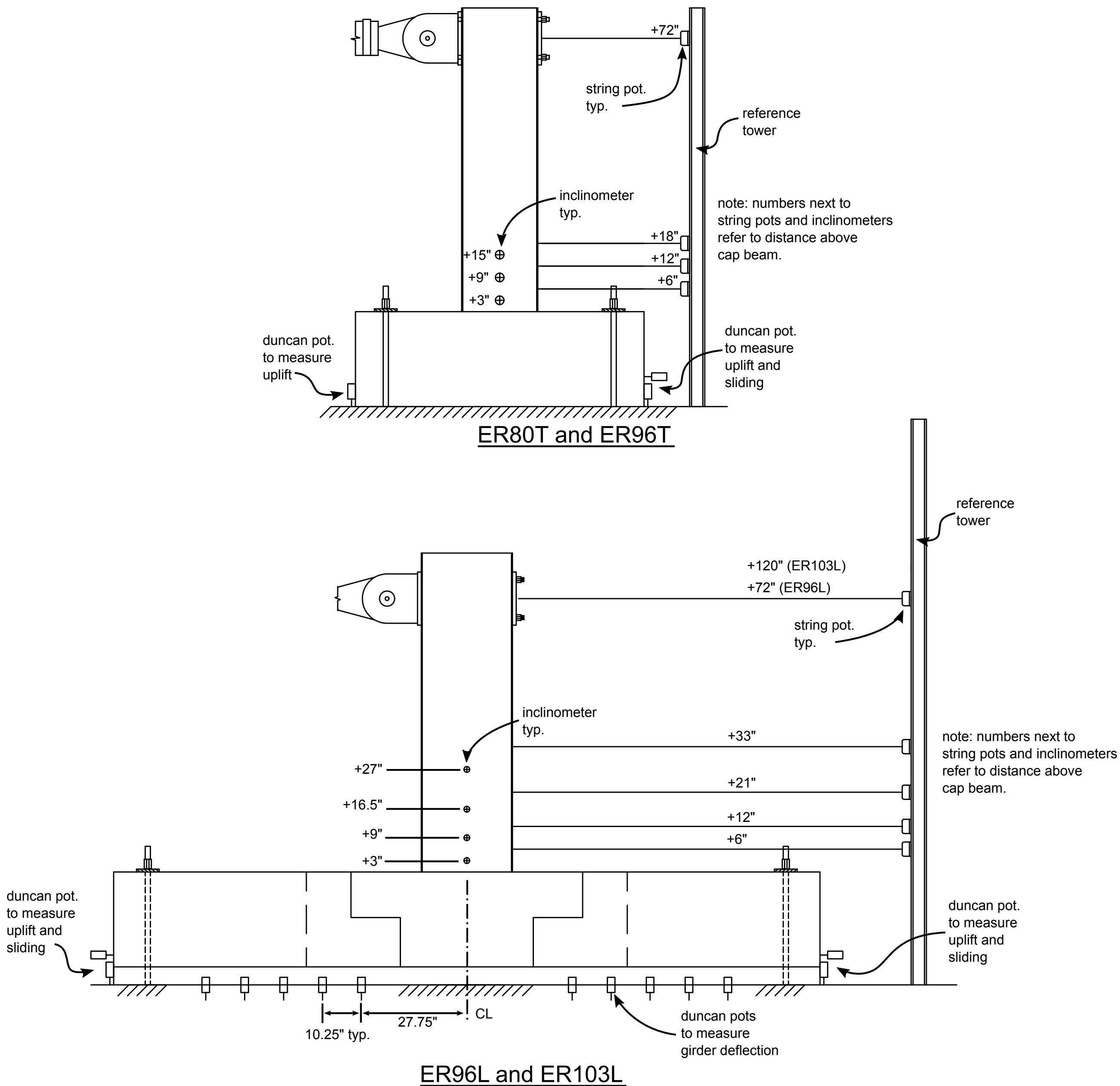

Figure 5.14: String Potentiometer, Duncan Potentiometer, and Inclinometer Locations

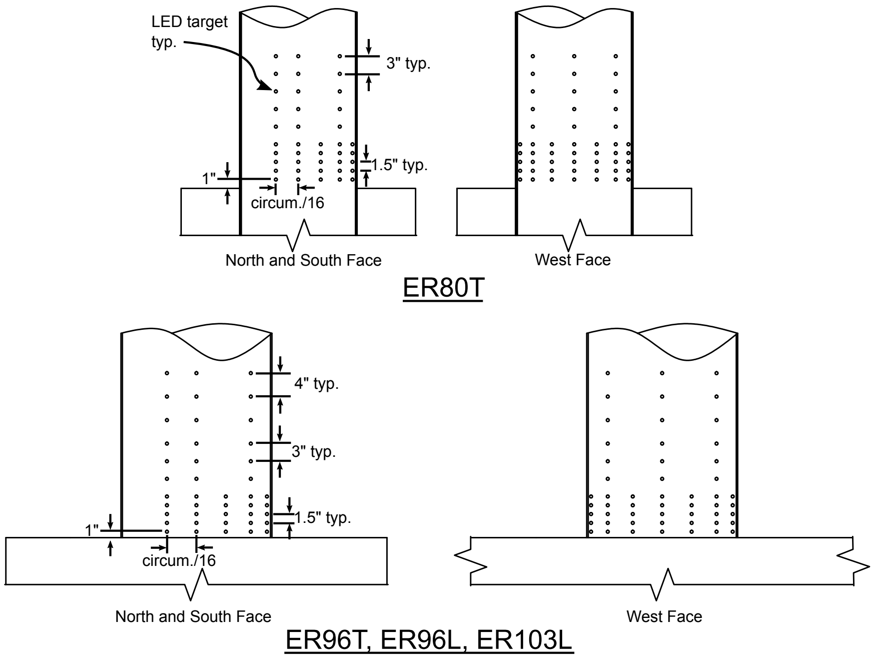

Figure 5.15: Optotrak Target Layout

while $EI_{measured}/EI_{eff}$ values less than 1.0 would suggest a smaller initial stiffness. Note that the measured stiffness accounts for the flexibility of the ER connection (including steel strain penetration into the cap beam and bond characteristics between the steel tube and cap beam concrete), and therefore the ratio $EI_{measured}/EI_{eff}$ was expected to be lower than 1 in all cases.

Similarly, the moment resistance of each connection was evaluated by calculating the ratio of the maximum observed moment to the theoretical moment capacity of the CFST ($M_{max}/M_{P,PSDM}$) as calculated using the PSDM. This method for estimating the combined moment-axial capacity of CFST components is discussed in detail in literature [Lehman and Roeder, 2012b,a]. Using this method, $M_{max}/M_{P,PSDM}$ values greater than 1.0 suggest that the connection exceeded the theoretical plastic moment capacity of the CFST, while $M_{max}/M_{P,PSDM}$ values less than 1.0 suggest that the connection did not provide as much resistance as the theoretical plastic capacity expected for the CFST component.

Table 5.2: Experimental Results

Specimen	Initial Stiffness $\frac{EI_{measured}}{EI_{eff}}$	Yield Drift, %	$\frac{M_{peak}}{M_{P,PSDM}}$	Drift at peak Moment, %	Drift at 20% Degradation, %
ER80T	0.98	1.3	1.2	7	7
ER96T	0.77	0.97	1.12	4.5	8.6
ER96L	0.6	1.1	1.19	4.4	8
ER103L	0.96	1.4	1.13	1.8	5

Table 5.3: Measured Test Day Material Properties

Specimen	$F_{y,st}$, ksi	$F_{u,st}$, ksi	$\epsilon_{u,st}$, %	f'_c Column, ksi	f'_c Cap, ksi	f'_g, ksi
ER80T	60.2	68.5	27.5	10.7	9.9	6.8
ER96T	53	68.9	33.5	8.3	10.1	8.7
ER96L	53	68.9	33.5	7.9	7.7	8.9
ER103L	58	69.3	27.5	8.4	9.9	4.3

Damage state progression tables were used to evaluate the severity of damage in the specimens for each applied drift range. Damage states for the ER connections progress from initial yielding of the CFST component to tearing at the apex of the buckled region adjacent to the surface of the cap beam as illustrated in Table 5.4. Damage states in the cap beam range from hairline cracking to extreme cracking as illustrated in Table 5.5. The damage states were correlated to four post-event repair scenarios based on the severity of the damage:

1. **No Repair Required** - Essentially elastic foundation/cap beam. Steel tube yielding and limited concrete/grout damage in ductile elements.

2. **Repair Required** - Foundation/cap beam cracks greater than 0.15-in. This corresponds to reinforcing strain greater than $2\epsilon_y$ in the non-ductile element. Repair consists of injecting cracks in foundation/cap beam.

3. **Partial Replacement** - Steel tube residual buckling amplitude greater than $4t$ or steel tube tearing. Partial replacement consists of shifting plastic hinge out of the damaged region in the column as described in D.E. Lehman [2000].

4. **Replacement Required** - Foundation/cap beam cracks greater than 0.30-in.

Table 5.4: ER Damage State Descriptions

Symbol	**Description**	**Detailed Description**	**Photo**
Y1	Initial Yielding	Yielding of steel tube.	No observable damage.
B1	Initial Buckling	Residual out-of-plane displacement at the apex of the buckled region exceeds 0.	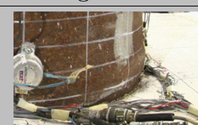
B2	Buckling<3t	Residual out-of-plane displacement at the apex of the buckled region less than 2t.	
B3	Buckling>3t	Residual out-of-plane displacement at the apex of the buckled region exceeds 4t.	
T1	Tube Tearing	Visual tearing initiation in the buckled region of the steel tube.	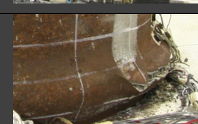

Repair States:
No Repair
Repair
Partial Replace

5.3.1 *Summary of Individual Test Results*

The following section provides a summary of the test results for each specimen including the hysteretic response, and damage progression. Note that the moment-drift behaviors have been normalized by the theoretical plastic moment capacity of the CFST component as calculated using the PSDM.

Table 5.5: Cap Beam Damage State Descriptions

Symbol	Description	Detailed Description	Photo
C1	Essentially Elastic	Crack widths up to 0.125-in. visible in cap beam (corresponding to flexural steel strains up to $\sim 2\epsilon_y$.	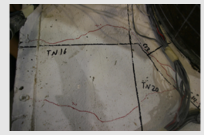
C2	0.125-in.<Cracking< in.	Crack widths up to 0.25-in. (corresponding to flexural steel strains up to $\sim 4\epsilon_y$.	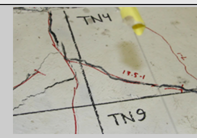
C3	Cracking>0.2 in.	Crack widths greater than 0.25-in. (corresponding to flexural steel strains greater than $\sim 4\epsilon_y$	

Repair States:
No Repair
Repair
Partial Replace
Full Replace

5.3.1.1 ER80T

ER80T utilized a 20-in. diameter spiral welded ASTM A1018 grade steel tube with an ER connection. The thickness of the steel tube was 0.25-in., resulting in $D/t = 80$, and it was evaluated for loads and deformation transverse to the axis of the bridge. The purpose of this specimen was to evaluate the performance of the connection and cap beam using a reduced annular ring outer diameter ($D + 16t$) and a reduced cap beam width of $2D$. The revisions were proposed based upon a series of non-linear analysis of design parameters for this connection discussed in Chapter 4. The measured moment-drift response is illustrated in Fig. 5.16 and the damage progression is summarized in Table 5.6. This specimen exhibited an initial stiffness $EI_{measured}/EI_{eff} = 0.98$, and a maximum moment $M_{max}/M_{P,PSDM} = 1.2$. The large effective stiffness resulted from a nearly fixed connection condition at the cap beam interface created by the mechanical bond between the cap beam concrete and spiral weld in

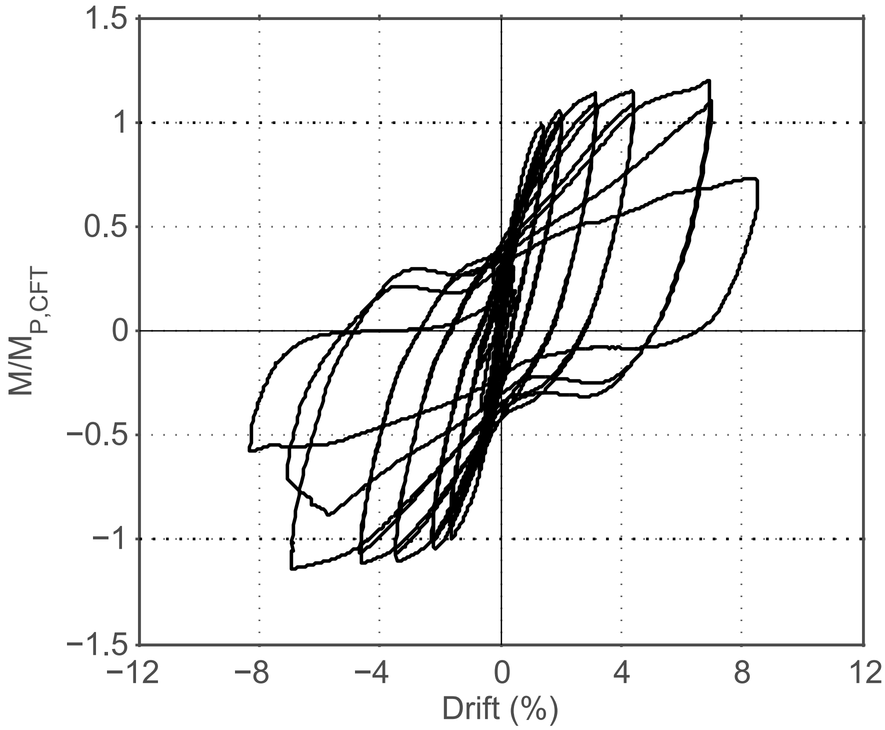

Figure 5.16: Moment-Drift Behavior of Specimen ER80T

the steel tube. Bond characteristics between spiral welded tube and conventional concrete are discussed in Appendix F.

During loading at 1.3% drift, yielding of the steel tube was measured by strain gauges located on the CFST column 3-in. from the surface of the cap beam on both the North and South sides of the column. At 1.45% drift, circumferential hairline cracks initiated along the grout interface on the North side of the specimen, as shown in Fig. 5.17a. At this same drift, cracks were observed propagating radially in the grout pad and the cap beam, as shown in Fig. 5.17a. These cracks were hairline in width, and they continued propagating down the East and West sides of the cap beam. During the third cycle at 1.45% drift, slight flaking of the grouted region was observed near the grout-cap beam interface, as shown in Fig. 5.17. The portions of grout that flaked off ranged between 0.5-in. and 1-in. in diameter, and were less than 0.25-in. in thickness.

Table 5.6: ER80T Damage State Progression

Drift Ratio, %	$M/M_{P,PSDM}$	Column	Cap Beam
0.04	0.17		
0.10	0.18		
0.10	0.28		
0.18	0.29		
0.24	0.40		
0.34	0.41		
0.41	0.54		
0.52	0.55		
0.57	0.63	Y1	
0.69	0.64		
1.45	0.92		C1
1.67	0.94		
2.00	1.0		
2.25	1.0		
3.19	1.1	B1	
3.45	1.1		
4.43	1.1	B2	
4.64	1.1		
7.00	1.1	B3/T1	
7.07	0.88		
8.54	0.73		
8.30	0.57		

Repair States:
No Repair
Repair
Partial Replace
Full Replace

Initial buckling of the North and South sides of the steel tube was observed visually during loading at 3.19% and -3.45% drift, respectively. The apex of the buckled region was approximately 1.75-in. away from the surface of the cap beam and had very small amplitude, as shown in Fig. 5.17b. Additional hairline cracks formed radially in the top surface of the cap beam, as well as vertically and diagonally down the East and West faces of the cap beam. No cracks were observed on the North and South faces of the cap beam. Cyclic deformation continued to increase with virtually no deterioration in resistance, but increased amplitude of the buckled shape up to 7.7% drift.

Tearing initiated at the apex of the buckled region on both the North and South sides of the column during cycling at 7.7% drift, and continued to grow with increasing lateral deformations. At 8.54% drift, the tearing propagated around the base of the column. The test was stopped after cycling at 8.75% drift as tearing continued to propagate around the base of the column as illustrated in Fig. 5.17f. However, the lateral resistance remained at around 50% of the maximum at this damaged state. The concrete was well confined at the point. There was no spalling or significant damage to the concrete fill, and the column retained its ability to support the full axial load.

5.3.1.2 ER96T

ER96T utilized a 24-in. diameter straight seam API 5L X-42 grade steel with an embedded ring connection. The thickness of the steel tube was 0.25-in., resulting in $D/t = 96$. This specimen had similarities with ER80T, but used a larger D/t ratio and a different grade of steel. The API 5L specification has tighter requirements on the material properties and manufacturing of the tube. However, the increased D/t ratio is generally expected to to cause earlier buckling and deterioration of resistance. The D/t ratio of this specimen satisfies the D/t requirement for the current AASHTOa [2015] specification, but is approximately within 7% of the limit. The measured moment-drift response is illustrated in Fig. 5.18 and the damage progression is summarized in Table 5.7. This specimen exhibited an initial stiffness $EI_{measured}/EI_{eff} = 0.77$, and a maximum moment $M_{max}/M_{P,PSDM} = 1.12$. The low effective stiffness relative to ER80T is the result of large steel strain penetration resulting from bond failure between the straight seam steel tube and cap beam concrete. Bond characteristics between straight seam tube and conventional concrete are discussed in Appendix F.

There was no visible damage to the cap beam or column during the initial load cycles up to 0.5% drift. At 0.5% drift, circumferential hairline cracks initiated along the column-grout interface on both the North and South sides of the specimen, as each side was respectively subjected to tensile loading. Yielding was measured by strain gages located on the CFST column 3-in. from the surface of the cap beam during cycling at 0.97% drift.

(a) 1.5% Drift

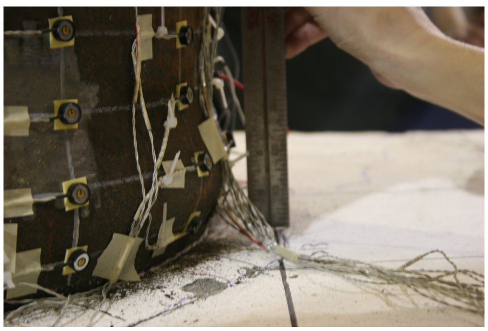

(b) 3.75% Drift

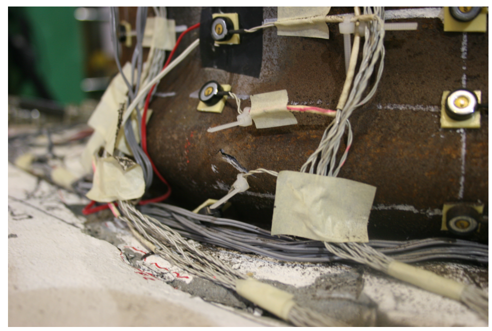

(c) 7.5% Drift

(d) 7.5% Drift

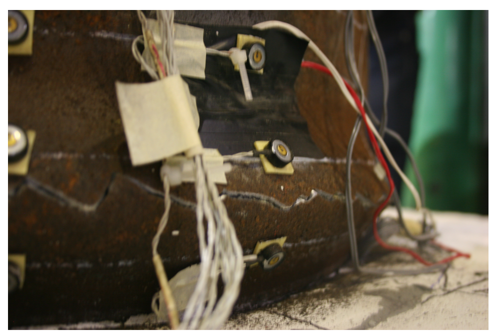

(e) 7.5% Drift

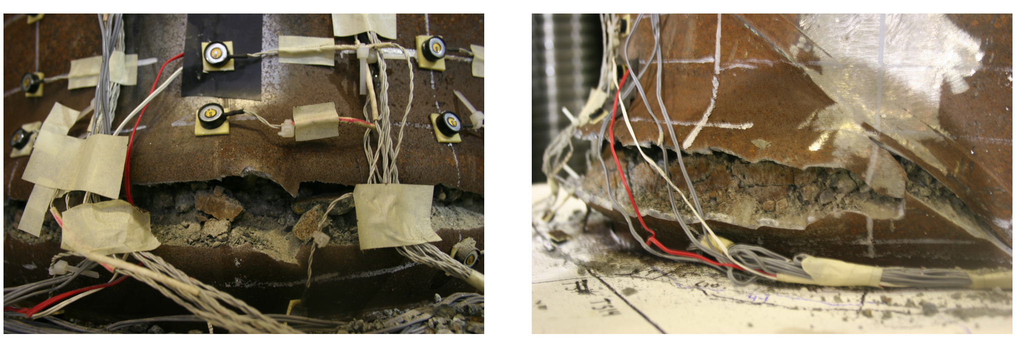

(f) final state (8.75% Drift)

Figure 5.17: Photos of Primary Damage States of Specimen ER80T

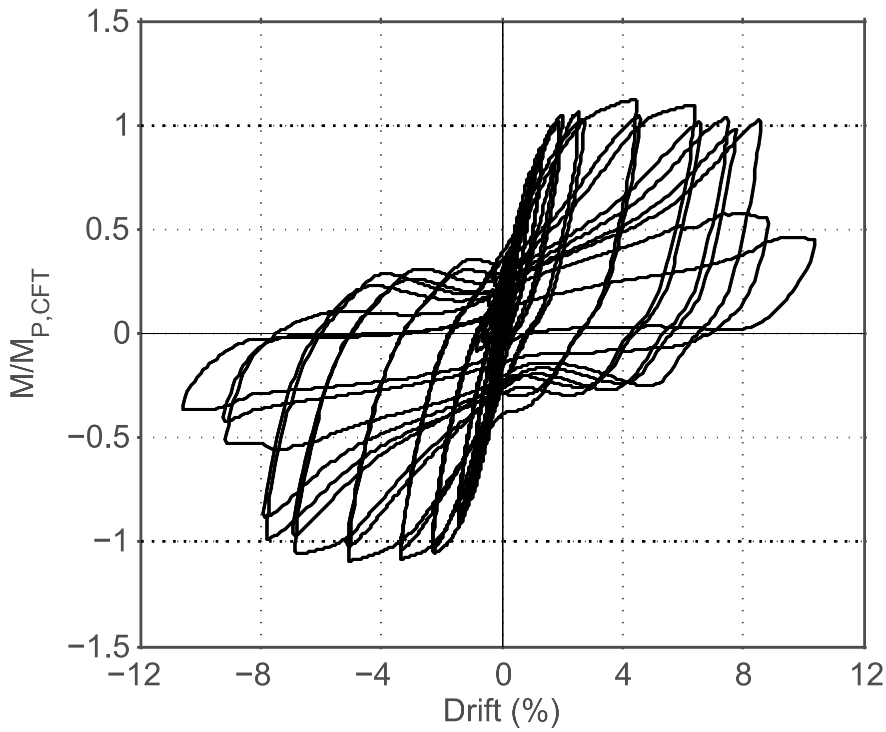

Figure 5.18: Moment-Drift Behavior of Specimen ER96T

Table 5.7: ER96T Damage State Progression

Drift Ratio, %	$M/M_{P,PSDM}$	Column	Cap Beam
0.07	0.17		
0.08	0.14		
0.13	0.27		
0.14	0.25		
0.31	0.37		
0.32	0.38		
0.49	0.51		
0.47	0.49		
0.65	0.59	Y1	
0.65	0.60		
0.94	0.74		
1.02	0.76		
1.29	0.87		
1.44	0.89		
2.01	1.04		
2.28	1.06		
2.55	1.04	B1	
3.36	1.04		
4.46	1.04	B2	C1
5.07	1.03		
6.39	1.01	B3	
6.86	0.97		
7.50	0.98	T1	
7.81	0.87		
8.60	0.58		
9.15	0.42		
10.40	0.46		
10.60	0.37		

Repair States:
No Repair
Repair
Partial Replace
Full Replace

Local buckling was observed during the 3% drift cycle as illustrated in Fig. 5.19. The apex of the buckle was approximately 2.5-in. from the surface of the cap beam, but the amplitude of the buckle was quite small as shown in Fig. 5.19a. There was no significant cracking observed in the cap beam or grout region during subsequent cycles, and the out of plane displacement of the buckled region continued to grow as shown in Fig. 5.19b. Tearing initiated at the apex of the buckled region on the North side of the column, and at the

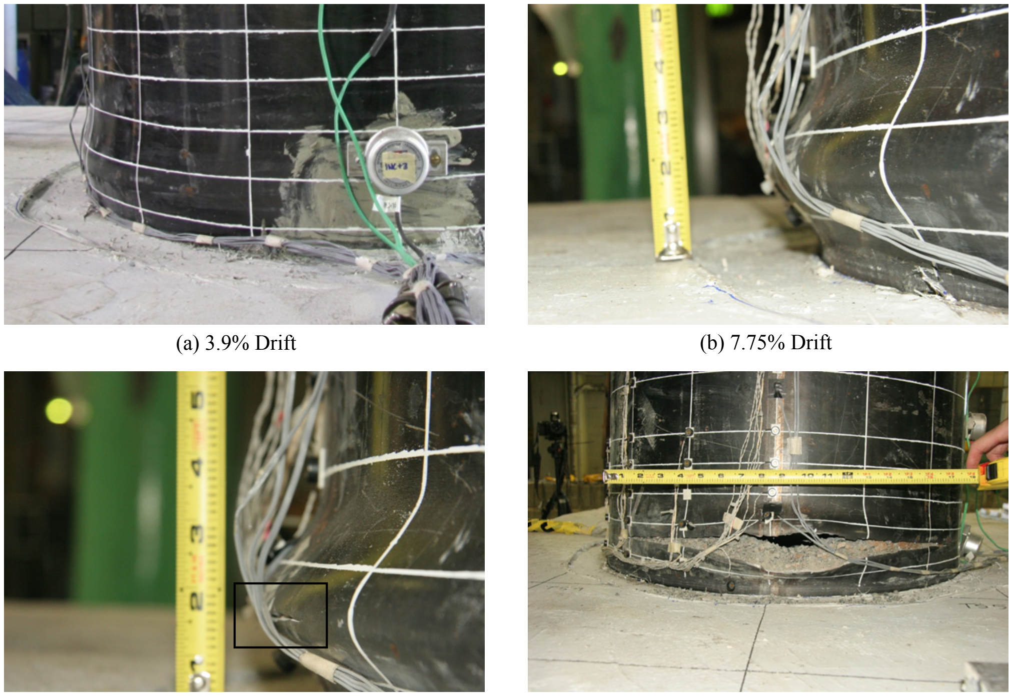

(a) 3.9% Drift

(b) 7.75% Drift

(c) 8.75% Drift

(d) 9.75% Drift

Figure 5.19: Photos of Primary Damage States of Specimen ER96T

interface between the column and cap beam on the South side of the column during cycling at 8.75% as shown in Fig. 5.19. Tearing propagated around the base of the column during cycling at 9.15% drift, and the test was stopped due to significant strength degradation. The CFST column retained approximately 35% of its maximum moment capacity at 9.75% drift, while supporting the full axial load. There was virtually no damage to the concrete fill at these large deformations as shown in Fig. 5.19d.

5.3.1.3 ER96L

EMB96L utilized a 24-in. diameter straight seam API 5L X-42 grade steel with an embedded flange connection. The thickness of the steel tube was Â$\frac{1}{4}$-in., resulting in D/t = 96. The specimen was similar to ER96T except that it evaluated the effect of loads and deformations in the longitudinal axis of the bridge instead of the transverse direction as for ER96T.

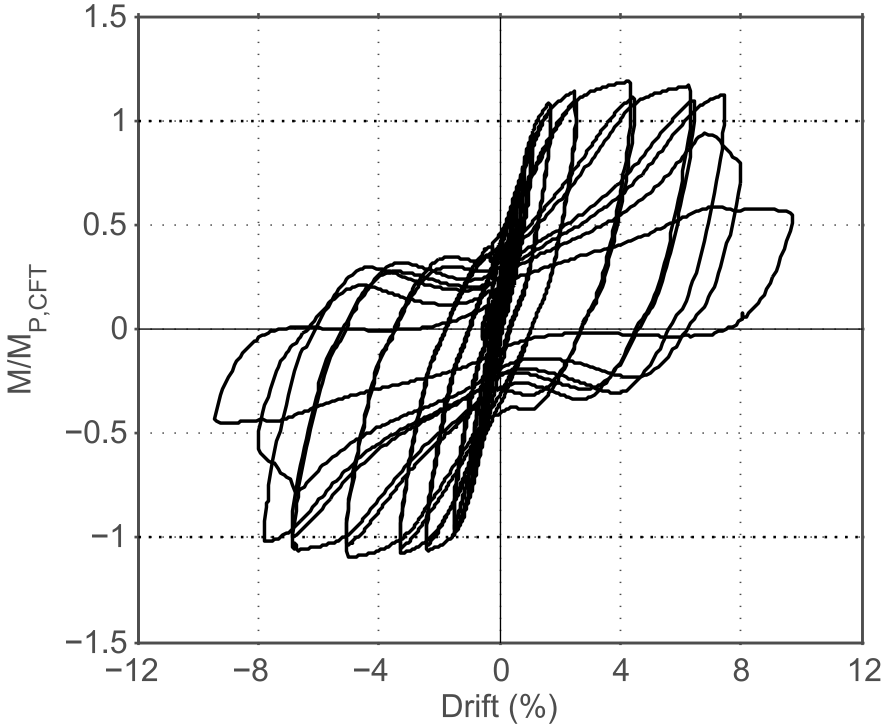

Figure 5.20: Moment-Drift Behavior of Specimen ER96L

The measured moment-drift response is illustrated in Fig. 5.20 and the damage progression is summarized in Table 5.8. This specimen exhibited an initial stiffness $EI_{measured}/EI_{eff} = 0.6$, and a maximum moment $M_{max}/M_{P,PSDM} = 1.19$. It should be noted that the reduced stiffness is at least partially due to increased deformation caused by the longer length of the longitudinal beams compared to the beam cap length for the transverse specimens. As for ER96T, the lower effective stiffness relative to the spiral welded specimens can partially be attributed to large steel strain penetration resulting from bond failure between the straight seam steel tube and cap beam concrete.

There was very limited visible damage to the column or cap beam through cycling at 0.5% drift. At this point, several circumferential hairline cracks developed at the grout-to-corrugated pipe interface. Several hairline cracks additionally extended radially into the cap

Table 5.8: ER96L Damage State Progression

Drift Ratio, %	$M/M_{P,PSDM}$	Column	Cap Beam
0.03	0.14		
0.10	0.13		
0.10	0.24		
0.18	0.22		
0.28	0.37		
0.35	0.35		
0.42	0.50		C1
0.52	0.49		
0.56	0.60		
0.70	0.59		
0.78	0.76		
1.02	0.79		
1.07	0.92	Y1	
1.52	0.96		
1.70	1.05		
2.41	1.04		
2.58	1.09	B1	
3.30	1.05		
4.50	1.11	B2	
5.10	1.04		
6.48	1.10	B3	
6.88	1.00		
7.97	0.93	T1	
8.01	0.79		
9.69	0.59		
9.42	0.44		

Repair States:
No Repair
Repair
Partial Replace
Full Replace

beam from the column. Yielding was measured by the strain gages on the CFST column located 3-in. from the surface of the cap beam during cycling at 1.1% drift.

Local buckling was observed during cycling at 3% drift, and the amplitude of the bulge was relatively small at 3.5% drift as illustrated in Fig. 5.21a. The apex of the buckle was approximately 2-in. above the surface of the cap beam. There was no significant cracking observed in the cap beam or grout region during subsequent cycling, and the out-of-plane deformation of the buckled region continued to grow as shown in Fig. 5.21b. Tearing initiated

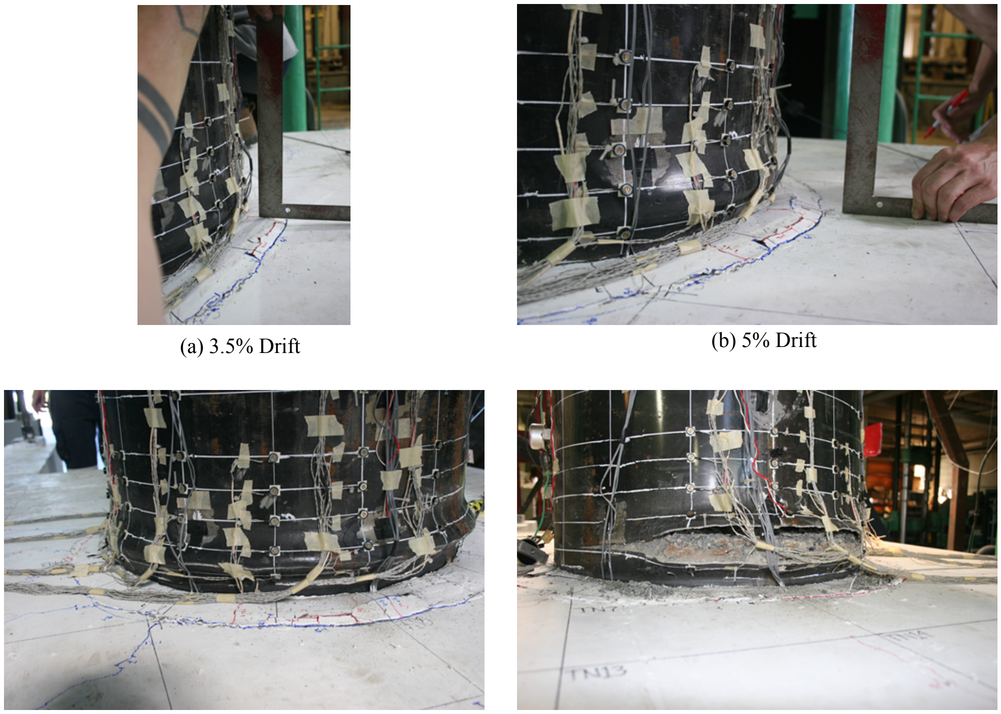

(a) 3.5% Drift (b) 5% Drift

(b) 7.5% Drift (c) 9% Drift

Figure 5.21: Photos of Primary Damage States of Specimen ER96L

at the apex of the buckled region on both the North and South side of the column during cycling at 7.5% drift as seen in Fig. 5.21c. Tearing propagated around the base of the column at 9% drift, and the test was stopped due to degradation of resistance. The specimen retained approximately 40% of its maximum moment capacity and support the full axial load at more than 9% drift.

5.3.1.4 ER103L

ER103L utilized a 25.75-in. diameter spiral welded ASTM A1018 grade steel with an embedded flange connection. The thickness of the steel tube was 0.25-in., resulting in D/t = 103. This specimen was loaded and deformed in the longitudinal direction of the bridge as for ER96L, but it employed a lower grade of steel than ER96L. It also had a larger D/t ratio than the prior ER connection specimens, and it was expected to buckle at smaller

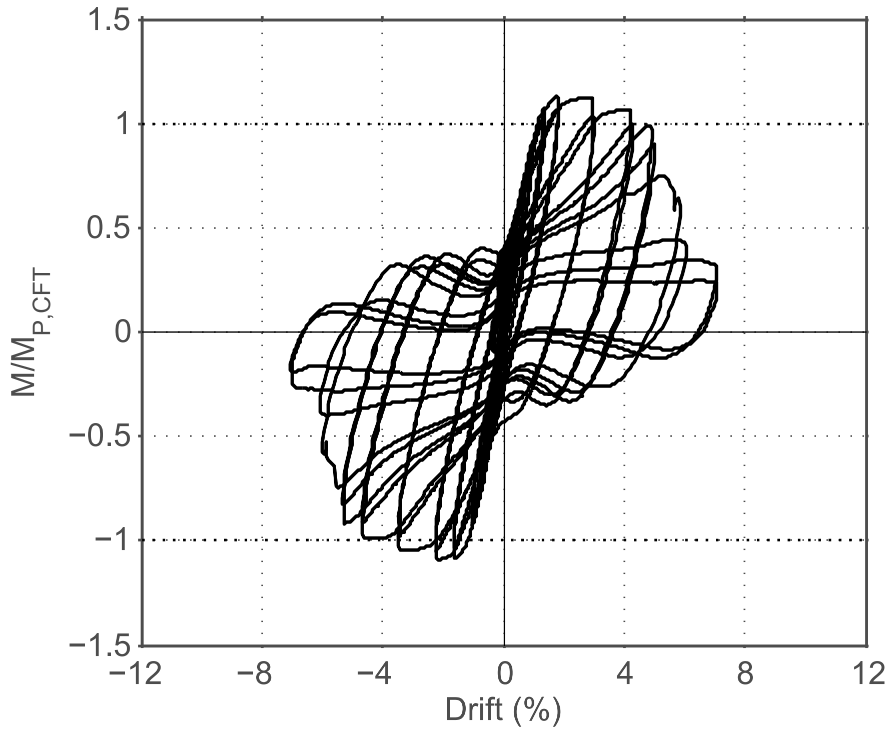

Figure 5.22: Moment-Drift Behavior of Specimen ER103L

deformations and to sustain earlier deterioration of resistance and tearing of the buckled steel. The CFST member exceeds the D/t limit permitted by the current AASHTO LRFD specification by approximately 18%. The purpose of this specimen was to evaluate the performance of the connection and cap beam for loading in the longitudinal direction of the bridge with a different grade of steel tube.

The measured moment-drift response is illustrated in Fig. 5.22 and the damage progression is shown in Table 5.9. This specimen exhibited an initial stiffness $EI_{measured}/EI_{eff} = 0.96$, and a maximum moment $Mmax/M_{P,PSDM} = 1.13$. As with ER80T, the large effective stiffness resulted from a nearly fixed connection condition at the cap beam interface created by the mechanical bond between the cap beam concrete and spiral weld in the steel tube. It is, however, interesting to note that this specimen did not experience the reduced stiffness for longitudinal deformation noted with the other specimens.

Table 5.9: ER103L Damage State Progression

Drift Ratio, %	$M/M_{P,PSDM}$	Column	Cap Beam
0.04	0.14		
0.05	0.11		
0.10	0.24		
0.11	0.22		
0.22	0.39		
0.23	0.37		
0.34	0.49		
0.36	0.47		
0.46	0.58		
0.48	0.58		
0.71	0.76		
0.74	0.75		C1
0.93	0.89		
1.02	0.92	Y1	
1.33	1.08		
1.63	1.09		
1.79	1.12		
2.25	1.12		
3.02	1.13		
3.50	1.09	B1	
4.28	1.13		
4.68	1.05	B2	
4.98	0.62	B3	
5.32	0.58		
6.05	0.55	T1	
6.08	0.48		
7.08	0.47		
7.03	0.47		

Repair States:
No Repair
Repair
Partial Replace
Full Replace

There was very limited visible damage to the column or cap beam through cycling at 0.75% drift. At this point, several circumferential hairline cracks developed at the grout-to-corrugated pipe interface. Several hairline cracks additionally extended radially into the cap beam from the column. Yielding was measured by the strain gages located in the CFST column 3-in. from the surface of the cap beam during cycling at 0.96% drift.

(a) 3.5% Drift

(b) 5.5% Drift

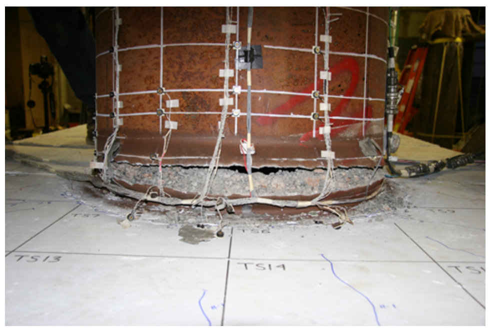

(c) 7.5% Drift

Figure 5.23: Photos of Primary Damage States of Specimen ER103L

Local buckling was observed during cycling at 3.5% drift as shown in Fig. 5.23a. The apex of the buckle was approximately 1.5-in from the surface of the cap beam. Tearing initiated at the apex of the buckled region on the North and South sides during the 5.5% drift cycles. The length of the initial observed tear was rather large (6-in.) as illustrated in Fig. 5.23b. Tearing propagated around the base of the steel tube during cycling at 7.5% drift, and the test was stopped due to significant strength degradation. The moment capacity was approximately 20% of the maximum tearing of the tube, and the full axial compression capacity was maintained. The earlier buckling and tearing of this tube illustrate the importance of the D/t slenderness limit.

5.3.2 *Influence of D/t Ratio and Ultimate Steel Strain Capacity on the Performance of the ER Connection*

The ER connections exhibited largely stable hysteretic responses and exceeded the theoretical plastic capacity of the CFST component. The progression of damage was similar for this class of specimens and is illustrated in Fig. 5.19 using Specimen ER96T. All ER specimens exhibited hairline radial cracks extending outwards from the column during early cycles (1% drift), however these cracks remained small throughout the tests, and did not influence behavior. Buckling initiated near the cap beam interface from approximately 1.5%-3.5% drift. Out-of-plane deformation in the buckled region increased with increasing cyclic deformations, and finally tearing initiated at the apex of the buckled region.

The experimental results discussed here, along with the results of all ER specimens which exhibited a ductile failure mode in Table 3.1 indicate that higher D/t ratios cause an earlier initiation of local buckling, and more ductile steels tend to lead to larger drift capacities prior to tearing of the steel.

Fig. 5.24a and Fig. 5.25a summarize the influence of the D/t ratio on the drift at the initiation of local buckling. Note that D/t in Fig. 5.25 has been normalized by the compactness limit ((D/t)limit) specified in the 2015 AASHTO LRFD to account for different steel strengths. Specimens which exceeded the specified compactness limit buckled at earlier drifts. Comparing ER96L and ER103L specifically, visual buckling occurred at 3.2% for a D/t ratio of 80 relative to 2.5% for a D/t ratio of 103 (as illustrated in Fig. 5.24). Note that buckling does not result in degradation in lateral resistance, but results in an earlier initiation of tearing due to low cycle fatigue at the apex of the buckled region.

Fig. 5.24c and Fig. 5.25b summarize the influence of the ultimate tube steel strain (ϵ_{su}) on the drift at the initiation of tube tearing. Note that ϵ_{su} was determined using steel coupon tests. As is indicated in these figures, specimens which utilized tube steel with larger ultimate strain capacities developed tube tearing at larger drifts even for specimens with higher D/t ratios. Fig. 5.26 shows the buckling shapes of ER103L and ER96L at selected drift ratios as

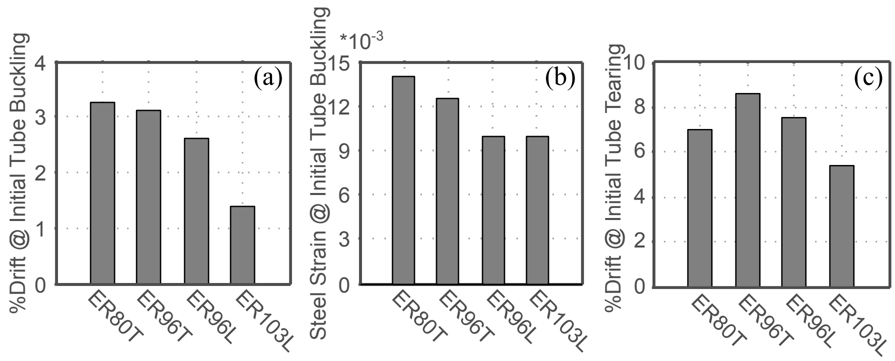

Figure 5.24: (a) Influence of D/t Ratio on Buckling Drift, (b) Steel Tube Strain at Initiation of Buckling, and (c) Influence of Tube Steel Strain Capacity (ϵ_{su}) on Tearing Drift for Specimens Evaluated in this Program

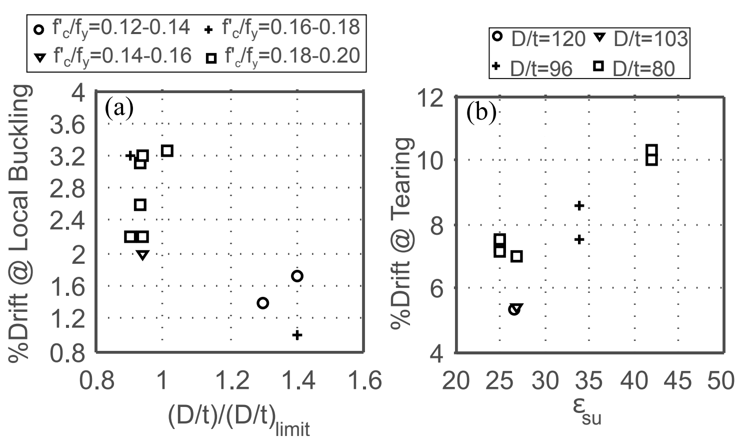

Figure 5.25: Influence of D/t Ratio on Buckling Drift and Tube Steel Strain Capacity (ϵ_{su}) on Tearing Drift For all Specimens Including Specimens in Table 3.1

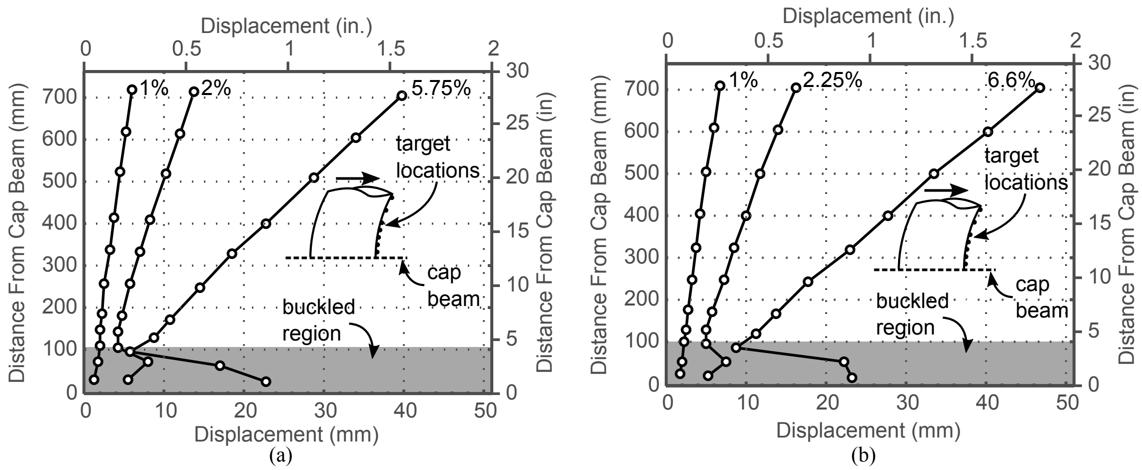

Figure 5.26: Buckled Profile of (a) ER103L and (b) ER96L

determined using the Optotrak Motion Certus System. These two specimens had different D/t ratios as well as different ϵ_{su} values of 27.5% and 33.5%, respectively Despite having a similar buckled profile at comparable strains, tearing in ER103L developed at much lower drifts compared to ER96L (5.4% drift compared to 7.5% drift, respectively). This premature tearing is a result of the lower strain capacity exacerbated by the high D/t ratio, which results in the lowest drift capacity in all ER specimens. Local tube buckling did not result in loss of lateral-load carrying capacity as long as the concrete fill in the buckled region remained intact. Similarly, ER80T failed at drift levels less than the ER96L and ER96T specimens; this earlier failure is attributed to the smaller fracture strain capacity of the ASTM A1018-07 SS steel. Note that the compressive steel strain in the buckled region at the initiation of local buckling has also been recorded and is illustrated in Fig. 5.24b. From this figure, it is clear that the strain at the initiation of local buckling is relatively constant for the range of D/t ratios tested here.

5.3.3 Comparison of Transverse and Longitudinal Loading

The direction of loading did not influence the behavior of the embedded connection type. EMB96T and EMB96L were selected to evaluate the influence of the direction of loading as

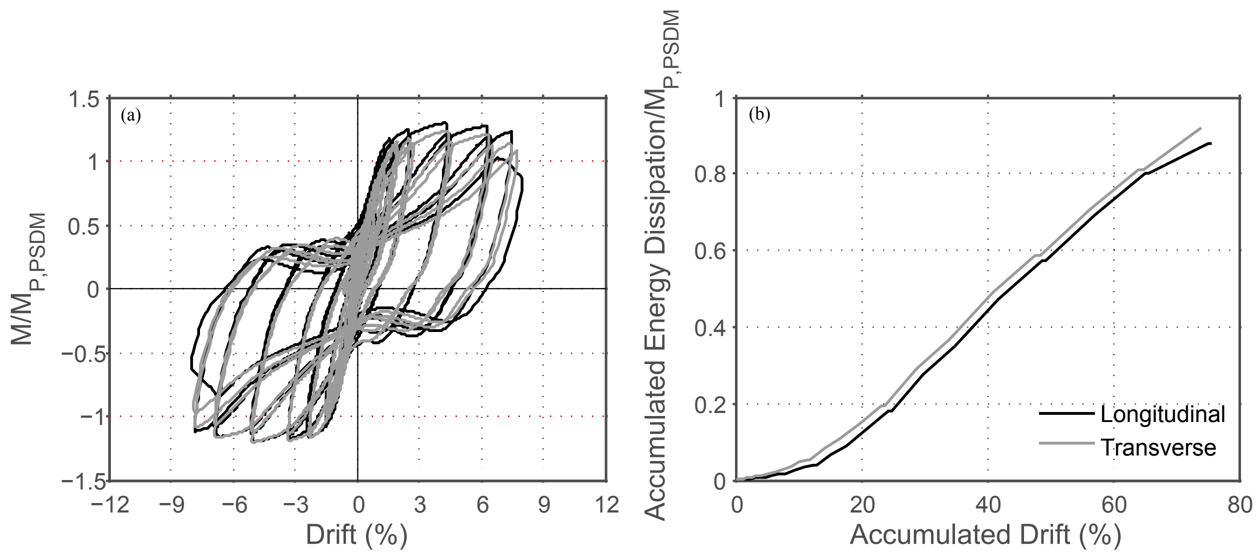

Figure 5.27: Comparison of (a) Hysteretic Response and (b) Energy Dissipation in Transverse (EMB96T) and Longitudinal (EMB96L) Specimens

these specimens had the same cap-beam reinforcing details and axial load; the only variable was the direction of loading. Both specimens exhibited similar moment-drift behaviors and energy dissipation characteristics as shown in Fig. 5.27. The moment-drift behaviors in Fig. 5.27 exhibit similar strengths and overall hysteretic shape. The accumulated energy dissipation and drift were larger in the transverse specimen because this specimen was subjected to additional cycles after tearing propagated around the base of the column. Very similar accumulated energy dissipation characteristics were exhibited up to this point. The stiffness of the transverse specimen was greater than that of the longitudinal specimen as is given in Table 5.2, however this is due to the boundary conditions used during testing; the longitudinal specimen developed some rotation through flexural deformation in the girders.

5.3.4 Fragility Curves

The experimental results discussed here, along with the results of all ER specimens which exhibited a ductile failure mode in Table 3.1 were used to fit lognormal cumulative distribution functions (CDF) for the damage state of the CFST as correlated to the drift range in which the damage was observed. The lognormal CDF is defined in Equation 5.2 where x is a particular value of drift, θ_d is the logarithmic mean, and β_d is the logarithmic standard deviation. Using the experimental observations, the lognormal CDF was fitted such that θ_d and β_d were optimized to reduce the bias, where the bias is the difference between the experimental and lognormal CDF as illustrated in Fig. 5.28. The constants θ_d and β_d were optimized using a numerical optimization program in Python which minimizes user-defined objective functions based on constraints on its variables as is generalized in Equation 5.1, where the value of the objective function is based on the input variable $x_0, x_1, ..., x_N$ [Nocedal and Wright, 2006].

$$min \sum_{i=1}^{n} f(x_0, x_1, ..., x_N) \tag{5.1}$$

The generalized optimization function for reducing the bias is defined in Equation 5.3 where P^{emp} is the empirical probability of occurrence, and $P^{theo}(\theta_d, \beta_d)$ is the probability of occurrence from the fitted lognormal CDF. The empirical and fitted lognormal CDFs are plotted in Fig. 5.29 and Fig. 5.30 for ASTM 1018 and API 5L tube steel respectively. Note that numerical optimization has been used to fit lognormal CDF in previous research, and is recommended when structural analyses are expensive or limited experimental data is available [Baker, 2014].

$$F_d(x) = \Phi\left(\frac{ln(x/\theta_d)}{\beta_d}\right) \tag{5.2}$$

$$min \sum_{i=1}^{n} |Bias_i| = min \sum_{i=1}^{n} |P_i^{emp} - P^{theo}(\theta_d, \beta_d)| \tag{5.3}$$

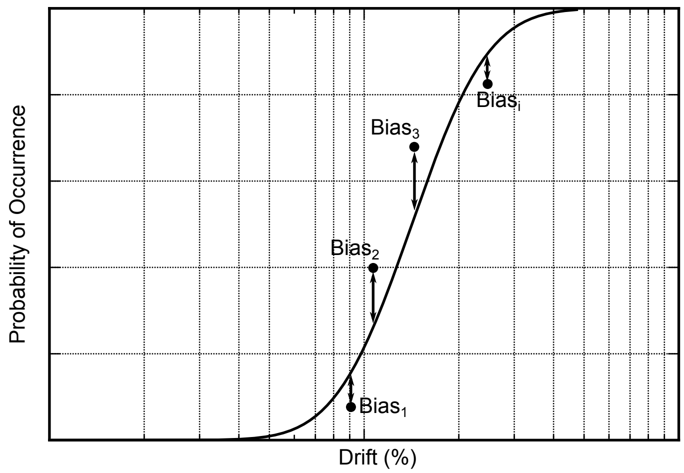

Figure 5.28: Definition of Bias for Optimization of the Lognormal Constants θ_d and β_d

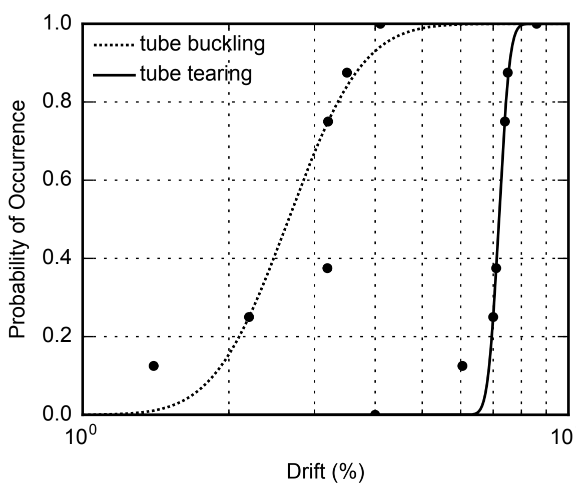

Figure 5.29: Fragility Curves for Yielding, Buckling, and Tearing of Spiral Welded CFST Specimens

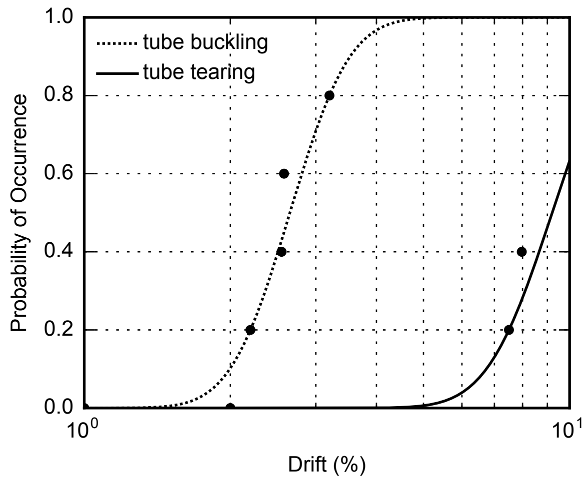

Figure 5.30: Fragility Curves for Yielding, Buckling, and Tearing of Straight Seam CFST Specimens

5.4 Proposed Design Expressions

The experimental results and observations were used to develop practical design expressions for the ER cap beam connection. This connection can be employed using cast-in-place (CIP) or precast super-structure cap beam. For precast construction, a partial height pocket must be included in the precast elements through use of a corrugated pipe, which meets the specifications outlined below. For CIP construction either a monolithic or partial height pocket connection can be used although only the partial height pocket connection was studied here. When using the partial height pocket connection, the steel tube and annular ring are grouted into place using a high-strength fiber-reinforced grout to ensure shear transfer and bond strength precluding failure of the grout.

An overview of the design procedure for the ER connection is given in Fig. 5.31. Note that the flow chart in Fig. 5.31 does not include procedures for designing the CFST component. A design procedure for CFST components is included in the ER connection design example in Appendix C.

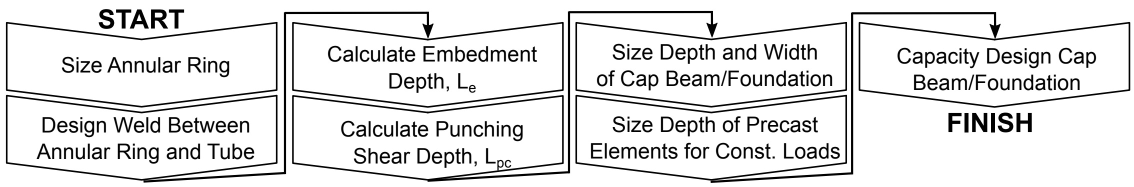

Figure 5.31: Flow Chart for Design of ER Connection

The following sections summarize the materials and design expressions for the ER connection. Proposed specification language for inclusion in the Caltrans SDC has been drafted and is provided in Appendix C of this report. Note that design requirements should conform to the AASHTOa [2015] or Caltrans [2010] specification unless otherwise specified here. The design variables in the following sections are annotated in Fig 5.1.

5.4.1 Materials

Materials for the specified connections should conform to the AASHTOa [2015] or Caltrans [2010] standards, with several specific provisions included in this section.

5.4.1.1 Grout

When precast components are used, the fiber-reinforced grout consisting of prepackaged, cementitious grout and meeting ASTM C-1107 for grades A, B, and C non-shrink grout is used. The grout conforms to several additional performance requirements including compressive strength, compatibility, constructability, and durability. These requirements are summarized in Table 5.10. The 28-day grout strength f'_g must be at least equal to f'_c of the surrounding concrete components. Grout using metallic formulations shall not be permitted, and grout shall be free of chlorides. No additives shall be added to pre-packaged grout.

These requirements ensure the grout has properties that provide adequate strength and longevity. These requirements adapted from recommendations provided in Restrepo et al.

[2011]. Grouts with chloride are not permitted as these materials can accelerate corrosion in the connection reinforcing and steel tube. Additives are not permitted because pre-packaged grouts are proprietary mixes which should not be modified.

Table 5.10: Grout Specifications

Property	Permitted Values
Mechanical	
Compressive Strength	Must exceed f'_c of surrounding concrete at 28-days. Minimum grout strength f'_g must exceed 6-ksi.
Compatibility	
Non-Shrink	Grade A, B, or C per ASTM C-1107
Constructability	
Flow	Mix to flowable consistency according to manufacturer specifications.
Durability	
Freeze thaw	300 cycles, relative durability factor 90% per ASTM C666
Sulfate resistance	Expansion at 26 weeks ¡ 0.3% per ASTM C1012

5.4.1.2 Fiber Reinforcing

Macro polypropylene fiber with a minimum volume of 0.2% is included to provide crack resistance and bounding characteristics between the tube and corrugated metal duct. Test results to date have not evaluated the use of alternative fibers such as steel fibers.

5.4.1.3 Corrugated Metal Duct

Corrugated metal ducts are used to provide voids in precast components. The ducts are galvanized steel according to ASTM A653. Duct diameter is selected based on construction tolerances. Plastic ducts should not be used as the purpose of the ducts it to be a bond crack arrestor, act as confinement and provide shear transfer from the grout to the outer concrete. The use of corrugated metal ducts for grouted connections is supported by this research as well as a wealth of seismic precast connection data, such as the references discussed in Section Chapter 3.

5.4.1.4 Tube Steel

Steel tubes may either be straight seam or spiral welded and must conform to either ASTM 1018 or API 5L requirements. Spiral welded tubes must be welded using a double submerged arc welding process, and weld metal properties must match properties of the base metal and meet minimum toughness requirements of AISC demand critical welds [AISC, 2011].

Selection of tube material designation (ASTM 1018 or API 5L) plays a role in the ductility of the full strength embedded CFST connection. API 5L grade steel has stricter requirements regarding chemical composition than ASTM 1018 steel, and can therefore provide additional ductility for both spiral welded and straight seam tubes. Experiments were conducted on API 5L and ASTM 1018 tubes which slightly exceeded the upper bound slenderness requirements for CFSTs specified in the AASHTOa [2015]. Results from these tests showed that embedded ring connections which utilize API 5L steel can exceed 8% drift prior to tube fracture, while connections which use ASTM 1018 steels tend to fracture at 6% drift.

5.4.2 Annular Ring

The annular ring is welded to the end of the steel tube to provide anchorage and stress transfer to the concrete and reinforcing in the cap beam. The ring is made of steel of the same thickness and yield strength as the steel tube. The ring projects both in to and out from the steel tube a distance 8 times the thickness of the steel tube.

The ring is welded to the steel tube using complete joint penetration (CJP) welds of matching metal, or fillet welds designed to develop the tensile capacity of the steel tube. The minimum fillet weld size is:

$$w \geq \frac{1.31 F_{u,st} t}{F_{EXX}} \tag{5.4}$$

where $F_{u,st}$ is the ultimate strength of the steel tube, and F_{EXX} is the minimum tensile strength of the weld metal. The CJP or fillet welds should, as a minimum, satisfy theAISC [2011] toughness criteria for demand critical welds.

5.4.3 Embedment Depth

Equation 5.5 is used to calculate the required embedment depth (L_e) to develop the yield strength or full plastic capacity of the CFST component where D is the outer diameter of the steel tube, t is the thickness of the steel tube, $f'_{c,cap}$ is the compressive strength of the cap beam concrete, F_{xx} is the ultimate strength of the steel tube ($F_{u,st}$) or the yield strength of the steel tube ($F_{y,st}$) for the seismic and non-seismic design cases respectively, and the coefficient n is 6 for the seismic design case and 8 for the non-seismic design case when f'_c is in psi.

$$L_e = \sqrt{\frac{D^2}{4} + \frac{DtF_{x,st}}{n\sqrt{f'_{c,cap}}}} - \frac{D}{2} \; (f'_{c,cap} \text{ in psi}) \tag{5.5}$$

Equation 5.5 was derived based on the pullout model illustrated in Fig. 5.32a [Lehman and Roeder, 2012b,a; Stephens et al., 2015]. Using this model, the ultimate tensile strength of the steel tube was equilibrated with the tensile strength of a concrete cone over that same tensile region, and the experimental results were used to determine the limiting concrete tensile strength, $n\sqrt{f'_c}$. Specifically, the model was evaluated for each ER specimen (including the ER foundation specimens describe in Table 3.1), and the corresponding n value was determined via equilibrium. The n values for each specimen are compared to performance, deformation capacity, and ultimate failure in Fig. 5.32b. Based on this comparison, a limiting concrete tensile stress of $8\sqrt{f'_c}$ and $6\sqrt{f'_c}$ are proposed for yielding and plastic performance respectively when f'_c is in psi.

5.4.4 Punching Shear Requirements

The specific depth, Lpc, above the embedded tube is designed to prevent a punching shear failure. This has been previously derived [Lehman and Roeder, 2012b,a] for the ER foundation connection using the ACI procedure for punching shear in flat slabs, and is presented in Equation 3. C_c and C_s are the compressive forces in the concrete and steel due to the maximum combined axial load and bending moment as calculated using the PSDM

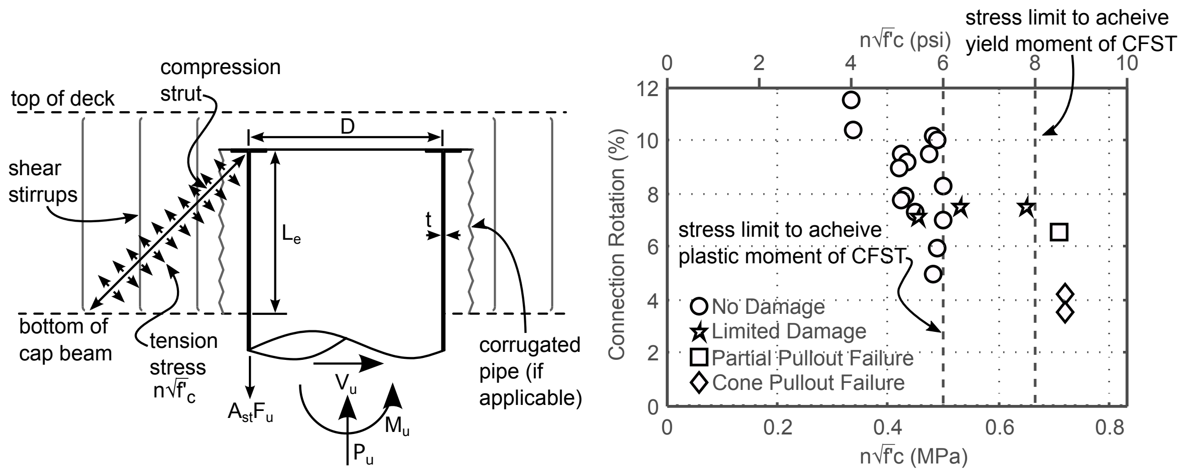

(a) Cone Pullout Model (b) Evaluation of Stress Demand on Conical Surface

Figure 5.32: Conical Pullout Model and Evaluation of Experimental Stress Demand on Conical Surface

(illustrated in Fig. 2.1a). For convenience, C_c plus C_s has been plotted in Fig. 5.33 for a range of D/t ratios and tube thicknesses assuming a nominal yield strength of 50-ksi and a concrete strength of 6-ksi.

$$L_{pc} = \sqrt{\frac{D^2}{4} + \frac{C_c + C_s}{6\sqrt{f'_{c,cap}}}} - \frac{D}{2} - L_e \ (f'_{c,cap} \text{ in psi}) \tag{5.6}$$

5.4.5 Flexure Reinforcing in the Cap Beam

Longitudinal flexural reinforcing steel in the cap beam/foundation within the column region must resist 1.25Mp,CFST to ensure the cap beam remains elastic. The top or bottom level of longitudinal reinforcing (for the cap beam or foundation respectively) steel is continuous and spaced uniformly across the width of the cap beam (indicated by (1) in Fig. 5.34). The bottom layer of flexural reinforcing steel within the diameter of the corrugate pipe or steel tube are hooked and not included in the strength calculation (as indicated by (2) in Fig. 5.34). Instead only the continuous reinforcement is designed to resist 1.25Mp of the

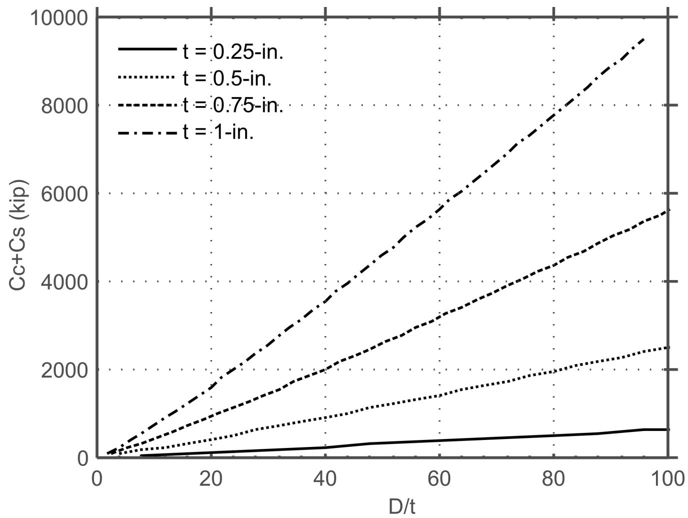

Figure 5.33: $C_c + C_s$ Values Calculated using the PSDM for f'_c=6-ksi and f_y=50-ksi

CFST column (i.e. continuous positive flexure reinforcing must be placed to the outside of the steel tube or corrugated pipe as indicated by (3) in Fig. 5.34).

5.4.6 Vertical Reinforcing in Cap Beam

Additional vertical reinforcing steel in the joint region (indicated by (4) in Fig. 5.34) is required to prevent cone pullout failure; however this steel may also be used to carry service. The required area of vertical reinforcing, A_s^{jv}, is determined using the relationship shown in Fig. 5.35a where A_{st} is the total area of the steel tube embedded into the cap beam. The steel area A_s^{jv} should be distributed uniformly around the CFST column within a distance Le extending from the end of the annular ring when monolithic construction is used, and extending from the outer diameter of the corrugated pipe when the grouted connection is used. The hatched region in Fig. 5.35b indicates this area.

The relationship illustrated in Fig. 5.35a was derived using the cone pullout failure model illustrated in Fig. 5.32a. As discussed previously, a limiting principal tension stress of $6\sqrt{f'c}$ (where f'_c is in psi) was empirically derived along a 45-degree conical failure plane extending from the outer diameter of the embedded CFST to the surface of the foundation or cap

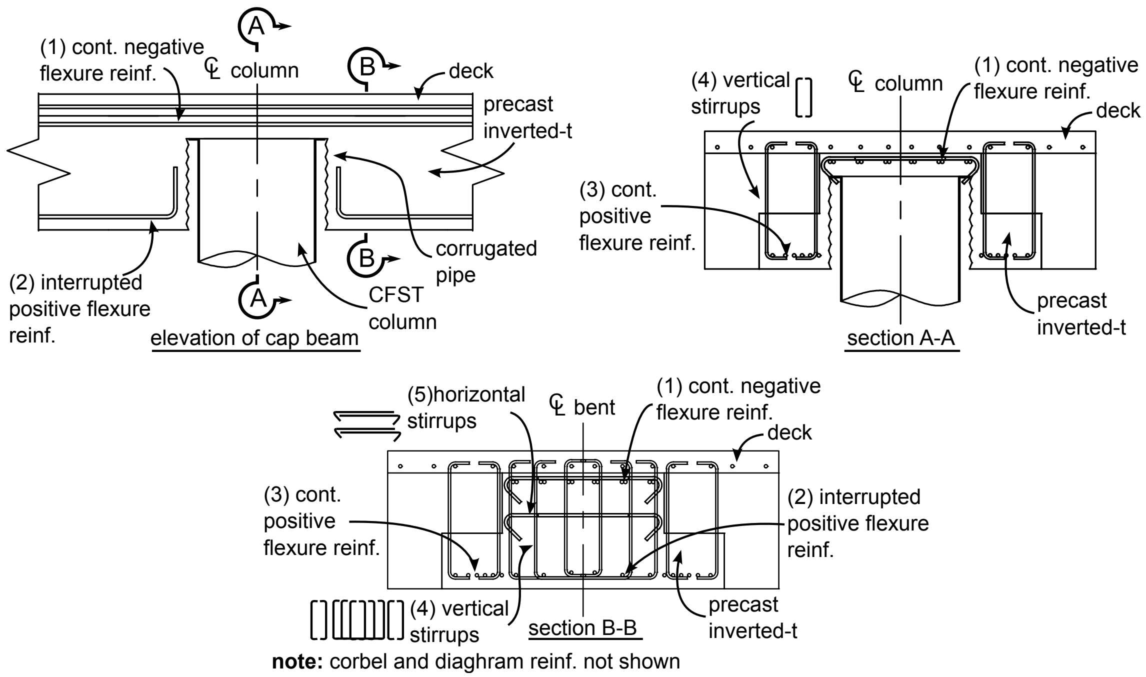

Figure 5.34: Sample Cap Beam Reinforcing Details for ER Connection

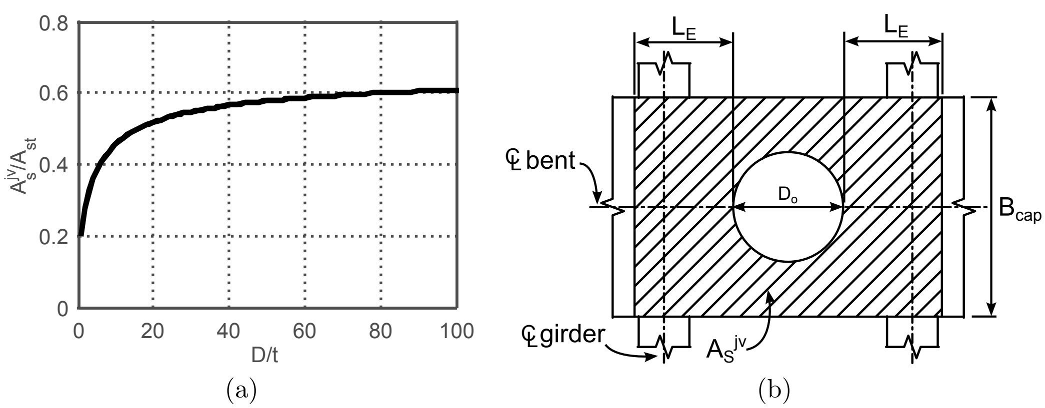

Figure 5.35: (a) Required Area of Vertical Stirrups related to D/t for the ER Connetion and (b) Required Location of Vertical Stirrups in the Cap Beam

beam. The concrete along this failure plane is assumed to carry a stress of $2\sqrt{f'c}$, while the vertical reinforcing in the joint region carries $4\sqrt{f'c}$. Using this assumption, the area of vertical reinforcing required to resist a cone pullout failure can be calculated as a function of the embedment depth, L_e, and D. This relationship was simplified to relate the ratio of the required vertical reinforcing area to the area of the tube, A_s^{jv}/A_{st}, to the D/t ratio of the steel tube as is illustrated in Fig. 5.32a for all D/t ratios which would be commonly seen in practice. In lieu of using the relationship illustrated in Fig. 5.32a, the required area of vertical stirrups in the joint region can be conservatively simplified according to Equation 5.7. A minimum of two vertical bars must cross the strut region (as illustrated in Fig. 5.32a), which is L_e extending from each side of the column.

$$A_s^{jv} = 0.65A_{st} \tag{5.7}$$

5.4.7 Horizontal Stirrups in Cap Beam

Horizontal stirrups placed transversely around the vertical stirrups in two or more intermediate layers are required by the AASHTOb [2011]. Note that one layer of horizontal stirrups should pass above the embedded CFST as shown in Section A-A in Fig. 5.34.

5.4.8 Configuration of Columns and Longitudinal Girders

When using the ER connection, the columns should be laid out between the longitudinal girders to allow for positive moment continuity in the superstructure in the longitudinal direction of the bridge.

5.4.9 Plastic Hinge Length

A plastic hinge length estimation for numerical modeling of the ER connection is given in Equation 5.8 where the constant α is taken as 0.25. The constant α was derived using experimental data and Equation 5.9 where Δ_y and Δ_u are the yield and ultimate column displacements respectively, ϕ_y and ϕ_u are the yield and ultimate curvatures respectively, L is the distance from the point of contraflexure of the column to the center of the maximum moment, and l_p is the plastic hinge length. Δ_y and ϕ_y were estimated using the yield strain of the steel tube ϵ_y, ϕ_u was estimated using the ultimate strain of the steel tube reduced to account for low cycle fatigue $0.75\epsilon_u$, and the ultimate displacement Δ_u was taken from the ER connection experiments. The ratio of the estimated plastic hinge lengths to CFST diameter (l_p/D) are plotted as a function of D in Fig. 5.36 for all ER connections evaluated in this study as well as the ER connections discussed in Lehman and Roeder [2012b]. The constant α was taken as the mean of the lp/D ratios, as statistically significant regression could not be developed using the limited data set.

$$l_p = \alpha \times D \tag{5.8}$$

$$\Delta_u = \Delta_y + (\phi_u - \phi_y) \times l_p \times \left(L - \frac{l_p}{2}\right) \tag{5.9}$$

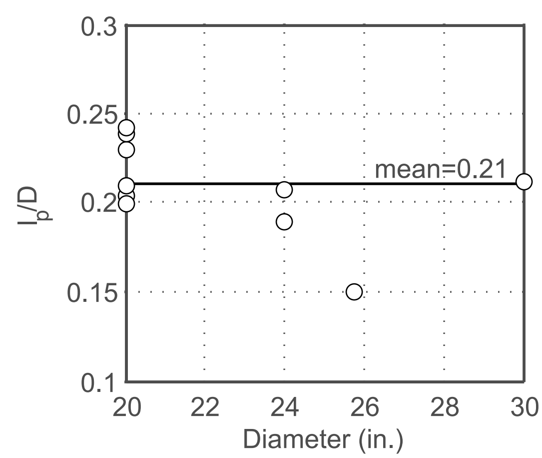

Figure 5.36: Plastic Hinge Length for ER Connection

Chapter 6

PARTIAL HEIGHT POCKET DOWEL CONNECTIONS (WD AND RC)

This chapter discusses large scale experiments and proposed design expressions for the WD and RC connections. A detailed overview of the connection is provided in Section 6.1. A supplemental welded dowel pullout experiment is discussed in Section 6.2.1. The large scale experimental program including specimen geometry, specimen construction, test apparatus, and instrumentation is described in Sections 6.2.2-6.2.5. Experimental results are given in Section 6.3, and finally design expressions are proposed in Section 6.4.

6.1 Connection Overview

Fig. 6.1a and Fig. 6.1b show partial height pocket WD and RC connections respectively. These connections utilize T-headed reinforcing dowels that extend from the CFST column into the cap beam to provide axial, moment, and shear transfer. Both connections can be used in traditional cast-in-place construction, or can be integrated into precast elements using a partial height pocket similar to that described for the ER connection.

The WD connection utilizes headed reinforcing bars welded to the inside wall of the steel tube and anchored into the cap beam. The weld transfers stress from the walls of the steel tube to the dowels, and provides the maximum moment arm within the CFST column. The dowels transfer forces to the cap beam, similar to a traditional RC connection. The steel tube provides confinement to and enhances the shear resistance of the concrete fill. A flange is welded to the exterior of the steel tube to increase compressive bearing area on the soffit. The reinforcing bars can be bonded or debonded in the column-to-cap beam interface region

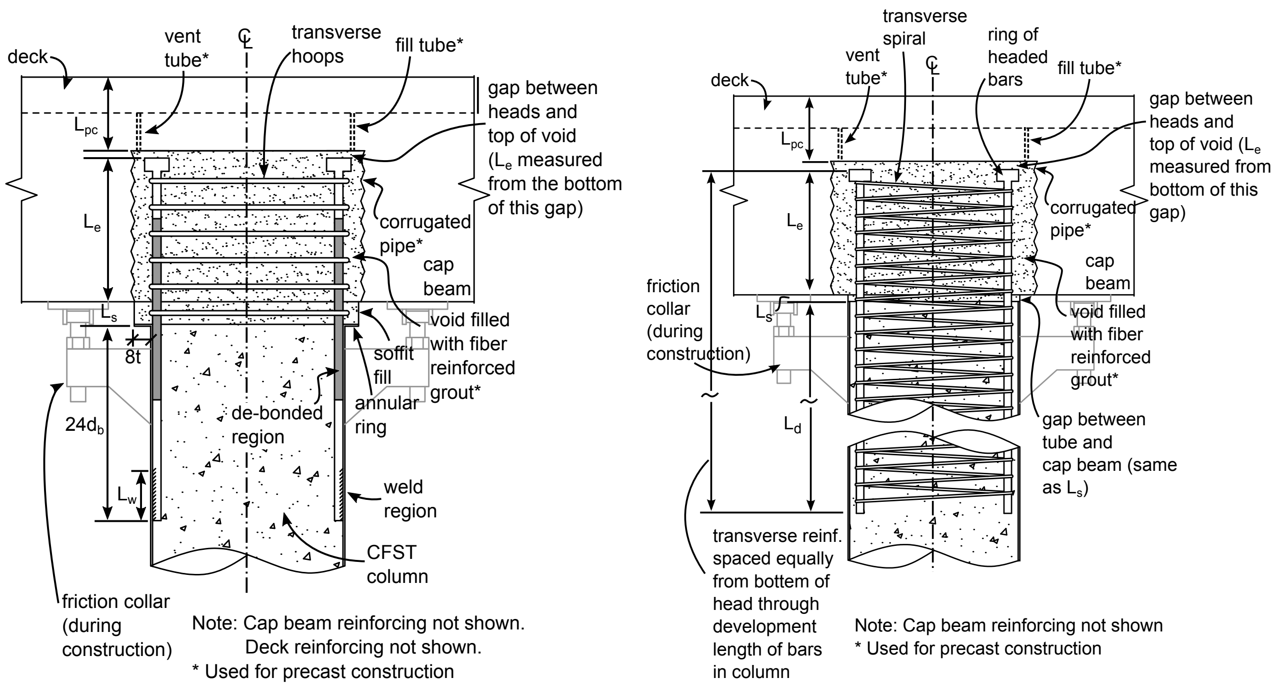

(a) WD Connection

(b) RC Connection

Figure 6.1: Overview of Dowel Type Connections

to increase ductility of the connection and reduce local strain demand to the reinforcing and damage to the cap beam.

The RC connection utilizes an internal reinforcing cage consisting of spiral and longitudinal reinforcement that extends from within the CFST column into the cap beam. There is a finite distance between the reinforcing cage and steel tube within the column of the RC connection. A gap is left between the steel tube and cap beam to limit direct force transfer from the CFST component into the cap beam [Montejo et al., 2009].

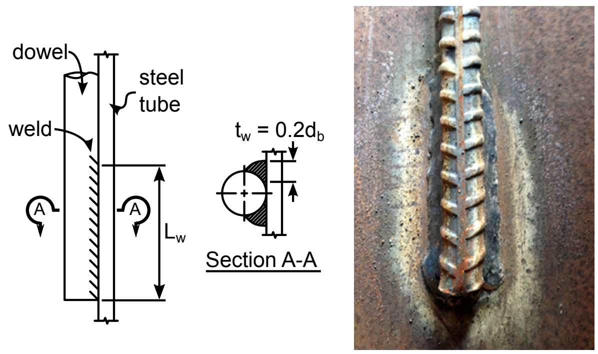

Figure 6.2: Flare Bevel Groove Weld

6.2 Experimental Program

6.2.1 Welded Dowel Pullout Experiments

The welds joining the dowel bars to the tubes are critical to the performance of the WD connections, and a limited experimental study was conducted on this weld detail. Of particular concern were the weld properties required to transfer the full tensile capacity of the dowels to the tube and potential local damage to the tube and the concrete fill. AWS [2010] specifies requirements for flare bevel groove welds as illustrated in Fig. 6.2 to attach rebar to steel plates.

An experimental study evaluated the impact of weld strength and length, bar size and debonding of the bar. An overview of the experimental matrix is given in Table 6.1. Four 20-in. diameter steel tubes with 0.25-in. wall thickness each had six dowels welded to the inside prior to being filled with self-consolidating, low-shrinkage concrete. As indicated in the table, sixteen No. 7, 4 No. 9, and 4 No. 11 A706 dowels were tested with a pull-out test rig which is illustrated in Fig. 6.3a. Design strengths of the flare bevel welds (based upon the AWS D1.4) ranged from 80% to 120% of the nominal dowel strength. The dowels extended into the tube from $18d_b$ and $24d_b$ per discussions with several Caltrans bridge engineers, where d_b is the diameter of the dowel bar prior to the start of the weld. The weld process was a self-shielded flux core arc welding method with E71T8 electrodes. The measured material properties of the steel tube were consistent with the properties listed for WD80T1 and WD80T2 in Table 6.4.

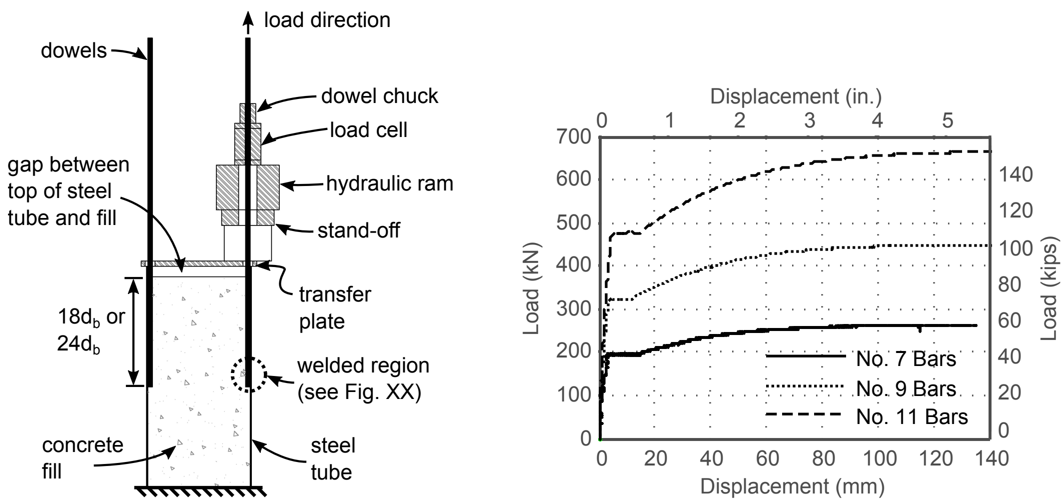

(a) WD Connection (b) RC Connection

Figure 6.3: Welded Dowel Pullout Experimental Test Setup and Typical Dowel Force Displacement Behaviors

Bonded and debonded dowels were alternated around the circumference of each tube to limit the influence of potential concrete cone pullout on adjacent dowels. The debonded length extended from the surface into the concrete and was achieved using duct-tape to cover the dowel deformations. A gap was left between the top of the steel tube and the concrete surface to allow for extension of the dowel, and a transfer plate was used to transfer force through the steel tube. Axial load and overall bar displacement were monitored electronically using a load cell and string potentiometers, respectively.

Typical force-axial bar displacement curves are illustrated in Fig. 6.3b. The failure mode in all tests was fracture of the dowel. The steel tube was removed following the experiments to evaluate the influence of de-bonding the dowels on the amount of concrete damage (illustrated in Fig. 6.4). Based on the experiences and recorded results the following conclusions and observations were drawn from the study:

Table 6.1: Pullout Test Matrix

Specimen Number	Bar Size	Debonded	Specified Strength Ratio $\frac{\phi R_n}{P_n}$	Actual Strength Ratio from Measured Length $\frac{\phi R_n}{P_n}$	Length Dowel Extended into Tube
1	No. 7	No	0.8	1.06	$24d_b$
2	No. 7	No	1.0	1.27	$24d_b$
3	No. 7	No	1.1	1.08	$24d_b$
4	No. 7	No	1.2	1.40	$24d_b$
5	No. 7	Yes	0.8	0.99	$24d_b$
6	No. 7	Yes	1.0	1.24	$24d_b$
7	No. 7	Yes	1.1	1.36	$24d_b$
8	No. 7	Yes	1.2	1.31	$24d_b$
9	No. 7	No	0.8	0.99	$24d_b$
10	No. 7	No	1.0	1.18	$24d_b$
11	No. 7	No	1.1	1.19	$24d_b$
12	No. 7	No	1.2	1.31	$24d_b$
13	No. 7	Yes	0.8	0.92	$24d_b$
14	No. 7	Yes	1.0	1.16	$24d_b$
15	No. 7	Yes	1.1	1.23	$24d_b$
16	No. 7	Yes	1.2	1.29	$24d_b$
17	No. 9	No	1.0	0.98	$18d_b$
18	No. 9	Yes	1.0	1.0	$18d_b$
19	No. 9	No	1.0	0.98	$24d_b$
20	No. 9	Yes	1.0	0.95	$24d_b$
21	No. 11	No	1.0	1.03	$18d_b$
22	No. 11	Yes	1.0	1.01	$18d_b$
23	No. 11	No	1.0	1.0	$24d_b$
23	No. 11	Yes	1.0	1.6	$24d_b$

- No damage was observed in the steel tube in any of the tests.

- Full development of the dowels was observed for each dowel size for design weld strengths of at least 90% the nominal dowel strength. A design weld strength of at least 100% the nominal dowel strength including strength reduction factors is recommended to provide a reasonable factor of safety.

- Full development of the dowels was observed for embedment depths at low as $16d_b$, however $24d_b$ is recommended to provide a reasonable factor of safety.

- De-bonding the dowels decreased the concrete damage (as illustrated in Fig. 6.4).

Based on these recommendations, the dowels in the connection were extended into the steel tube for a distance of $24d_b$, and weld strengths equal to 100% of the nominal dowel capacity were designed for the large-scale connection experiments.

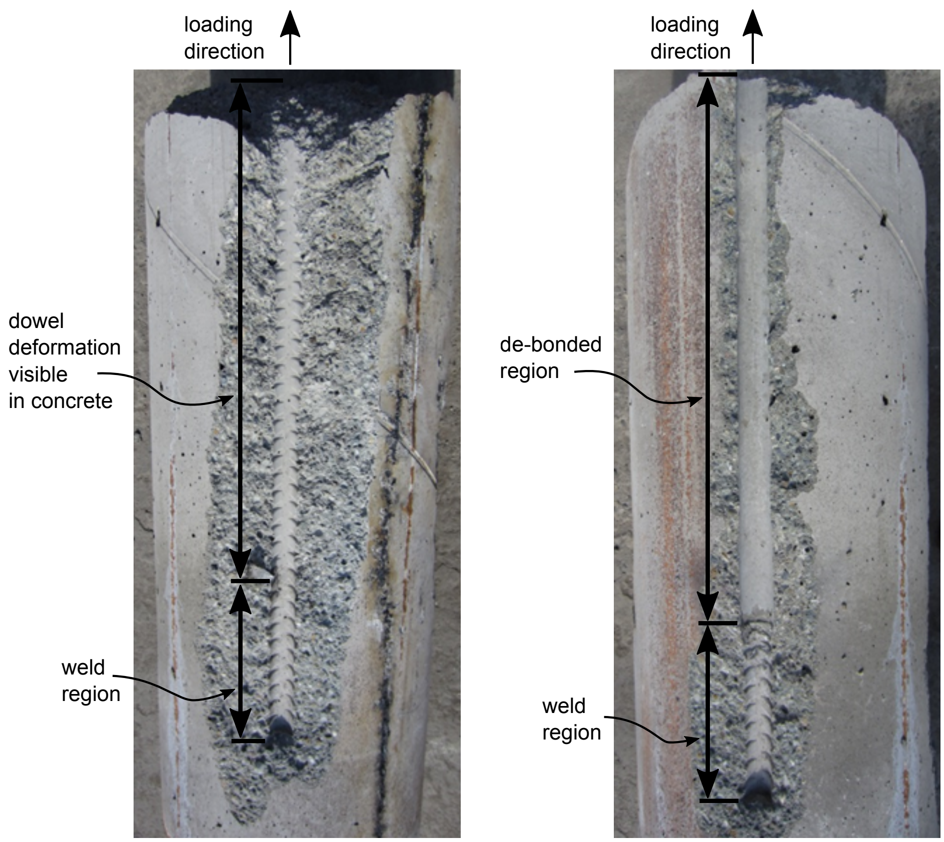

(a) Fully Bonded Dowel (b) Fully De-Bonded Dowel

Figure 6.4: Concrete Fill Damage in Pullout Specimens

6.2.2 Reference Specimens

The non-linear numerical analysis discussed in Chapter 4 formed the basis for the final design of the ER and WD connection test specimens, and the test matrix is summarized in Table 6.2.

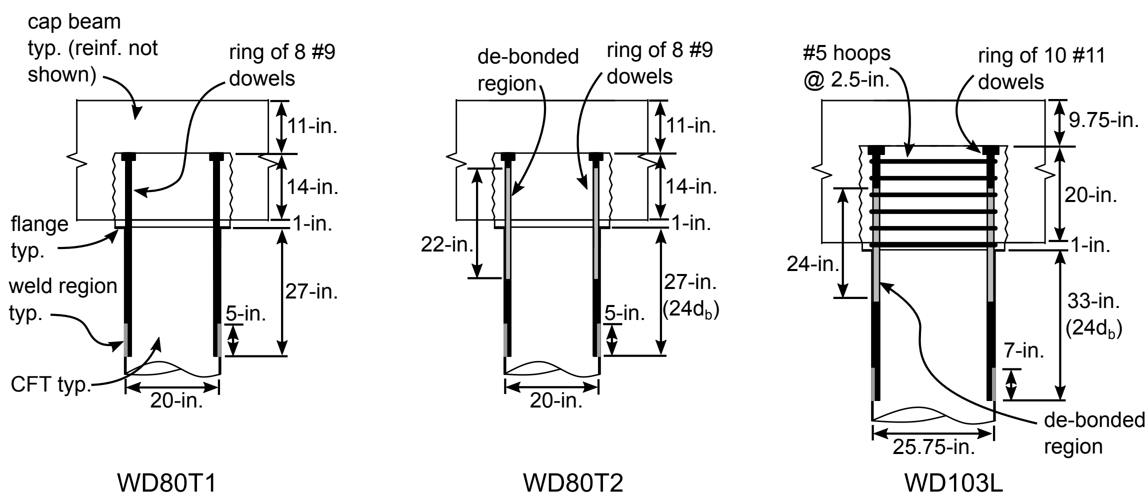

Figure 6.5: Connection Details for WD Specimens

All tubes had a nominal wall thickness of 0.25-in., and, as previously stated, specimens denoted with T and L were constructed to represent the transverse (normal to axis of the bridge) and longitudinal directions, respectively. The global transverse and longitudinal specimen geometries were consistent with the geometries defined in Fig. 5.2. Geometric variables in Fig. 5.2 are defined in Table 6.2.

6.2.2.1 WD Connection

Three WD connections were tested. WD specimen connection details are illustrated in Fig. 6.5. Geometric variables in Fig. 5.2 are defined in Table 6.2. The dowel bars were A706 Grade 60 reinforcing bars with a nominal yield stress of 60-ksi that extended 12db into the cap beam per ACI [2011] requirements for the development of headed reinforcing bars, and 24db into the CFST column based on results from the weld pullout experiments (Note that AASHTO specifications were used wherever possible; ACI specifications were used if AASHTO specifications were absent). The yield stress of the rebar was significantly larger than the yield stress of the steel tubes.

Table 6.2: Experimental Matrix and Specimen Properties

Specimen	Steel Tube Type	D, in.	t, in.	D/t	L_e, in.	L_{pc}, in.	Long. Dowels	Trans. Reinf.	ρ, %	h_{col}, in.	L_{cap}, in.	h_{cap}, in.	b_{cap}, in.	Axial Load Ratio, %
WD80T1	ASTM A1018-07	20	0.25	80	14	11	8-No.9	None	2.5	72	76	25	40	10
WD80T2	ASTM A1018-07	20	0.25	80	14	11	8-No.9	None	2.5	72	76	25	40	10
WD103L	ASTM A1018-07	25.75	0.25	103	20.25	9.5	10-No.11	No.5 @ 5-in.	3	83	186	29.75	65	10
RC80T	ASTM A1018-07	20	0.25	80	14	11	8-No.9	No.3 @ 2.5-in.	2.5	72	76	25	40	10

The bars were welded to the inside of the steel tubes using flare bevel groove welds designed to develop the nominal capacity of the dowels. All of the tubes were ASTM 1018 grade 50 steel with flanges that projected 2-in. outside the steel tube. The connections also had a 1-in. thick soffit, which extended from the surface of the cap beam as shown in Fig. 6.5. Specimens WD80T2 and WD103L had dowel bars debonded 22-in. and 24-in. respectively to increase deformation capacity and reduce deterioration of resistance as shown in Fig 6.5. The debonded lengths were calculated based on recommendations provided by Stringer [2010] and were selected to achieve a connection rotation demand of 10% drift prior to dowel bar fracture. The WD specimens were as follows:

- Specimen WD80T1 had fully bonded bars. The longitudinal reinforcing in the connection region was selected with a target longitudinal reinforcing ratio of 3%, resulting in eight evenly distributed No. 9 dowels.

- Specimen WD80T2 was nominally identical to Specimen WD80T1 but the bars were debonded 12-in. into the tube and 12-in. into the connection (24-in. total debonded length) using PVC pipe.

- Specimen WD103L used ten evenly distributed No. 11 debonded dowel bars with No. 5 spiral hoop reinforcement spaced at 5-in. to provide additional confinement to the soffit and joint region as illustrated in Fig. 6.5. The dowel bars were debonded 12-in. into the tube and 12-in. into the connection using PVC pipe.

6.2.2.2 RC Connection

One RC specimen was constructed (RC80T). As illustrated in Fig. 6.6, the longitudinal reinforcing consisted of eight evenly distributed No. 9 headed bars, resulting in a longitudinal reinforcing ratio of 3.0%. The bars extended $12d_b$ into the cap beam per the ACI 318 development requirements for headed reinforcement, and $30d_b$ into the CFST column per development requirements for straight deformed bars. The bars were confined by a No. 3

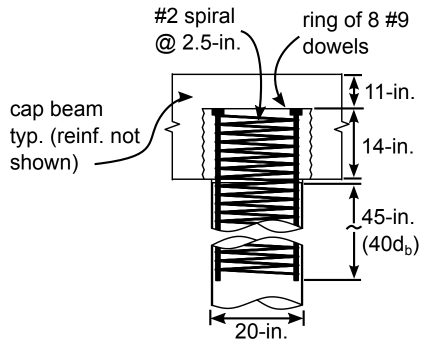

Figure 6.6: Connection Details for RC Specimen

spiral at a spacing of 2.5-in., as shown in Fig. 6.6. A clear cover of 1-in. was provided between the steel tube and the spiral reinforcing.

6.2.3 Specimen Construction

The specimens were constructed in the Structural Testing Laboratory at the University of Washington. To eliminate the need for the construction of temporary shoring, all of the specimens were constructed upside-down (i.e. the columns were cast into the cap-beams while the cap-beams rested on the floor). This resulted in construction sequences and practices which would not be used in the field. An overview of the construction sequence for the WD and RC specimens is given in the following sections.

6.2.3.1 WD Specimen Construction

An overview of the construction sequence for the WD specimens is given in Fig. 6.7. The construction sequence was as follows:

1. The flange was welded to the end of the steel tube.

2. The longitudinal dowels were temporarily supported and welded to the inside of the steel tube.

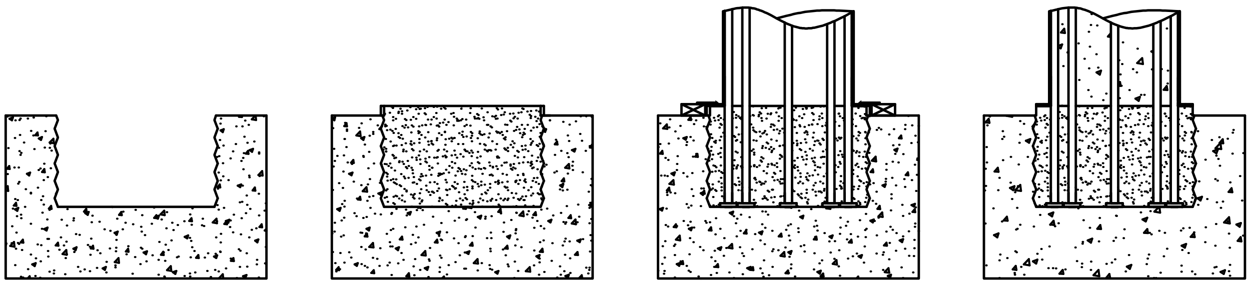

Figure 6.7: WD Construction Sequence

(a) Flange (b) Welded Dowels (b) Dowels Placed into Void in Cap

Figure 6.8: WD Construction Photos

3. The longitudinal dowels were grouted into the void in the cap beam.

4. The column was cast using self-consolidating concrete with low shrinkage admixture

Construction photos are shown in Fig. 6.8

6.2.3.2 RC Specimen Construction

An overview of the construction sequence for the RC specimen is given in Fig. 6.9. The construction sequence was as follows:

1. The reinforcing cage was assembled and grouted into the void.

2. The steel tube was temporarily supported above the reinforcing cage.

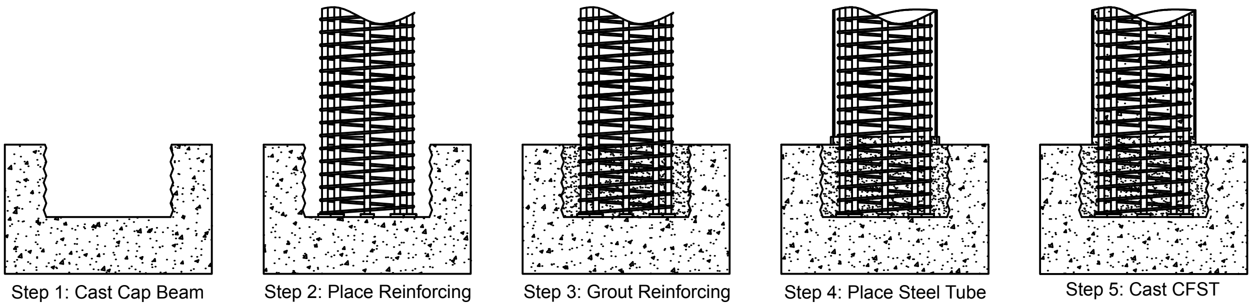

Figure 6.9: RC Construction Sequence

Figure 6.10: RC Construction Photos

3. The column was cast using self-consolidating concrete with low shrinkage admixture

Construction photos are shown in Fig. 6.10

6.2.4 Test Setup

The WD and RC specimens were tested in the test setup described in Section 5.2.3. Each specimen was subjected to a constant axial load of 10% of the gross crush capacity of the CFST column ($P_o = (A_{st}F_{y,st} + 0.95A_cf'_{cf})$) as well as a reversed cyclic lateral load with incrementally increasing displacements. The lateral load displacement protocol was adapted from that of previous University of Washington tests, and the ATC-24 [1992] guidelines, in which the imposed displacements are based on incremental multiples of the member's yield displacement. The target lateral load protocol for each specimen is illustrated in Fig. 5.12. Note that the displacement protocol used in the WD and RC experiments was based on the estimated yield displacement of the CFST column rather than the yield displacement of the longitudinal dowels in the connection region to allow for a more direct performance comparison of the ER, WD, and RC specimens (i.e. the same displacement protocol was used for ER80T, WD80T1, WD80T2, and RC80T).

6.2.5 Instrumentation

Strain gages, linear potentiometers, string potentiometers, and an Optotrak motion capture system were attached to each specimen. The instruments were electronically recorded using computer controlled data acquisition systems.

The applied gravity and lateral loads were directly measured using load cells, which were calibrated prior to testing for all tests. Strain gages were attached to the longitudinal dowels as illustrated in Fig. 6.11, and were used primarily to measure elastic strains in the dowels for evaluation of elastic curvature, elastic bending moments, and the plastic strain distribution in critical regions of the connection.

Displacements were measured using string potentiometers and short stroke Duncan potentiometers. The string pot and potentiometer locations used in WD80T1, WD80T2, RC80T, and WD103L are consistent with the locations given in Fig. 5.14.

An Optotrak Certus motion capture system was used to monitor the deformed shape of the columns during testing. An overview of the system is provided in Section 5.2.4 For the WD and RC specimens, the system was used to capture inelastic rotation, and relative displacement fields in the plastic hinge region of the columns. The placement of the LED targets is shown in Fig. 6.12.

6.3 Experimental Results

Key results from the experiments for the three WD specimens and one RC specimens are summarized in Table 6.3, while test day material strengths are given in Table 6.4. As for the ER specimens, the performance of each connection was assessed based on the secant stiffness

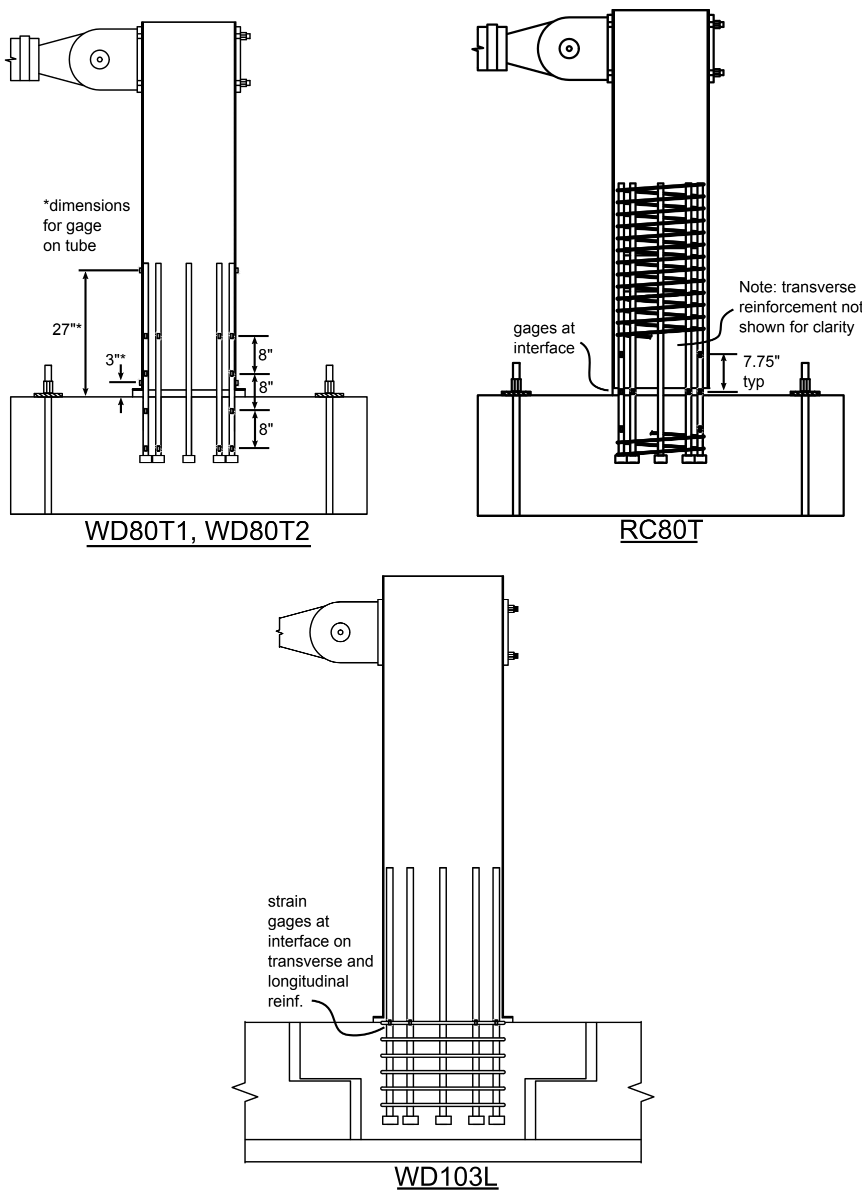

Figure 6.11: Strain Gage Schematic

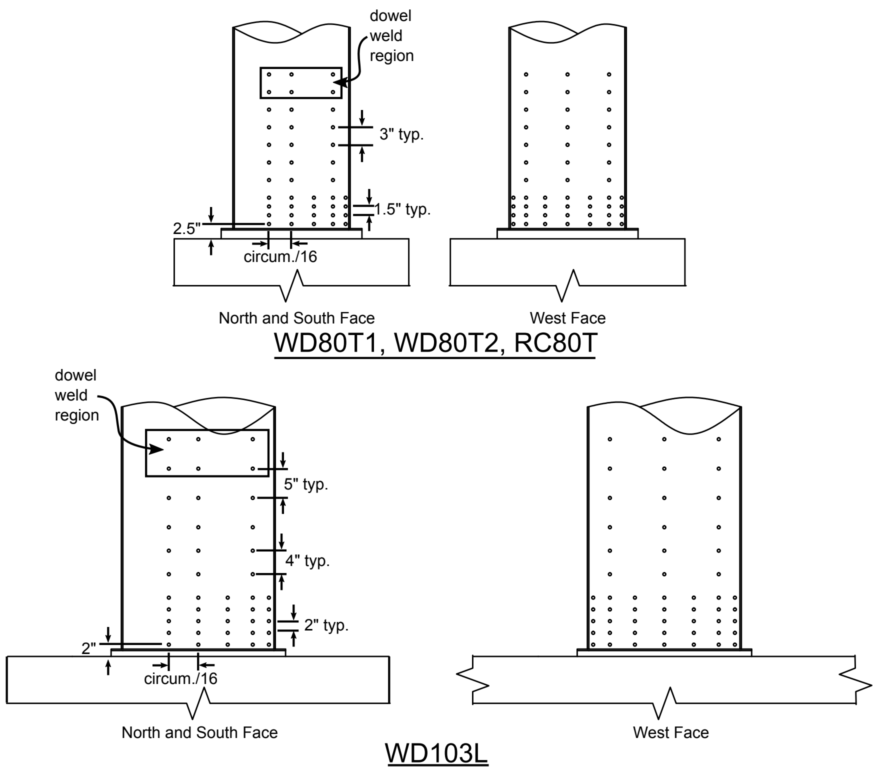

Figure 6.12: Optotrak Target Layout

to $0.8M_y$ of the CFST, maximum moment resistance, maximum drift, and the drift where the resistance decreased to 80% of its maximum.

Table 6.3: Experimental Results

Specimen	Initial Stiffness $\frac{EI_{measured}}{EI_{eff}}$	Yield Drift, %	$\frac{M_{peak}}{M_{P,PSDM}}$	Drift at peak Moment, %	Drift at 20% Degradation, %
WD80T1	0.86	0.56	1.4	9.5	11.5
WD80T2	0.71	0.69	1.05	9.75	12.2
WD103L	0.65	1.08	1.1	11.8	N/A
RC80T	0.69	0.67	0.92	7	10

Table 6.4: Measured Test Day Material Properties

Specimen	$F_{y,st}$, ksi	$F_{u,st}$, ksi	$F_{y,b}$, ksi	$F_{u,b}$, ksi	f'_c Column, ksi	f'_c Cap, ksi	f'_g, ksi
WD80T1	60.2	68.5	68.8	95.6	7.9	9.8	7.9
WD80T2	60.2	68.5	68.8	95.6	7.5	9.5	8.1
WD103L	58	69.3	68.1	95	7.7	7.8	8.6
RC80T	60.2	68.5	68.8	95.6	9.7	10	10.6

Damage state progression tables were used to evaluate the severity of damage in the specimens for each applied drift range. Damage states for the WD and RC connections progress from initial yielding of the longitudinal dowels to tearing at the apex of the buckled region adjacent to the surface of the cap beam as illustrated in Table 6.5. Damage states in the cap beam are consistent with the damage states define in Table 6.5. As for the ER specimens, the damage states were correlated to three post-event repair scenarios based on the severity of the damage: (1) No repair required, (2) Repair/Partial Replace, (3) Full Replacement. Note that dowel yielding was measured from strain gage data, while the other damage states were visually observed during testing.

Table 6.5: WD/RC Damage State Descriptions

Symbol	Description	Detailed Description	Photo
Y1	Initial Yielding	Yielding of longitudinal dowels.	No observable damage.
G1	Grout Cracking	Hairline radial cracks visible in grout pad.	
G2	Grout Crushing	Crushing of grout pad.	
DV	Dowels Visible	Longitudinal dowels visible.	
DF	Dowel Fracture	Longitudinal dowel fracture.	

Repair States:
No Repair
Repair
Partial Replace

6.3.1 *Summary of Individual Test Results*

The following section provides a summary of the test results for each specimen including the hysteretic response, and damage progression. Note that the moment-drift behaviors have been normalized by the theoretical plastic moment capacity of the CFST component as calculated using the PSDM.

6.3.1.1 *WD80T1*

WD80T1 utilized a 20-in. diameter spiral welded ASTM A1018 grade steel tube with a welded dowel connection consisting of 8 No. 9 headed bars embedded into the cap beam and welded to the steel tube. The purpose of this specimen was to evaluate the behavior of this

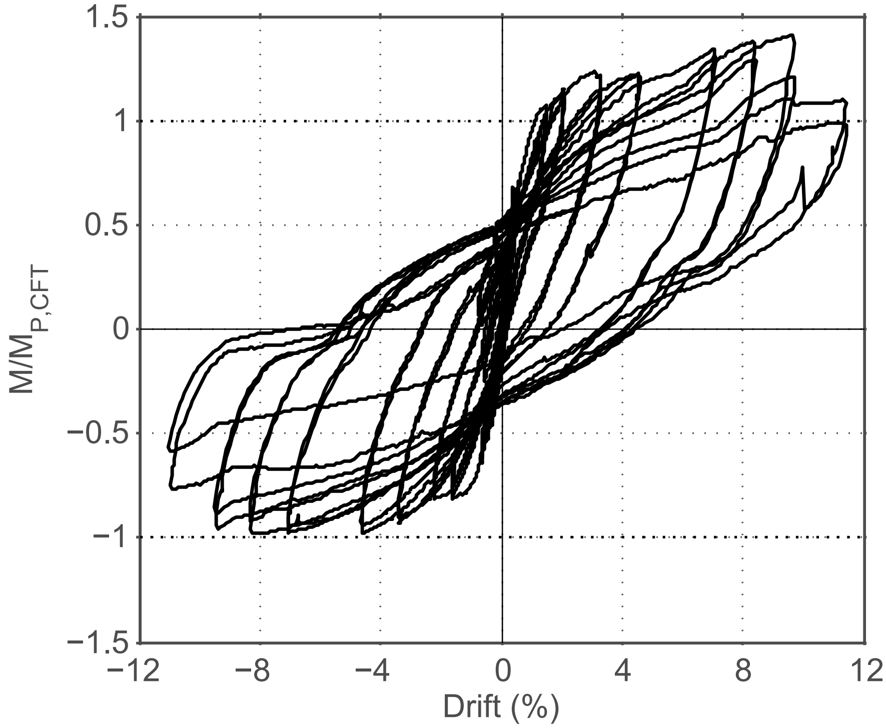

Figure 6.13: Moment-Drift Behavior of Specimen WD80T1

connection type, and to provide comparison to the embedded ring connections. The measured moment-drift response is given in Fig. 6.13 and the damage progression is summarized in Table 6.6. The steel tube was similar to that of ER80T. The area of the 8 No. 9 bars was significantly smaller than the area of the steel tube, but the tensile capacity of the bars and the tube were similar, because the ultimate tensile stress of the reinforcing bars was significantly larger than that of the tube. The rebar was bonded to the concrete throughout the connection. The specimen exhibited an initial stiffness $EI_{measured}/EI_{eff} = 0.86$, and a maximum moment $M_{max}/M_{P,PSDM} = 1.4$ in one direction, but only 1.0 or less in the other.

Primary damage states of WD80T1 are illustrated in Fig. 6.14. There was no observed damage to the specimen during cycling up to 0.5% drift. During the third drift set at 0.5% drift, a hairline crack initiated circumferentially along the grout soffit fill-steel flange interface on both the North and South sides of the specimen. On the South side of the

Table 6.6: WD80T1 Damage State Progression

Drift Ratio, %	$M/M_{P,PSDM}$	Column	Cap Beam
0.07	0.1		
0.06	0.2		
0.14	0.22		
0.15	0.31		
0.27	0.23	Y1	
0.32	0.32		
0.43	0.43		
0.50	0.46		
0.59	0.60		
0.67	0.53		
1.48	0.71	G1	C1
1.62	0.62		
2.08	1.04		
2.24	0.76		
3.30	1.11		
3.43	0.79		
4.58	1.15		
4.63	0.93		
7.08	1.31	G2	C2
7.04	0.93		
8.43	1.29	DV	
8.33	0.92		C3
9.71	1.21		
9.46	0.89		
11.47	0.99		
11.01	0.59		
12.96	1.02		
12.35	0.6		

Repair States:
No Repair
Repair
Partial Replace
Full Replace

specimen, a circumferential hairline crack also initiated along the base of the soffit fill, at the grout-cap beam interface. The existing circumferential cracks along the grout soffit fill gradually widened with increasing drift levels. During cycling at 0.5% drift, the openings between the soffit fill and the flange on both the North and South sides of the column opened to approximately 0.16-in. while they were each subjected to tensile loading. The existing opening between the soffit fill and cap beam on the South side of the specimen increased to approximately 0.125-in., while circumferential hairline cracks began to just initiate at the base of the soffit fill on the North side of the specimen. Yielding was measured by the strain gages on the longitudinal dowels during cycling at 0.56% drift. During the cycling at 1.5% drift, hairline cracks initiated radially in the grouted soffit fill, as well as in the cap beam. The cap beam cracks formed at approximate angles of 30-45° of one another, and continued vertically down the East and West faces of the cap beam.

For drifts greater than 2%, cracks continued to initiate radially from the column as target drift levels increased. During the 2.5% drift set, some of the existing radial cracks in both the cap beam and grout pad were observed to have widened slightly, such that they were no longer hairline in width. In addition, the opening between the grout pad and the column flange increased to approximately 0.25-in. as each side of the specimen was cycled into tensile loading (illustrated in Fig. 8.10b). The longitudinal reinforcing became visible during cycling at 7.08% drift, and soffit fill and cap beam damage continued to grow. The column began to pull out of the cap beam during cycling at 8.33% drift, as large cracks developed between the anchor rods and column. These cracks continued to grow until cycling at 13% drift at which point the test was terminated as a result of cap beam damage as illustrated in Fig. 6.14f. The specimen developed large resistance and deformation, but did great damage to the cap beam. The resistance shown in Fig. 6.13 is much larger in one direction than the other, and this is partially attributed to the severe damage to the concrete caused by the initial yielding cycles of the rebar. The bonded bar contributes greater resistance, but the greater structural damage is expected with bonded bars.

6.3.1.2 WD80T2

WD80T2 has the same tube, reinforcing bars, and connection details of WD80T1, except the longitudinal dowels were de-bonded for a length of 22-in. The dowels were de-bonded to improve the inelastic deformation capacity and significantly reduce the concrete damage in the connection.

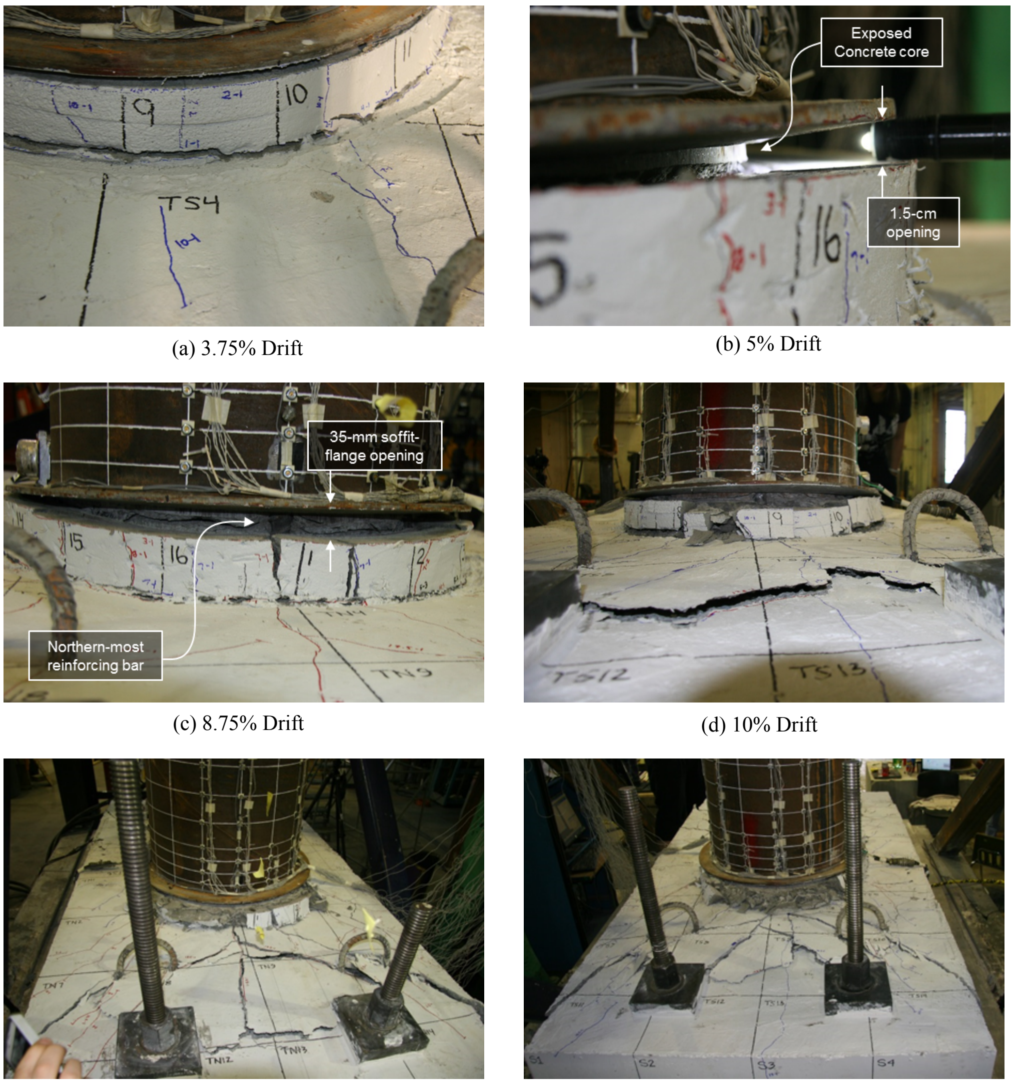

(a) 3.75% Drift

(b) 5% Drift

(c) 8.75% Drift

(d) 10% Drift

(e) 11.25% Drift

(f) 13% Drift (final state)

Figure 6.14: Photos of Primary Damage States of Specimen WD80T1

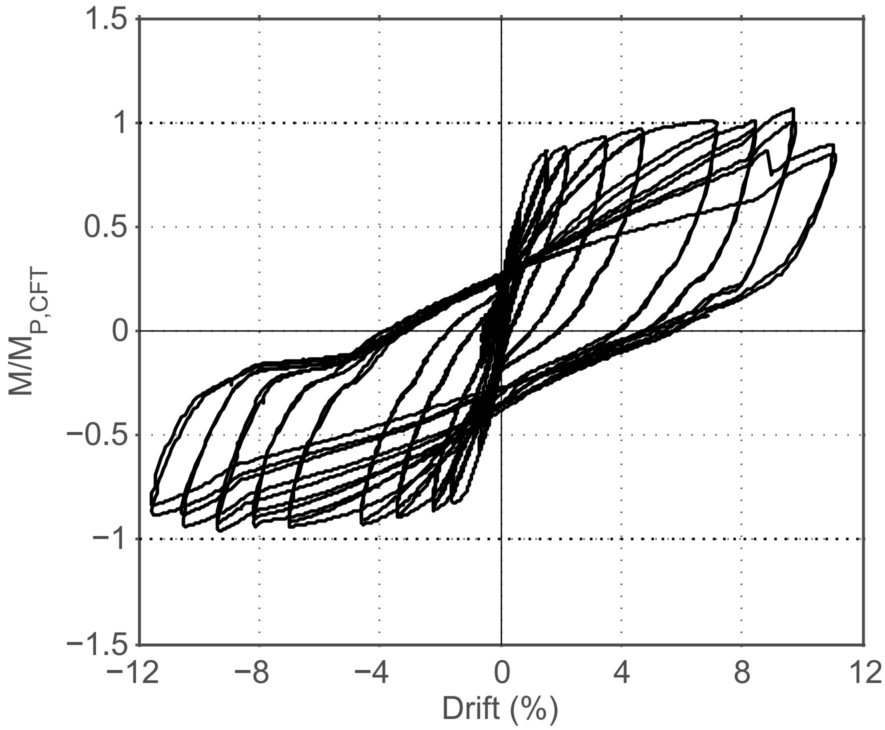

Figure 6.15: Moment-Drift Behavior of Specimen WD80T2

The measured moment-drift response is given in Fig. 6.15 and the damage progression is summarized in Table 6.7. The specimen exhibited an initial stiffness $EI_{measured}/EI_{eff} = 0.71$, and a maximum moment $M_{max}/M_{P,PSDM} = 1.05$in one direction, but less in the other direction.

Yielding was measured by strain gages on the longitudinal dowels during cycling at 0.69% drift. A circumferential crack initiated on the North side of the soffit fill as the specimen was subjected to 1.58% drift in South direction. At this drift level, radial hairline cracking was observed in the grouted soffit fill region, as well as in the cap beam. The cap beam cracks initiated radially from the grouted region, and propagated vertically and diagonally down the East and West sides of the cap beam. As the column cycled back and forth, an opening formed between the soffit fill and the annular ring on the side of the specimen subjected to tensile loading as shown in Fig. 6.16a.

Table 6.7: WD80T2 Damage State Progression

Drift Ratio, %	$M/M_{P,PSDM}$	Column	Cap Beam
0.07	0.16		
0.09	0.17		
0.13	0.27		
0.16	0.27		
0.31	0.41	Y1	
0.34	0.41		
0.48	0.50		
0.52	0.49		
0.65	0.58		
0.69	0.57		
1.58	0.81	G1	C1
1.63	0.78		
2.24	0.85		
2.24	0.84		
3.51	0.90		
3.42	0.89		
4.72	0.94	G2	
4.62	0.91		
7.17	0.97	DV (PVC)	
7.00	0.92		
8.46	0.97		
8.19	0.90		C2
9.76	1.0		
9.39	0.93		
11.07	0.88	DF	
10.53	0.88		C3
12.27	0.80		
11.58	0.84		

Repair States:
No Repair
Repair
Partial Replace
Full Replace

As drift levels increased, new radial cracks continued to develop throughout the grout pad and the cap beam. While the majority of the cracks remained hairline in width for several proceeding cycles, a few of the cracks increased slightly in width during the 1.5% drift set. At 2.24% drift to the South, the cracks propagating in the NE and NW directions increased to approximately 0.5-mm in width. The opening between the soffit fill and the flange on the North side of the specimen reached approximately 10-mm as it was subjected to peak tensile loading, as shown in Fig. 6.16. A majority of the cracks remained hairline during subsequent cycling, and the longitudinal dowels became visible at 7% drift as shown in Fig. 6.16. At the same time, radial cracks in the cab beam between the column and anchors began to grow.

The northern most longitudinal dowel fractured during the first excursion to 11% drift, resulting in 33% degradation in strength. A second reinforcing bar fractured on the north side on the second excursion to 11% drift, resulting in 46% degradation in strength. Although the cap-beam appeared to remain elastic for loading in the Southern direction (i.e. when tension was applied to the Northern most bars), large radial cracks developed on the South side of the cap beam during cycling at 11% drift as illustrated in Fig. 6.16d.

6.3.1.3 WD103L

WD103L utilized 25.75-in. diameter spiral welded ASTM A1018 grade steel tube with a welded dowel connection consisting of 10 No. 11 headed bars embedded into the cap beam and welded into the steel tube. This steel tube is the same as that of ER103L. The area of the steel tube is 34% larger than the area of the 10 No. 11 longitudinal dowels, but the tensile strength of the dowels is 63% larger than the yield stress of the steel tube. Hence this specimen was expected to be approximately 4% stronger compared to ER103L.

The purpose of this specimen was to evaluate the behavior of this connection type for loading in the longitudinal direction of the bridge. Additionally, transverse reinforcing in the form of discrete No. 5 hoops was included around the dowels in the joint region with the intent of increasing confinement as illustrated in Fig. 6.5. (transverse reinforcing in the joint region was not included in the transverse welded dowel connections).

The measured moment-drift response is given in Fig. 6.17 and the damage progression is summarized in Table 6.8. The specimen exhibited an initial stiffness $EI_{measured}/EI_{eff} =$ 0.65, and a maximum moment $M_{max}/M_{P,PSDM} = 1.1$.

Primary damage states observed in WD103L are illustrated in Fig. 6.18. Very limited cap beam or soffit fill damage was observed during cycling at low drift levels (¡2%), and dowel

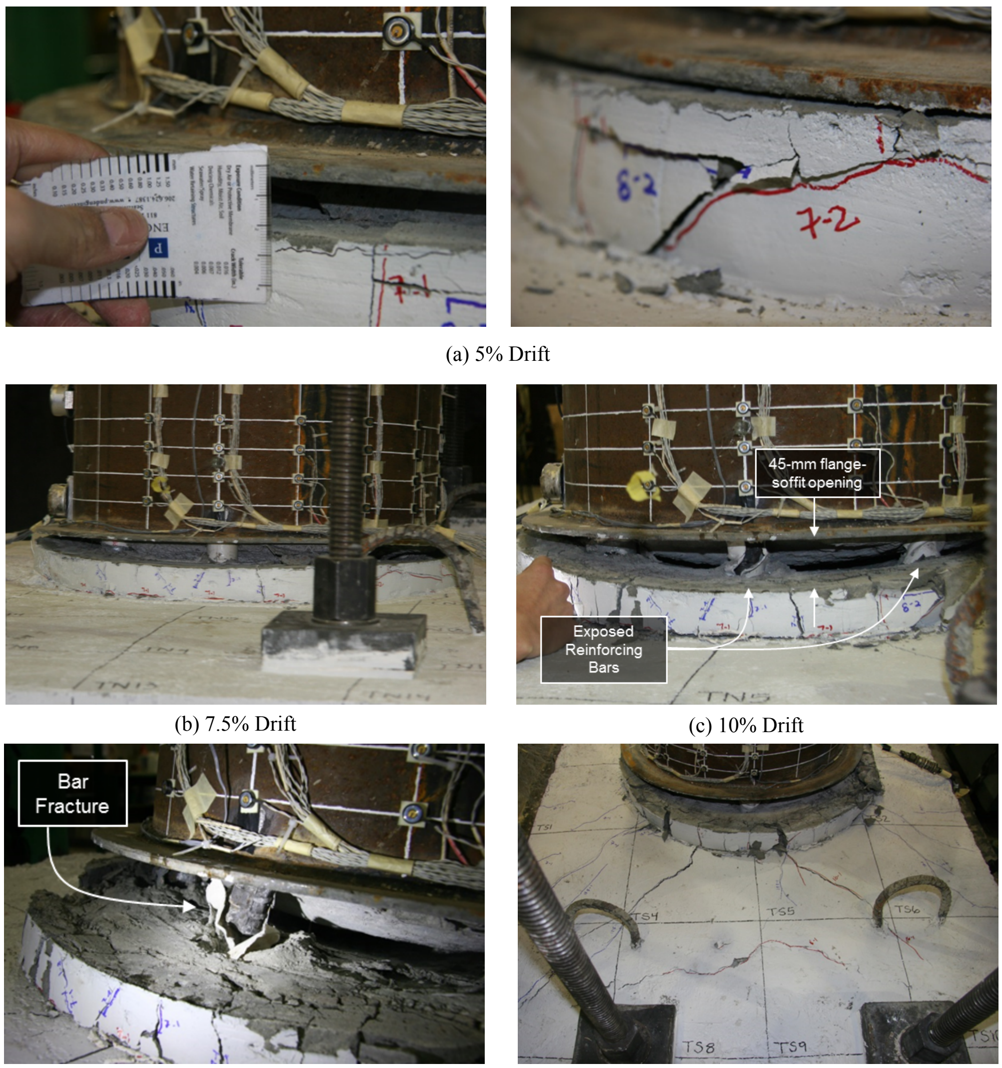

(a) 5% Drift

(b) 7.5% Drift

(c) 10% Drift

(d) 12.5% Drift

Figure 6.16: Photos of Primary Damage States of Specimen WD80T2

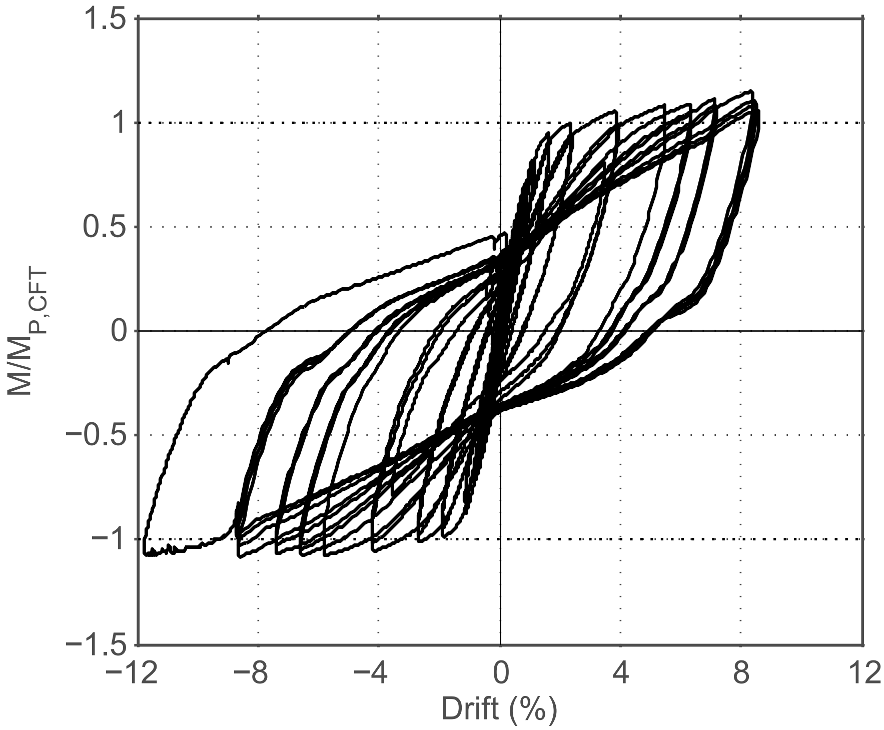

Figure 6.17: Moment-Drift Behavior of Specimen WD103L

Table 6.8: WD103L Damage State Progression

Drift Ratio, %	$M/M_{P,PSDM}$	Column	Cap Beam
0.05	0.12		
0.05	0.17		
0.11	0.20		
0.11	0.27		
0.25	0.33		
0.26	0.39		
0.41	0.44		
0.42	0.40		
0.56	0.53		
0.55	0.49		
0.90	0.71	G1	
0.79	0.56		
1.14	0.80	Y1	
1.13	0.69		
1.65	0.91		
1.90	0.82		
2.39	0.94		C1
2.67	0.95		
3.93	0.99	DV	
4.23	0.98		
5.50	1.08	G2	
5.80	1.12		
6.36	1.05		
6.60	1.07		
7.16	1.08		
7.41	1.04		
8.48	1.11		
8.71	1.03		
8.57	1.06		
11.75	1.08		

Repair States:
No Repair
Repair
Partial Replace
Full Replace

yielding was recorded by strain gages on the longitudinal dowels during cycling at 1.08% drift.

The PVC used to de-bond the longitudinal dowels was exposed during cycling at 5% drift, as a gap of 0.83-in was recorded between the annular ring and soffit fill. Moderate soffit fill crushing to the exterior of the grout pad under the annular ring was noted at 8% drift, as the transverse hoop in the soffit fill region provided confinement for the grout to the interior of the column. Large cracks developed in the soffit fill during cycling at 8.4% drift, and significant crushing was observed.

The displacement capacity of the actuator was achieved at 9.5% drift, and no strength degradation was observed. Significant grout pad crushing was observed, and the transverse hoop through the thickness of the soffit fill was entirely exposed in regions of the extreme fibers as illustrated in Fig. 6.18. The transverse hoop appeared un-deformed, suggesting that longitudinal bar buckling had not developed.

In an attempt to fail the specimen, the actuator was retracted, and spacers were placed between the actuator head and column such that a large monotonic push could be applied. The specimen was pushed for 1/2 cycle to 12% drift with no strength degradation or increase in visual damage. A maximum moment $M_{max}/M_{P,PSDM} = 1.1$ was recorded at 12% drift.

This specimen provided good resistance with little damage to the cap beam. The grout pad sustained some limited damage. These de-bonded connections sustained great benefit through uplift of the flange from the grout pad in tension, and increased moment arm contributed by the CFST on the grout pad in compression through the flange. The specimen was slightly weaker than ER103L, but it was considerably more flexible than that specimen.

6.3.1.4 RC80T

RC80T utilized 20-in. diameter spiral welded ASTM A1018 grade steel tube with a reinforced concrete connection consisting of 8 No. 9 headed bars embedded into the cap beam and developed into the steel tube. No. 3 spiral was additionally included for the length of the longitudinal dowels, and a concrete cover of 1-in. was provided between the steel tube and reinforcing cage. This connection is clearly a reinforced concrete connection, and it is somewhat comparible to ER80T and WD80T1. The measured moment-drift response is given in Fig. 5.16 and the damage progression is summarized in Table 6.9. The specimen exhibited

(a) 3.5% Drift

(b) 7.5% Drift

(c) 9% Drift

Figure 6.18: Photos of Primary Damage States of Specimen WD103L

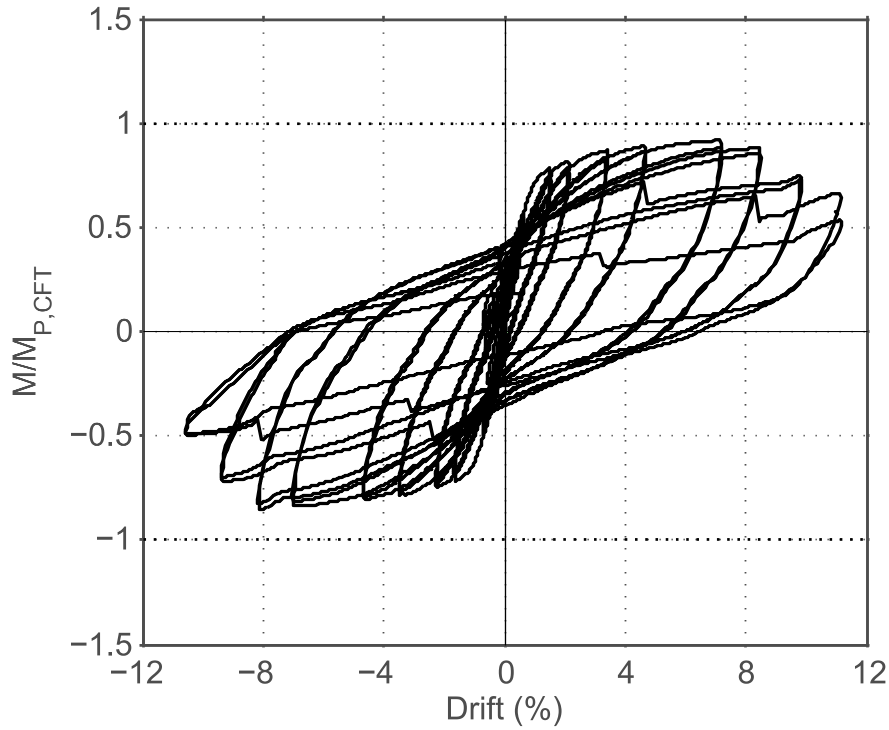

Figure 6.19: Moment-Drift Behavior of Specimen RC80T

an initial stiffness $EI_{measured}/EI_{eff} = 0.69$, and a maximum moment $M_{max}/M_{P,PSDM} = 0.92$.

Very limited cap beam or soffit fill damage was observed during cycling at drifts less than 2%, and dowel yielding was recorded by strain gages on the longitudinal dowels during cycling at 0.67% drift. The embedded dowel connection exhibited a ductile hysteretic response, as inelastic deformation was limited to the longitudinal dowels and grout in the soffit fill region. Severe soffit fill crushing developed during cycling at 5% drift. Deterioration of moment began at around 7% drift, as the soffit fill continued to crush. Transverse and longitudinal reinforcing became visible at 8.15% drift. The transverse reinforcing was bent around the longitudinal dowels, suggesting that dowel buckling had developed. The dowels located at the north and south extreme fibers fractured during cycling at 9.4% drift. The NE, NW, SE, and SW dowels fractured in the subsequent cycle leaving only the dowels at the center of the

Table 6.9: RC80T Damage State Progression

Drift Ratio, %	$M/M_{P,PSDM}$	Column	Cap Beam
0.04	0.18		
0.08	0.10		
0.12	0.28		
0.16	0.21		
0.28	0.40	Y1, G1	
0.33	0.32		
0.44	0.47		
0.51	0.40		
0.62	0.55		
0.70	0.49		
1.54	0.75		C1
1.67	0.69		
2.14	0.78	G2	
2.27	0.72		
3.42	0.84		
3.50	0.77		
4.67	0.86		
4.70	0.79		C2
7.20	0.88		
7.02	0.82		
8.46	0.86		
8.15	0.83	DV	
9.83	0.73	DF	
9.40	0.70		
11.19	0.53		
10.57	0.49		

Repair States:
No Repair
Repair
Partial Replace
Full Replace

column in-tact. The test was terminated at 10% drift, as the strength degradation exceeded 20%. The damaged soffit fill and exposed transverse reinforcing are show in Fig. 6.20.

6.3.2 *Impact of Debonded Longitudinal Dowels and Transverse Reinforcing in the Joint Region*

The welded dowel connections exhibited a ductile and stable hysteretic behavior, and inelastic deformation was largely isolated to the longitudinal dowels in the connection region. De-

(a) 2.5% Drift

(b) 5% Drift

(c) 11.25% Drift

(c) 11.25% Drift (spalled grout removed) bonding the reinforcing bars tended to decreased damage to the cap beam, as severe cap beam damage was observed in the specimen with fully bonded bars (WD80T1) as is illustrated in Fig. 6.14c. Debonding the dowels did not decrease the stiffness or strength of the WD connection as indicated in Table 6.3. All of the welded dowel specimens exhibited severe soffit crushing (shown in Fig. 6.16c); however this did not influence the load carrying capacity of the connections. Including transverse reinforcing in the joint region effectively confined the grout in the soffit region thereby decreasing the amount of overall soffit damage as is illustrated in Fig. 6.18c for WD103L.

6.4 Proposed Design Expressions

The experimental results and observations were used to develop practical design expressions for the WD and RC cap beam connections. These connections can be employed using cast-in-place (CIP) or precast super-structure cap beam. For precast construction, a partial height pocket must be included in the precast elements through use of a corrugated pipe, which meets the specifications outlined in Section 5.4.1.3. For CIP construction either a monolithic or partial height pocket connection can be used although only the partial height pocket connection was studied here. When using the partial height pocket connection, the steel tube and annular ring are grouted into place using a high-strength fiber-reinforced grout to ensure shear transfer and bond strength precluding failure of the grout. Design recommendations for the fiber reinforced grout are provided in Sections 5.4.1.1 and 5.4.1.2. Note that the design variables in the following sections are annotated in Fig 6.1.

6.4.1 Welded Dowel Connection

An overview of the design procedure for the WD connection is given in Fig. 6.21. The following sections summarize the materials and design expressions for the WD connection.

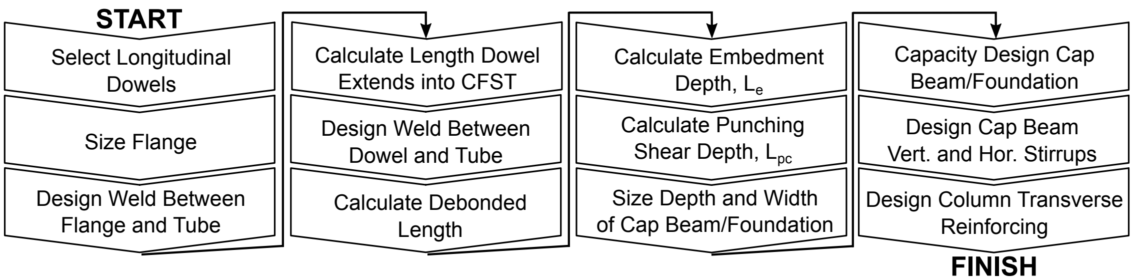

Figure 6.21: Flow Chart for Design of WD Connection

6.4.1.1 Longitudinal Dowels

Reinforcing in the connection region shall conform to ASTM A706 Gr. 60 (or Gr. 80 if allowed) requirements for weldable reinforcing. ASTM A706places restrictions on the chemical composition of reinforcing bars to enhance welding properties. Weld properties are discussed below.

6.4.1.2 Flange

The flange is welded to end of the steel tube to provide a larger area to transfer compressive stress from the steel tube into the soffit fill. In this connection the flange does not transfer tensile stresses but does provide some compressive force transfer.

The flange is made from steel of the same thickness and yield strength as the steel tube, and projects outside of the steel tube a distance 8 times the thickness of the steel tube. The flange is welded to the end of the steel tube using CJP welds, or fillet welds on the exterior of the tube. The minimum fillet weld size to attach the flange is defined in Equation 5.4. Welds should meet a minimum CVN toughness of 40-ft-lbs at 70°F.

6.4.1.3 Length Dowels Extend into the Cap Beam and Column

The headed reinforcing extends into the cap beam to fully develop the longitudinal dowels while also eliminating the potential for a conical pullout failure. The headed dowels must extend into the cap beam for the largest length calculated using Equation 6.1, 6.2, and 6.3. Equation 6.1 defines the required development length to develop reinforcing bars with mechanical anchors as specified in ACI [2011], where ψ_e is the reinforcing bar coating factor defined in ACI [2011] and $F_{y,b}$ is the yield strength of the longitudinal dowels. Note that ACI is referenced because neither the AASHTO nor the Caltrans SDC provide development expressions for headed bars.

Equation 6.2 defines the required embedment depth to eliminate a conical pullout as determined using the transfer mechanism illustrated in Fig. 6.22 where $A_{st,b}$ is the total area of longitudinal dowels which extend into the cap beam, and $F_{y,b}$ and f'_g are in psi. In lieu of a large pool of experimental data on the welded dowel connection, Equation 6.2 was derived assuming a limiting tensile principal stress of $6\sqrt{f'_c}$ [Lehman and Roeder, 2012b,a] where $F_{u,b}$ and $f'_{c,cap}$ are in psi.

A final embedment depth requirement has been specified in Equation 6.3 to ensure a minimum bonded length of $3d_b$ is included adjacent to the head on the end of the dowel where L_{db} is the total length over which the longitudinal dowels are de-bonded. This equation is presented assuming one half of the full de-bonded length extends into the cap beam, and must be modified in cases in which a different de-bonded length is extended into the cap.

$$L_e \geq \frac{0.016 * \psi * F_{y,b}}{\sqrt{f'_g}} \; (f'_g \text{ in psi}) \tag{6.1}$$

$$L_e \geq \sqrt{\frac{D^2}{4} + \frac{1.2F_{y,b}A_{st,b}}{6\pi\sqrt{f'_{c,cap}}}} - D/2 \; (f'_{c,cap} \text{ in psi}) \tag{6.2}$$

$$L_e \geq 3d_b + 0.5L_{db} \tag{6.3}$$

The longitudinal dowels must also extend into the CFST for a distance adequate to develop the full strength of the dowels. Results from the welded dowel tests (discussed above)

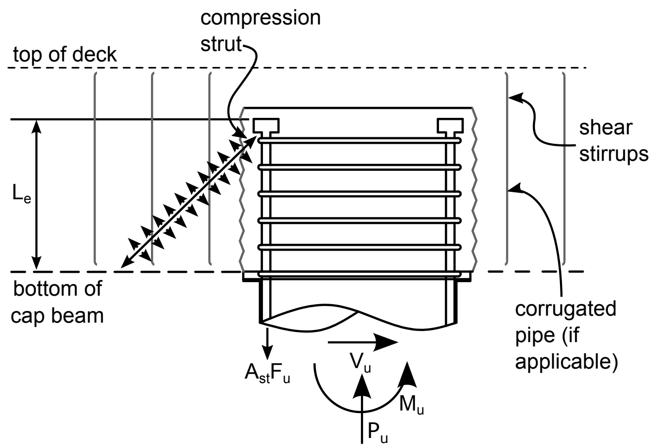

Figure 6.22: Transfer Mechanism Used in Derivation of Equation 6.2

suggest that the embedment can be as low as $18d_b$ for full dowel development, however a distance of $24d_b$ is recommended here to provide a reasonable factor of safety.

6.4.1.4 Joint Region Reinforcing

Cap beam detailing requirements specified in Caltrans [2010] or AASHTOb [2011] should be followed when designing the welded dowel connection.

6.4.1.5 Soffit Fill Depth

The soffit fill depth, L_s, is calculated according to Equation 6.4 to ensure that the annular ring does not come in to contact with the bottom of the cap beam at the maximum expected drift angle, θ_u where D is the outer diameter of the annular ring. The expression for L_s was derived using a rigid body rotation as illustrated in Fig. 6.23.

$$L_s \geq sin\left(\theta_u\right)\left(\frac{D}{2} + 8t\right) \tag{6.4}$$

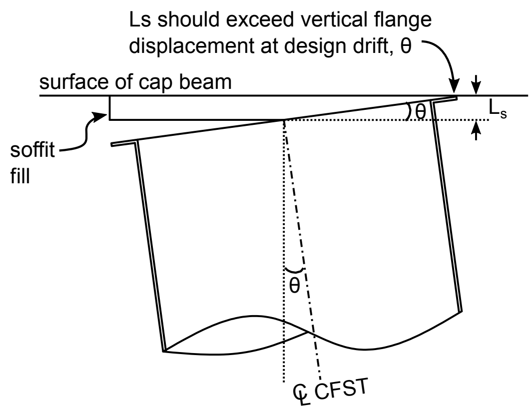

Figure 6.23: Rigid Body Rotation for Calculation of Required Soffit Fill Depth, L_s

6.4.1.6 Dowel Debonded Length

Longitudinal dowels should be de-bonded from the concrete in the connection region with the intent of increasing connection ductility. The required de-bonded length the achieve a pre-determined connection rotation, θ_u, prior to bar fracture is calculated using Equation 6.5 or 6.6, where ϕ_u is a curvature limit corresponding to a maximum steel strain as obtained from a moment-curvature analysis. Half of the de-bonded length extends into the cap beam, and half of the de-bonded length extends into the CFST column as illustrated in Fig. 6.24.

$$L_{db} = \frac{\theta_u}{\phi_u} \tag{6.5}$$

$$L_{db} = \frac{tan\theta(D - t - d_b/2)}{0.7\epsilon_u} \tag{6.6}$$

Equation 6.6 is a simplified method for estimating the required de-bonded length of the longitudinal reinforcing to achieve a pre-determined drift ratio prior to bar fracture. Although this method does not require a moment curvature analysis, it results in larger de-bonded lengths than those calculated using a moment-curvature analysis, as required in Equation 6.5.

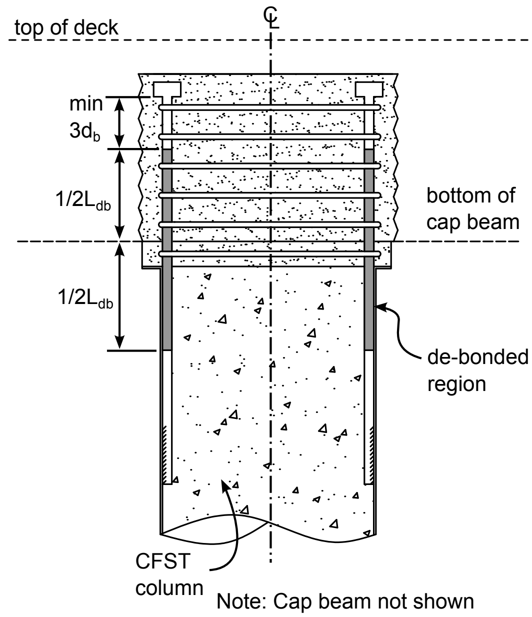

Figure 6.24: Welded Dowel Connection Debonding Dimensions

The method for de-bonding the reinforcing shall be specified. Several de-bonding methods have been evaluated in previous research including encasing the bars in tight-fitting PVC pipe, or wrapping the bars with duct tape. Other methods may be considered if it has been shown to adequately de-bond the reinforcing from the surrounding concrete.

6.4.1.7 Dowel-to-Steel Tube Welds

Longitudinal dowels are welded to the inside of the steel tube using flare bevel groove welds on both sides of the dowels, as illustrated in Fig. 6.1. The required weld lengths to develop the nominal capacity of the longitudinal dowels are specified in Equations 6.7 to 6.9 and are based on typical weld limit states for flare bevel groove welds. Equation 6.7 is based on failure of the weld metal, Equation 6.8 is based on yielding of the tube steel, and Equation 6.9 is based on rupture of the tube steel. A strength reduction factor of 0.9 has been included for yielding limit states in Equation 6.7 and Equation 6.8, while a strength reduction factor of 0.75 has been included based on a tube steel rupture limit state in Equation 6.9.

$$L_w = \frac{5.6 A_b F_{y,b}}{F_{EXX} d_b} \tag{6.7}$$

$$L_w = \frac{0.83 A_b F_{y,b}}{F_{y,st} t} \tag{6.8}$$

$$L_w = \frac{1.11 A_b F_{y,b}}{F_{u,st} t} \tag{6.9}$$

6.4.1.8 Use of Spiral Reinforcement in Column and Extension into the Joint Region

Spiral reinforcing should be included around the longitudinal dowels, which extend into the cap beam according to requirements in the California Department of Transportation Seismic Design Criteria [Caltrans, 2010]. At least one hoop must be placed in the soffit fill depth if individual hoops are used.

6.4.1.9 Longitudinal Girder and Column Layout when Using the WD Connection

When using the partial height pocket WD connection, the columns should be laid out between the longitudinal girders to allow for positive moment continuity in the superstructure in the longitudinal direction of the bridge.

6.4.1.10 Requirements for Headed Reinforcing

Minimum cover shall be provided when headed reinforcing is anchored into the cap beam. These requirements are summarized in Fig. 6.25.

1. The thickness of side cover around the head must be equal to or greater than the diameter of the head.

2. A minimum depth of $3d_h$ shall be included above the heads in the headed reinforcing where d_h is the diameter of the head.

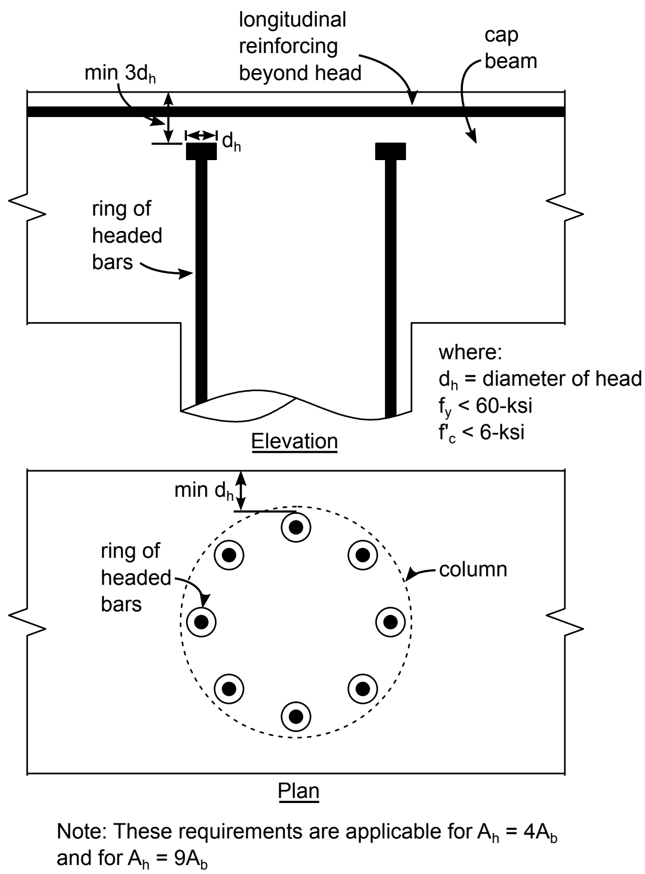

Figure 6.25: Cover Requirements for Headed Dowels

3. Nominal amounts of longitudinal reinforcing (e.g. reinforcing steel in the plane orthogonal to the headed reinforcement) shall be placed above the head.

6.4.2 Reinforced Concrete Connection

The RC connection consists of a more traditional reinforced concrete dowel connection, as both transverse and longitudinal reinforcing extend from the CFST column into the cap beam. As such, the design requirements for this connection are generally consistent with design of RC bridge columns unless otherwise specified in the following sections.

6.4.2.1 Reinforcing Embedment Length into Cap Beam and Column

Longitudinal dowels shall extend into the cap beam as specified in this section. Longitudinal dowels shall extend a distance L_d into the CFST column according to Equation 6.10 where ψ_e is the reinforcing bar coating factor as defined in ACI 318 [ACI, 2011] (1.0 for uncoated bars, and 1.2 for epoxy coated bars) and F_y and f'_{cf} are in psi.

$$L_d = \left(\frac{F_{y,b}\psi_e}{25\sqrt{f'_{cf}}}\right) d_b \tag{6.10}$$

The headed reinforcing must extend into the CFST column for a length sufficient to fully develop the reinforcing bar. Equation 6.10 defines the required development length as specified in Article 12.2 of ACI 318 [ACI, 2011] for deformed reinforcing. Equation 6.10 is a simplified development length equation which pertains to geometries commonly found in reinforced concrete bridge columns. For uncommon geometries or reinforcing layouts, The Engineer shall reference Article 12.2 of ACI 318 [ACI, 2011].

6.4.2.2 TransverseReinforcing

Discrete hoops or spiral shall extend from the cap beam and into the column for a distance L_d as illustrated in Fig. 6.1b.

6.4.2.3 Joint Region Reinforcing

Cap beam detailing requirements specified in AASHTOb [2011] or Caltrans [2010] should be followed when designing the welded dowel connection.

6.4.2.4 Requirements for Headed Reinforcing

Cover for headed reinforcing is sized according to requirements in Section 6.4.1.10.

6.4.2.5 Longitudinal Girder and Column Layout for RC Connection

The bridge layout shall correspond to requirements in Section 6.4.1.9.

Chapter 7

ANALYSIS AND COMPARISON OF PROPOSED CONNECTIONS

This chapter provides a comparison of the proposed connections in terms of seismic performance and accelerated construction as well as a design comparison between a CFST and RC structure at the prototype level.

7.1 Seismic Performance

The seismic performance of the connections is assessed based on the overall hysteretic response (including stiffness, strength, and energy dissipation) as well as the recorded damage progression and corresponding performance state.

7.1.1 Hysteretic Response

Moment-drift curves for all specimens have been plotted in Fig. 7.1 and backbone curves and energy dissipation characteristics for selected specimens are plotted in Fig. 7.2. Secant stiffness at 80% yield, maximum moments ($M_{max}/M_{P,PSDM}$) and drift at 20% strength degradation are compared in Fig. 7.3 and connection rotation contributions are plotted in Fig. 7.4.

In general, the ER connections exhibited larger stiffness, larger strength, and comparable energy dissipation characteristics to the WD and RC connections. The larger stiffness of the ER specimens is a result of the location of the tube as well as the confinement of the concrete fill. The comparable strengths in the ER and WD Connections are a result of these having similar effective reinforcing ratios and moment arms (reinforcing ratios are given in Table 5.1 for ER specimens and Table 6.2 for WD and RC specimens).

To provide a direct comparison of the performance of the different connection types in terms of stiffness and strength, only columns with the same diameter, axial load, and loading direction are directly compared (i.e. ER80T is compared with WD80T1, WD80T2, and RC80T for loading in the transverse direction, while ER103L is compared with WD103L for loading in the longitudinal direction). Furthermore, the direction of loading (transverse or longitudinal) did not have a large impact on the performance of the embedded connection. ER96T and ER96L are used to provide a comparison in response for the two different loading directions.

7.1.1.1 Effective Stiffness and Strength

ER80T and ER103L achieved the theoretical stiffness of the CFST component, with $EI_{measured}/EI_{eff,CFST}$ values of 0.98 and 0.96 respectively. The initial stiffness values of WD80T1, WD80T2, and RC80T were 12.2%, 27.5%, and 29.6% lower than the initial stiffness recorded in ER80T respectively. The initial stiffness of WD103L was 32.2% lower than the stiffness recorded in ER103L. As previously stated in Section 5.3, note that the measured stiffness of the ER connections includes flexibility from strain penetration in the section of the steel tube embedded in the cap beam.

The ER connections also exhibited larger peak capacities than the comparable dowel connections. The peak moment capacities of WD80T2 and RC80T were 12.5% and 23% lower than the peak capacity recorded in ER80T, while the peak moment capacity of WD103L was 2% lower than the peak capacity of ER103L. (Note that WD80T1 has been excluded from the peak moment comparison due to the large asymmetry observed in the hysteresis as discussed above.)

Finally, the energy dissipation characteristics of the ER and dowel type connections are compared in Fig. 7.2b. Note that although energy dissipation is largely a function of the applied displacement history, all of the connections were subjected to the same protocol. The energy dissipation in Fig. 7.2b has been normalized by the theoretical plastic moment capacity of the CFST as calculated using the PSDM. From the figure, the embedded

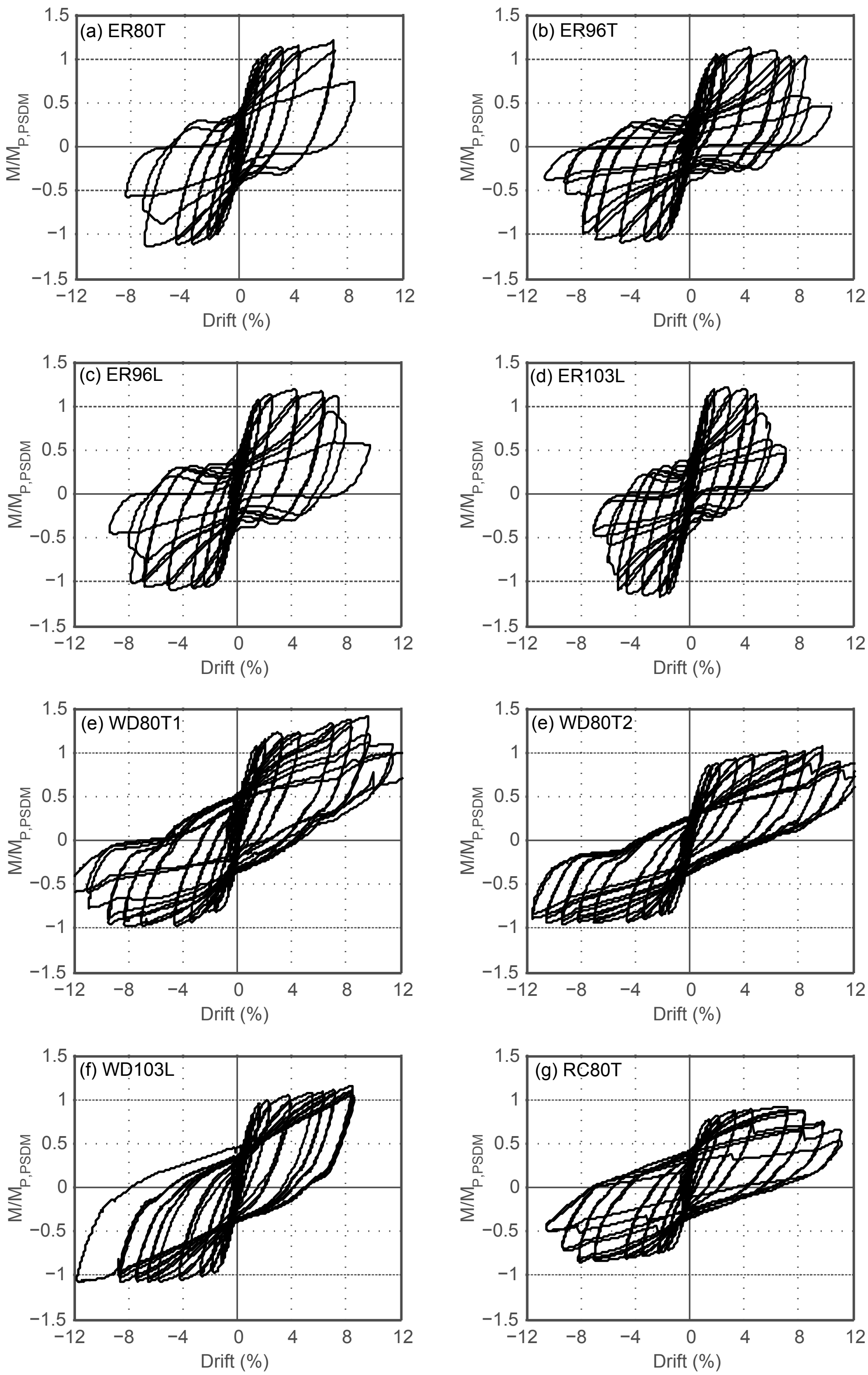

Figure 7.1: Hysteretic Response of All Specimens

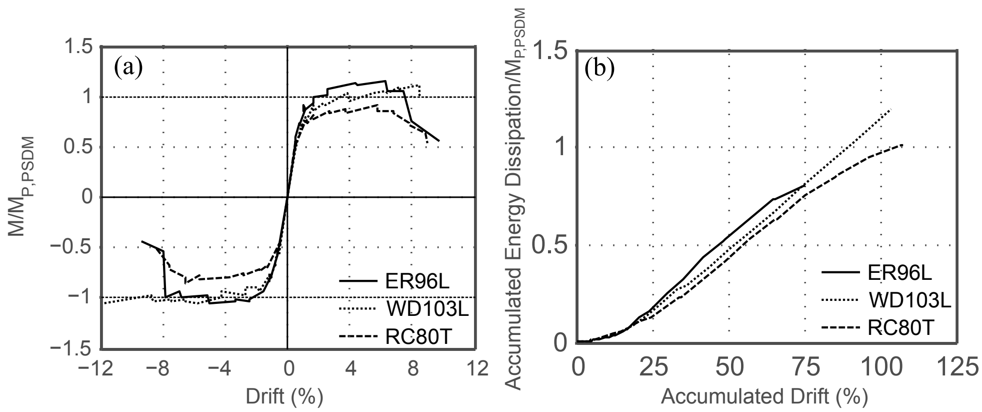

Figure 7.2: (a) Back Bone Curves and (b) Energy Dissipation of Selected Specimens

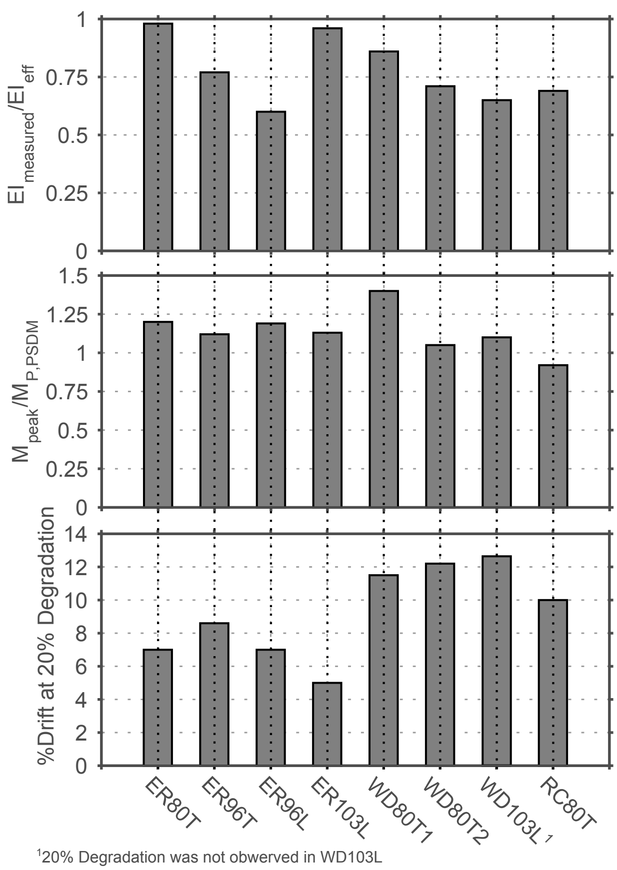

Figure 7.3: Performance Comparison of all Specimens in Terms of Stiffness, Strength, and Drift Capacity

connections exhibited slightly larger energy dissipations at moderate drifts, however the energy dissipation characteristics of all the connection types were largely similar.

7.1.1.2 Connection Rotation Contribution

The connection rotation contribution to the total measured column rotation has been plotted in Fig. 7.4 for all specimens. Connection rotation here is defined as rotation measured less than 3-in. from the surface of the cap beam (including any rotation which may result from cap beam deformation). In all cases, column deformation dominated the measured rotation for column drifts less than 1%. For drifts greater than 1%, the ER connections exhibited less connection rotation than the WD and RC connections. ER connection rotation contributions tended to asymptotically approach 50% to 80% for column drifts up to 5%, while WD and RC connection rotation contributions tended to approach 80% to 100% in the same column drift range. These trends suggest that the ER connection develops more distributed plasticity in the effective length of the column than the WD and RC connections.

7.1.2 Repair Requirement Progression

The repair state progression for all specimens have been illustrated in Table 7.1. The damage states which result in these repair requirements have been defined in Chapter 5 and Chapter 6 for the ER and dowel type connections respectively. The comparisons in this section are based on observed column and cap beam damage. In general, the ER connections achieve higher drifts than the WD and RC connections before repair is required. The early *Repair* requirement in the dowel type connections generally resulted from damage and spalling in the unconfined grout pad or soffit (e.g. see Fig. 6.16). All the ER specimens transitioned directly from the *No Repair* state to the *Partial Replace* state based on the damage state definitions in Chapter 5. Note that Table 7.1 highlights the influence of the D/t ratio on the *No Repair* drift capacity of the ER connection; specimens with lower D/t ratios tended to achieve larger drifts before exceeding the *Partial Replace* repair state.

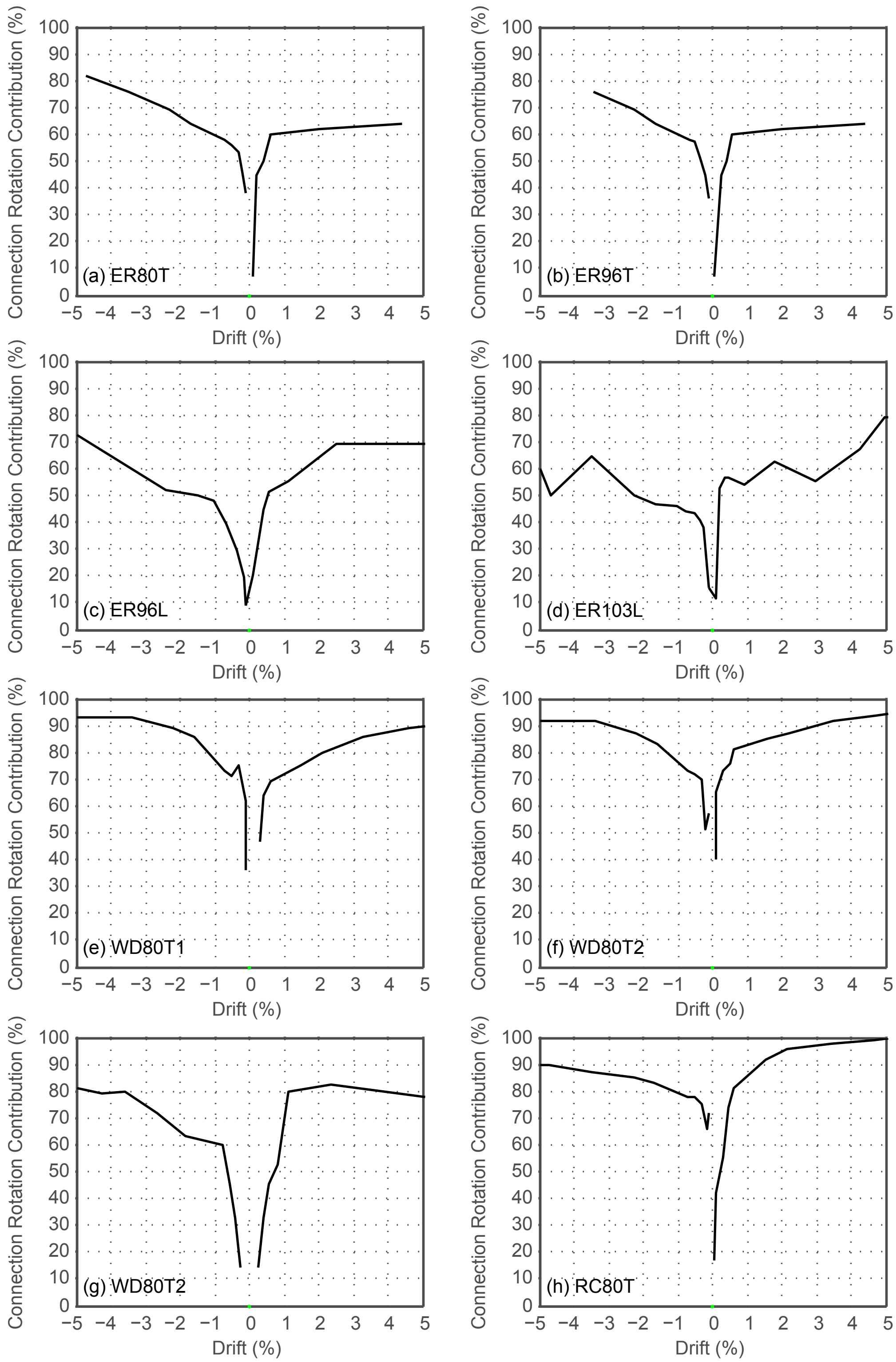

Figure 7.4: Contribution of Connection Rotation to Total Column Rotation

WD80T1 and WD80T2 exceeded the *Full Replace* repair state due to the development of significant damage in the cap beam. Debonding the longitudinal dowels increased the *Full Replace* drift capacity of the WD connection (WD80T2 had a 47% larger full replace drift capacity than WD80T1). Including transverse reinforcing around the longitudinal dowels in the joint region of the cap beam further improved the performance of the WD connection, as is evidenced by the repair progression for WD103L. This specimen utilized debonded dowels as well as transverse reinforcing in the joint region and did not exceed the *full replace* repair state through 12% drift.

Table 7.1: Repair State Progression

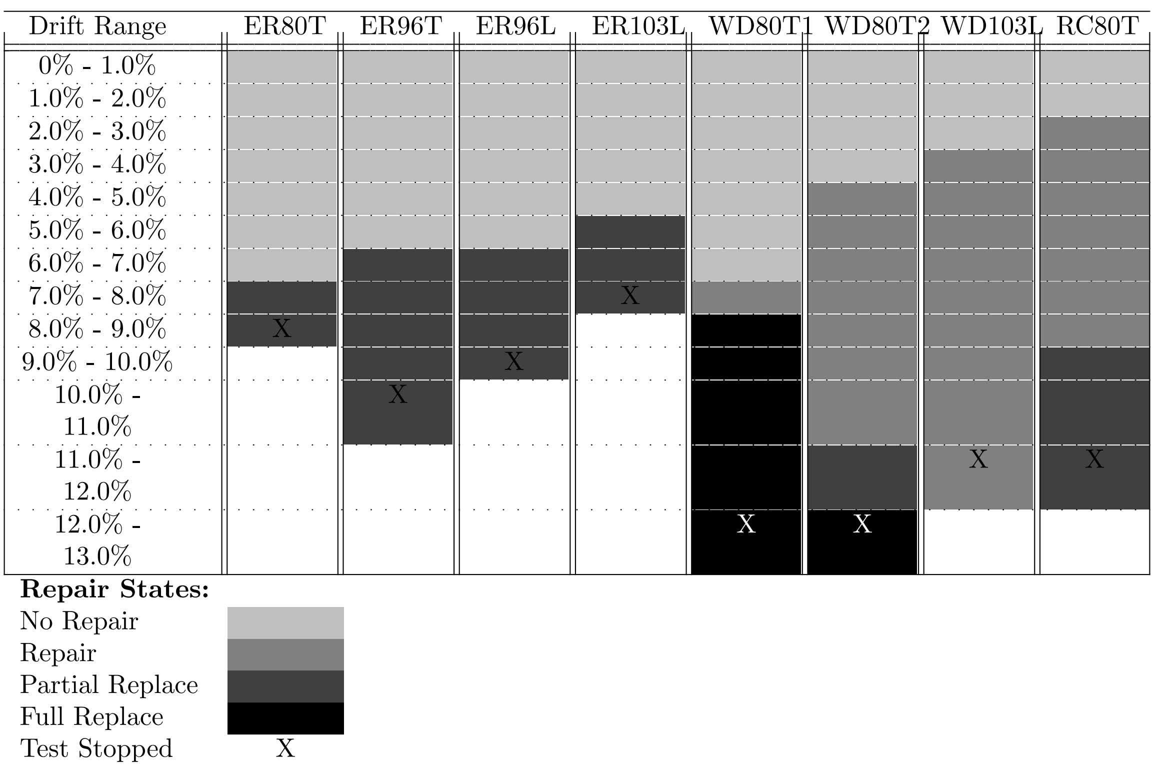

7.2 Accelerated Construction and Post Event Inspection

The following sections identify the characteristics of each connection in terms of facilitating ABC as well as post event inspection and repair. Typical field construction sequences for the ER, WD, and RC connections are illustrated in Fig. 7.5, Fig. 7.6, and Fig. 7.7 respectively.

7.2.1 ER Connection

The field construction sequence for the ER connection is illustrated in Fig 7.5. The ER connection offers several distinct advantages in terms of optimizing the objectives of accelerated construction and decreasing labor. After the column is cast, precast super-structure elements can be placed directly onto the CFST; no shoring, friction collars, or temporary support is required. Furthermore, this connection does not require any internal transverse or longitudinal reinforcing. There are no dowels or flexible reinforcing cages that need to be tied and placed.

The ER connection also offers several advantages in terms of post-event inspection and repair. The damage state of the ER connection can be readily identified based on the condition of the steel tube in the connection region; the concrete in the tube is generally in pristine condition. In addition, the accessibility to the steel tube (which acts as the primary longitudinal reinforcing) provides a unique opportunity for repair which will be more difficult in dowel or RC type connections in which extensive spalling and concrete damage are noted, and the longitudinal steel is embedded in the column concrete. Developing robust repair strategies for the ER connection will be a focus of future work.

7.2.2 WD Connection

The field construction sequence for the WD connection is illustrated in Fig. 7.6. The WD connection in its current form has several disadvantages in terms of optimizing the objectives of accelerated bridge construction and decreasing labor. After the column is cast, precast super-structure elements must be supported using temporary shoring or a friction

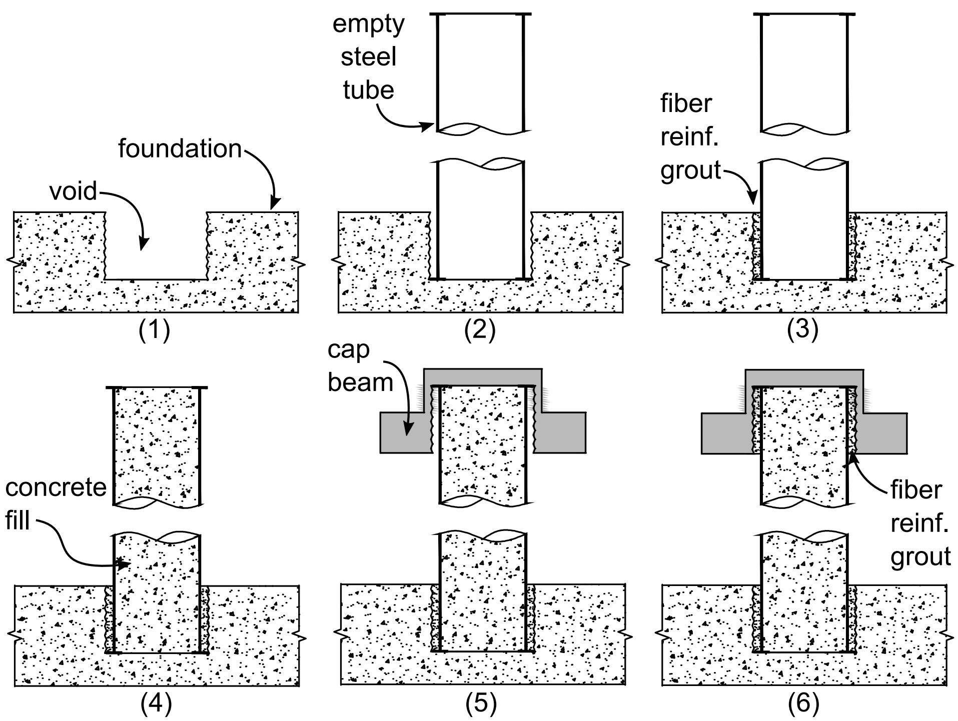

Figure 7.5: Field Construction Sequence for ER Connection

collar until the void can be grouted. Using individual ducts in place of a large corrugated pipe can potentially solve this issue (while decreasing construction tolerances), however using individual ducts was not evaluated in the testing program described in this report. Furthermore, dowels must be welded to the inside of the steel tube which requires skilled labor and additional time. Further, the welds are well inside the tube, and this increases the difficulty of welding and inspection of the welds. As these welds provide the primary load transfer from the steel tube into the connection dowels, they should be inspected according to requirements for fracture critical welds. As a final point, transverse reinforcing must be placed around the dowels before they are inserted into the cap beam, which requires additional labor.

The WD connection offers the same challenges encountered with traditional RC columns in terms of post-event inspection and repair. The longitudinal dowels are encased in concrete and grout, which makes it difficult to determine the damage state of the connection. This also increases the difficulty of developing repair strategies for this connection type. Further, significant damage to the concrete in the soffit fill is expected, while the concrete within the tube remains in very good condition.

7.2.3 RC Connection

The field construction sequence for the WD connection is illustrated in Fig. 7.7. The RC connection has many disadvantages in terms of optimizing the objectives of accelerated construction and decreasing labor. A flexible reinforcing cage must be constructed and temporarily supported within the steel tube. After the column is cast, precast super-structure elements must be supported using temporary showing or a friction collar until the void can be grouted. Similar to the WD connection, using individual ducts in place of a large corrugated pipe can potentially solve this issue (while decreasing construction tolerances), however this configuration was not evaluated in this testing program.

The RC connection offers the same challenges encountered with traditional RC columns in terms of post-event inspection and repair. The longitudinal dowels are encased in concrete

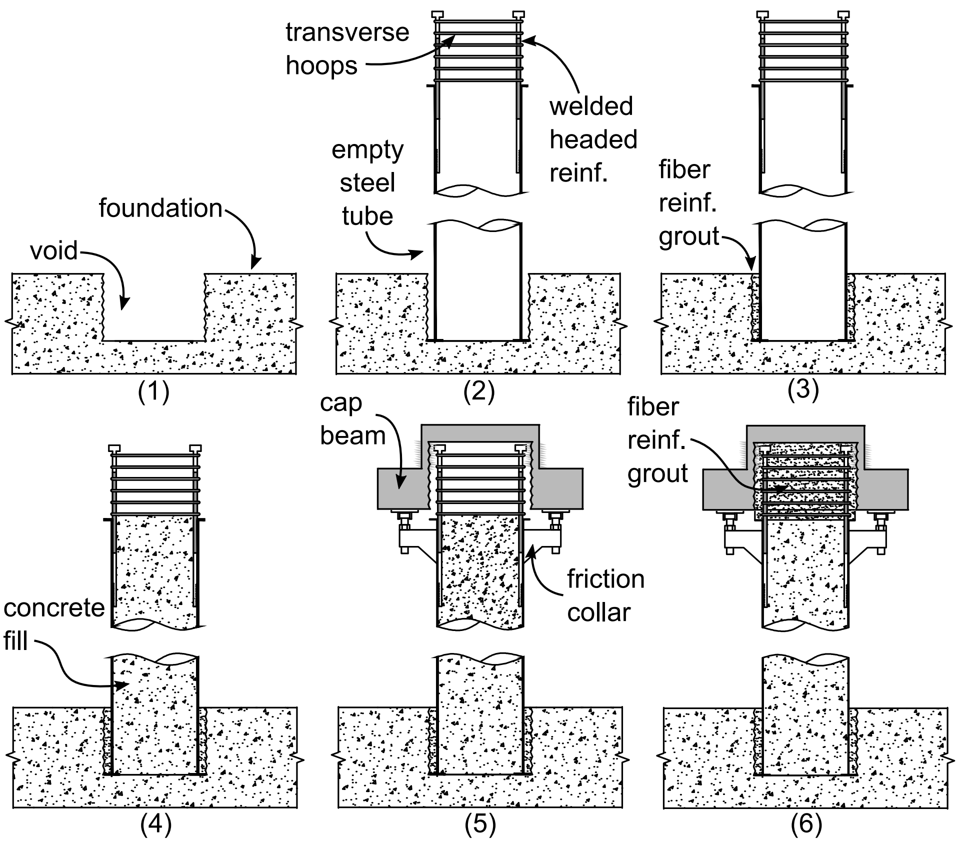

Figure 7.6: Field Construction Sequence for WD Connection

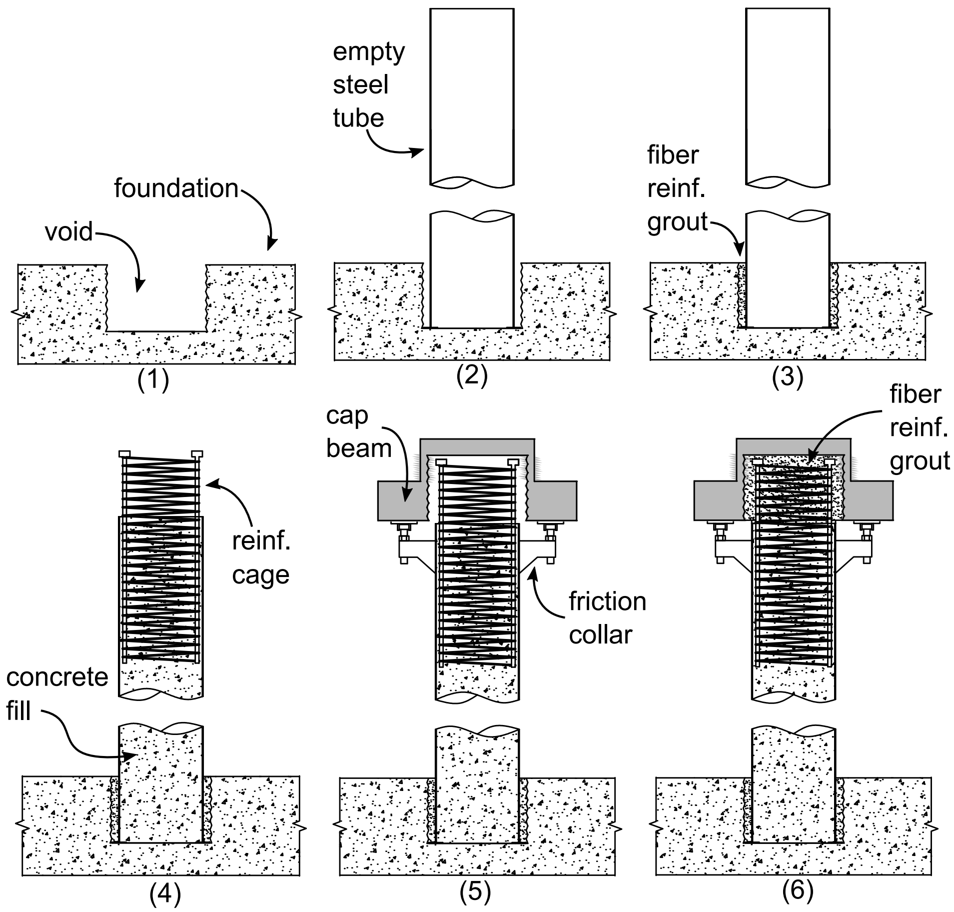

Figure 7.7: Field Construction Sequence for RC Connection

and grout, which makes it difficult to determine the damage state of the connection. This also increases the difficulty of developing repair strategies for this connection type.

7.3 Design Comparison of CFST and RC Bridge at the Prototype Level

To illustrate the design of a CFST bridge using the ER and WD cap beam connections, detailed design examples are included in Appendix A. The examples are a redesign of the prototype RC structure illustrated in Fig. 4.1. The cap beam connection was selected for the examples, because this connection offers unique design constraints relative to the foundation connection including limits on geometry in precast components. A foundation ER connection example can be found in a reference report [Lehman and Roeder, 2012b]. As previously discussed in Chapter 4, the prototype RC columns are 15-ft tall (from the bottom of the cap beam to the top of the drilled shaft), with a diameter of 48-in., 32 bundled No. 11 bars in the longitudinal direction, and No. 8 hoops at 6-in. in the transverse direction. This column and connection were redesigned using the design expressions for CFST columns in AASHTOa [2015] as well as the ER connection design expressions presented herein. The resulting CFST column has a steel thickness and diameter of 0.5-in and 44-in. respectively. Details of the re-designed column and cap beam are illustrated in Fig. 7.8.

Several key parameters were selected to compare the design of the columns and cap beam in the original RC prototype and the redesigned CFST structure with ER and WD connections. These parameters have been summarized in Table 7.2. The columns have been compared according to column diameter (D_{CFST}/D_{RC}), volumetric steel ratio ($\rho_{v,CFST}/\rho_{v,RC}$), plastic moment capacity ($M_{p,CFST}/M_{p,RC}$), and effective flexural stiffness (EI_{CFST}/EI_{RC}). The volumetric steel ratios of the RC and CFST columns were calculated based on the volume of steel over one hoop spacing in the RC structure (i.e. $\rho_{v,RC} = (A_{st,b}s + \pi d_{hoop}A_{hoop})/A_g s$ and $\rho_{v,CFST} = A_{st}/A_g$ where $A_{st,b}$ and A_{hoop} are the areas of the longitudinal and one transvere hoop in the RC column respectively, d_{hoop} is the diameter to the center line of a single hoop, s is the center-center hoop spacing, and A_g is the gross column area). A comparison of these parameters shows that the re-designed CFST column and ER connection has a smaller diameter and a greater volumetric steel ratio, moment strength, and effective stiffness than the RC column. The dowels in the connection region of the WD connection had an identical longitudinal reiforcing ratio and volumetric steel ratio in the joint region.

The cap beams have been compared according to the longitudinal reinforcing ratio ($\rho_{L,CFST}/\rho_{L,RC}$), the total area of vertical stirrups in the joint region ($A^{sjv}_{CFST}/A^{sjv}_{RC}$) as well as the height ($H_{cap,CFST}/H_{cap,RC}$) and width ($B_{cap,CFST}/B_{cap,RC}$) of the cap beam. These parameters illustrate that the design of the cap beam remains largely the same when the CFST ER connection is implemented, and identical when the WD connection is used. The longitudinal reinforcing ratio in the cap beam for the ER connection is slightly higher than in the original prototype structure, however the required vertical reinforcing and cap beam dimensions remain unchanged. Further, detailing in the joint region of the cap beam in the RC prototype and CFST structure with the ER and WD connections are very similar as illustrated in Fig. 7.8.

Note that the controlling limit state in the prototype structure (large moment and low axial load) is not the ideal load case to highlight the efficiency of CFST components relative to RC components. The primary intention of this example is to provide the reader with the tools required to design the two proposed connections, and to highlight that the cap beam design remains largely unchanged for both the ER and WD cases. The efficiency of CFST relative to RC construction is highlighted in the next section using several additional bridges from California and Washington State.

Table 7.2: Comparison of RC and CFST Columns and Cap Beams Based on a Re-design of the Prototype Structure

	Column/Connection Region[1]				Cap Beam			
	D_{CFST} $/D_{RC}$	$\rho_{v,CFST}$ $/\rho_{v,RC}$	$M_{p,CFST}$ $/M_{p,RC}$	EI_{CFST} $/EI_{RC}$	$\rho_{L,CFST}$ $/\rho_{L,RC}$	A^{sjv}_{CFST} $/A^{sjv}_{RC}$	$H_{cap,CFST}$ $/H_{cap,RC}$	$B_{cap,CFST}$ $/B_{cap,RC}$
ER	0.92	1.18	1.08	1.79	1.21	1.01	1.0	1.0
WD	0.92	1.0	1.0	1.0	1.0	1.0	1.0	1.0

[1]For the ER connection the Column/Connection Region properties are the properties of the CFST column, while for the WD connection the Column/Connection Region properties are the properties of the longitudinal dowels which extend from the CFST into the cap beam.

7.4 Material Weight Comparison of CFST and RC Bridge Columns at the Prototype Level

This section assesses the material weight cost advantages of CFST bridge columns by redesigning four RC bridges using CFST columns. Two of the bridges were provided by the Washington Department of Transportation (Cow Creek Bridge and Cold Water Creek Bridge), and two were provided by the California Department of Transportation (Laguna de Santa Rosa Bridge and Caltrans Bridge 1). All of the bridges were recently designed

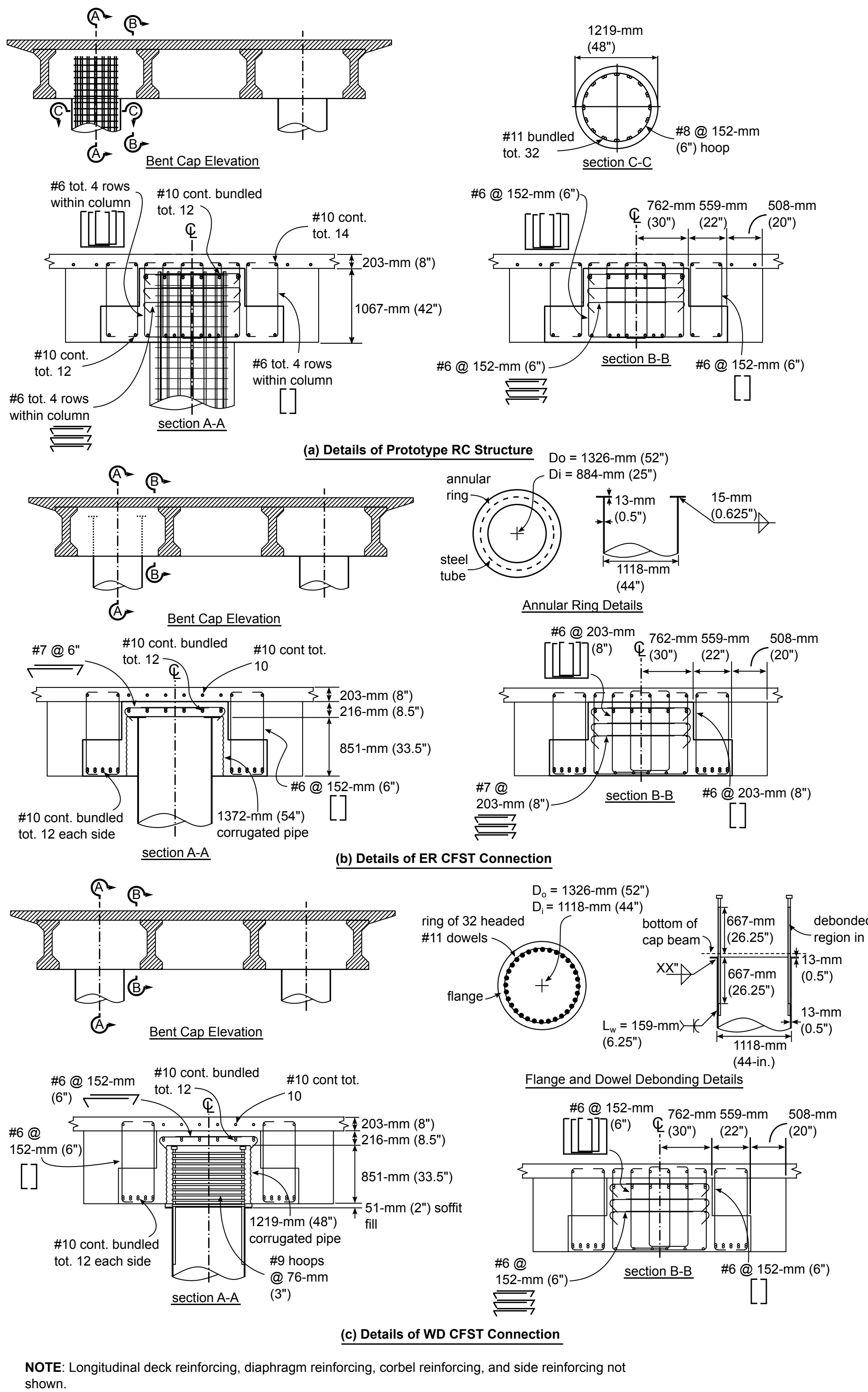

Figure 7.8: Details of RC Prototype Structure and Redesigned CFST Structure with ER Connection

and constructed according to provisions similar to current code provisions, and all were built in regions of high seismicity. Note that the P-M interaction diagrams for the CFST columns were constructed according to the provisions in AASHTOa [2015]. The original and redesigned structures were compared in terms of individual pier weight. An overview of the RC and CFST structures including material savings is given in Table 7.3. Significant weight savings were observed for all redesigned structures; ranging from 20.5% in the Laguna de Santa Rosa Bridge, to 63% in the Cold Water Creek Bridge. The following sections briefly discuss the geometry and strength of the original and redesigned structures.

7.4.1 Cold Water Creek Bridge

An overview of the Cold Water Creek Bridge is illustrated in Fig. 7.9. The columns in this bridge are reinforced concrete with 72-in. diameter, and are detailed using 42 No. 11 longitudinal bars, and No. 4 spiral at 3.5-in. on-center in the transverse direction. These columns were redesigned using CFST columns with equivalent strength under combined axial-moment (P-M) loading as well as equivalent stiffness, which resulted in CFST members with a thickness and diameter of 0.75-in. and 42-in. respectfully and a diameter to thickness ratio (D/t) of 56. An overview of the original RC and redesigned CFST column as well as the P-M interaction diagrams for each column are given in Fig. 7.10.

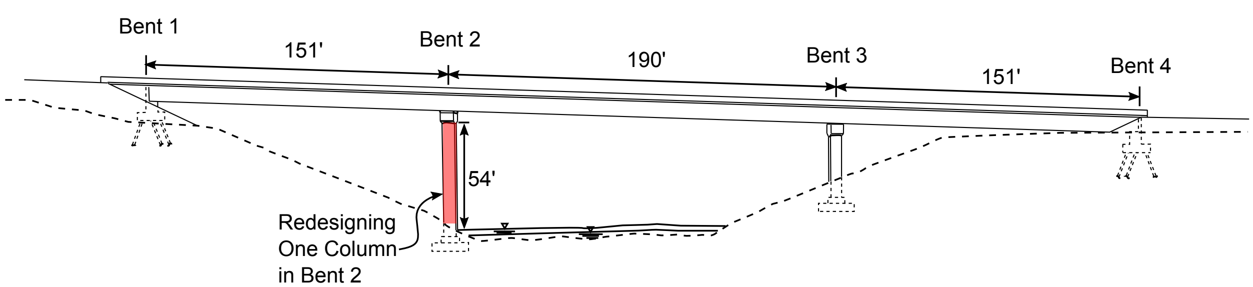

Figure 7.9: Details of RC Prototype Structure and Redesigned CFST Structure with ER Connection

Table 7.3: Properties of Original RC and Redesigned CFST Columns

	Cold Water Creek		Cow Creek		Caltrans Bridge 1		Laguna de Santa Rosa	
	Original RC Pier	CFST Pier	Original RC Pier	CFST Pier	Original RC Pier	CFST Pier	Original RC Pier	CFST Pier
Concrete Strength (ksi)	4.0	4.0	4.0	4.0	4.0	4.0	6.0	6.0
Steel Strength (ksi)	60.0	50.0	60.0	50.0	60.0	50.0	60.0	50.0
Diameter ($in.$)	72.0	42.0	144x84 rectangle	84.0	72.0	50.0	48.0	44.0
Tube Thickness ($in.$)	n/a	0.75	n/a	1.5	n/a	0.625	n/a	0.5
Concrete Area ($in.^2$)	4000.0	1288.0	11990.0	5153.0	4072.0	1866.0	1810.0	1452.0
Steel Area ($in.^2$)	101.0	97.2	231.0	389.0	92.0	96.9	73.0	68.0
Weight/ft of Pier (kips)	4.4	1.63	14.5	6.5	4.4	2.2	2.1	1.7
Total Pier Weight (kips)	231.0	85.4	828.0	371.0	209.0	104	34.0	27.0
Difference in Pier Weight	**63% Reduction**		**55% Reduction**		**50% Reduction**		**20.5% Reduction**	

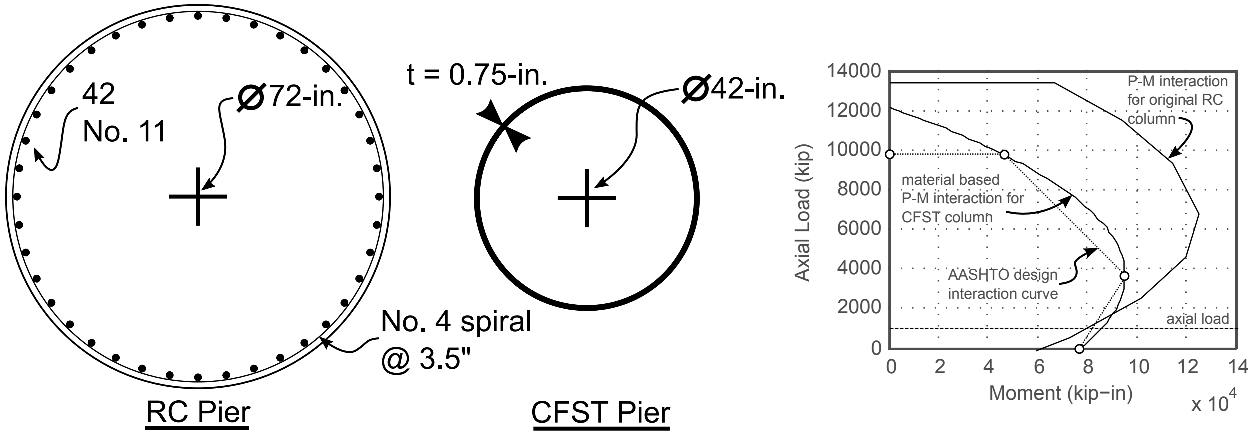

(a) Cross Sections

(b) P-M Interaction Curves

Figure 7.10: Details of RC Prototype Structure and Redesigned CFST Structure with ER Connection

7.4.2 Cow Creek Bridge

An overview of the Cow Creek Bridge is illustrated in Fig. 7.11. The columns in this bridge are 144-in.x84-in. rectangular reinforced concrete detailed using 44 No. 14 longitudinal bars, and No. 6 ties at 8-in. on-center in the transverse direction. These columns were redesigned using CFST columns with equivalent strength under combined axial-moment (P-M) loading as well as equivalent stiffness, which resulted in CFST members with a thickness and diameter of 1.5-in. and 84-in. respectfully and a diameter to thickness ratio (D/t) of 56. An overview of the original RC and redesigned CFST column as well as the P-M interaction diagrams for each column are given in Fig. 7.12.

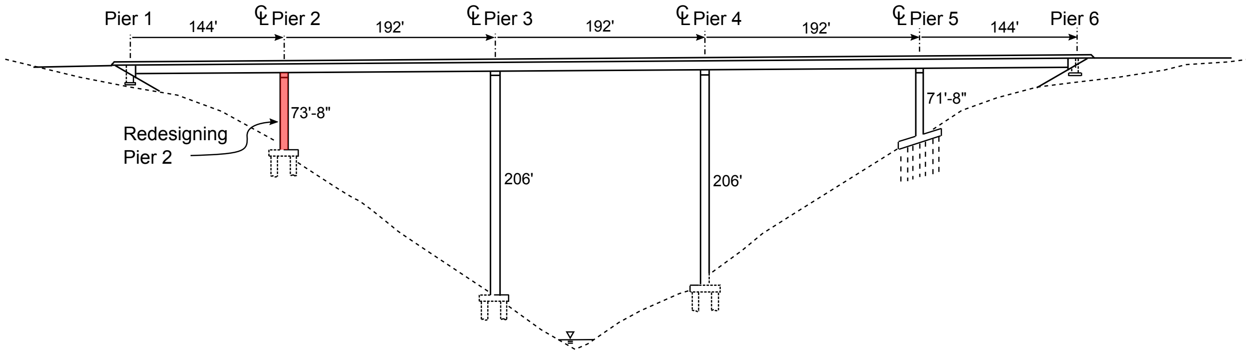

Figure 7.11: Details of RC Prototype Structure and Redesigned CFST Structure with ER Connection

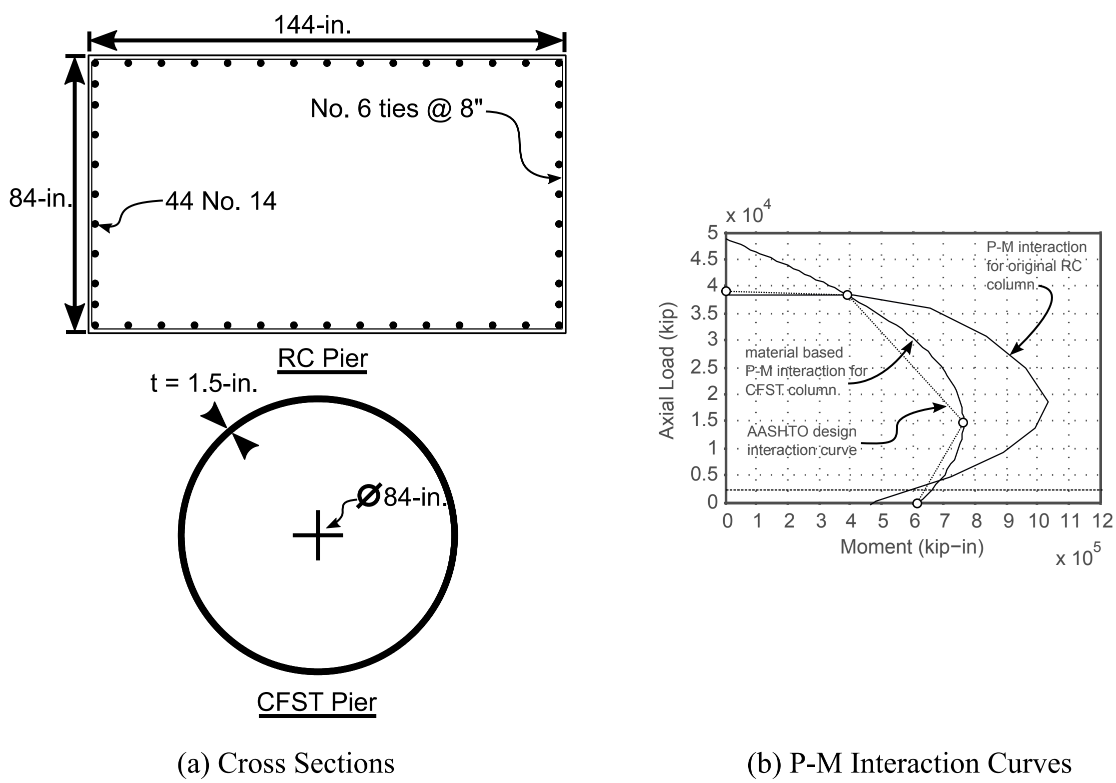

Figure 7.12: Details of RC Prototype Structure and Redesigned CFST Structure with ER Connection

7.4.3 Caltrans Bridge 1

An overview of Caltrans Bridge 1 is illustrated in Fig. 7.13. The columns in this bridge are reinforced concrete with 72-in. diameter, and are detailed using 36 No. 11 longitudinal bars, and No. 8 ties at 6-in. on-center in the transverse direction. These columns were redesigned using CFST columns with equivalent strength under combined axial-moment (P-M) loading as well as equivalent stiffness, which resulted in CFST members with a thickness and diameter of 0.625-in. and 50-in. respectfully and a diameter to thickness ratio (D/t) of 80. An overview of the original RC and redesigned CFST column as well as the P-M interaction diagrams for each column are given in Fig. 7.14.

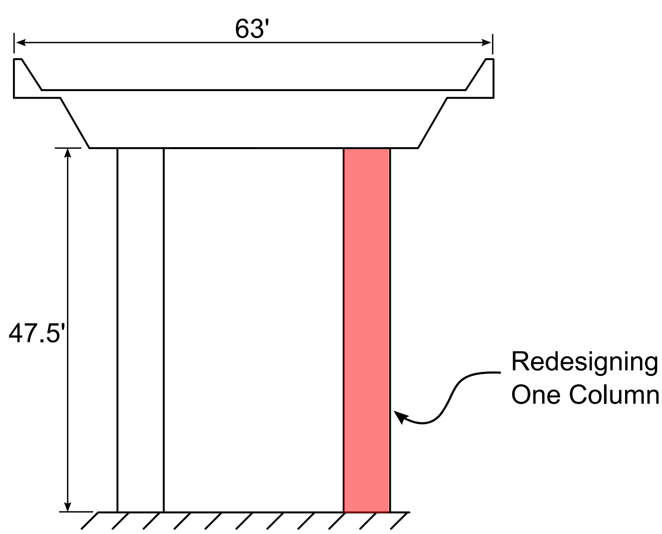

Figure 7.13: Details of RC Prototype Structure and Redesigned CFST Structure with ER Connection

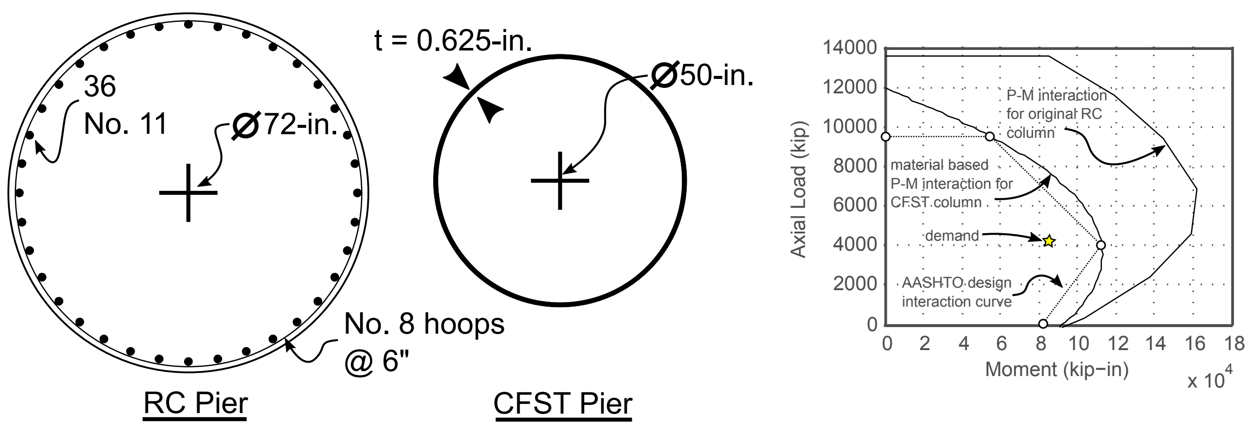

(a) Cross Sections (b) P-M Interaction Curves

Figure 7.14: Details of RC Prototype Structure and Redesigned CFST Structure with ER Connection

7.4.4 Laguna de Santa Rosa Bridge

An overview of the prototype bridge is shown in Fig. 4.1. The details of the original RC structure and redesign CFST structure were discussed in Section 7.3. An overview of the original RC and redesigned CFST column as well as the P-M interaction diagrams for each column are given in Fig. 7.15.

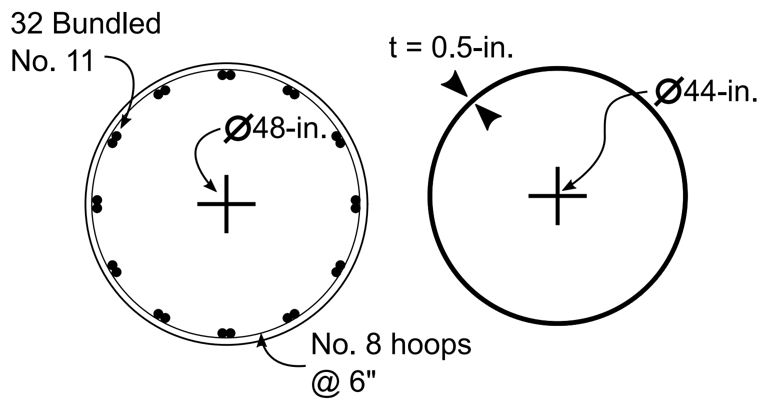

(a) Cross Sections

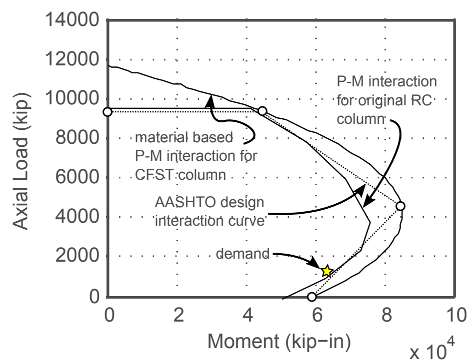

(b) P-M Interaction Curves

Figure 7.15: Details of RC Prototype Structure and Redesigned CFST Structure with ER Connection

Chapter 8

VALIDATION OF FIBER-BASED LINE ELEMENT MODELS FOR RC AND CFST PIERS

The performance of common highway bridges subjected to extreme lateral loading is controlled by the stiffness, strength, and inelastic response of the columns. Thus, analytical models of the columns must reliably predict both elastic and inelastic performance. Chapter 4 discussed a high-resolution finite element model for capturing the non-linear behavior of CFST piers, and similar high-resolution techniques have been used to evaluate RC bridge systems. Although these techniques are very effective in predicting behavior and capturing local effects (including steel buckling and concrete cracking) they are generally very computationally expensive, and are therefore not practical for completing non-linear dynamic analyses on large structural systems.

This chapter introduces non-linear line element models which effectively capture the elastic and inelastic response of RC and CFST bridge piers subjected to lateral loading with the ultimate objective of using performance based earthquake engineering tools to compare the seismic response of the two systems. The line element models were developed using the open-source numerical platform OpenSees to simulate nonlinear dynamic response to earthquake excitation. The process for development and validation of the column models was as follows: (1) fiber based line element models were developed in OpenSees for RC and CFST bridge columns, (2) non-linear constitutive properties were assigned to the concrete and steel materials to capture the inelastic response of the bridge piers including the effects of yielding, buckling, and fracture, and (3) experimental data was used to validate the modeling procedures. Similar OpenSees models have been used to model RC columns in previous research [Berry, 2006; Ranf, 2007].

8.1 Overview of Modeling Approach

An overview of the fiber element models including the foundation, effective length of the column, and cap beam are illustrated in Fig. 8.1a. Distributed plasticity beam-column elements were used to model plasticity along the effective length of the columns, and nonlinear zero-length fiber elements (herein referred to as connection elements) to capture local effects at the column-anchorage interface such as bar/tube buckling and strain penetration. A force-based element formulation was selected for the beam-column and connection elements was selected because this formulation has been shown to be more efficient than displacement based elements in terms of convergence and computation time [Terzic, 2011]. Five integration points were used along the length of the column based on convergence studies conducted in previous research [Berry, 2006; Ranf, 2007]. Fiber elements with concrete and steel constitutive models were defined at each integration point to define the cross section of the RC and CFST columns. The sections were discretized according to recommendations by Berry [2006] as illustrated in Fig. 8.1c. This discretization scheme was shown to adequately capture the moment-curvature behavior while maintaining computational efficiency. To capture the shear and torsion behavior of the columns, elastic shear and torsion flexibilities were aggregated into the force-based beam column elements based on the gross shear and torsion properties of the cross section. Boundary conditions for the validation tests were assigned based on boundary conditions used in previous subassembly experiments to facilitate a model validation study as illustrated in Fig 8.1b.

8.2 NonLinear Material Models

Tensile yielding and compression buckling in longitudinal reinforcing (in the case of RC) or steel tube (in the case of CFST) as well as concrete cracking and crushing are highly nonlinear behaviors, and are key elements in the seismic response of RC and CFST bridge piers. Strain penetration at the column-to-foundation or column-to-cap beam interface may also play a role in behavior. Simplified discrete component models including distributed

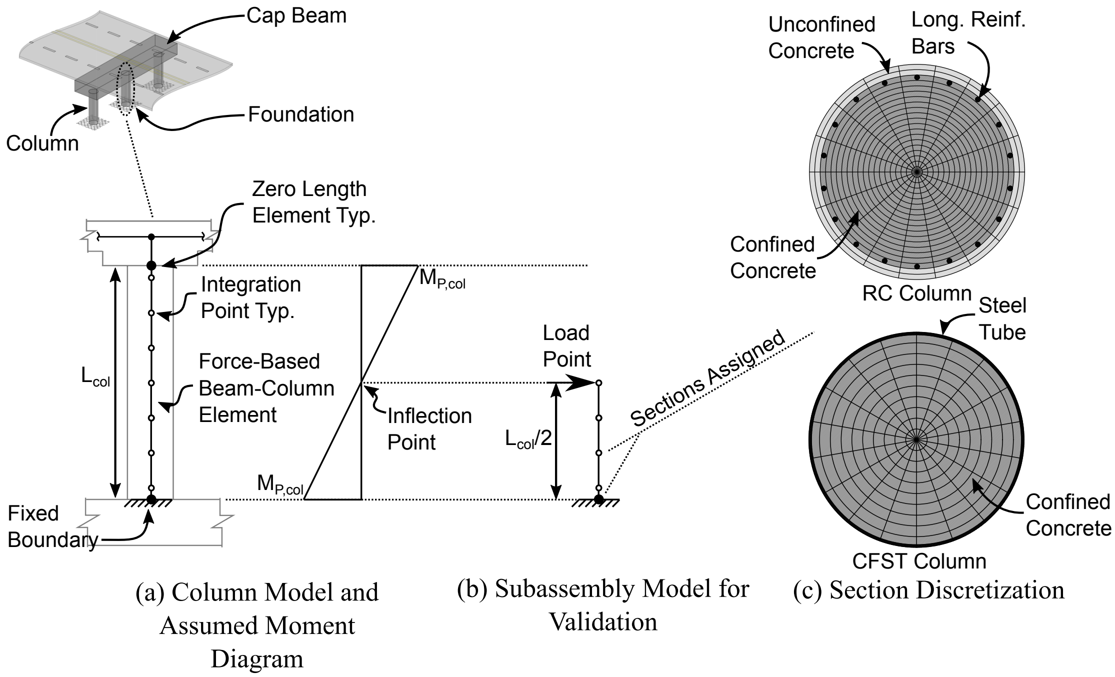

Figure 8.1: Overview of RC and CFST Component Models

plasticity beam-column elements and zero length elements were used in OpenSees to capture these behaviors. Non-linear constitutive models available in OpenSees were used to model the non-linear behavior of the concrete and reinforcing or tube steel. An overview of the material formulations implemented in OpenSees is given in Table 8.1. The structure of Table 8.1 is such that the parameters used to define the materials in OpenSees are highlighted in bold font, i.e. to define unconfined concrete the user would call ***uniaxialMaterial Concrete02 matTag fpc epsc0 fpcu epsU lambda ft Ets***.

8.2.1 Material Models for RC Column

As indicated in Fig. 8.1, the cross section of the RC section includes unconfined and confined concrete (outside and inside the transverse reinforcing in the column respectively), as well as longitudinal reinforcing steel. Unconfined and confined concrete was modeled using a linear tension softening referred to as *Concrete02* in OpenSees. Confinement properties for the

Table 8.1: OpenSees Material Defintions

Material	Unconfined Concrete[d]	Confined Concrete[d,e]	Reinforcing Steel[d]	Reinforcing Steel in Connection Element[d]	Tube Steel in Connection Element[e]
OpenSees Material Model	***Concrete02***	***Concrete02***	***ReinforcingSteel***	***Hysteretic***	***Hysteretic***
Yield Strength[a]/ Compression Strength[b]	**fpc** $= f'_c$ (ksi)	**fpc** $= f'_{cc}{}^{c,d,e}$ (ksi)	**fy** $= f_y$ (ksi)	**s1p** $= 82^l$	**s1p** $= f_y$ (ksi), **s1n** $= -f_y$ (ksi)
Ultimate Strength	**fpcu** $= 0.5f'_c$ (ksi)	**fpcu** $= 0.75f'_c{}^d$ (ksi), **fpcu** $= f'c^e$ (ksi)	**fu** $= f_u$ (ksi)	**s2p** $= 100^l$ (ksi)	**s2p** $= b^m \times E_s(d2_p - d1_p) + s1_p$ (ksi), **s2n** $= b^m \times E_s(-d2_n + d1_n) + s1_n$ (ksi)
Yield Strain[a]/Strain at Compressive Strength[b]	**epsc0** $= 0.003$	**epsc0** $= \epsilon_{cc}{}^{c,d,e}$	$e_y = fy/Es^g$	**d1p** $= 0.015^l$ (in.)	**d1p** $= \epsilon_y \times L_{strain}{}^n$ (in.), **d1n** $= -\epsilon_y \times L_{strain}{}^n$ (in.)
Ultimate Strain	**epsU** $= 0.006$	**epsU** $= 0.1^{d,e}$	**eult** $= \epsilon_u$	**d2p** $= 0.14^l$ (in.)	**d2p** $= 0.175 \times L_{strain}{}^n$ (in.) **d2n** $= -\epsilon_b^p \times L_{strain}{}^n$ (in.)
Misc.	n/a	**lambda** $= 0.1^{d,f}$ **lambda** $= 0.99^{e,f}$	**Es** $= 29000$ (ksi), **Esh** $= 0.01Es^h$, **esh** $= 0.005^i$, **Isr** $= 2.0^j$, **beta** $= 1.0^j$, **r** $= 1.0^j$, **gamma** $= 0.9^j$, **Cf** $= 0.5^k$, **alpha** $= 0.45^k$, **Cd** $= 0.27^k$	n/a	**s3n** $= \alpha_2 \times s2_n{}^o$ (ksi), **d3n** $= L_{strain}((s2_n - s3_n)/(0.03E_s) - \epsilon_b)^p$ (in.), **pinchX** $= 0.05$, **pinchY** $= 0.05$, **damage1** $= 0.000275$ **damage2** $= 0$
Hysteretic Response	Refer to Fig. 8.2	Refer to Fig. 8.2[d] or Fig. 8.5[e]	Refer to Fig. 8.3	Refer to Fig. 8.4	Refer to Fig. 8.6

[a] Steel constitutive models
[b] Concrete constitutive models
[c] As calculated using the J.B. Mander [1988] confinement model
[d] Applicable to RC columns
[e] Applicable to CFST columns
[f] Lambda is a material constant which controls the unloading stiffness of concrete as illustrated in Fig. 8.2
[g] Computed internally in OpenSees
[h] Tangent at initial strain hardening as illustrated in Fig. 8.3
[i] Strain corresponding to initial strain hardening as illustrated in Fig. 8.3
[j] Parameters for A. Gomes [1997] buckling model
[k] Fatigue parameter for *ReinforcingSteel* material model
[l] Calibrated by Ranf [2007] and illustrated in Fig. 8.4
[m] Factor $b = 0.01$
[n] Factor $L_{strain} = L_e \times \alpha_1$ where $\alpha_1 = 0.054$ as determined using a numerical optimization
[o] Factor $\alpha 2 = 0.63$ is the residual steel strength after buckling as calibrated using a numerical optimization
[p] ϵ_b calculated using recommendations by M.D. Denavit [2010] (defined in Equation 3.9 in this document)

confined concrete were calculated according to the Mander confinement model [J.B. Mander, 1988]. Properties of the confined and unconfined concrete are illustrated in Fig. 8.2.

Longitudinal reinforcing steel was modeled using the *ReinforcingSteel* material model available in OpenSees. This model utilizes Menegotto-Pinto curve parameters and accounts for local buckling and strength reduction due the effects of fatigue. Local buckling parameters were defined based on buckling parameters developed by A. Gomes [1997]. These parameters account for the slenderness of individual reinforcing bars as well as the residual compression capacity after bar buckling develops. Degradation due to fatigue was captured using a Coffin-Manson Fatigue model with parameters suggested by J. Brown [2000]. The properties of the reinforcing steel model are illustrated in Fig. 8.3.

8.2.1.1 Column Anchorage Bond Slip (Fixed End Rotation)

The flexibility due to anchorage slip was modeled using a connection element at the column-anchorage interface. The connection element was assigned the same geometric fiber element definition as the force-based beam column elements; however a bond slip constitutive model was assigned to the reinforcing steel. Parameters of the bond slip constitutive model were defined based on recommendations by Ranf [2007], and the properties of this model are shown in Fig. 8.4.

8.2.2 Material Models for CFST Column

Non-linear constitutive models available in OpenSees were used to model the non-linear behavior of the concrete and steel tube. The concrete fill was modeled using a uniaxial Kent-Park-Scott model (referred to as *Concrete02* in OpenSees) with parameters calculated according to M.D. Denavit [2010]. Using this approach, concrete confinement is defined as a function of the D/t ratio of the steel tube as described in Section 3.1.3.2. The properties of the concrete fill are illustrated in Fig. 8.5. Note that the ascending branch of the concrete model maintains a large residual stress capacity over a large compression strain range to account for the extreme confinement provided by the steel tube.

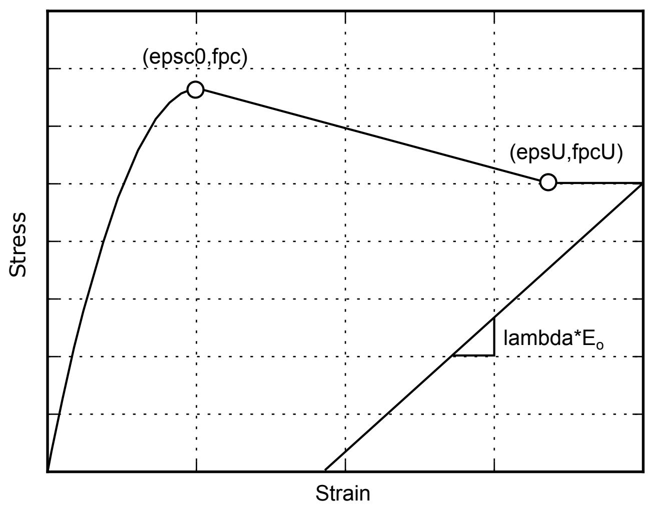

(a) Concrete 02

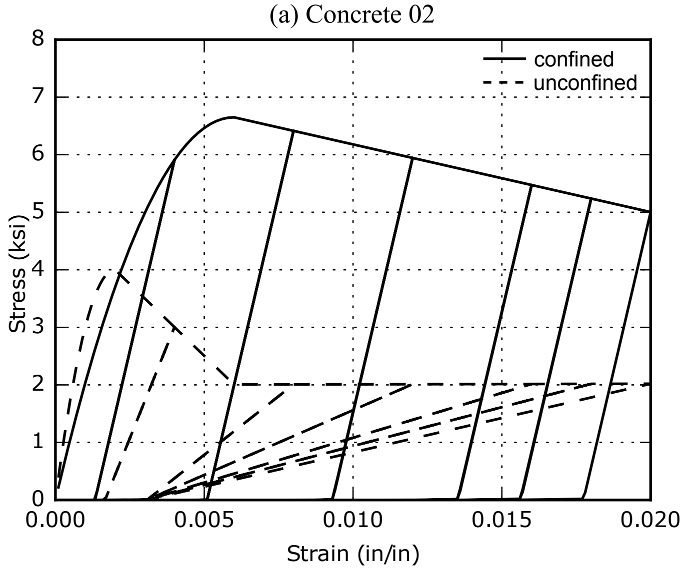

(b) Material Repsonse in Model

Figure 8.2: Confined and Unconfined Concrete Models for RC Column

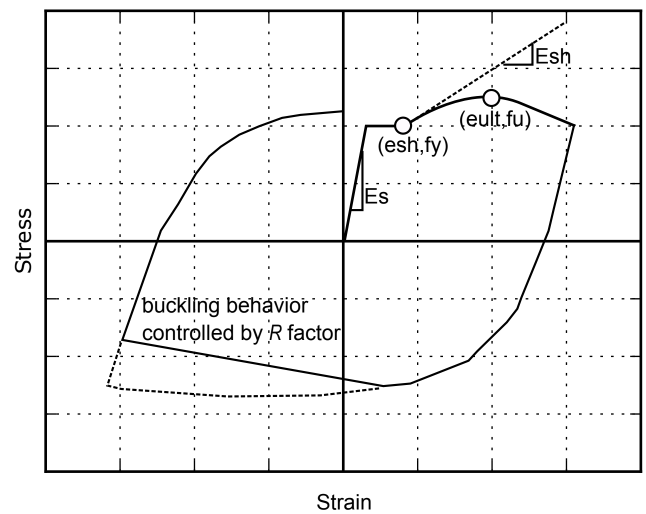

(a) Reinforcing Steel

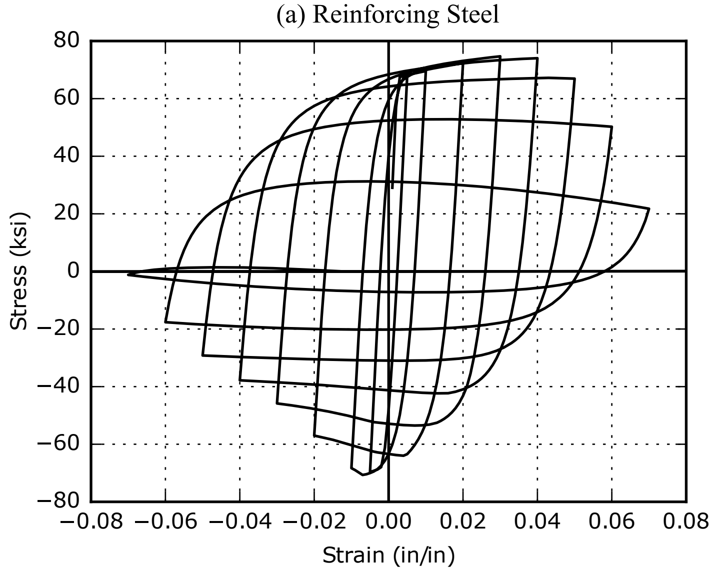

(b) Material Repsonse in Model

Figure 8.3: Longitudinal Reinforcing Material Model for RC Column

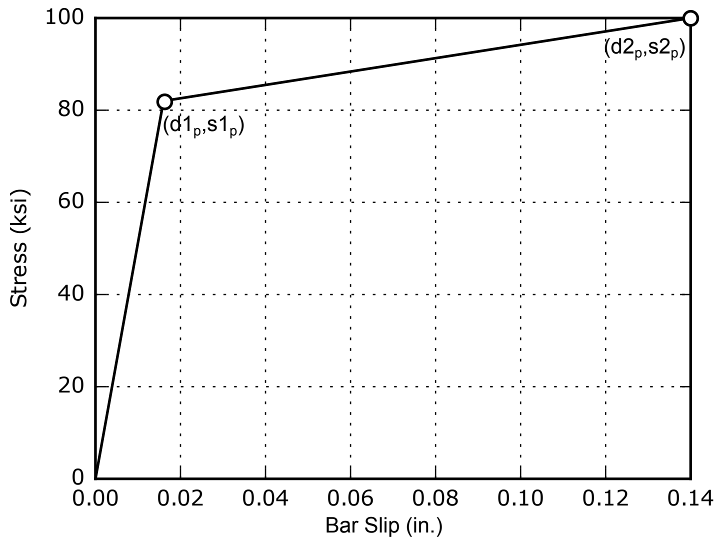

Figure 8.4: Estimated Reinforcing Bar Stress-Slip Relationship Based on Recommendations by Ranf [2007]

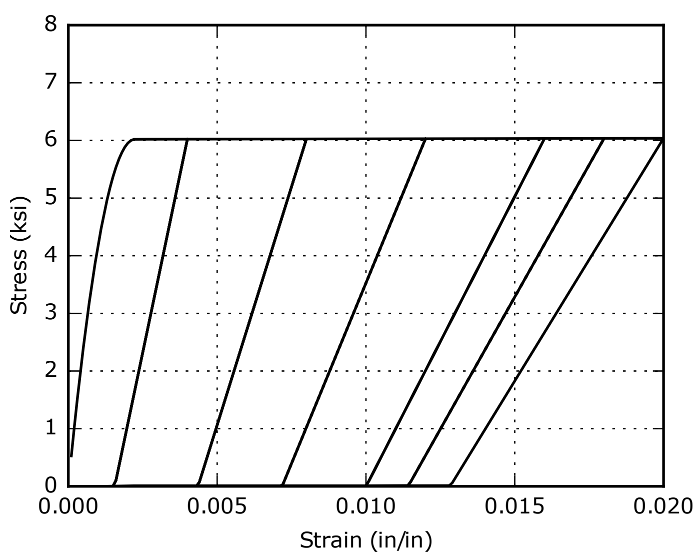

Figure 8.5: Confined Concrete Fill Model for CFST Column

The effective length of the steel tube was modeled using a Giuffre-Menegotto-Pinto model (referred to as *Steel02* in OpenSees) which accounts for isotropic hardening. Material parameters were selected according to common properties for ASTM 1018 or API 5L grade steel.

8.2.2.1 Strain Penetration and Local Tube Buckling in the ER Connection

The influence of tube yielding in the embedded section of the steel tube as well as local tube buckling was modeled using a connection element at the foundation/cap beam interface. The connection element was assigned the same geometric fiber element definition as the force-based beam column elements; however the OpenSees *Hysteretic* material model was assigned to the tube steel. A tri-linear force-displacement curve with pinching was defined using the *Hysteretic* material formulation in OpenSees as illustrated in Fig. 8.6. In this figure, d refers to displacement, s refers to force, and the subscripts p and n refer to tension and compression respectively. Note that the steel tube was discretized such that the area of the steel fiber elements was equal to $1 - in^2$, and thus force values defined in the tri-linear curve were equal to stress values (i.e. $\sigma_y = s_1$).

Column flexibility as a result of steel tube strain penetration was modeled by assuming a constant tube strain extending a distance $\alpha_1 L_e$ (referred to as L_{strain} in Table 8.1) into the foundation/cap beam where L_e is the tube embedment depth, and α_1 is a constant less than 1. Using this approach, the displacement values defined in the tri-linear hysteretic material model were defined as a function of $\alpha_1 L_e$. I.e. $d1_p$ in Fig. 8.6 was defined as $\epsilon_y \times \alpha_1 L_e$ where ϵ_y was the yield strain of the steel tube. In lieu of high-resolution experimental strain data, the constant $\alpha_1 L_e$ was estimated using numerical optimization as discussed below.

Local buckling of the steel tube results in a diminished compressive stress carrying capacity of the steel in the buckled region as well as a pinched hysteretic response at load reversals. The pinched hysteretic response develops as the buckled steel transitions from compression into tension as shown in Fig. 8.6. This phenomenon was modeled using the *pinchx* and *pinchy* constants built into the $Hysteretic$ material model. As recommendations

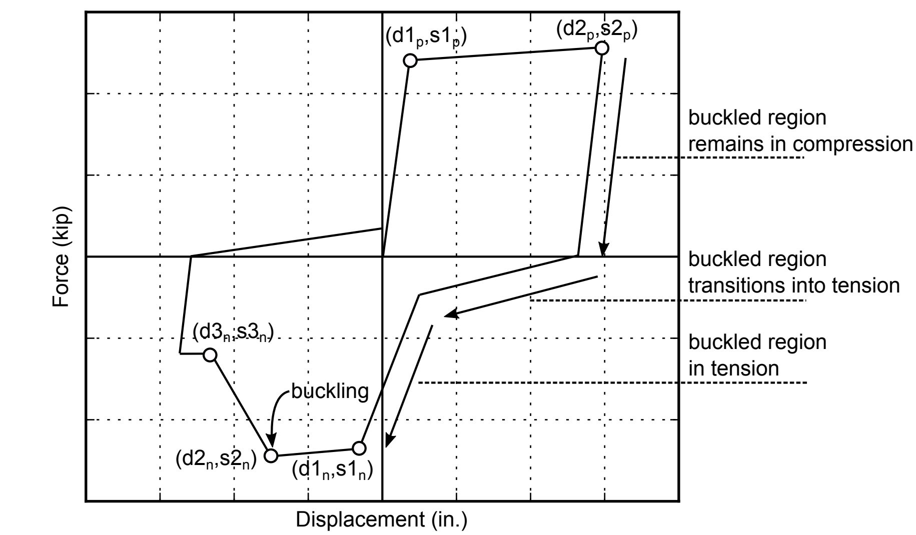

(a) Hysteretic Material

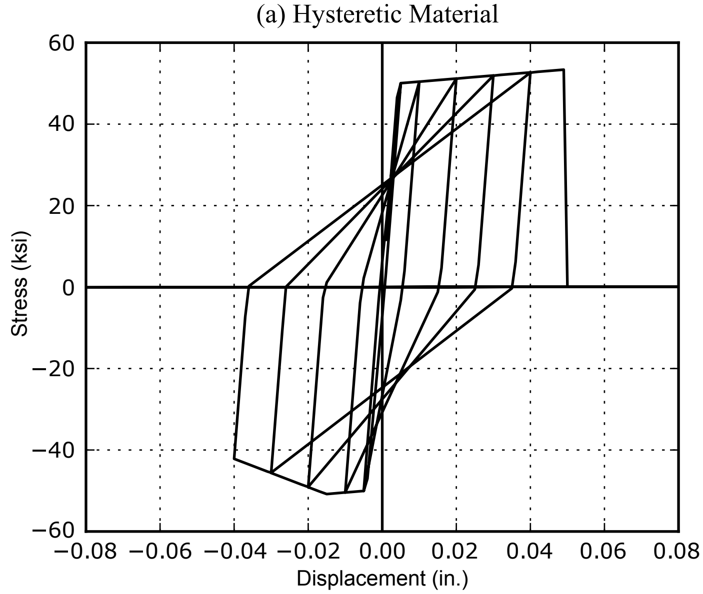

(b) Material Response in Model

Figure 8.6: Tube Steel Material Model for CFST Column

for pinching were not found in a survey of previous research, these factors were determined using numerical optimization.

The diminished compression capacity in the buckled region was modeled by setting a compression strain limit at the initiation of buckling using recommendations by M.D. Denavit [2010], which estimates the buckling strain as a function of D/t ratio as indicated in Equation 3.9. The residual compression capacity of the steel in the buckled region (indicated as $s3_n$ in Fig. 8.6) was defined as $\alpha_2 \times s3_n$ where α_2 was estimated using numerical optimization.

8.2.2.2 Determination of Material Constants

The material constants α_1, $pinchx$, $pinchy$, and α_2 were estimated using a numerical optimization program available in Python as discussed in Section 5.3.4. The numerical constants α_1, $pinchx$, $pinchy$, and α_2 were optimized by minimizing the sum of the errors in the moment recorded at each time step of the numerical model. The error at each time step was defined as the difference in the experimental moment and numerical moment recorded at common displacement increments($Error = M(d)_i^{exp} - M(d)_i^{num}$) where $M(d)_i^{exp}$ and $M(d)_i^{num}$ are the experimental and numerical moments at displacement d_i respectively. The numerical moment is defined as a function of α_1, $pinchx$, $pinchy$,α_2,$damage1$, and $damage2$ as $M(d)_i^{num} = f(\alpha_1, pinchx, pinchy, \alpha_2, damage1, damage2)_i$. Thus the generalized optimization function was defined as:

$$min \sum_{i=1}^{t} M(d)_i^{exp} - f(\alpha_1, pinchx, pinchy, \alpha_2, damage1, damage2)_i \tag{8.1}$$

The optimization program was run using four experimental tests(ER80T, ER96T, ER96L, and ER103L), and the final values of the constants α_1, $pinchx$, $pinchy$, α_2, $damage1$, and $damage2$ were taken as the mean of the optimized values for the four runs (the mean values are indicated in Table 8.2). Note that the material constants were calibrated over a characteristic length which was taken as a function of the embedded length of the steel

Table 8.2: Calibrated Material Constants for Tube Steel in Connection Element

α_1	0.054
α_2	0.63
$pinchx$	0.05
$pinchy$	0.05
$damage1$	0.000275
$damage2$	0

tube, $\alpha_1 L_e$. As these embedment depths were fairly constant in the experimental specimens used for the validation study (18-in. to 22-in.), the constants may not be valid for embedment depths far outside of this range.

8.3 Validation Approach

A group of eight column specimens (4-RC and 4-CFST) was selected to evaluate the accuracy of the modeling procedures. An overview of specimen geometry and material properties are included in Fig. 8.7 and Table 8.3. Annotations in Fig. 8.7 are defined in Table 8.3. The specimens were selected to cover a wide range of RC and CFST column parameters. Specifically:

- Specimens 407, 415, 815, and 1015 were RC column specimens with aspect ratios ranging from 4 to 10, and longitudinal reinforcing ratios ranging from 0.75% to 1.5% [D.E. Lehman, 2000].

- Specimens ER80T, ER96T, ER96L, and ER103L were CFST column specimens with D/t ratios ranging from 80 to 103. ER80T and ER103L utilized spiral welded tube with ASTM grade 1018 steel, while ER96T and ER96L used straight seam tube with API 5L grade steel.

These specimens represent a common range of structural parameters which are used in highway bridges at the prototype scale. The failure mode of all the selected specimens

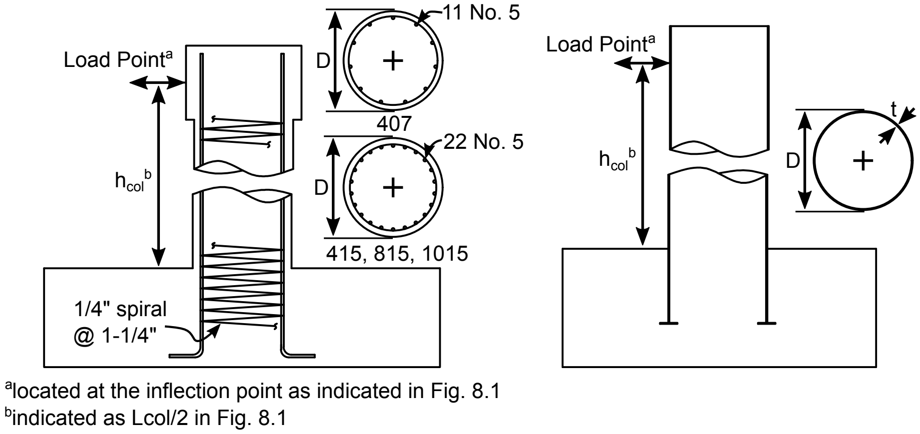

(a) RC (b) CFST

Figure 8.7: Geometry of Model Validation Specimens

was characterized by flexural hinging in the RC or CFST column (i.e. limited cap beam/foundation damage was observed in the experiments).

The material properties in Table 8.3 along with the material constants in Table 8.1 were used to define the nonlinear material properties in the RC and CFST column models as defined in Table 8.1.

A comparison of the experimental and numerical results is summarized in Table 8.3, while global hysteretic responses are plotted in Fig. 8.8and Fig. 8.9 for the RC and CFST columns respectively. The results are compared according to the *Error in Accumulated Peak Resistance* and the *Error in Total Energy Dissipated* as defined in Equation 8.2 and Equation 8.3 respectively where $M(d)_i$ is the moment measured at the peak measured displacement i in a given cycle, Ed_i is the energy dissipated in cycle i, and the superscripts ^{exp} and ^{num} refer to experimental and numerical data respectively.

$$\text{Error In Accumulated Peak Resistance} = \frac{\sum_{i=1}^{n} M(d)_i^{num} - M(d)_i^{exp}}{\sum_{i=1}^{n} M(d)_i^{exp}} \times 100 \qquad (8.2)$$

$$\text{Error In Accumulated Energy Dissipated} = \frac{\sum_{i=1}^{n} Ed_i^{num} - Ed_i^{exp}}{\sum_{i=1}^{n} Ed_i^{exp}} \times 100 \qquad (8.3)$$

In general, the numerical results accurately predicted the peak resistance and energy dissipation characteristics of the RC and CFST columns. The error in accumulated peak resistance and total energy dissipation were less than 10% for all RC specimens. Maximum errors recorded in the CFST models were slightly larger; 23.4% and 25.1% in accumulated peak resistance and total energy dissipated respectively (observed for ER96L). The accumulated peak resistance error was significantly lower in specimens ER80T and ER103L which both utilized spiral welded tubes (10.6% and 14.0% for ER80T and ER103L respectively). Note that due to the size of the columns used for the system analysis discussed in the next chapter, it is assumed that they would be spiral welded.

Table 8.3: Validation Model Specimen Geometry and Error Analysis

	Column Data								Error Analysis	
Specimen	f'_c (ksi)	f_y (ksi)	f_u (ksi)	h_{col} (in.)	D (in.)	t (in.)	Long. Dowels	ρ (%)	Error in Accumulated Peak Resistance (%)	Error in Accumulated Energy Dissipated (%)
407	4.3	68.4	93.3	96	24	-	11 No. 5	0.75	3.9	7.1
415	4.4	68.4	93.3	96	24	-	22 No. 5	1.5	2.2	6.4
815	4.9	68.4	93.3	192	24	-	22 No. 5	1.5	4.5	4.6
1015	4.9	68.4	93.3	240	24	-	22 No. 5	1.5	5.0	4.6
ER80T	10.7	60.2	68.5	72	20	0.25	-	5	10.6	11.6
ER96T	8.3	53	68.9	72	24	0.25	-	4	20.5	21.2
ER96L	7.9	53	68.9	72	24	0.25	-	4	23.4	25.1
ER103L	8.4	58	69.3	108	25.75	0.25	-	4	14.0	24.9

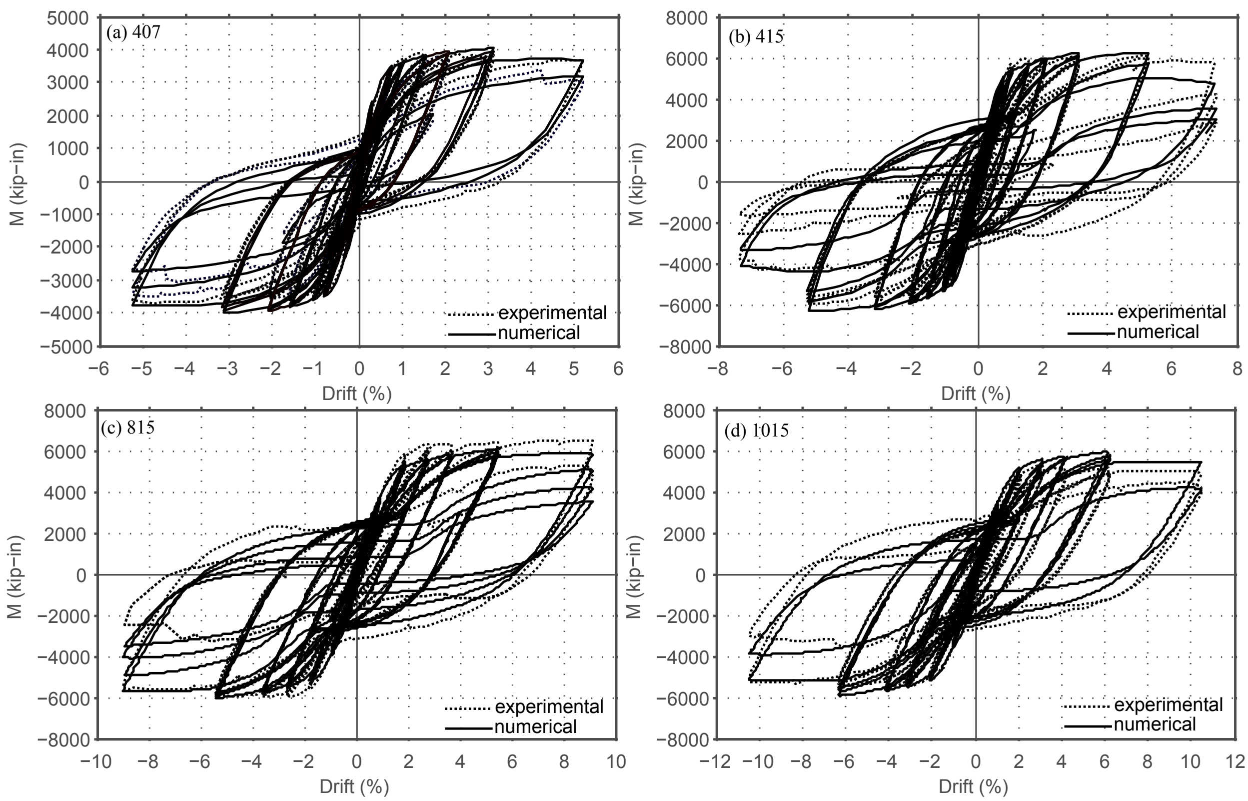

Figure 8.8: Simulated and Measured Responses of RC Column Experiments

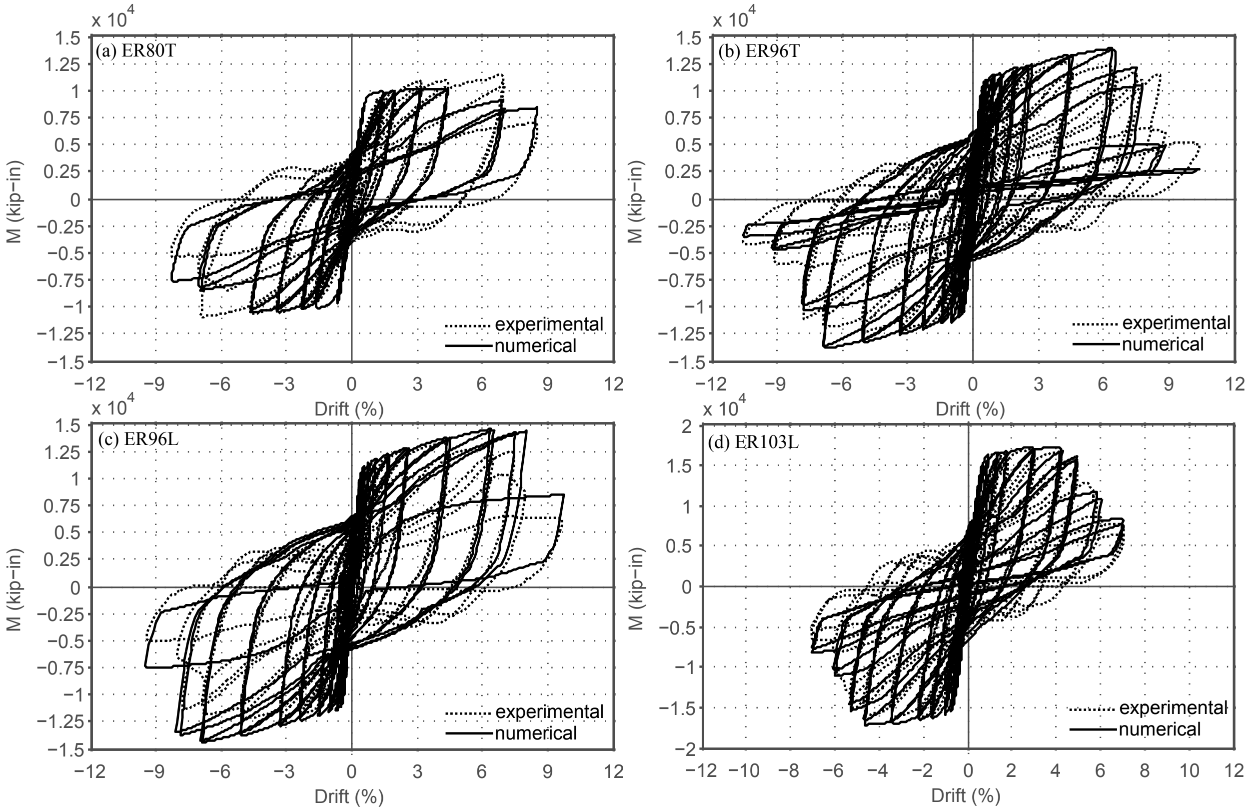

Figure 8.9: Simulated and Measured Responses of CFST Column Experiments

Chapter 9

DYNAMIC RESPONSE AND COLLAPSE POTENTIAL OF RC AND CFST BRIDGES SUBJECTED TO LATERAL LOADING

In this chapter, advanced performance based earthquake engineering (PBEE) tools are used to compare the seismic performance of a prototype scale RC and CFST bridge, including fragility functions that express the likelihood of damage and reparability, nonlinear analysis methods that capture the full cyclic response of the structural system, and incremental dynamic analyses (IDAs) to evaluate collapse potential. The process for the comparison was as follows: (1) the selected bridge was designed using RC and CFST columns, with the objective of having the same strength and stiffness, (2) the structures were subjected to a suite of crustal and subduction zone motions scaled to represent serviceability (10% probability of exceedance in 50 years), design (7% probability of exceedance in 75 years), and maximum considered (2% probability of exceedance in 50 years) seismic hazard levels, (3) fragility curves were used to compare the performance of the bridge including damage state as well as maximum and residual drift, and (4) IDAs were conducted in conjunction with lognormal cumulative distribution functions to compare the damage and collapse probability.

9.1 Prototype Structure

The Gold Creek Bridge located near mile post 55 on Interstate 90 in Washington State was selected as the prototype for the dynamic analysis. An overview of the structure is shown in Fig. 9.1 and illustrated in Fig. 9.2. The bridge has seven 155-ft. spans, and was selected to limit the influence of the abutments on global response. The columns in the RC bridge are reinforced concrete with 60-in. diameter, and are detailed using 18 No. 11 longitudinal bars, and No. 6 spiral at 3-in. on-center in the transverse direction. These columns were

Figure 9.1: Gold Creek Bridge

redesigned using CFST columns with equivalent strength under combined axial-moment (P-M) loading as well as equivalent stiffness, which resulted in CFST members with a thickness and diameter of 0.625-in. and 50-in. respectfully and a diameter to thickness ratio (D/t) of 80.

9.2 Model Overview

The open source structural analysis software OpenSees was used to conduct the dynamic analyses. Model geometry included the columns, cap beams, diaphragms, precast girders, deck, and abutments as illustrated in Fig. 9.3.

All components of the superstructure (including cap beams, diaphragms, longitudinal girders, and deck) were idealized using elastic beam column elements assuming that the structure was capacity designed such that inelastic deformation was isolated to the columns and their connections. In the longitudinal direction, the cross sectional properties of the longitudinal girders, deck, and overlay were aggregated to a single line of elements placed at the center of mass of the superstructure. In the transverse direction, the cross sectional properties of the cap beam and diaphragm were aggregated to a single line of elements also

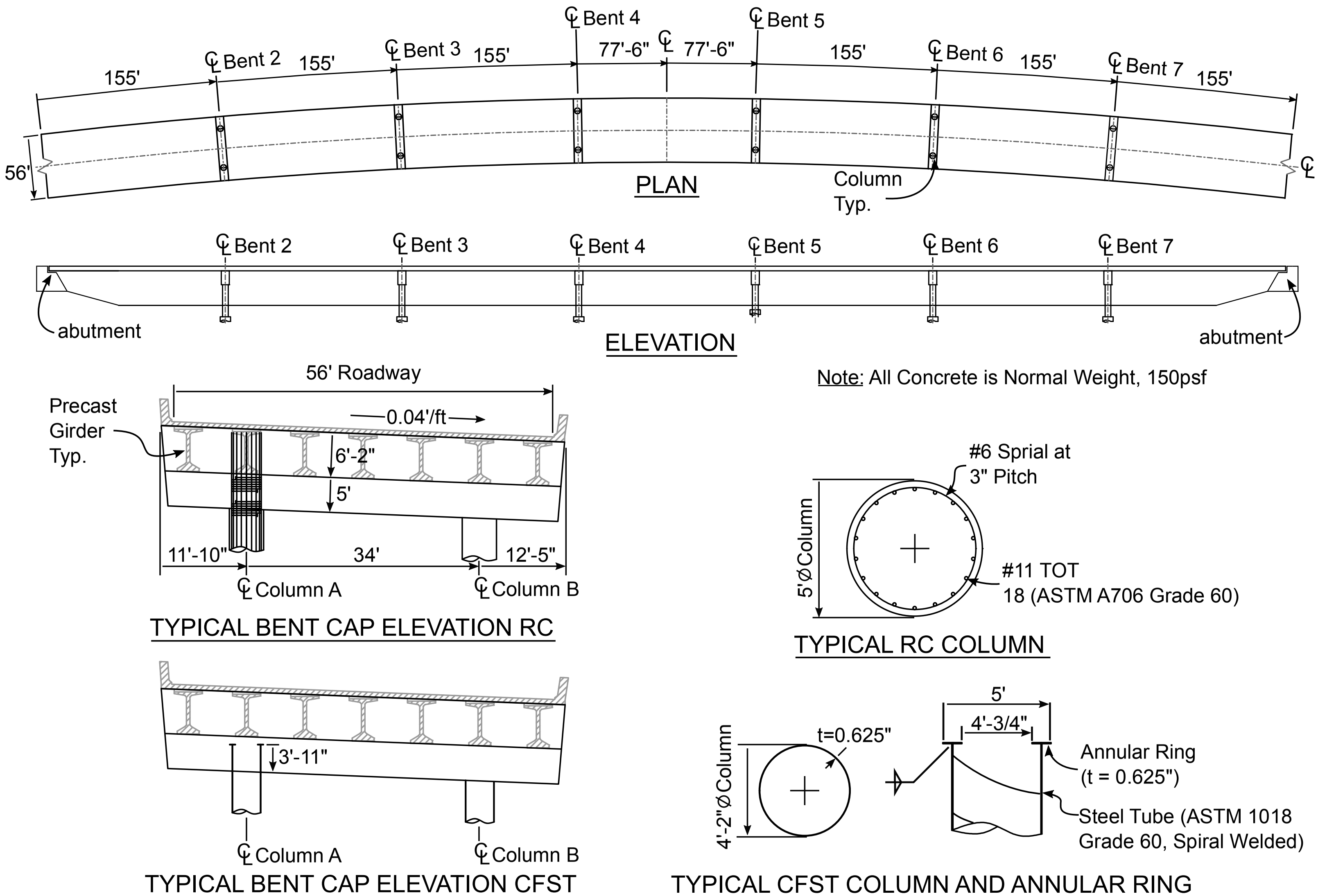

Figure 9.2: Prototype RC and CFST Bridge

located at the center of mass of the superstructure (illustrated in Fig. 9.3). Mass was lumped at nodes between elements.

The RC and CFST columns were modeled using the techniques discussed in Chapter 8. Fixed boundary conditions were applied to the base of each column in the transverse and longitudinal direction of the bridge. The top of the columns were attached to a rigid link which modeled the offset from the top of the column to the center of mass of the superstructure as illustrated in Fig. 9.3.

The influence of the abutments was modeled using springs attached to the superstructure at both ends of the bridge as indicated in Fig. 9.3. The stiffness of the springs was calculated based on recommendations in AASHTOa [2015] for the vertical and transverse stiffness of the elastomeric bearing pads between the longitudinal girders and abutment seats.

Dynamic orthogonal ground motions were applied to each fixed boundary condition using a built-in function in OpenSees as indicated in Fig. 9.3.

9.3 Multi-Performance Level Evaluation

The performance of the RC and CFST structures were evaluated for a range of seismic hazard levels at the site of the bridge, and multiple system performance states were evaluated (i.e. bar buckling and tube buckling in the RC and CFST structure respectively). The recommended FEMA P695 ground motion set was used in this investigation. Characteristics of the selected ground motion set are given in Appendix E. The ground motions were scaled to 10/50 (serviceability level), 7/75 (design level), and 2/50 (MCE) hazard levels. The target spectra for the 10/50 and 2/50 hazards followed NEHRP recommended provisions using the corresponding USGS mapped spectral acceleration values representative of the different hazard levels. The target spectra for the 7/75 hazard was developed based on requirements in AASHTOb [2011]. All of the records were scaled using fundamental period of each structure such that the mean spectrum did not drop below 71% of the target spectra over a period range from 0.2T to 1.5T as specified by ASCE [2013]. The target and mean acceleration spectra for the three hazards are illustrated in Fig. 9.4. Note that the fundamental periods

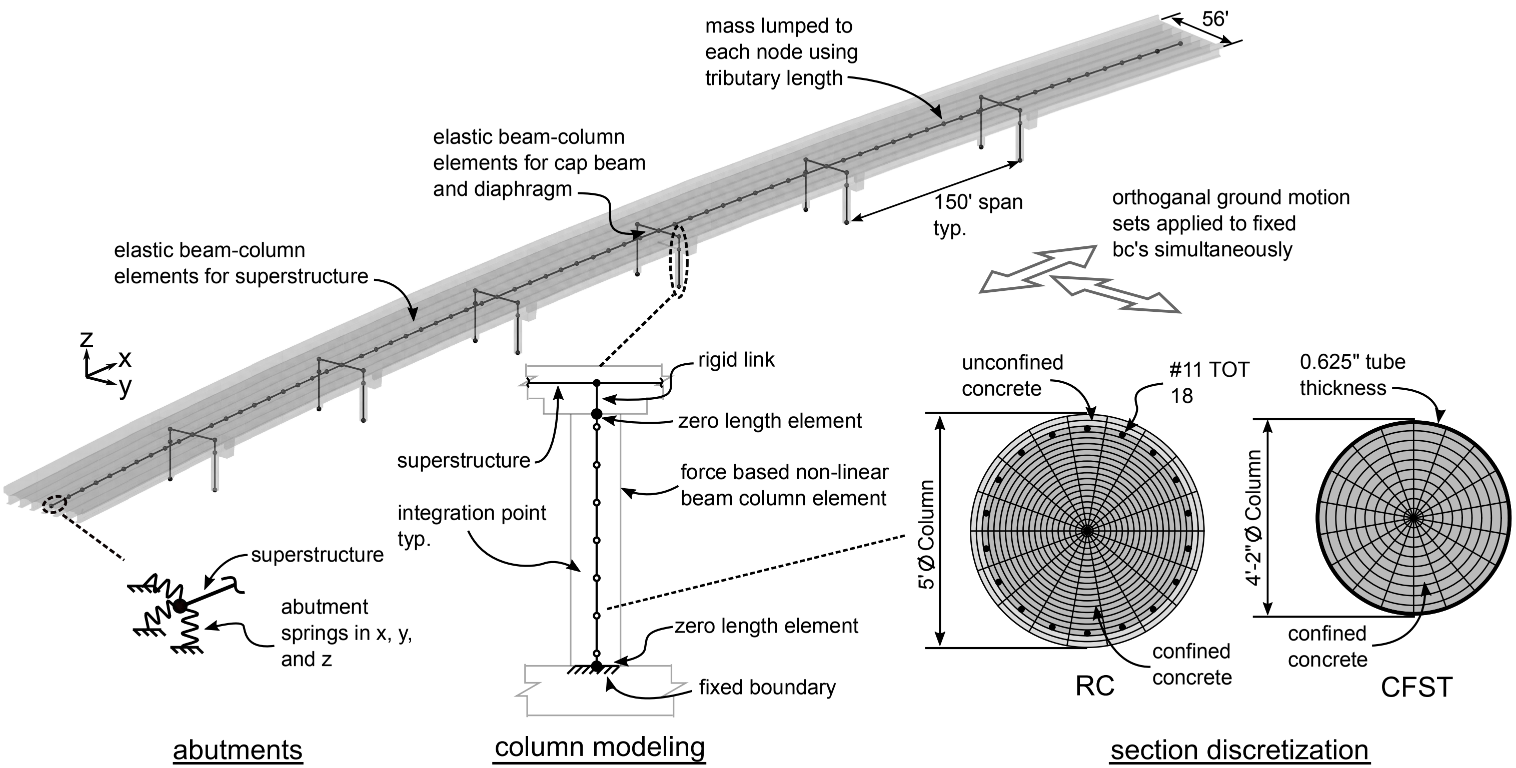

Figure 9.3: Model Overview

of the RC and CFST structure were both approximately 1-sec as calculated using an Eigen value analysis.

The damage state of the RC and CFST structures were estimated based on the maximum and residual drifts recorded in the dynamic analyses. Damage in the RC strucuture was approximated using recommendations from M.P. Berry [2003, 2005] which estimate damage in flexural RC members based on maximum recorded drift. Maximum drifts which result in concrete spalling and longitudinal bar buckling are defined in Equations 9.1 and 9.2 respectively where $\delta_{spallcalc}$ and δ_{bbcalc} are the column displacements at concrete spalling and bar buckling, $k_{e_b b}$ is an empirically derived constant (150 for spiral columns), ρ_{eff} is the effective confinement ratio, and d_b is the diameter of the longitudinal reinforcing bars. Note that for the Gold Creek Bridge, $\delta_{spallcalc}$ and δ_{bbcalc} were calculated as 2.21% and 3.98% drift respectively respectively. Damage in the CFST structure was estimated using the fragility curves illustrated in Fig. 5.29.

$$\frac{\delta_{spallcalc}}{L}(\%) \cong 1.6\left(1-\frac{P}{A_g f'_c}\right)\left(1+\frac{L}{10D}\right) \tag{9.1}$$

$$\frac{\delta_{bbcalc}}{L}(\%) \cong 3.25\left(1+k_{ebb}\rho_{eff}\frac{d_b}{D}\right)\left(1-\frac{P}{A_g f'_c}\right)\left(1+\frac{L}{10D}\right) \tag{9.2}$$

The performance of the RC and CFST structures were evaluated based on the required post-event repair effort correlated to the estimated severity of damage. As the superstructure and foundation were assumed to remain elastic in the numerical model, only repair scenarios related to column damage and residual deformation are considered here. Repair scenarios for the RC and CFST columns are defined in Table 9.1. Note that damage in the CFST column progresses from steel tube buckling (which requires no repair), to steel tube tearing (which requires partial column replacement). Partial replacement for both column types consists of shifting plastic hinge out of the damaged region in the column as described in D.E. Lehman [2000].

Table 9.1: Required Repair Effort for RC and CFST Structures

Required Repair Effort	Damage Description for RC Repair Effort	Damage Description for CFST Repair Effort
No Repair	Longitudinal Dowel Yielding	Steel Tube Yielding and Buckling
Repair	Limited Column Spalling Inject Cracks with Grout	n/a
Partial Replace	Longitudinal Bar Buckling/Fracture Shift Plastic Hinge Region	Steel Tube Tearing Shift Plastic Hinge Region

Table 9.2: Mean ($\bar{x}$) and Standard Deviation (σ) of Maximum Recorded Drifts for the 10/50, 7/75, and 2/50 Seismic Hazard Levels

	10/50		7/75		2/50	
	$\bar{x}$	σ	$\bar{x}$	σ	$\bar{x}$	σ
RC	0.52	0.18	1.04	0.33	1.58	0.51
CFST	0.55	0.14	0.95	0.24	1.44	0.42

In general, the RC and CFST structures performed well when subjected to the varying seismic hazards. The median maximum recorded drift levels were similar for both structures as indicated in Table 9.2 and Fig. 9.5. The RC structure exceeded the drift threshold for repair in 2.6%, 46.2%, and 94.9% of the ground motions for the 10/50, 7/75, and 2/50 seismic hazards respectively, indicating that the RC columns would need at least limited repair at the design level hazard. The CFST structure remained well below the maximum drift threshold for tube tearing for all of the motions.

The CFST structure exhibited lower residual drifts than the RC structure for all hazards as indicated in Table 9.3 and Fig. 9.6. Median residual drifts recorded for the CFST structure were 0.03-in., 0.10-in., and 0.17-in. lower than the median residual drifts recorded in the RC structure for the 10/50, 7/75, and 2/50 hazards respectively.

9.4 Incremental Dynamic Analysis

The performance of the RC and CFST structures was additionally evaluated using an incremental dynamic analysis (IDA) in which the structures were subjected to a suite of

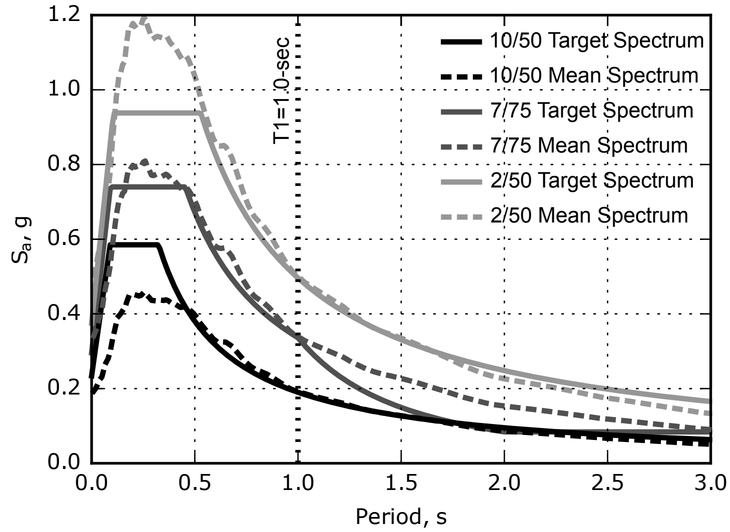

Figure 9.4: Scaled Mean Acceleration Spectra and Corresponding Target Spectra

Table 9.3: Mean ($\bar{x}$) and Standard Deviation (σ) of Residual Recorded Drifts for the 10/50, 7/75, and 2/50 Seismic Hazard Levels

	10/50		7/75		2/50	
	$\bar{x}$	σ	$\bar{x}$	σ	$\bar{x}$	σ
RC	0.04	0.09	0.14	0.13	0.22	0.19
CFST	0.01	0.02	0.04	0.04	0.05	0.08

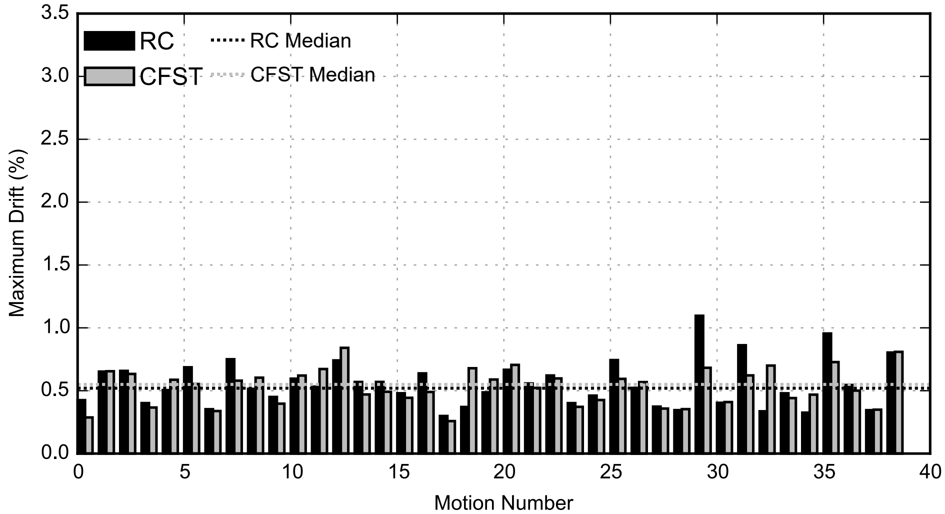

(a) 10/50 Hazard Level

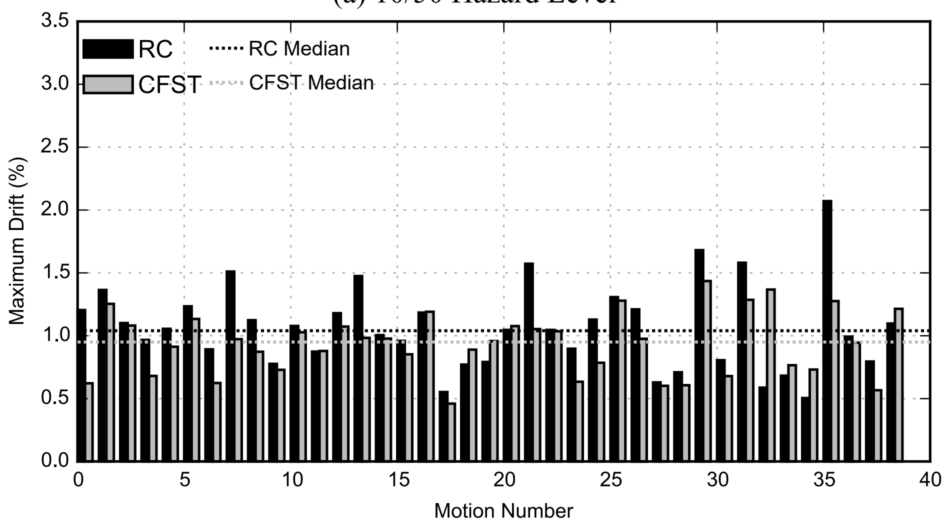

(b) 7/75 Hazard Level

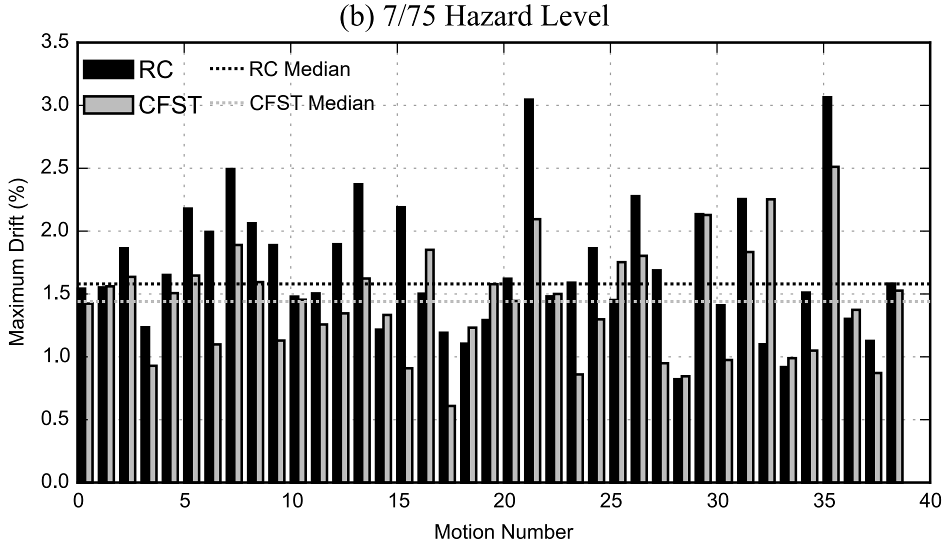

(c) 2/50 Hazard Level

Figure 9.5: Maximum and Median Maximum Drifts for the 10/50 (serviceability), 7/75 (design level), and 2/50 (MCE) Hazard Levels

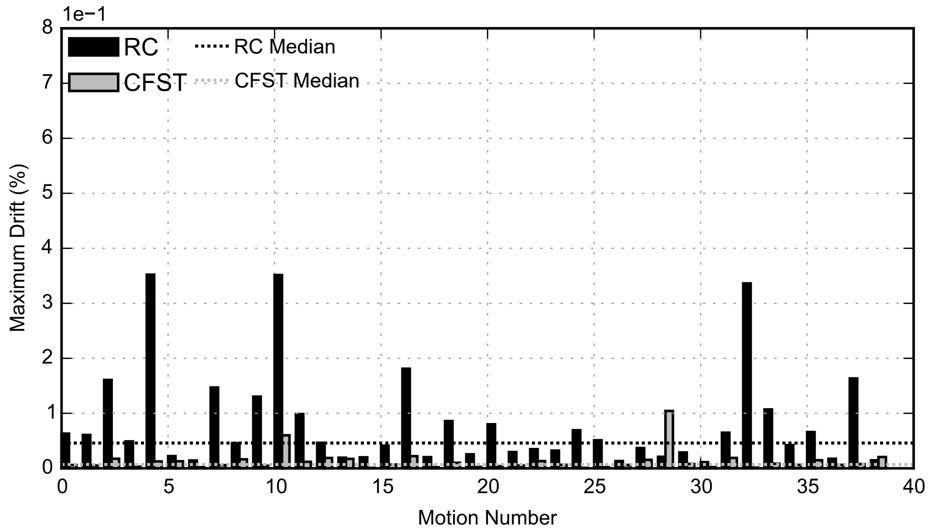

(a) 10/50 Hazard Level

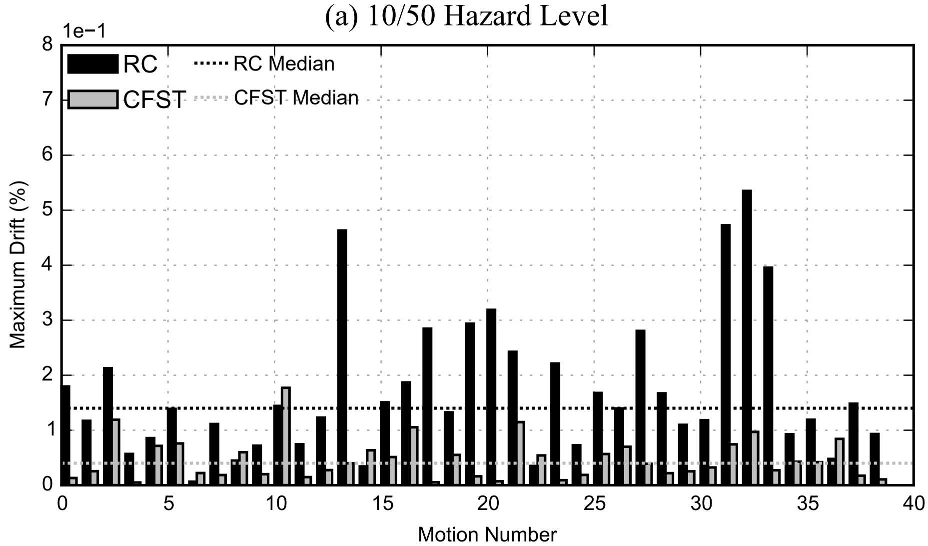

(b) 7/75 Hazard Level

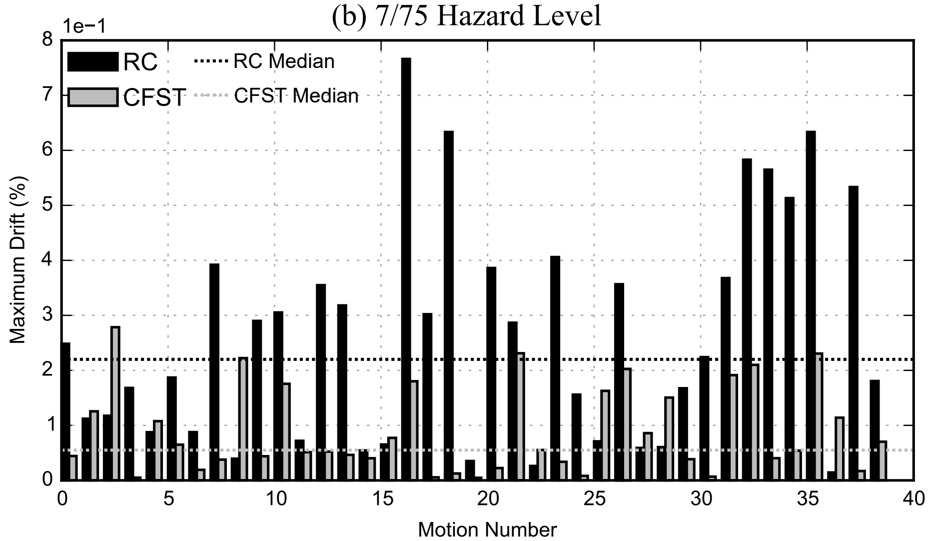

(c) 2/50 Hazard Level

Figure 9.6: Residual and Median Residual Drifts for the 10/50, 7/75, and 2/50 Hazard Levels

ground motions scaled to multiple levels of intensity. The recommended FEMA P695 ground motion set was used to perform the IDA. Characteristics of this ground motion set are given in Appendix E. The ground motions were individually scaled at the fundamental period of the two structures (T_1 1.0-sec) until 50% of the motions resulted in collapse, which has been defined as a maximum recorded drift exceeding 10%. This drift limit was selected for two primary reasons: (1) to limit the influence of the abutments on the recorded response and (2) because experimentation has indicated that bridge piers do not retain sufficient resistance beyond this drift.

IDA curves for the maximum recorded drift and shear demand are plotted in Fig. 9.7 and Fig. 9.8 respectively. The shear demand has been normalized to the theoretical shear capacity of the RC and CFST columns (V_n), and was evaluated in-part to ensure the columns were flexurally dominated, as column shear response for both the RC and CFST columns was modeled elastically as discussed in the previous chapter (note that $V/V_n < 1$ indicates flexurally dominated behavior). The theoretical shear capacity of the RC column was calculated according to AASHTOa [2015], while the theoretical shear capacity of the CFST was calculated using Equation 9.3, which has been proposed for adoption in the 2016 Washington Department of Transportation Bridge Design Manual where f'_c is in ksi. Note that the shear demand-to-capacity ratio in the CFST columns remains much lower than the RC columns as the spectral acceleration is increased in the IDA.

$$V_n = 2\left(0.6 f_y 0.5 A_s\right) + 0.0136 \times 3 A_c \sqrt{f'_c} \tag{9.3}$$

Results from the IDA were used to fit lognormal cumulative distribution functions (CDF) for the required post-event repair effort as correlated to the maximum recorded spectral acceleration. The lognormal CDF is defined in Equation 9.4 where Φ is the Gaussian, x is a particular value of spectral acceleration, θ_d is the logarithmic mean, and β_d is the logarithmic standard deviation. Using the empirical CDF generated from the IDA, the lognormal CDF was fitted such that θ_d and β_d were optimized to reduce the bias, where the

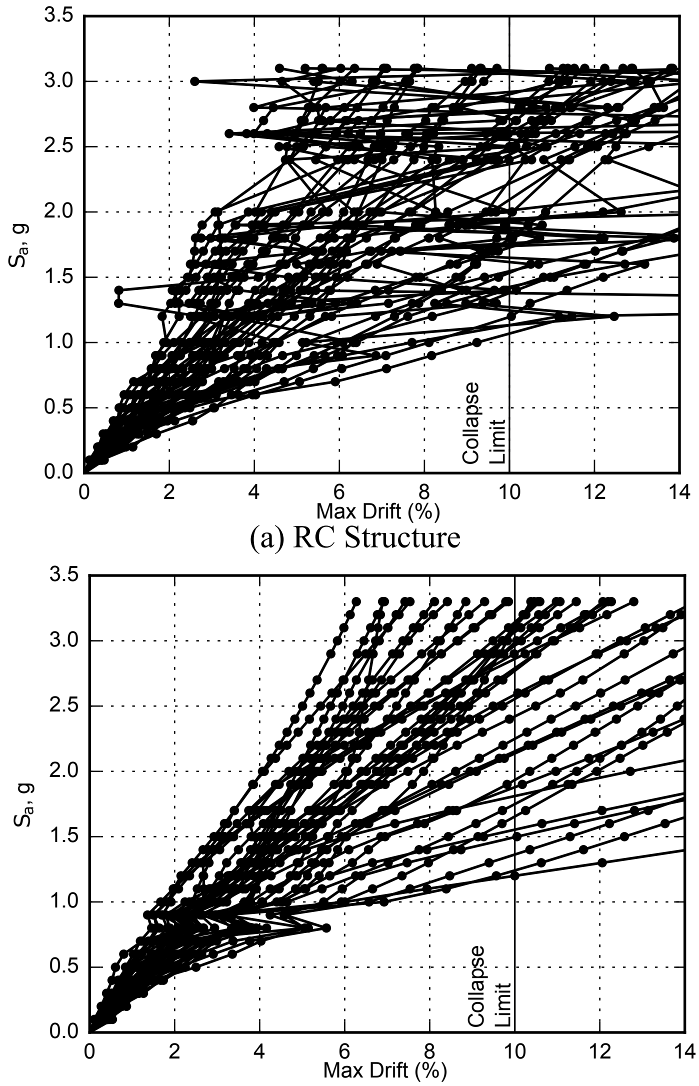

(a) RC Structure

(b) CFST Structure

Figure 9.7: Maximum Recorded Drift from IDA

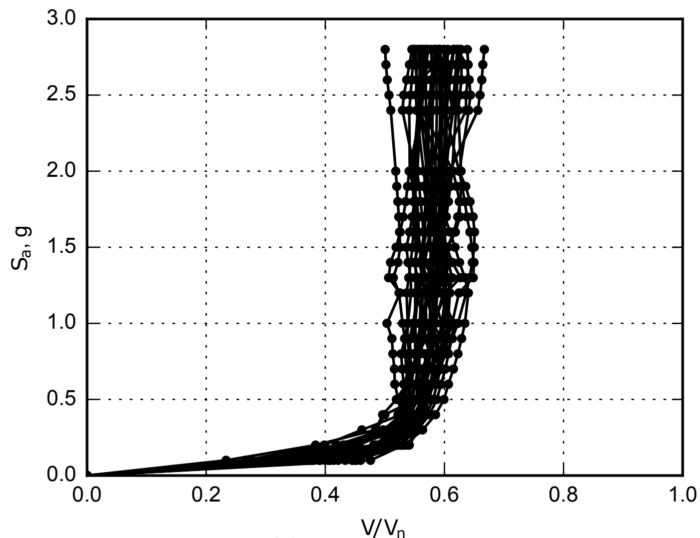

(a) RC Structure

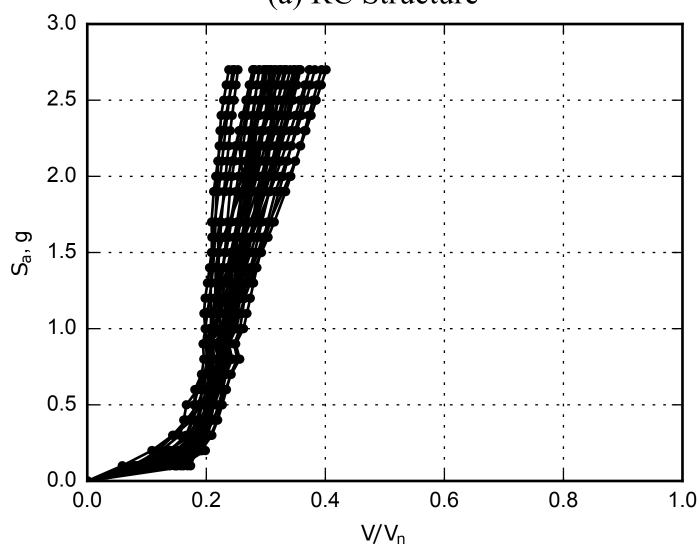

(b) CFST Structure

Figure 9.8: Maximum Recorded Shear Demand to Capacity Ratio from IDA

bias is the difference between the empirical and lognormal CDF as illustrated in Fig. 9.9. The constants θ_d and β_d were optimized using a numerical optimization program as discussed in Section 5.3.4. The generalized optimization function is defined in Equation 9.5 where P^{IDA} is the empirical probability of occurrence, and $P^{theo}(\theta_d, \beta_d)$ is the probability of occurrence from the fitted lognormal CDF. Optimized θ_d and β_d are defined in Table 9.4 for the repair, partial replace, and collapse limit states. The empirical and fitted lognormal CDFs are plotted in Fig. 9.10. Note that numerical optimization has been used to fit lognormal CDF in previous research, and is recommended when structural analyses are expensive [Baker, 2014]. Note that the standard deviation, β_d, only accounts for uncertainties in the ground motion record-to-record variability; uncertainties in the structural design requirements, test data, and modeling are not considered.

$$F_d(x) = \Phi\left(\frac{ln(x/\theta_d)}{\beta_d}\right) \tag{9.4}$$

$$min\sum_{i=1}^{n}|Bias_i| = min\sum_{i=1}^{n}|P_i^{IDA} - P^{theo}(\theta_d, \beta_d)| \tag{9.5}$$

Table 9.4: Logarithmic Mean (θ_d), Logarithmic Standard Deviation (β_d), and Arithmetic Mean ($\bar{x}$) for Fitted Fragility Curves in Fig. 9.10

	Repair			Partial Replace			Collapse		
	θ_d	β_d	$\bar{x}$	θ_d	β_d	$\bar{x}$	θ_d	β_d	$\bar{x}$
RC	-1.04	0.53	0.35	-0.01	0.40	0.99	0.85	0.53	2.34
CFST	n/a	n/a	n/a	0.69	0.35	1.99	1.03	0.52	2.8

The performance of the RC and CFST structures were evaluated based on the lognormal CDFs for the *Repair*, *Partial Replace*, and *Collapse* limit states as illustrated in Fig. 9.10. These limit states have been expressed in terms of the repair margin ratio (RMR), partial replace margin ratio (PRMR), and collapse margin ratio (CMR) as defined in Equations 9.6-9.8, where $\widehat{S}_{MT}$ is the design earthquake spectral acceleration at the period of the structure (the 7/75 target spectrum in Fig. 9.4), and $\widehat{S}_{RT}$, $\widehat{S}_{PRT}$, and $\widehat{S}_{CT}$ are the median spectral

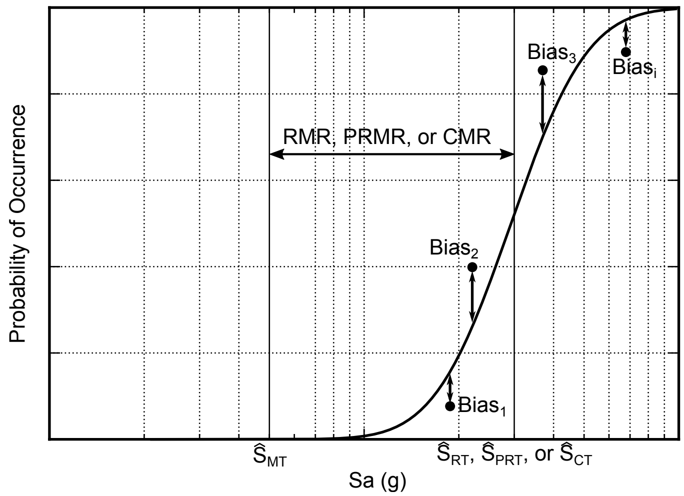

Figure 9.9: Bias for Optimization of the Lognormal Constants θ_d and β_d and Defintion of Repair Margin Ratio (RMR), Partial Replace Margin Ratio (PRMR), and Collapse Margin Ratio (CMR)

accelerations recorded for the repair, partial replace, and collapse limit states respectively. The RMR, PRMR, and CMR are summarized in Table 9.5.

$$RMR = \frac{\widehat{S}_{RT}}{\widehat{S}_{mt}} \tag{9.6}$$

$$PRMR = \frac{\widehat{S}_{PRT}}{\widehat{S}_{mt}} \tag{9.7}$$

$$CMR = \frac{\widehat{S}_{CT}}{\widehat{S}_{mt}} \tag{9.8}$$

Table 9.5: Summary of RMR, PRMR, and CMR from IDA

	RMR	PRMR	CMR
RC	1.0	2.82	6.68
CFST	n/a	5.68	8
% Difference	n/a	106	20

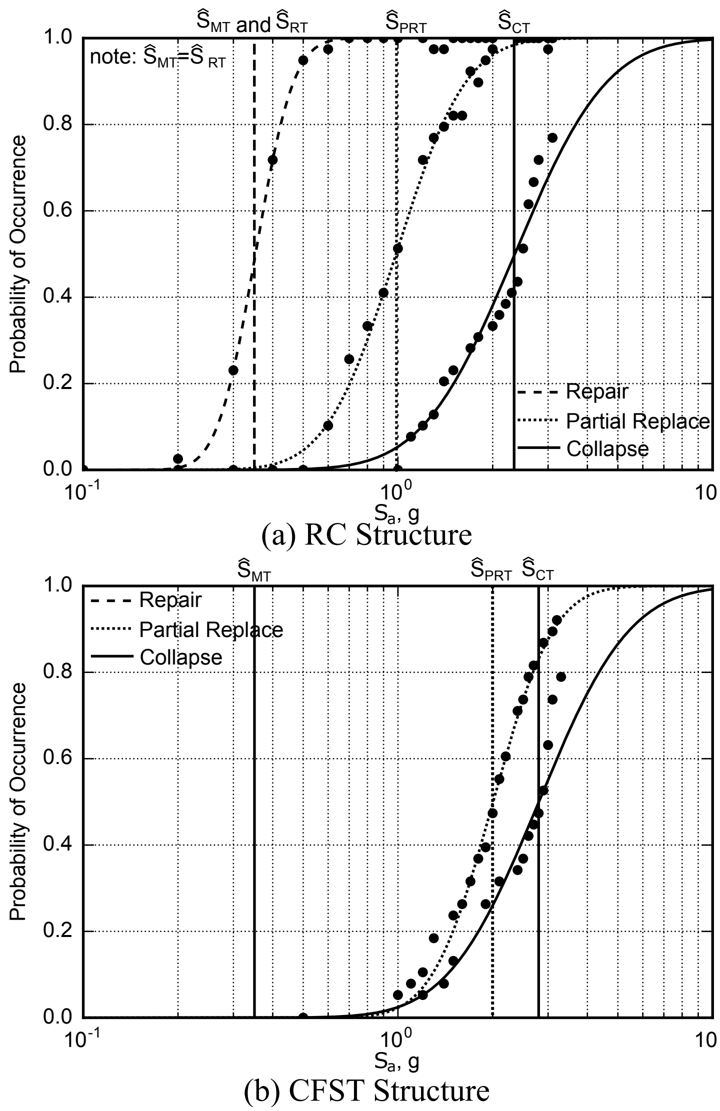

Figure 9.10: Probability of Required Repair Effort Based on Spectral Acceleration

The CFST structure outperformed the RC structure in terms of the RMR, PRMR, and CMR ratios as indicated in Table 9.5. The CFST structure exhibited significantly larger PRMR and CMR than the RC structure, suggesting the post-event repair effort on the CFST bridge would be less than that required for the RC bridge. An RMR of one was recorded for the RC structure, indicating a likelihood that repair would be necessary for the design level hazard. Note that no *Repair* limit state exists for CFST columns thus giving the CFST structure a further advantage over the RC system. The advantages of the CFST structure are additionally highlighted by the lognormal CDF curves in Fig. 9.10, which indicate higher probabilities of repair, partial replacement, and collapse of the RC structure for lower spectral accelerations.

Chapter 10

SUMMARY, CONCLUSIONS, AND RECOMMENDATIONS FOR FUTURE WORK

Concrete filled steel tubes (CFSTs) are composite structural elements that provide large strength and stiffness while permitting rapid construction. In bridges, CFSTs may be used as piers, piles and drilled shaft foundations. The steel tube serves as formwork and reinforcement to the concrete fill, eliminating the need for flexible reinforcing cages, shoring, and temporary formwork and increasing safety and reducing labor. The placement of the concrete fill may be further expedited by using self-consolidating concrete (SCC) because vibration is not required.

The steel tube is placed at the optimal location for flexural resistance, thereby maximizing strength and stiffness while minimizing weight and material requirements. In addition, the steel tube provides optimal confinement and shear strength to the concrete fill in contrast to transverse spiral reinforcement that is typically used for circular reinforced concrete (RC) columns. The concrete fill restrains local buckling, and significantly increases compressive strength and stiffness of the tube. In comparison to an RC column of the same geometry, a CFST generally has larger axial, shear and flexural capacity and has larger stiffness, a result of the optimal placement of the steel, reduced cracking and increased confinement.

The use of CFSTs in bridge construction in moderate and high seismic regions is limited in the United States in part due to a lack of practical and economical connections, and in part because the seismic advantages of CFST systems have not been quantified relative to traditional RC systems. Recent research has addressed the connection limitation through the development of CFST foundation connections, however research related to the cap beam connection is limited, and seismic response comparisons between CFST and RC systems have not been thoroughly investigated.

The studies in this dissertation were conducted to address these deficiencies by (1) proposing and experimentally demonstrating a range of CFST column-to-precast cap beam connections and (2) by evaluating and comparing the seismic performance of an RC and CFST bridge at prototype scale.

10.1 CFST Column to Cap Beam Connections

Several new CFST column-to-cap beam connections were proposed and experimentally studied using increasing cyclic deformations. These connections include (1) an embedded ring connection in which an annular ring is welded to the top of the steel tube and embedded into the cap beam (2) a welded dowel connection in which a ring of headed dowels is welded to the inside of one end of the steel tube and developed into the cap beam, and (3) an reinforced concrete connection in which a traditional reinforcing cage consisting of a ring of headed dowels with transverse reinforcing is developed into the CFST column and cap beam. All of the connections were demonstrated using a grouted connection detail, which can be integrated with precast cap beam components for ABC; however the connections can also be used in tradition CIP construction. Further, the benefits of ABC vary somewhat with the 3 connection types.

A series of transverse and longitudinal test specimens was developed (note that transverse and longitudinal refers to the direction of the bridge). Initially salient design parameters including the width of the cap beam, geometry of the ring at the end of the tube for the embedded connection and axial load ratio were numerically evaluated. From this study, a series of specimens were tested to evaluate the behavior of the different connection types, and to assess the influence of several parameters on the performance of the connections. The experimental results were used to develop practical engineering expressions for the proposed connections. Based on the experiences and recorded results, the following observations and conclusions were drawn from the study.

10.1.1 Embedded Ring Connection

The embedded ring connection uses a circular ring welded to the end of the steel tube to provide anchorage and stress transfer to the concrete and reinforcing in the cap beam. The flange extends a distance 8 times the thickness of the tube ($8t$) both inside and outside of the tube. When precast cap beams are used, a void is cast into the precast elements using a galvanized corrugated pipe. The precast cap beam is placed onto the column after the column is set, and the recess between the tube and corrugated pipe is filled with high strength fiber reinforced grout.

Experimental results demonstrated that this connection provides large strength, stiffness, and deformation capacity, and the predictions were accurate with modest and predictable over-strength. All of the specimens which utilized this connection type achieved the theoretical plastic moment capacity of the CFST component as calculated using the PSDM. The failure mode in all cases was characterized by ductile tearing near the column-to-cap beam interface. Local buckling was observed in the steel tube at around 4% drift in all cases, however the initiation of buckling did not influence the stiffness or moment resistance of the connection. The influence of several parameters on the behavior the ER connection are noted below.

- The cap beam width for this connection may be as narrow as 2 times the diameter of the CFST column.

- Decreasing the external projection of the annular ring to 8 times the thickness of the steel tube does not influence the performance of the embedded connection. This is lower than the external projection of 16 times the thickness of the steel tube recommended in previous research

The ER connection offers several distinct advantages in terms of optimizing the objectives of accelerated construction and decreasing labor. After the column is cast, precast cap beams can be placed directly onto the CFST; no shoring, friction collars, or temporary support is required. Furthermore, this connection does not require any internal transverse or longitudinal reinforcing. There are no dowels or flexible reinforcing cages that need to be tied and placed.

The ER connection also offers several advantages in terms of post-event inspection and repair. The damage state of the ER connection can be readily identified based on the condition of the steel tube in the connection region; the concrete in the tube is generally in pristine condition. In addition, the accessibility to the steel tube (which acts as the primary longitudinal reinforcing) provides a unique opportunity for repair which will be more difficult in dowel or RC type connections in which extensive spalling and concrete damage are noted, and the longitudinal steel is embedded in the column concrete. Developing robust repair strategies for the ER connection will be a focus of future work.

10.1.2 Welded Dowel Connection

The WD connection utilizes a ring of headed dowels to resist the flexural demand. The tensile forces in the dowels is developed by welding the dowels to the steel tube. The dowels then transfer forces and moment into the cap beam using a high-strength, fiber-reinforced grouted connection. Welding the dowel directly to the tube, as opposed to embedding the dowel directly into the connection maximizes the moment capacity of the dowel connection. A soffit fill is included between the steel tube and cap beam. A flange with an outer diameter of D+8t is welded to the exterior of the steel tube, and this flange bears on the soffit fill and the surface of the cap beam thereby increasing the moment arm and moment capacity of the connection.

Experimental results demonstrated that this connection can offer large strength, stiffness, and deformation capacity. However, the stiffness and strength of this connection is controlled by the effective reinforcing ratio of the dowels which extend from the CFST into the cap beam, and therefore lower stiffness and strength values were recorded than comparable ER connections. The strength of the WD connection may be similar to that of the ER connection if adequate reinforcing ratios are used. However some of this resistance is contributed by the compressive bearing of the flange on the steel tube, and this added strength which is not considered in the current design equations. Hence, the WD connection is prone to large and variable over-strength to the design values.

Two distinct failure modes were observed: (1) cap beam failure in which the headed dowels pulled out of the cap beam and (2) yielding and fracture of the longitudinal dowels within the soffit fill region. In all cases, significant soffit fill crushing was observed. The specimens that exhibited yielding and fracture of the longitudinal dowels demonstrated that extending the longitudinal dowels for a length of 24db into the CFST column and welding them to the steel tube using a flare bevel groove weld will assure good performance, good distribution of stress to the steel, and prevent damage to the tube. The influence of several parameters on the WD connection are noted below.

- De-bonding the longitudinal dowel in the connection region increases deformation capacity and significantly decreases damage to the cap beam.

- Providing transverse steel in the connection region with at least one hoop through the thickness of the soffit fill increases ductility and decreases cap beam damage by providing additional confinement in the joint region.

The WD connection in its current form has several disadvantages in terms of optimizing the objectives of accelerated bridge construction and decreasing labor. After the column is cast, precast super-structure elements must be supported using temporary shoring or a friction collar until the void can be grouted. Using individual ducts in place of a large corrugated pipe can potentially solve this issue (while significantly decreasing construction tolerances), however using individual ducts was not evaluated in the testing program described in this report. Furthermore, dowels must be welded to the inside of the steel tube which requires skilled labor and additional time. Further, the welds are well inside the tube, and this increases the difficulty of welding and inspection of the welds. As these welds provide the primary load transfer from the steel tube into the connection dowels, they should be inspected according to requirements for fracture critical welds. As a final point, transverse reinforcing must be placed around the dowels before they are inserted into the cap beam, which requires additional labor.

The WD connection offers the same challenges encountered with traditional RC columns in terms of post-event inspection and repair. The longitudinal dowels are encased in concrete and grout, which makes it difficult to determine the damage state of the connection. This also increases the difficulty of developing repair strategies for this connection type. Further, significant damage to the concrete in the soffit fill is expected, while the concrete within the tube remains in very good condition.

10.1.3 Reinforced Concrete Connection

The RC connection utilizes both longitudinal and transverse reinforcing to transfer forces from the CFST column into the cap beam. A traditional reinforcing cage is extended from the CFST column into the cap beam, and cover is provided between the reinforcing cage and steel tube within the column. A gap is left between the steel tube and cap beam to permit development of the dowel bars. Tensile forces in the bars are developed by bond transfer between the bars and the concrete, shear stress and strain within the concrete, and ultimately bond stress transfer between the concrete fill and the steel tube. The concrete fill is very well confined by the steel tube to facilitate this transfer.

Experimental results demonstrated that the RC connection exhibits stiffness and strength significantly lower than the stiffness and strength of the CFST component, because the stiffness and strength of the RC connection is controlled both by the effective longitudinal reinforcing ratio in the connection region and the reduced moment arm. Failure of this connection was characterized by yielding and fracture of the longitudinal reinforcing in the gap between the steel tube and cap beam. Significant grout crushing was also observed in this region. As only one specimen which used the RC connection was tested, there is currently no basis to report the influence of any parameters on the behavior of this connection type.

The RC connection has many disadvantages in terms of optimizing the objectives of accelerated construction and decreasing labor. A flexible reinforcing cage must be constructed and temporarily supported within the steel tube. After the column is cast, precast super-structure elements must be supported using temporary showing or a friction collar until the void can be grouted. Similar to the WD connection, using individual ducts in place of a large corrugated pipe can potentially solve this issue (while decreasing construction tolerances), however this configuration was not evaluated in this testing program.

The RC connection offers the same challenges encountered with traditional RC columns in terms of post-event inspection and repair. The longitudinal dowels are encased in concrete and grout, which makes it difficult to determine the damage state of the connection. This also increases the difficult of developing repair strategies for this connection type.

10.2 Dynamic Response and Collapse Potential of RC and CFST Bridges Subjected to Lateral Loading

Advanced performance based earthquake engineering (PBEE) tools were used to compare the seismic performance of an RC and CFST bridge, including fragility functions, nonlinear analysis methods that capture the full cyclic response of the structural system, and incremental dynamic analyses (IDAs) to evaluate repair state and collapse potential. The process for the comparison was as follows: (1) non-linear fiber element models were developed using the structural analysis software OpenSees and numerical results were compared using experimental data, (2) a prototype scale bridge was designed using RC and CFST columns, with the objective of having the same strength and stiffness, (3) the structures were subjected to a suite FEMA P695 motions scaled to represent serviceability (10% probability of exceedance in 50 years), design (7% probability of exceedance in 75 years), and maximum considered (2% probability of exceedance in 50 years) seismic hazard levels(this is referred to as a /textitMultiple Hazard Analysis here), (4) fragility curves were used to compare the performance of the bridge including damage state as well as maximum and residual drift, and (5) IDAs were conducted to compare the repair state and collapse probabilities.

The RC and CFST structures performed well in the multiple hazard and IDA evaluations, however the performance of the CFST structure exceeded that of the RC structure for all metrics evaluated. The CFST structure exhibited lower maximum and residual drifts for all hazards in the multiple hazard analysis. Further, maximum drifts in the CFST structure remained below the threshold which would require post-event repair for all hazards, while the RC structure exceeded the threshold for severe concrete spalling in 6/39 motions for the 2/50 hazard level.

Performance of the RC and CFST structures in the IDA was evaluated based on lognormal CDFs developed for *Repair*, *Partial Replace*, and *Collapse* limit states. These limit states were quantified in terms of the design spectral acceleration by evaluating the Repair Margin Ratio (RMR), Partial Replace Margin Ratio (PRMR), and Collapse Margin Ratio (CMR) which are defined as the median spectral acceleration for the given limit state divided by the design spectral acceleration. The RC and CFST structures performed well in terms of the RMR, PRMR, and CMR, as all of the recorded values were well above 1. The CFST structure exhibited significantly larger PRMR and CMR than the RC structure, suggesting the post event repair effort on the CFST bridge would be less than that required for the RC bridge. The advantages of the CFST structure were further highlighted by the lognormal CDF curves developed for each limit state, which indicate higher probabilities of repair, partial replacement, and collapse of the RC structure for lower spectral accelerations.

10.3 Recommended Future Research

Additional research should be conducted to (1) further refine the design expressions proposed here, (2) expand the number of connections types, (3) evaluate the response of CFST components and connections to combined torsion/shear/flexure/axial loading, (4) develop repair strategies for CFST, and (5) expand the system level modeling to include evaluation of multi-hazard scenarios. Thus, five primary areas of future work are recommended:

1. Utilize detailed finite element models developed for the initial connection evaluation to conduct extensive parameter studies on the proposed connections.

2. Develop additional connections such that CFSTs are more versatile for bridge construction including CFST-to-pile and multiple pile cap connections.

3. CFSTs should have larger torsional strength and deformability relative to RC columns. A research program aimed at evaluating the response of CFST columns and connections subjected to combined torsional, shear, flexure and axial loading is needed. In addition this program should develop a connection capable of transferring torsion to the superstructure for skewed bridges.

4. Evaluate repair strategies for CFST columns which have been moderately damaged following lateral loading events. The damage state of the ER connection can be readily identified based on the condition of the steel tube in the connection region; the concrete in the tube is generally in pristine condition. In addition, the accessibility to the steel tube (which acts as the primary longitudinal reinforcing) provides a unique opportunity for repair which will be more difficult in dowel or RC type connections in which extensive spalling and concrete damage are noted, and the longitudinal steel is embedded in the column concrete.

5. Perform dynamic analyses and develop CDFs which account for uncertainties in structural design requirements, test data, and modeling as well as ground motion-to-motion record uncertainties.

6. Evaluate and compare the performance of RC and CFST structures subjected to a sequential multi-hazard consisting of a seismic event followed by a tsunami impact load. In recent years, earthquakes and subsequent tsunamis impacts on coastal communities have resulted in significant loss of life and damage to infrastructure systems. The impact of the ground shaking and tsunami damage was greatly

exacerbated by the failure of the transportation infrastructure systems in these regions, which delayed emergency services, hampered recovery efforts, and had significant long-term impacts on local economies. CFST columns provide larger strength and stiffness than comparable RC columns, and therefore offer a possible solution for the sequential multi-hazard scenario.

BIBLIOGRAPHY

A. Gomes, J. A. (1997). Nonlinear cyclic stress-strain relationship of reinforcing bars including buckling. *Engineering Structures*, 19(10):822–826.

A. Mehrsoroush, M. S. S. (2014). Experimental and analytical seismic studies of bridge piers with innovative pipe pin column footing connections and precast ben caps. Technical Report UNR/CCEER 14-07, University of Nevada Reno.

AASHTOa (2015). *AASHTO LRFD Bridge Design Specification*. American Association of State Highway and Transportation Official, Washington, DC.

AASHTOb (2011). *AASHTO Guide Specificaitons for LRFD Seismic Bridge Design*. American Association of State Highway and Transportation Official, Washington, DC, 2 edition.

ACI (2011). *Building Code Requirements for Structural Concrete*. American Concrete Institute, Farmington Hills, MI.

AISC (2011). *Steel Construction Manual*. American Institute of Steel Construction, Chicago, IL, 14 edition.

ASCE (2013). *Seismic Evaluation and Retrofit of Existing Buildings*. American Society of Civil Engineers, Reston, VA.

ATC-24 (1992). *Guidelines for Testing Steel Components*. Applied Technology Council, Redwood City, CA.

AWS (2010). *Structural Welding Code - Reinforcing Steel*. American Welding Society, Miami, FL.

Baker, J. (2014). Efficient analytical fragility function fitting using dynamic structural analysis. Technical Note.

Berry, M. (2006). *Experimental Calibration of OpenSees Components Using the PEER Column Database*. PhD thesis, University of Washington.

Bishop, E. (2009). Evaluation of the flexural resistance and stiffness models for circular concrete-filled steel tube members subjected to combined axial-flexural loading. Master's thesis, University of Washington.

Boyd, P., Cofer, W., and Mclean, D. (1995). Seismic performance of steel-encased concrete columns under flexural loading. *ACI Structural Journal*, 92(3):355–364.

Caltrans (2010). *Caltrans Seismic Design Criteria*. California Department of Transportation, Sacramento, CA.

Culmo, M. (2011). *Acclerated Bridge Construction - Experience in Design, Fabrication, and Erection of Prefabricated Bridge Elements and Systems*. Federal Highway Administration, McLean, VA.

D.E. Lehman, J. M. (2000). Seismic performance of well-confined concrete bridge columns. Technical Report 1998/01, Pacific Earthquake Engineering Research-Center.

Elchalakani, M., Zhao, X., and Grzebieta, R. (2001). Concrete-filled circular steel tubes subjected to pure bending. *Journal of Constructional Research*, 57:1141–1168.

Elremaily, A. and Azizinamini, A. (2002). Behavior and strength of circular steel tubes subjected to pure bending. *Journal of Constructional Research*, 8:1567–1591.

F.E Richart, A. Brandzaeg, R. B. (1929). The failure of plain and spirally reinforced columns in compression. Bulletin No. 190, University of Illinois Engineering Experimental Station.

Fujimoto, T., Mukai, A., Nishiyama, I., and Sakino, K. (2004). Behavior of eccentrically-loaded concrete-filled steel tubular columns. *Journal of Structural Engineering*, 130(2):203–212.

Furlong, R. (1967). Strength of steel-encased concrete beam columns. *Journal of The Structural Division*, 93(ST5):113–124.

Goode, C. and Lam, D. (2008). Concrete-filled tube columns - tests compared with eurocode 4. In *Engineering Foundation Conference*, Devils Thumb Ranch, CO.

Han, L., Lu, H., Yao, G., and Liao, F. (2006). Further study on the flexural behaviour of concrete-filled steel tubes. *Journal of Constructional Steel Research*, 62:554–565.

Haraldsson, O., James, T., Eberhard, M., and Stanton, J. (2012a). Laboratory tests of column-to-footing socket connections. Technical report, U.S. Department of Transportation, Federal Highway Administration.

Haraldsson, O., James, T., Eberhard, M., and Stanton, J. (2012b). Seismic resistance of socket connections between footing and precast column. *Journal of Bridge Engineering*.

Hitaka, T., Suita, K., and Kato, M. (2003). Cfst column base design and practice in japan. Technical Report NCREE-0.-0.26, National Center for Research in Earthquake Engineering.

Hsu, T. and Mo, Y. (2010). *Unified Theory of Concrete Structures*. John Wiley and Sons, Inc., 2 edition.

J. Brown, S. K. (2000). Low cycle fatigue behavior of longitudinal reinforcement in reinforced concrete bridge columns. Technical Report 00-0007, NCEER.

Janes, T. (2011). Precast column socket connections for thin spread footings. Master's thesis, University of Washington.

J.B. Mander, M.J.N. Priestley, R. P. (1988). Theoretical stress-strain model for confined concrete. *Journal of Journal of Structural Engineering*, 114(8):1804–1826.

Jellen, A. (2008). Improved seismic connections for pile-wharf construction. Master's thesis, University of Washington.

JRA (2012). *Specifications for Highway Bridges*. Japan Roads Association, Tokyo, Japan.

Kadoya, H., Kawaguchi, J., and Morino, S. (2004). Experimental study on strength and stiffness of bare type cft columns base with central reinforcing bars. In of Civil Engineers, A. S., editor, *Composite Construction in Steel and Concrete V; Proceedings of the 5th Internation Conference*, pages 18–23, Reston, Virginia. United Engineering Foundation.

Kappes, L., Berry, M., and Stephens, J. (2013). Performance of steel pipe pile-to-concrete cap connections subjected to seismic or high transverse loading. Technical Report FHWA/MT-13-001/8203, Montana Department of Transportation.

Kappes, L., Berry, M., Stephens, J., and McKittrick, L. (2012). Concrete filled steel tube piles to concrete pile-cap connections. In ASCE, editor, *Proceedings from the 2012 Structures Congress*, Washington, D.C.

Kawaguchi, J. and Morino, S. (2006). Experimental study on strength and stiffness of bare type cft column base with central reinforcing bars. *Composite Construction in Steel and Concrete V*.

Kingsley, A. (2005). Experimental and analytical investigation of embedded column base connections for concrete filled high strength steel tubes. Master's thesis, University of Washington.

Lee, J. (2011). Experimental investigation of embedded connections for concrete-filled steel tube columns subjected to combined axial-flexural loading. Master's thesis, University of Washington.

Lee, J. and Fenves, G. (1998). Platic-damage modeling for cyclic loading of concrete structures. *Journal of Engineering Mechanics*, 124(8):892–900.

Lehman, D. and Roeder, C. (2012a). Foundation connection for circular concrete filled tubes. *Journal of Constructional Steel Research*, 78:212–225.

Lehman, D. and Roeder, C. (2012b). Rapid construction of bridge piers with improved seismic performance: An initial study in the use of concrete filled steel tubes for bridge piers and foundation connections. Technical Report CA12-1972, California Department of Transportation.

Marson, J. and Bruneau, M. (2004). Cyclic testing of concrete-filled circular steel bridge piers having encased fixed-base detail. *ASCE Journal of Bridge Engineering*, 9(1):14–23.

Matsumoto, E. (2009). Emulative precast bent cap connections for seismic regions: Grouted duct and cap pocket test results: Grouted duct and cap pocket test results, design and construction specifications, design examples, and connection details. Technical Report ECS-CSUS-2009-05, Sacramento State University.

M.D. Denavit, J. H. (2010). Nonlinear seismic analysis of circular concrete-filled steel tube members and frames. Technical Report NSEL-023, NSEL.

Montejo, L., Gonzalez-Roman, L. A., and Kowalsky, M. (2013). Seismic performance evaluation of reinforced concrete-filled steel tube pile/column bridge bents. *Journal of Earthquake Engineering*, 16(3):401–424.

Montejo, L., Kowalsky, M., and Hassan, T. (2009). Seismic behavior of flexural dominated reinfored concrete bridge columns at low temperatures. *Journal of Cold Regions Engineering*, 23:18–42.

Moon, J., Lehman, D., Roeder, C., and Lee, H. (2013). Strength of circular concrete-filled tubes with and without internal reinforcement under combined loading. *Journal of Journal of Structural Engineering*, 139(12).

Morino, S., Kawaguchi, J., Tsuji, A., and Kadoya, H. (2003). Strength and stiffness of cfst semi-embedded type column base. In *Proceedings of ASSCCA 2003*, Sydney, Australia.

Morino, S., Sakino, K., Mukai, A., and Yoshioka, K. (1997). Experimental studies of cft column systems - u.s.-japan cooperative research. *ASCE*, pages 1106–1110.

M.P. Berry, M. E. (2003). Performance models for flexural damage in reinforced concrete columns. Technical Report 2003/18, Pacific Earthquake Engineering Research-Center.

M.P. Berry, M. E. (2005). Practical performance model for bar buckling. *Journal of Structural Engineering*, 131(7):1060–1070.

Nocedal, J. and Wright, S. (2006). *Numerical Optimization*. Springer, 2 edition.

O'Shea, M. and Bridge, R. (1997). Design of circular thin-walled concrete filled steel tubes. *Journal of Structural Engineering*, 126(11):1295–1303.

Pang, J., Eberhard, M., and Stanton, J. (2010). Large-bar connection for precast bridge bents in seismic regions. *Journal of Bridge Engineering*, pages 231–239.

Pang, J., Steuck, K., Cohagen, L., Stanton, J., and Eberhard, M. (2008). Rapidly constructable large-bar precast bridge-bent seismic connections. Technical Report WA-RD 684.2, Washington State Department of Transportation.

Prion, H. and Boehme, J. (1997). Beam-column behaviour of steel tubes filled with high strength concrete. *Canadian Journal of Civil Engineering*, 21:207–218.

Rahai, A. (2004). Effect of earthquake vertical motion on rc bridge piers. In *Proceedings from the 13th World Conference on Earthquake Engineering*, Vancouver B.C.

Ranf, R. T. (2007). *Model Selection for Performance Based Earthquake Engieering of Bridges*. PhD thesis, University of Washington.

Raynor, D., Lehman, D., and Stanton, J. (2002). Bond-slip response of reinforcing bars grouted in ducts. *ACI Structural Journal*, 99(5):568–576.

Restrepo, J., Tobolski, M., and Matsumoto, E. (2011). Development of a Precast Bent Cap System for Seismic Regions. Technical Report 681, NCHRP.

Roeder, C., Lehman, D., and Bishop, E. (2010). Strength and stiffness of circular concrete filled tubes. *Journal of Structural Engineering*, 135(12):1545–1553.

Roeder, C., Lehman, D., and Stephens, M. (2014). Concrete filled tubes for accelerated bridge construction. In *Transportation Research Record*, Washington, D.C.

Saenz, L. (1964). Discussion of equation for the stress-strain curve of concrete. *ACI Journal*, 61:12229–1235.

Simulia (2015). *Abaqus Users Manual*. Dassault Systems, Providence, RI.

Stephens, M., Lehman, D., and Roeder, C. (2015). Concrete filled tube bridge pier connections for accelerated bridge construction. Technical Report CA15-2417, California Department of Transportation.

Stringer, S. (2010). Seismic performance of improved damage resistant pile to wharf deck connections. Master's thesis, University of Washington.

Stueck, J., Eberhard, M., and Stanton, J. (2009). Anchorage of large diameter reinforcing bars in ducts. *ACI Structural Journal*, pages 506–513.

Stueck, K., Eberhard, M., and Stanton, J. (2007). Anchorage of large bars in grouted ducts. Technical Report WA-RD 684.1, Washington State Department of Transportation.

Terzic, V. (2011). Force-based element vs. displacement based element. Presentation at UC Berkeley.

Thody, R. (2006). Experimental investigation of the flexural properties of high-strength concrete-filled steel tubes. Master's thesis, University of Washington.

Tran, H., Eberhard, M., and Stanton, J. (2012). Seismic-resistant connections between precast concrete columns and drilled shafts. Technical report, TRANSNOW.

Wheeler, A. and Bridge, R. (2006). The behavior of circular concrete-filled thin-walled steel tubes in flexure. In *Proceedings of the 5th International Conference on Composite Construction in Steel*, pages 412–423.

Williams, T. (2006). Experimental investigation of high strength concrete filled steel tubes in embedded column base foundation connections. Master's thesis, University of Washington.

Z.F. Alemdar, A. Matamoros, J. B. (2011). Modeling surface deformations and hinging regions in reinforced concrete bridge columns. Technical Report SL 11-2, Kansas University.

Zhang, G., Xiao, Y., and Kunnath, S. (2009). Low-cycle fatigue damage of circular concrete-filled tube columns. *ACI Structural Journal*, 106(2):151–159.

Appendix A

DESIGN EXAMPLES

A.1 ER Connection

A detailed design example is presented here to demonstrate the design of a CFST bridge column and ER connection to facilitate implementation into seismic bridge design practice. The example is a redesign of a conventional reinforced concrete bridge column and cap beam connection using the Laguna De Santa Rosa Bridge (located outside of Santa Rosa, California) as a prototype structure (details illustrated in Fig. 4.1 and 7.8). The design procedure is broken down into two primary components: (1) Design of the CFST component using recommendations in AASHTOa [2015], and (2) Design of the ER connection and cap beam using the recommendations presented herein. The design procedure is as follows.

Design of CFST Component

The first step was to redesign the RC columns as CFST columns. The columns were designed using the following procedure highlighted in the flow chart in Fig. reffig:CFSTComponentFlowChart. Note that the material properties used for design of the CFST columns are provided in Table A.1.

1. Determine Factored Loads ($P_u, M_u, andV_u$)

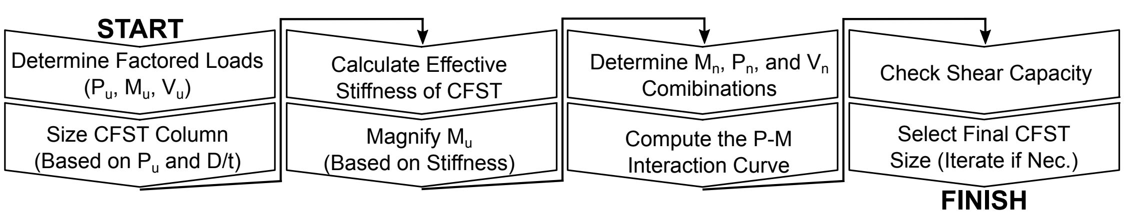

Figure A.1: Flow Chart for Design of CFST Component

Table A.1: Nominal Material Properties for Design of CFST Columns

f'_c	E_c	$F_{y,st}$	$F_{u,st}$	E_s
6-ksi	4415-ksi	50-ksi	60-ksi	29000-ksi

The following loads were provided by the California Department of Transportation.

$Service \longrightarrow P_u = 790 - kip, M_u = 1920kip - ft, V_u = 256 - kip$

$ControllingLimitStateLoad \longrightarrow P_u = 1300 - kip, M_u = 5300kip - ft, V_u = 707 - kip$

2. Size Initial CFST Column Based on Service Axial Load Range

The initial section is designed to have an axial load in the range of $0.1P_o - 0.2P_o$ where

$P_o = \pi DtF_{y,st} + 0.95(D^2/4)\pi f'_c$

Using a target $D/t = 90 \longrightarrow t = 90/D$

Solving for D (with an assumed service load of $0.1P_o$):

$10(790/0.75) = 10(1053.33) = \pi D(D/90)50 + 0.95(D^2/4)\pi 6 \longrightarrow D = 41.145$

Try $D = 44 - in., t = 0.5 - in., D/t = 88$

3. Calculate the Stiffness of the CFST Component

The effective stiffness is calculated using Equation 6.9.6.3.2-6 from AASHTOa [2015].

$EI_{eff} = E_sI_{st} + C'E_cI_c$

$\longrightarrow I_{st} = 16726 - in.^4$

$\longrightarrow I_c = 183984 - in.^4$

$\longrightarrow A_{st} = 69 - in.^2$

$\longrightarrow A_c = 1486 - in.^2$

$\longrightarrow C' = 0.15 + P/P_o + A_{st}/(A_{st} + A_c) = 0.15 + 1300/11700 + 68.72/(68.72 + 1486.17) = 0.305$

$EI_{eff} = 29000 \times 16726 + 0.305 \times 4415 \times 183984 = 7.33 \times 10^8 kip - in^2$

4. Calculate the Moment Magnification Factor and Magnify the Moment

$\delta_s = 1/(1 - P_u/(\phi P_e))$

$\longrightarrow P_e = \pi^2 EI_{eff}/(KL)^2 = \pi^2 \times 7.33 \times 10^8/(0.5 \times 15 \times 12)^2 = 893138 - kip)$

$\delta_s = 1/(1 - 1300/(0.9 \times 893138)) = 1$

5. Determine the P_n, M_n, V_n Combinations for Each Load Case

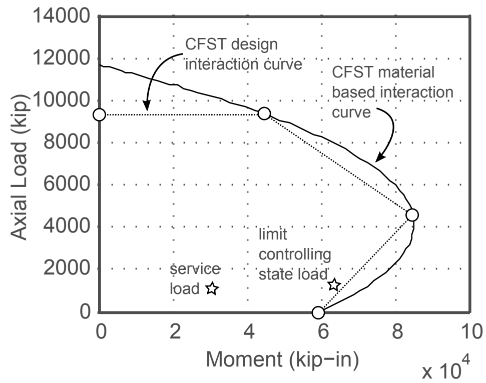

Figure A.2: P-M Interaction Curve for CFST Component

$ServiceLoads \longrightarrow P_n = P_u/\phi = 790/0.75 = 1053 - kip, M_n = M_u/\phi = 1920kip - ft/0.75 = 2560kip - ft, V_n = V_u/\phi = 256/0.9 = 285 - kip$

$ControllingLimitStateLoad(Seismic) \longrightarrow P_n = P_u/\phi = 1300/1.0 = 1300 - kip, M_n = M_u/\phi = 5300kip - ft/1.0 = 5300kip - ft, V_n = V_u/\phi = 707/1.0 = 707 - kip$

6. Compute P-M Interaction Diagram for CFST Component

The P-M interaction diagram was computed using the procedure specified in AASHTOa [2015]. First, the material based interaction surface was developed using the PSDM (as discussed in Chapter 2). Then, the influence of geometric nonlinearity was considered to develop the design interaction diagram. The interaction diagram and demands are illustrated in Fig. A.2. The CFST component has adequate capacity to sustain the combined loading combination, and the axial loads are in the range of 10% of the crushing load.

7. Calculate the Shear Strength of the CFST Component

The shear strength of the section is computed assuming that only the steel tube contributes to the strength. The following shear strength expression has been adopted from the AISC steel construction manual [AISC, 2011]. The shear capacity of the CFST component is greater than the controlling limit state shear demand.

$V_n = 0.6F_{y,st}A_v$

$\longrightarrow A_v = 0.5A_{st} = 0.5 \times 68.72 = 34.36 - in.^2$

$V_n = 0.6 \times 50 \times 34.36 = 1031 - kip > V_u/\phi = 785 - kip$

8. Select Final Size of CFST Component

Use D=44-in., t=0.5-in., D/t=88

Note that the final diameter of the CFST columns are less than that of the original RC columns, while, stiffness and strength of the CFSTs are greater than that of the RC sections as indicated in Table 7.2.

Design of ER Connection

Design of the ER CFST column-to-cap beam connection is demonstrated in this section. The procedure for designing this connection is summarized in the flow chart in Fig. 5.31. The final design, including reinforcing steel details, is illustrated in Fig. 7.8. Note that a similar design process is used for an ER moment resisting foundation connection. Note that the purpose of this example is to highlight the design requirements specific to the ER connection. Therefore corbel reinforcing and side reinforcing, which are consistent with requirements in [AASHTOa, 2015], are not included in the example.

1. Size the Annular Ring

The annular ring is the same thickness and the same steel properties as the steel tube. The ring projects into and out of the tube for a distance of 8t, where t is the thickness of the steel tube. For the example column, the outer, D_o, and inner, D_i, diameters of the ring are calculated as:

$D_o = D + 16t = 44 + 16 \times 0.5 = 52 - in.$

$D_i = D - st - 16t = 44 - 2 \times 0.5 - 16 \times 13 = 25 - in.$

Use an annular ring with $D_o = 52 - in.$ **and** $D_i = 25 - in.$

2. Design the Weld Between the Annular Ring and Tube

The weld between the steel tube and annular ring is calculated using Equation 5.4 assuming a weld metal strength of 70-ksi, which is greater than the yield strength of the tube.

$w \geq \frac{1.31 F_{u,st} t}{F_{exx}} \geq \frac{1.31 \times 60 \times 0.5}{70} = 0.57 - in.$

Use 0.625-in. fillet welds

Note: CJP welds can also be used.

3. Calculate the Required Embedment Depth

Calculate the required tube embedment depth into the cap using Equation 5.5 in this document.

$L_e \geq \sqrt{\frac{D^2}{4} + \frac{DtF_u}{6\sqrt{f'_{c,cap}}}} - \frac{D}{2} = \sqrt{\frac{44^2}{4} + \frac{44 \times 0.5 \times 60000}{6\sqrt{6000}}} - \frac{44}{2} = 33.5 - in.$

Use $L_e = 33.5 - in.$

4. Calculate the Required Depth Above the Embedded Tube to Eliminate Punching Shear

Calculate the required depth above the embedded tube using Equation 3. The required depth above the embedded tube is calculated for two load cases; first to size the inverted-t, and second to determine the total required depth of the superstructure above the embedded to resist the controlling limit state load.

For the purpose of sizing the inverted-t, the depth above the embedded tube is calculated to resist punching shear failure during construction prior to grouting the connection. This calculation is made according to ACI requirements for punching shear conservatively assuming one-way shear.

Assumed construction dead load = 55-kip based on the as-built drawings of the precast components in the prototype structure.

$\phi V_c = \phi 0.17\sqrt{f'_c} b_o d$

$\longrightarrow b_o = \pi(D_o + d) = \pi(52 + d)$

$\frac{55000}{0.75} = 2\sqrt{6000}\pi(52 + d)d \longrightarrow d = 2.75 - in.$

Next, calculate the total required depth (deck and inverted-t) above the embedded CFST to eliminate the potential for punching shear failure during seismic loading. Note that C_c and C_s are in kips (reference Fig. 5.33)

$L_p c = \sqrt{\frac{D^2}{4} + \frac{C_c + C_s}{6\sqrt{f'_{c,cap}}}} - \frac{D}{2} - L_e = \sqrt{\frac{44^2}{4} + \frac{2000000}{6\sqrt{6000}}} - \frac{44}{2} - 33.5 = 13.3 - in. forcontrollingstateload$

5. Size the Initial Depth of the Cap Beam Based on Steps 3 and 4

The inverted-t requires a depth above the tube of 2.75-in. for construction loads, while the total required depth is 11.5-in. for seismic loading. Assuming a deck depth of around 8-in. this allows 3.5-in. of depth above the embedded CFST in the inverted-T beam. Allowing additional space for reinforcing in the cap beam, a depth above the embedded CFST of 8.5 in. is selected.

Use a total depth of $Hcap = Le + Lpc = 42 - in.$ for the precast inverted-t.

The width of the stem in the inverted-T beam is selected based on the diameter of the corrugated pipe (assuming modular construction method). The inner diameter of the corrugated pipe must exceed Do (which was calculated in Step 1). Galvanized corrugated pipe with an inner diameter of 54 in. is commercially available. Thus the width of the stem of the inverted-T beam must exceed this diameter with standard cover requirements.

Use a stem width of 60-in.

6. Capacity Design the Cap Beam to Resist $1.25M_p$ of the CFST Column

The plastic capacity of the CFST column is $1.25M_{p,CFST} = 85000kip - in.$. A ledge width of 22-in. is assumed based on the dimensions of the prototype bridge. 20 No. 10 bars in the bottom of the inverted-t and 12 No. 10 bars in the top of the inverted-t are initially tried. Additional cap beam reinforcing consisting of 14 No. 10 bars is included in the deck. The primary flexural reinforcing is arranged as shown in Fig. 7.8. The resulting flexural capacity of the cap beam are calculated as:

$M_n^+ = 7199kip - ft$

$M_n^- = 7133kip - ft$

Use 20 No. 10 bars in the bottom of the inverted-t and 12 No. 10 bars in the top of the inverted-t. Include 14 No. 10 bars in the deck for additional negative moment capacity.

7a. Design Vertical Stirrups in the Joint Region

The required shear reinforcing in the joint region is calculated using the simplified expression in Equation 5.7 in this document. This reinforcing must be evenly distributed in the area hatched in Fig. 5.35b. The distribution of vertical shear reinforcing in the final design in this example is illustrated in Fig. 7.8.

$A_s^{jv} = 0.65A_{st} = 0.65 \times 68.72$

Use 100 No. 6 vertical stirrup legs evenly distributed around the column $\longrightarrow A_s^{jv} = 44 - in^2$

7b. Design Horizontal Stirrups in Joint Region

The required area of horizontal stirrups is consistent with the requirements in the Caltrans SDC. One layer of horizontal stirrups must pass above the embedded CFST as shown in Fig. 7.8.

$A_s^{jh} = 0.1A_{st} = 0.1 \times 0.1 \times 68.72 = 6.872 - in.^2$

Use 3 rows of No. 7 hooks $\longrightarrow A_s^{jh} = 7.2 - in.^2$

A.2 WD Connection

A detailed design example is presented here to demonstrate the design of a CFST bridge column and WD connection to facilitate implementation into seismic bridge design practice. The example is a redesign of a conventional reinforced concrete bridge column and cap beam connection using the Laguna De Santa Rosa Bridge (located outside of Santa Rosa, California) as a prototype structure (details illustrated in Fig. 4.1 and 7.8). The design procedure is broken down into two primary components: (1) Design of the CFST component and longitudinal dowels in the connection region using recommendations in AASHTOa [2015], and (2) Design of the WD connection and cap beam using the recommendations presented herein. The design procedure is as follows.

Design of CFST Component and Dowels in Connection Region

The first step was to redesign the RC columns as CFST columns. The columns were designed using the procedure highlighted in the ER connection design example above. The final CFST column had $D = 44 - in., t = 0.5 - in., D/t = 88$

1. Design of CFST Dowels in the Connection Region

The dowels in the connection region are designed to resist the applied loads. Based on the service and controlling limit state loads (provided in the previous example) assume 32 No. 11 dowels. Note that the dowel yield and rupture strengths are assumed to be 68-ksi and 98-ksi respectively.

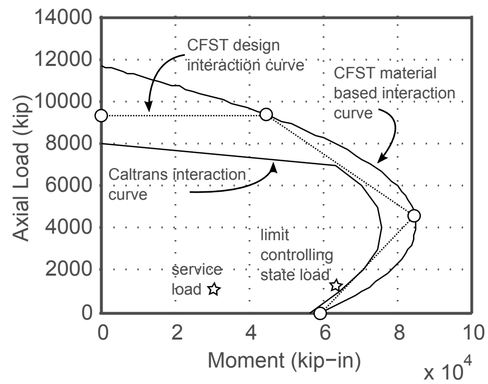

Figure A.3: P-M Interaction Curve for CFST Component and WD Connection

2. Check Crushing Capacity of CFST Connection

Check to ensure that the service axial load is approximately 10% of the crushing load of the WD connection.

$\frac{P_u}{P_o} \leq 0.1$

$\longrightarrow P_u = 790 - kip$

$\longrightarrow P_o = A_{st,b} + F_y + 0.85(D^2/4)\pi f_c' = 49.92 \times 68 + 0.85 \times (43^2/4) \times \pi \times 6 = 10800 - kip$

$\frac{790}{10800} = 0.07 \leq 0.1$ **OK!**

3. Calculate the Effective Stiffness of the WD Connection

$EI_{eff} = 4.09 \times 10^8 kip - in^2$ (from structural analysis program)

4. Calculate the Moment Magnification Factor

$\delta_s = 1/(1 - P_u/(\phi P_e))$

$\longrightarrow P_e = \pi^2 EI_{eff}/(KL)^2 = \pi^2 \times 4.09 \times 10^8/(0.5 \times 15 \times 12)^2 = 498354 - kip)$

$\delta_s = 1/(1 - 1300/(0.9 \times 498354)) = 1$

5. Compute P-M Interaction Diagrams for CFST and WD Connection

Development of the P-M interaction curve for the CFST component is discussed in the previous example. The P-M interaction diagrams for the CFST and WD connection are plotted in Fig. A.3. The interaction curve for the WD connection was calculated using Caltrans requirements for RC columns [Caltrans, 2010].

Design WD Connection

Design of the WD CFST column-to-cap beam connection is demonstrated in this section. The procedure for designing this connection is summarized in the flow chart in Fig. 6.21. The final design, including reinforcing steel details, is illustrated in Fig. 7.8. Note that the purpose of this example is to highlight the design requirements specific to the WD connection. Therefore corbel reinforcing and side reinforcing, which are consistent with requirements in [AASHTOa, 2015], are not included in the example.

1. Size Flange

$D_o = D + 16t = 44 + 16 \times 0.5 = 52 - in.$

Use a flange with $D_o = 52 - in.$**.**

2. Design Weld Between Flange and Tube

$w \geq \frac{1.31 F_{u,st} t}{F_{exx}} \geq \frac{1.31 \times 60 \times 0.5}{70} = 0.57 - in.$

Use 0.625-in. fillet welds

3. Calculate Length Dowel Extends into CFST

The dowels are required to extend into the steel tube for a distance of $24d_b$.

$24d_b = 24 \times (11/8) = 33 - in.$

Extend the dowels $33 - in.$ **into the steel tube.**

4. Design Weld Between Dowel and Tube

The weld length is the greatest of Equations 6.7 through 6.9 in this document. Assume 70XX electrodes with a tensile strength of 70-ksi.

$L_w = \frac{5.6 A_b F_{y,b}}{F_{EXX} d_b} = \frac{5.6 \times 1.56 \times 68}{70 \times 1.375} = 6.17 - in.$

$L_w = \frac{0.83 A_b F_{y,b}}{F_{y,st} t} = \frac{0.83 \times 1.56 \times 68}{50 \times 0.5} = 3.52 - in.$

$L_w = \frac{1.11 A_b F_{y,b}}{F_{u,st} t} = \frac{1.11 \times 1.56 \times 68}{70 \times 0.5} = 3.36 - in.$

Use a weld length $L_w = 6.25 - in.$

5. Calculate Dowel Debonded Length

The debonded length is calculated using Equation 6.6 in this document assuming a target rotation demand of 8% and a steel ultimate strain of 0.09-in./in.

$L_{db} = \frac{tan\theta(D - t - d_b/2)}{0.7\epsilon_u} = \frac{tan(0.08)(44 - 0.5 - 1.375/2)}{0.7 \times 0.09} = 54.5 - in.$

Use a debonded length $L_{db} = 54.5 - in.$

6. Calculate Dowel Embedment Depth into Cap Beam

The dowels are required to extend into the cap beam according to Equations 6.1 through 6.3 in this document.

$L_e \geq \frac{0.016*\psi*F_{y,b}}{\sqrt{f'_g}} = \frac{0.016\times1.0\times68000}{\sqrt{6000}} = 19.31 - in.$

$L_e \geq \sqrt{\frac{D^2}{4} + \frac{1.2F_{y,b}A_{st,b}}{6\pi\sqrt{f'_{c,cap}}}} - D/2 = \sqrt{\frac{44^2}{4} + \frac{1.2\times68000\times49.92}{6\pi\sqrt{6000}}} - 44/2 = 35.2 - in.$

$L_e \geq 3d_b + 0.5L_{db} = 3 \times 1.375 + 0.5 \times 54.5 = 31.375$

Extend the dowels for a distance $L_e = 35.25 - in.$ **into the cap beam.**

7. Calculate Required Punching Shear Depth Above the Headed Dowels

The required depth above the headed reinforcing to eliminate punching shear failure is defined in Section 6.4.1.10 in this document.

$L_{pc} \geq 3d_h = 3 \times 3.25 = 9.75 - in$

Use a depth of at least 9.75-in. above the top of the headed dowels

8. Size the Precast Inverted T

A total super structure depth of at least $L_e + L_{pc}$ is required. Assuming we have an 8-in. thick slab on this bridge, a clear cover above the headed reinforcing of at least 1.75-in. is required in the inverted-t. Use a clear distance of 6.75-in. in the inverted-t in the interest of maintaining the same super-structure depth as Example 1.

The depth of the inverted-t=6.75+35.25=42-in.

Use an inverted-t depth of 42-in.

The width of the stem in the inverted-T beam is selected based on the diameter of the corrugated pipe (assuming modular construction method). The inner diameter of the corrugated pipe must exceed the diameter of the CFST plus one dowel head diameter. Galvanized corrugated pipe with an inner diameter of 54 in. is commercially available. Thus the width of the stem of the inverted-T beam must exceed this diameter with standard cover requirements.

Use a stem width of 60-in.

9. Capacity Design the Cap Beam to Resist $1.2M_{p,WDConnection}$

The plastic capacity of the WD connection is $1.2M_{p,WDConnection} = 79800kip - in.$. A ledge width of 22-in. is assumed based on the dimensions of the prototype bridge. 20 No. 10 bars in the bottom of the inverted-t and 12 No. 10 bars in the top of the inverted-t are initially tried. Additional cap beam reinforcing consisting of 14 No. 10 bars is included in the deck. The primary flexural reinforcing is arranged as shown in Fig. 7.8. The resulting flexural capacity of the cap beam are calculated as:

$M_n^+ = 86382kip - in$

$M_n^- = 85593kip - in$

Use 20 No. 10 bars in the bottom of the inverted-t and 12 No. 10 bars in the top of the inverted-t. Include 14 No. 10 bars in the deck for additional negative moment capacity.

10a. Design Vertical Stirrups in the Joint Region

The required shear reinforcing in the joint region is calculated using Equation 7.19 in Caltrans [2010].

$A_s^{jv} = 0.2A_{st,b} = 0.5 \times 49.92 = 10 - in.^2$

Use No. 6 vertical stirrups arranged as shown in Fig. 7.8.

10b. Design Horizontal Stirrups in the Joint Region

The required area of horizontal stirrups is consistent with the requirements in the Caltrans SDC [Caltrans, 2010]. One layer of horizontal stirrups must pass above the corrugated metal duct as illustrated in Fig. 7.8.

$A_s^{jh} = 0.1A_{st} = 0.1 \times 49.92 = 5 - in.^2$

Use 3 rows of No. 6 hooks as shown in Fig. 7.8.

11. Design Transverse Column Reinforcing which Extends into the Cap Beam

The required transverse reinforcing ratio which extends into the joint region is defined in Equation 7.23 of Caltrans [2010].

$\rho_s = 0.4\frac{A_{st,b}}{L_e^2} = 0.4\frac{49.92}{35.25^2} = 0.016$

Try No. 9 hoops at 3-in. c-c $\longrightarrow \rho_s = 0.016$

Use No. 9 hoops at 3-in. c-c.

Appendix B

SPECIMEN REINFORCING DETAILS

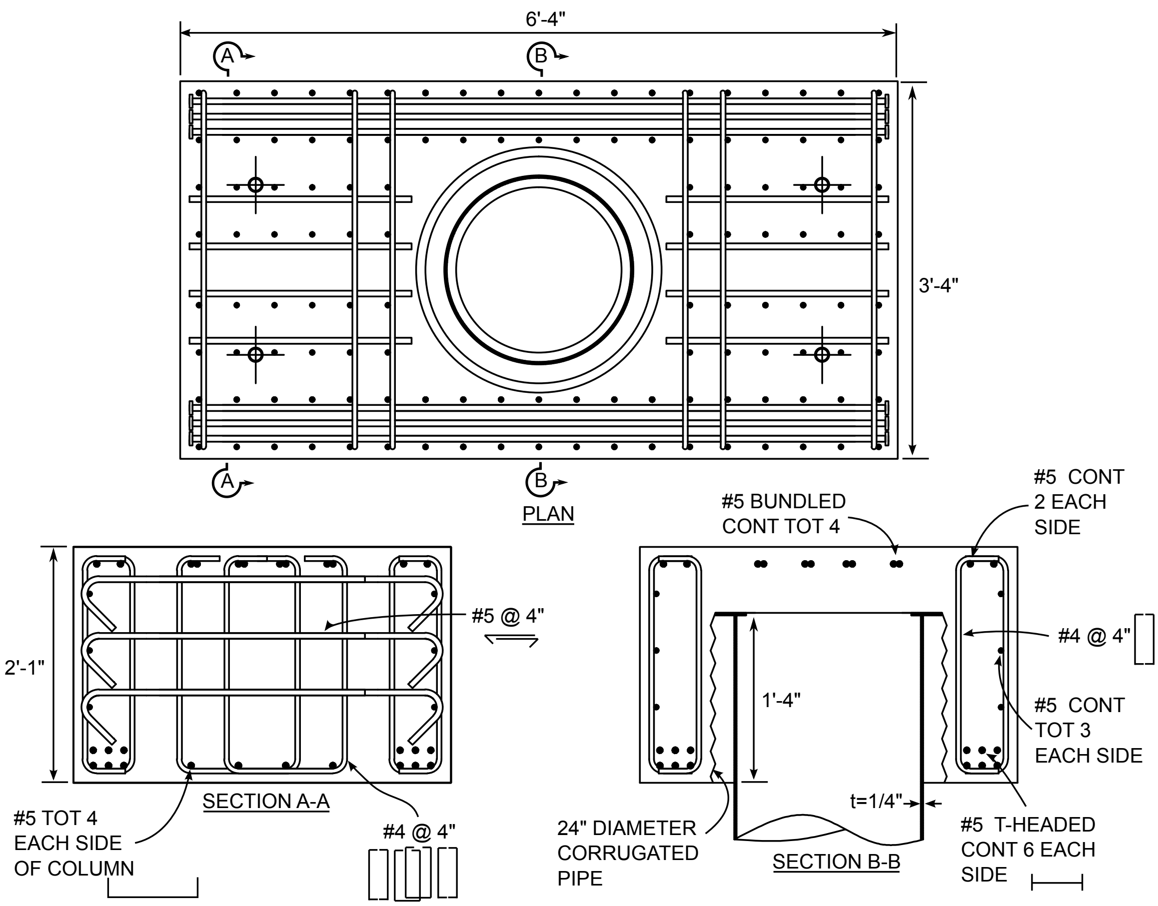

Figure B.1: ER80T Reinforcing Details

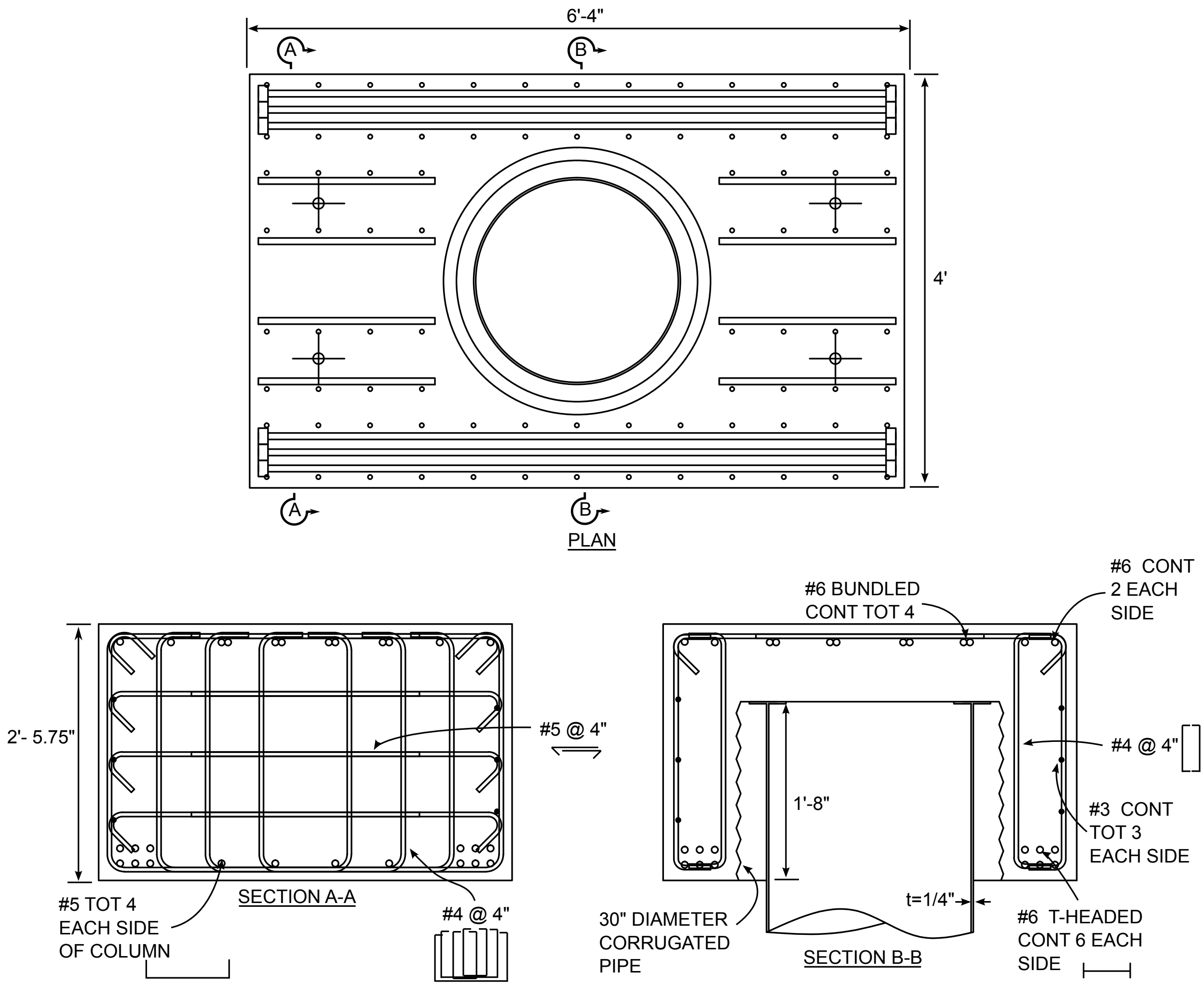

Figure B.2: ER96T Reinforcing Details

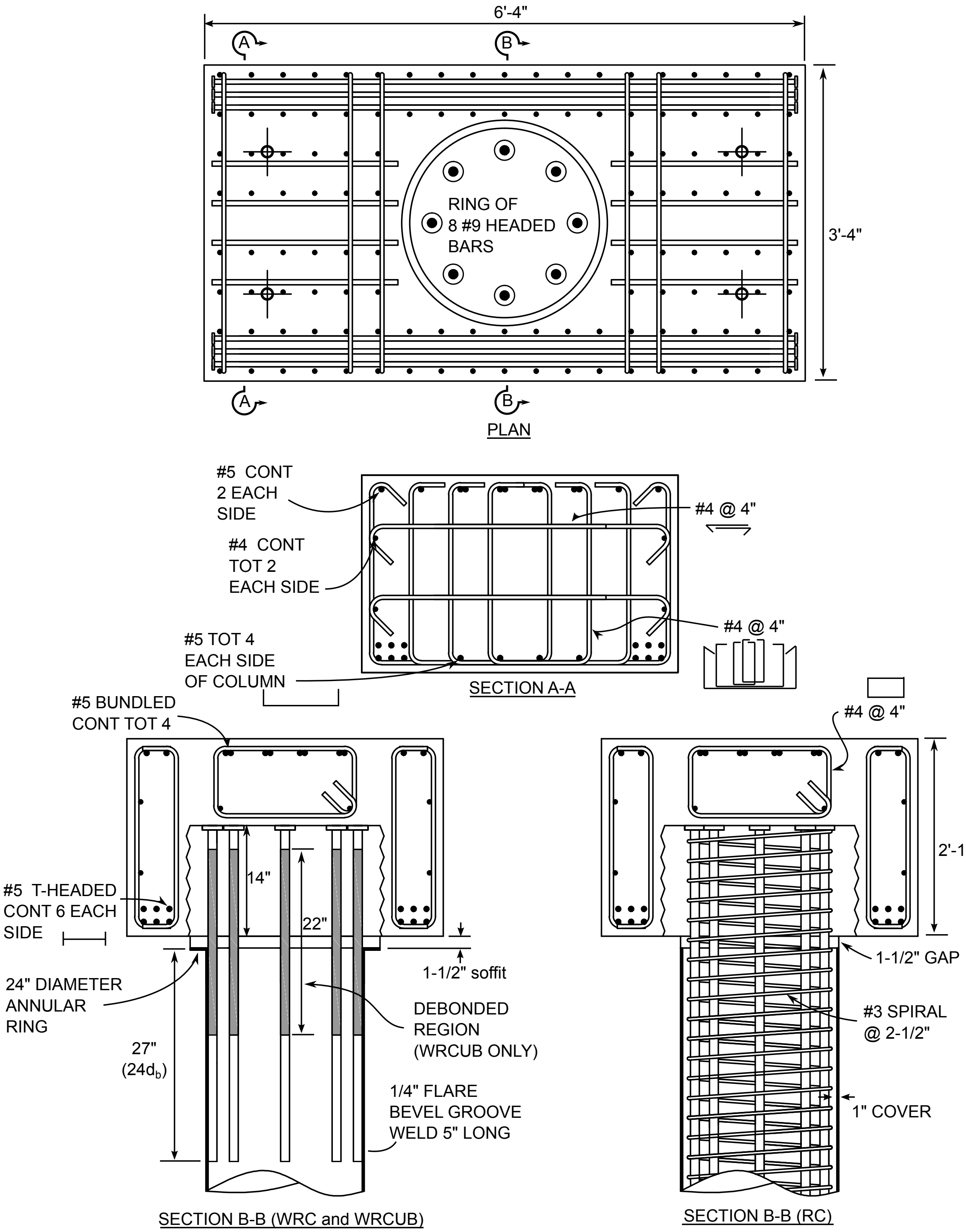

Figure B.3: WD80T1, WD80T2, and RC80T Reinforcing Details

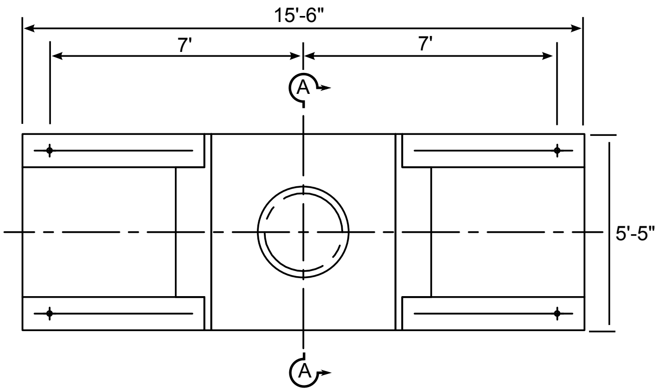

PLAN

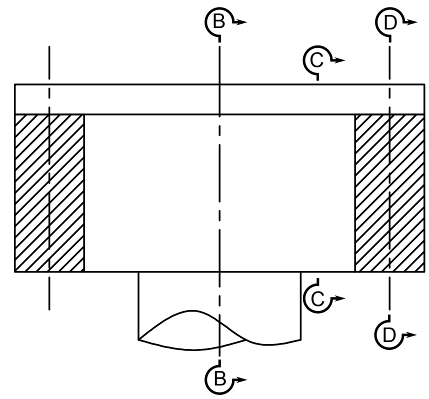

SECTION A-A

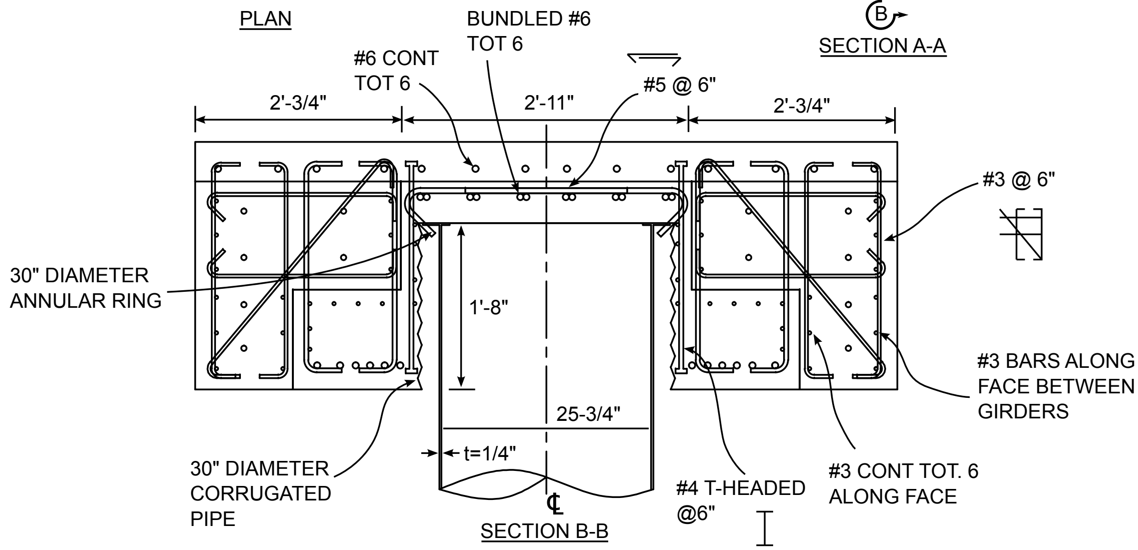

SECTION B-B

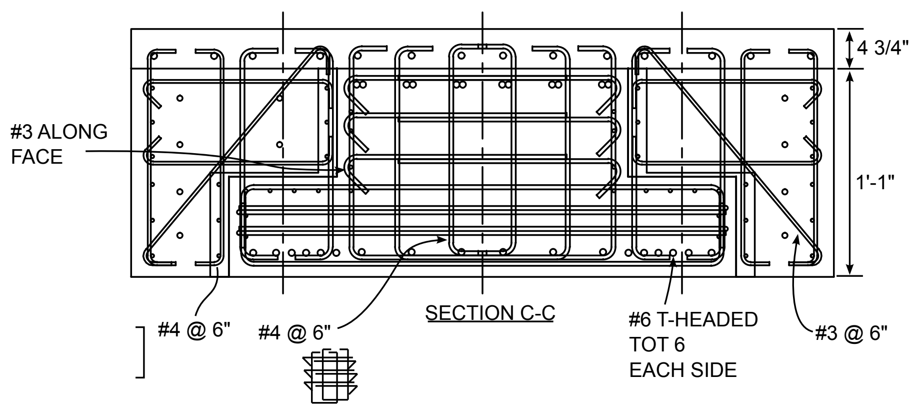

SECTION C-C

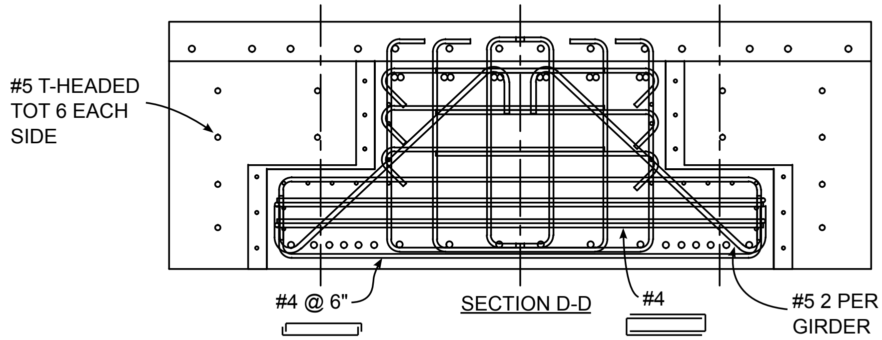

SECTION D-D

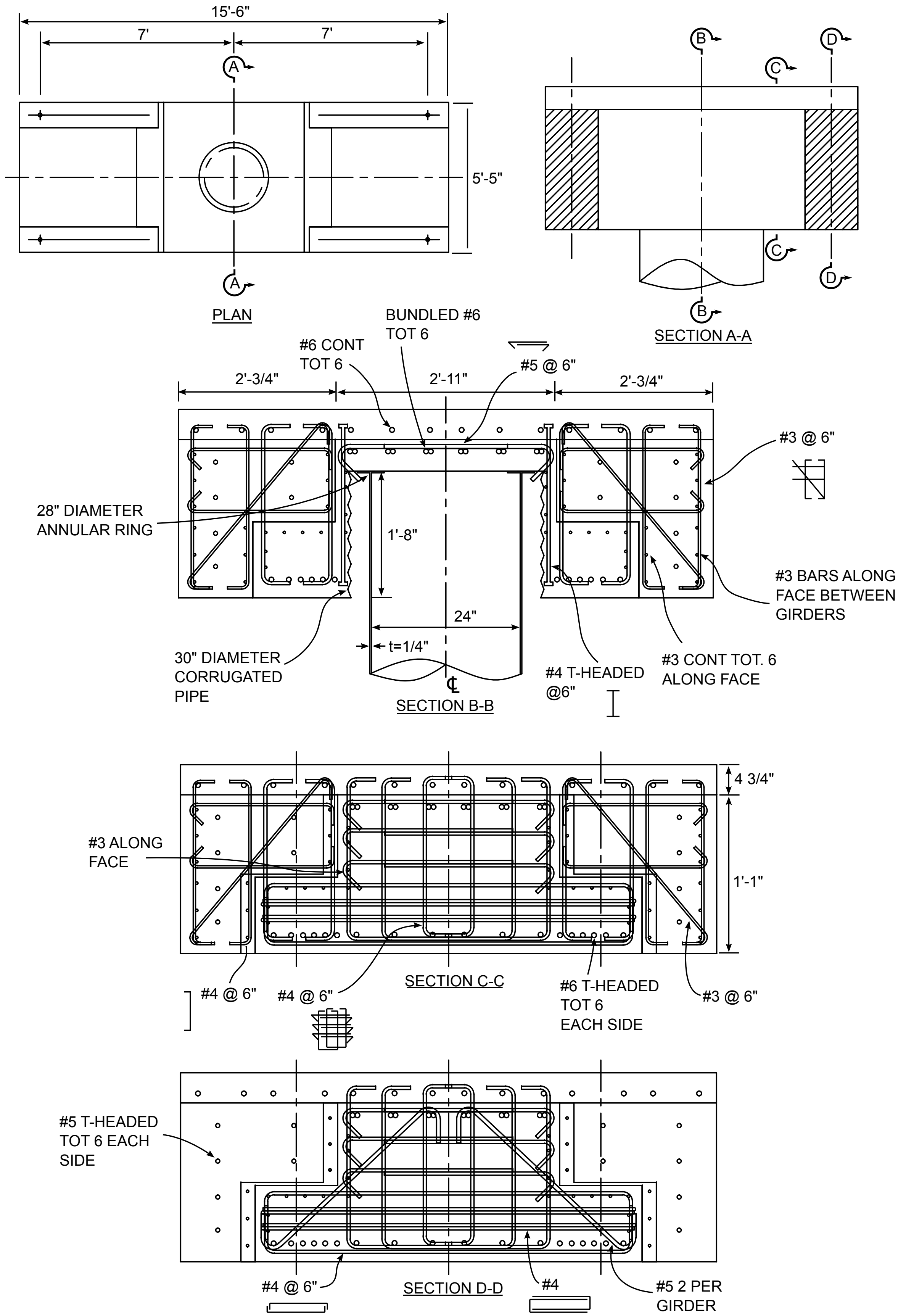
15'-6"
7'
7'
A
5'-5"
A
PLAN
B
D
C
C
D
B
SECTION A-A
BUNDLED #6
TOT 6
#6 CONT
TOT 6
#5 @ 6"
2'-3/4"
2'-11"
2'-3/4"
#3 @ 6"
28" DIAMETER
ANNULAR RING
1'-8"
#3 BARS ALONG
FACE BETWEEN
GIRDERS
24"
t=1/4"
30" DIAMETER
CORRUGATED
PIPE
SECTION B-B
#4 T-HEADED
@6"
#3 CONT TOT. 6
ALONG FACE
4 3/4"
#3 ALONG
FACE
1'-1"
#4 @ 6"
#4 @ 6"
SECTION C-C
#6 T-HEADED
TOT 6
EACH SIDE
#3 @ 6"
#5 T-HEADED
TOT 6 EACH
SIDE
#4 @ 6"
SECTION D-D
#4
#5 2 PER
GIRDER

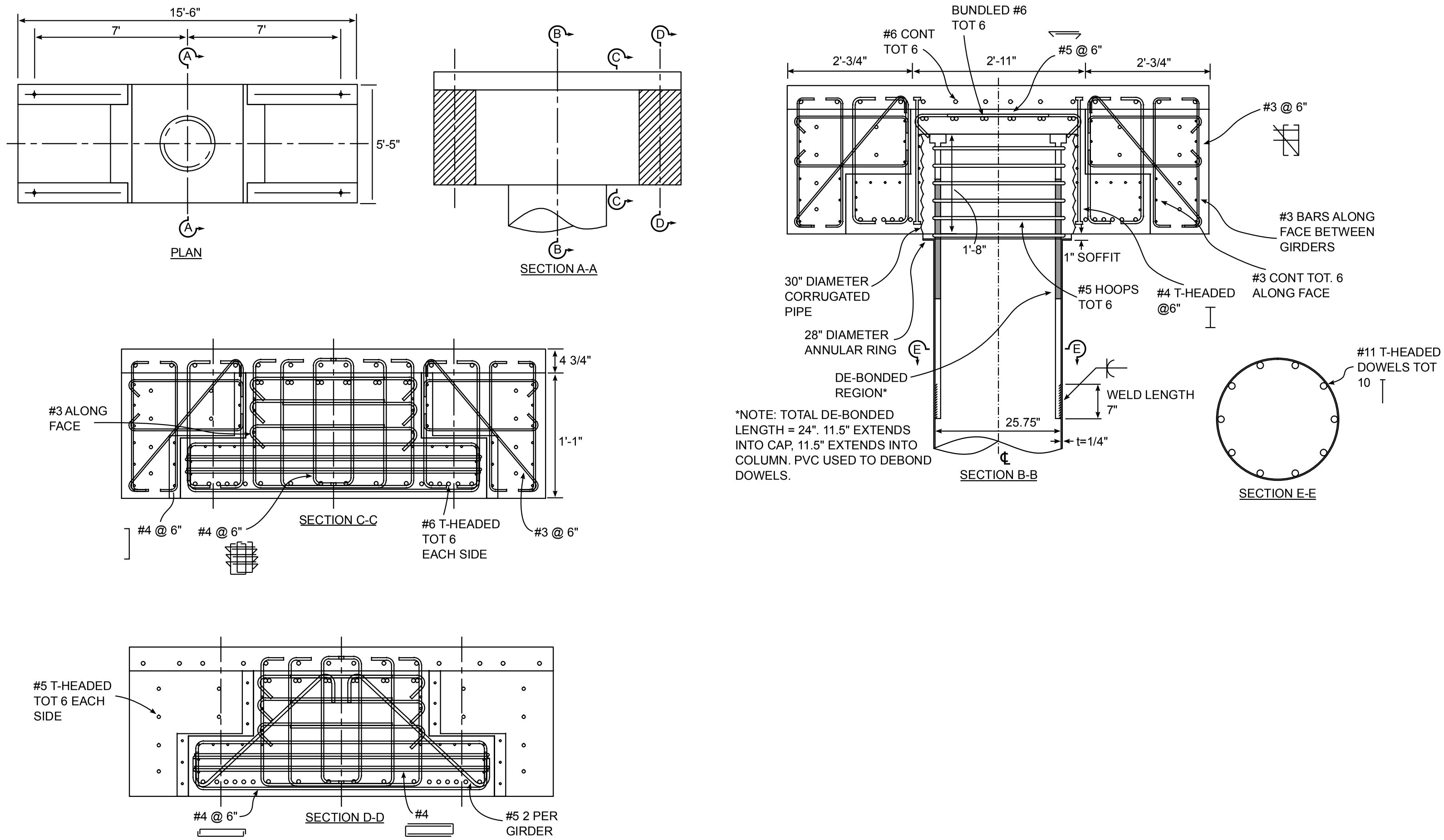

Figure B.6: WD103L Reinforcing Details

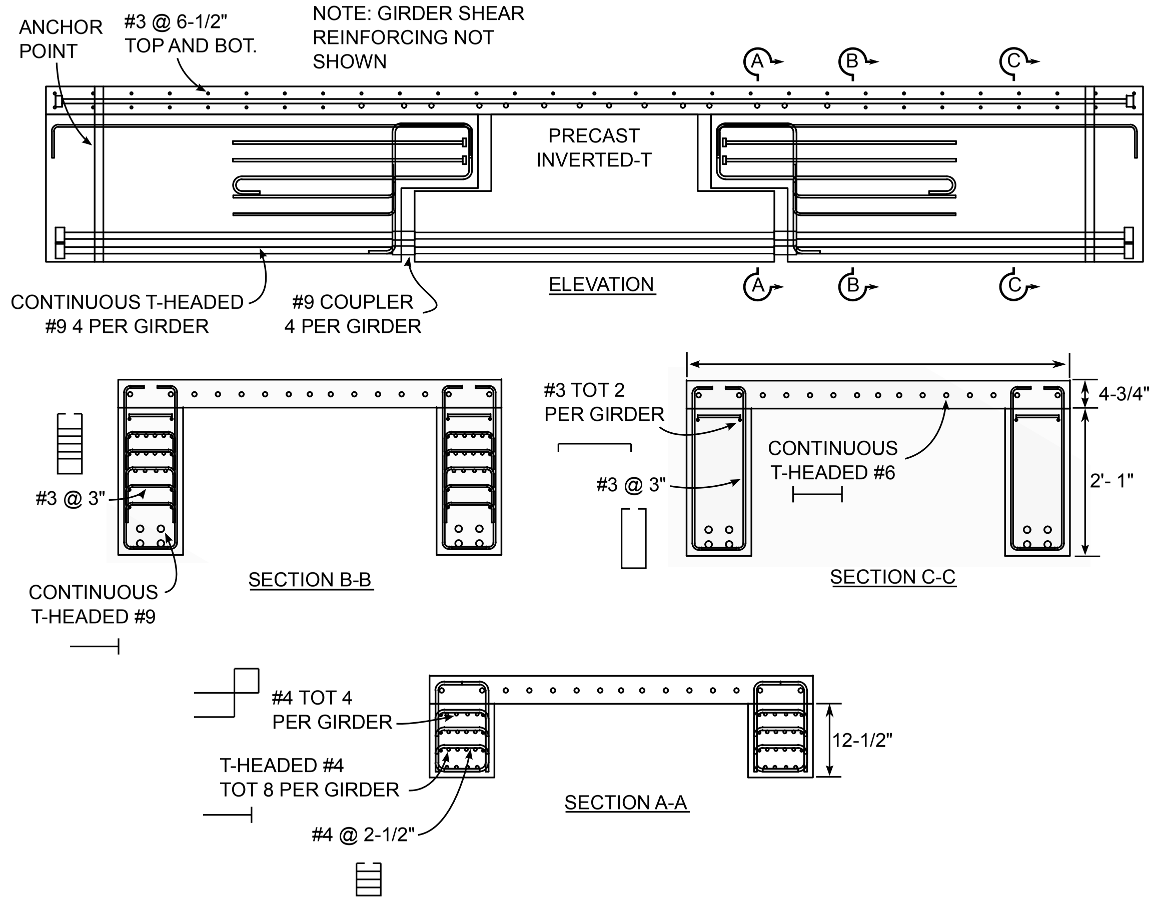

Figure B.7: Deck and Longitudinal Girder Reiforcing Details for Specimens ER96L, ER103L, and WD103L

Appendix C
PROPOSED SPECIFICATION LANGUAGE

1.Cap Beam Connections for CFST

1.1 General

CFST column to cap beam connections shall be designed using one of the following options:

1. An embedded Ring An embedded ring (ER) connection in which the CFST column is embedded into the cap beam as illustrated in Figure 1.3.1.

2. A welded dowel (WD) connection in which a ring of reinforcing bars are welded inside the CFST column and extend into the cap beam as illustrated in Figure 1.4.1.

3. A reinforced concrete (RC) connection in which a ring of headed reinforcing bars is developed into the steel tube and extend into the cap beam as illustrated in Figure 1.5.1.

C1. Cap Beam Connections for CFST

C1.1 General

The CFST column to cap beam connections presented in Articles 1.4, 1.5, and 1.6 have been researched extensively (Lehman and Roeder 2012), and range in performance in terms of stiffness and strength. All of the connections can be implemented using cast-in-place or precast super-structure elements.

For precast construction, a void must be included in the precast elements through use of a corrugated pipe which meets the specifications in Article 1.2.3. The connections are to be grouted into place using fiber-reinforced grout which is designed according to Articles 1.2.1 and 1.2.2.

The three different connection types provide differing strengths and stiffness. The embedded ring connection is a full strength connection in which the strength is controlled by the capacity of the CFST column. The welded dowel connection can be designed

Each of these options can be employed using cast-in-place or precast super-structure components. Embedded ring connections shall be embedded into the reinforced concrete cap beam with an embedment depth and cap beam depth specified in Article 1.4. Welded dowel connections shall include reinforcing welded into the steel tube and extending into the cap beam and CFST column according to Article 1.5. Reinforced concrete connections shall include transverse and longitudinal reinforcing extending from the CFST column into the cap beam according to Article 1.6. Cap beam design for the embedded CFST connection shall conform to requirements in Article 1.3.3, while cap beam design for the welded dowel and embedded dowel connections shall conform to joint shear requirements in Section 7.4 of the Caltrans SDC V. 1.8 unless otherwise specified in the following sections.

as a full or partial strength connection depending on the longitudinal reinforcing ratio in the connection region. The reinforced concrete connection is a partial strength connection which cannot achieve the plastic moment capacity of the CFST without exceeding a longitudinal reinforcing ratio in the connection region of 4%.

1.1.1 Limits of Application

None of these connections shall be used in bridges with skew greater than 20 degrees.

C1.1.1 Limitations of Application

To date, no experimental testing has been conducted to evaluate the performance of these connections on bridges with a skew greater than 20 degrees.

1.2 Materials

Materials for the specified connections shall conform to the Caltrans standards, with several specific provisions included in Section 1.2 of this document.

1.2.1 Grout

The fiber-reinforced grout shall consist of prepackaged, cementitious grout which meets ASTM C-1107 for grades A, B, and C non-shrink grout. The grout shall conform to several additional performance requirements including compressive strength, compatibility,
constructability, and durability. These requirements are summarized in Table 1.1.1. The 28-day grout strength f'g must exceed f'c of the surrounding concrete components. Grout using metallic formulations shall not be permitted, and grout shall be free of chlorides. No additives shall be added to pre-packaged grout.

C1.2.1 Grout

Provisions in 1.2.1 have been included to ensure the grout has properties that provide adequate strength, are conducive to longevity, and provide constructability such that the grout can be placed efficiently for ABC. These requirements are based loosely on recommendations provided in NCHRP Report 651. Grouts with chloride are not permitted as these materials can accelerate corrosion in the connection reinforcing and steel tube. Additives are not permitted because pre-packaged grouts are proprietary mixes which should not be modified.

Table 1.2.1.1 Grout Specifications

1.2.2 Fiber Reinforcing

Macro polypropylene fiber shall be included with a minimum volume of 0.2%, and shall be mixed according to manufacturer specification.

C1.2.2 Fiber Reinforcing

Macro polypropylene fiber (not micro) reinforcing is included to provide crack resistance and bounding characteristics between the tube and corrugated metal duct. Test results to date have not evaluated the use of alternative fibers including steel fibers.

Property	Permitted Values
Mechanical	
Compressive Strength	Must exceed f'_c of surrounding concrete at 28-days. Minimum grout strength f'_g must exceed 6-ksi.
Compatibility	
Non-Shrink	Grade A, B, or C per ASTM C-1107
Constructability	
Flow	Mix to flowable consistency according to manufacturer specifications.
Durability	
Freeze thaw	300 cycles, relative durability factor 90% per ASTM C666
Sulfate resistance	Expansion at 26 weeks ¡ 0.3% per ASTM C1012

1.2.3 Corrugated Metal Duct

Corrugated metal ducts are used to provide voids in precast components. The ducts shall be galvanized steel according to ASTM A653. Duct diameter shall be selected based on construction tolerances. Plastic ducts are not permitted.

C1.2.3 Corrugated Metal Duct

The use of corrugated metal ducts for grouted connections has been researched extensively. These ducts provide mechanical interlock between the cap beam concrete and grout, and provide confinement in the joint region. Research on the behavior of the connections using plastic ducts is limited, and therefore their use is currently not permitted.

1.2.4 Reinforcing

Column reinforcing dowels in the WD connection shall conform to ASTM A706 Gr. 60 (or Gr. 80 if allowed) requirements for weldable reinforcing.

C1.2.4 Reinforcing

ASTM A706 places restrictions on the chemical composition of reinforcing bars to enhance welding properties. Welding requirements are discussed in Article 1.4.3.

1.2.5 Tube Steel

C1.2.5 Tube Steel

Selection of tube material designation (ASTM or API) plays a role in the ductility of the full strength embedded CFST connection. API grade steels tend to be of higher quality

Steel tubes may either be straight seam or spiral welded and must conform to either ASTM or API requirements. Spiral welded tubes must be welded using a double submerged arc welding process, and weld metal properties must match properties of the base metal and meet minimum toughness requirements of AISC demand critical welds [AISC, 2011].

API steel can exceed 8% drift prior to tube fracture, while connections which use ASTM grade steels tend to fracture at 6% drift. Additional ductility can be expected for tubes with lower slenderness values [Lehman and Roeder, 2012b,a].

1.3 Embedded Ring Connection

The embedded ring CFST connection shall be design according to the requirements specified in Article 1.3

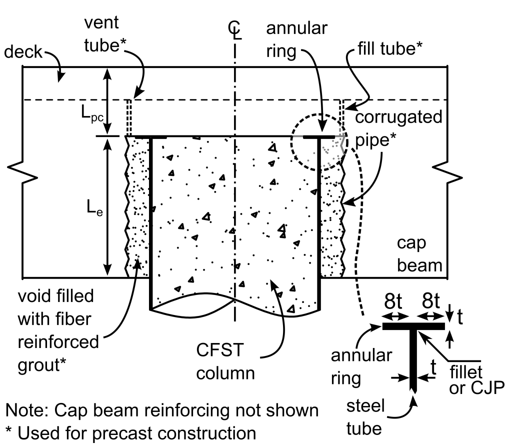

Figure 1.3.1 Embedded Ring Connection

C1.3 Embedded Ring Connection

The embedded ring connection utilizes a CFST fully embedded into the cap beam. The strength and ductility of this connection type is to be controlled by the CFST component, not by the cap beam or other superstructure components. For practical construction, the precast cap would be placed onto the column after the column was set, and the recess between the tube and corrugated pipe would be filled with high strength fiber reinforced grout.

1.3.1 Annular Ring

An annular ring shall be welded to the steel tube as illustrated in Figure 1.3.1. The

C1.3.1 Annular Ring

The annular ring is welded to the steel tube to provide anchorage and transfer stress to annular ring shall have the same thickness of the steel tube with a yield stress equal to or greater than that of the steel tube. The ring shall extend outside the tube 8 times the thickness of the tube, and project inside the steel tube 8 times the thickness of the tube as illustrated in Figure 1.3.1.

The annular ring shall be welded to the steel tube using complete joint penetration (CJP) welds of matching filler metal, or fillet welds on both the inside and outside of the tube. The minimum size, w, of the fillets shall be determined using Equation 1.3.1.1 where F_{EXX} and F_u,tube are the minimum tensile strength of the weld metal and steel tube in ksi or psi respectively.

$w \geq \frac{1.31 F_{u,st} t}{F_{EXX}}$ Equation 1.3.1.1

Welds shall provide a minimum CVN toughness of 40-ft-lbs at 70ËF.

the concrete and reinforcing in the cap beam. This ring is welded according to Article 1.3.1 to ensure the weld can develop the full tensile capacity of the steel tube.

C1.3.2 Embedment Depth

The tube shall be embedded into the cap beam a distance L_e as defined by Equation 1.3.1.1 where $f'_{c,cap}$ is the compressive strength of the cap beam in psi, D is the outside diameter of the steel tube, F_u is the minimum specified tensile strength of the steel tube in psi.

C1.3.2 Embedment Depth

The embedment requirement in Article 1.3.2 is required to develop the full tensile capacity of the CFST member in flexure prior to developing a conical pullout failure of the connection as illustrated in Figure C1.3.2.1. The cone depth and maximum concrete principal stress limits were derived

$$L_e = \sqrt{\frac{D^2}{4} + \frac{DtF_u}{6\sqrt{f'_{c,cap}}}} - \frac{D}{2} \; (f'_{c,cap} \text{ in psi})$$

Equation 1.3.1.2

using results from an extensive experimental program [Lehman and Roeder, 2012b,a].

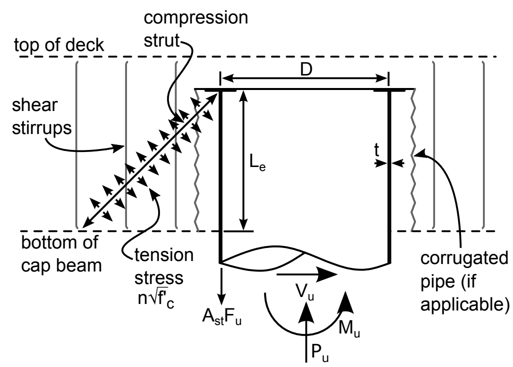

Figure C1.3.2.1 Transfer Mechanism

1.3.3 Requirements for Bridge Layout and Cap Beam Design

1.3.3.1 Bridge Layout

When using the embedded connection, the column shall be laid out between the longitudinal girders as illustrated in Figure 1.3.3.1 and Figure 1.3.3.2.

C1.3.3.1 Bridge Layout

The column must be placed between the longitudinal girders to facilitate the development of corbel reinforcing in the cap beam as well as positive moment continuity in the girders.

1.3.3.2 Required Cap Depth Above CFST Embedment

A minimum cap beam depth above the embedded CFST, L_{pc}, shall be included according to Equation 1.3.3.2.1 where C_c and C_s are the compressive forces (in lbs) in the concrete and steel due to the combined axial load and bending moment as computed

C1.3.3.2 Required Cap Depth Above CFST Embedment

Adequate concrete depth must be provided above the tube to eliminate the potential for punching shear failure in the cap beam. The ACI 318 [ACI, 2011] provisions for flat slabs in single shear were used as a basis to develop an expression for the minimum cap using a plastic stress distribution method and f'_c,cap is the compressive strength of the cap beam in psi.

$$L_{pc} = \sqrt{\frac{D^2}{4} + \frac{C_c+C_s}{6\sqrt{f'_{c,cap}}}} - \frac{D}{2} - L_e \ (f'_{c,cap} \text{ in psi})$$

Equation 1.3.3.2.1

1.3.3.3 Cap Beam Reinforcing

(A) Flexural Reinforcing

Longitudinal flexural reinforcing in the column region shall be designed to resist $1.25M_p$ of the CFST column per requirements in the Caltrans SDC. Longitudinal flexural reinforcing shall be spaced uniformly across the width of the cap beam. A minimum of one layer of reinforcing shall pass above the embedded CFST in the cap beam as shown in Figure 1.3.3.3.3. Some longitudinal reinforcing in the bottom layer will be interrupted by the embedded corrugated pipe. The bottom layer of flexural reinforcing not interrupted by the corrugate pipe shall be designed to resist $1.25M_p$ of the CFST column. Interrupted bars shall still be included and arranged as illustrated in Figure 1.3.3.3.

(B) Vertical Stirrups

Vertical reinforcing, A_s^{jv}, shall be included according to Equation 1.3.3.3.1 where A_st is

beam depth above the embedded CFST, L_{pc}, to avoid this failure mode.

(B) Vertical Stirrups

Vertical reinforcing is included a distance extending $D/2 + L_e$ from the column centerline to resist development of a conical the total area of the steel tube embedded into the cap beam.

$A_s^{jv} = 0.65 A_{st}$ Equation 1.3.3.3.1

Vertical stirrups or ties shall be distributed uniformly within a distance $D/2 + L_e$ extending from the column centerline as shown in Figure 1.3.3.3.1 and Figure 1.3.3.3.3. These stirrups can be used to meet other requirements documented elsewhere including shear in the bent cap.

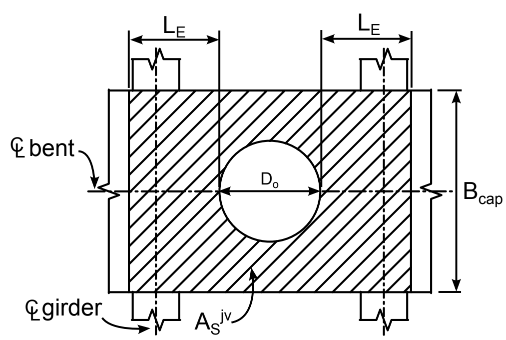

Figure 1.3.3.3.1 Location of Vertical Reinforcing

pullout failure as discussed in Article C1.3.2. The vertical reinforcing is included to resist $4\sqrt{f_c'}$ of the maximum principal stress illustrated in Figure C1.3.3. The remaining $2\sqrt{f_c'}$ is carried by the concrete.

(C) Horizontal Stirrups

Horizontal stirrups or ties shall be placed transversely around the vertical stirrups or ties in two or more intermediate layers spaced vertically at not more than 18-in apart. The horizontal reinforcing area, A_s^{jh}, shall be included according to Equation 1.3.3.3.2

(C) Horizontal Stirrups

Horizontal reinforcing requirements are consistent with requirements in Article 7.4.4.3 of the Caltrans SDC V. 1.8 with the exception that the horizontal stirrups must be placed within a distance $D_c/2 + L_e$ extending from the column centerline.

where Ast is the area of the steel tube embedded into the cap beam. The horizontal reinforcing shall be placed within a distance $D/2 + L_e$ extending from the column

$A_s^{jh} = 0.1 A_{st}$ Equation 1.3.3.3.2

In addition, the top layer of transverse reinforcing shall continue across top of the void in the cap beam as illustrated in Figure 1.3.3.3.3.

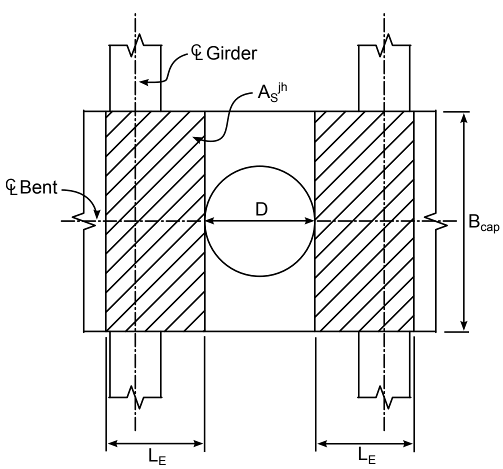

Figure 1.3.3.3.2 Location of Horizontal Reinforcing

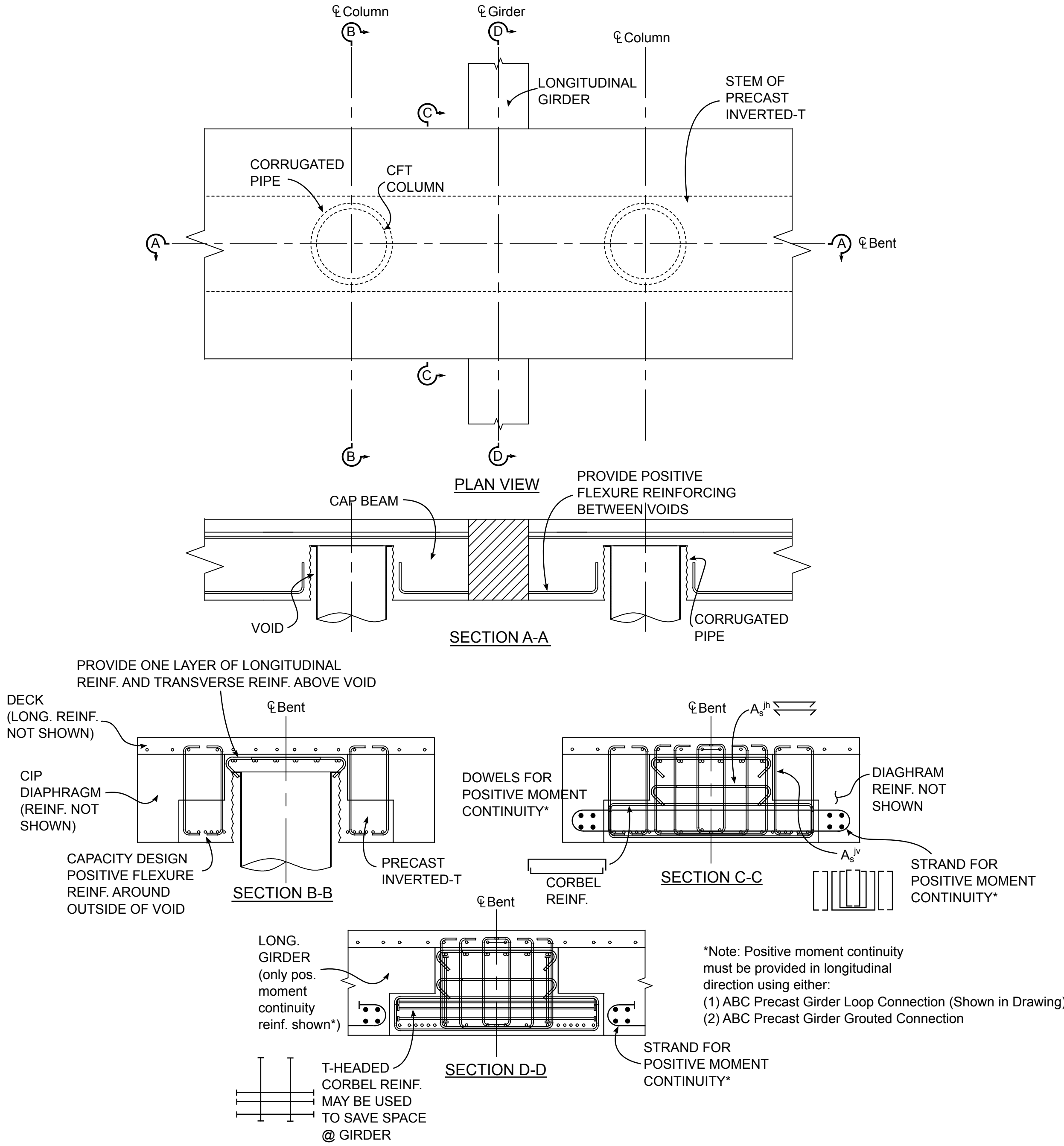

Figure 1.3.3.3 Sample Cap Beam Details for ER Connection

1.3.4 Construction Sequence

The embedded ring connection shall be constructed according to the sequence defined in Article 1.3.4 and illustrated in Figure 1.3.4.1C.

1. Cast foundation leaving a void for the steel tube using a corrugated pipe.
2. Place the steel pipe with annular rings welded to the top and bottom.
3. Grout the steel tube into the foundation using fiber-reinforced grout.
4. Cast concrete fill.
5. For precast construction, place precast element on top of the CFST. For CIP construction, build false work and cast cap beam around the CFST.
6. For precast construction, grout the steel tube into the cap beam using fiber-reinforced grout.

C1.3.4 Construction Sequence

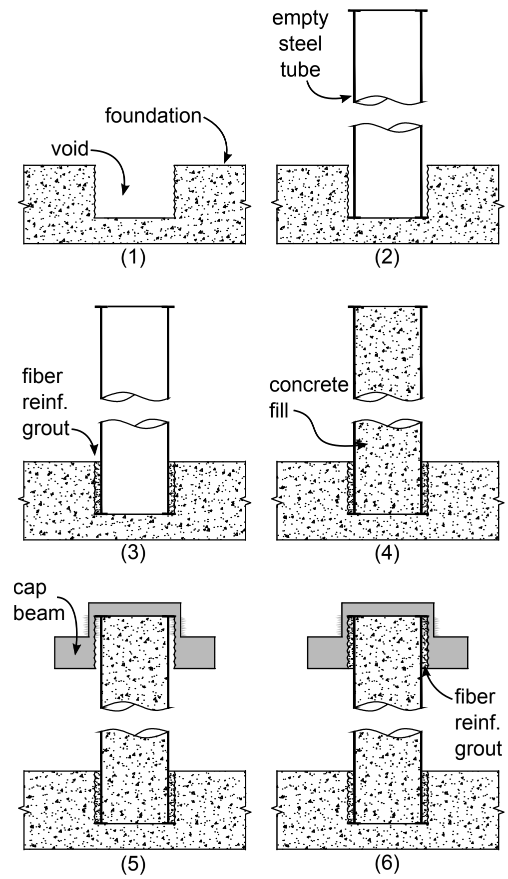

Figure 1.3.4.1C Construction Sequence for Embedded Ring Connection

1.4 Debonded Welded Dowel Connection

De-bonded welded dowel connections shall be designed according to requirements in Section 1.4.

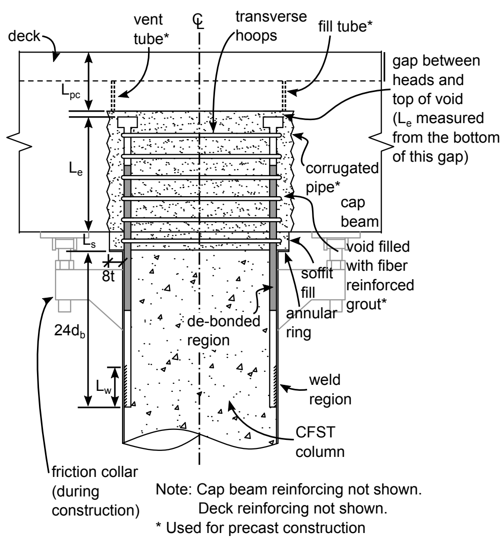

Figure 1.4.1 Welded Dowel Connection with Debonded Dowels

1.4.1 Flange

A flange shall be welded to the steel tube as illustrated in Figure 1.4.1. The annular ring shall have the same thickness of the steel tube with a yield stress equal to or greater than that of the steel tube. The ring shall extend outside the tube 8 times the thickness of the tube as illustrated in Figure 1.4.1.

The annular ring shall be welded to the steel tube using a fillet weld on the outside of the

C1.4 Debonded Welded Dowel Connection

The debonded welded bar connection utilizes a ring of headed reinforcing bars which are welded into the tube and developed into the cap beam. The strength and ductility of this connection type is controlled by the reinforcing ratio of the longitudinal reinforcing which extends from the column into the cap beam. The welded detail is primarily intended to decrease the development length and utilize the maximum moment arm within the CFST column.

tube. The fillet weld shall be the largest allowable based on the tube thickness as specified in AISC [2011]. Welds shall provide a minimum CVN toughness of 40-ft-lbs at 70=ˆnF.

1.4.2 Dowel Embedment into CFST and Cap Beam

C1.4.1 Flange

The annular ring is welded to the steel tube to provide a larger area to transfer compressive stress from the steel tube to the cap beam. This helps limit localized grout crushing. The fillet weld is designed to transfer to compressive stress from the tube into the annular ring.

1.4.2.1 Dowel Embedment into Cap Beam

Longitudinal column dowels shall extend into a void in the cap beam. The embedment length shall be the maximum length calculated using Equation 1.4.2.1.1 where ψ_e is the reinforcing bar coating factor defined in ACI 318 (1.0 for uncoated bars, and 1.2 for epoxy coated bars), L_{db} is the debonded length of the reinforcing bar as defined in Article 1.4.4.2, f'_c,cap is the compressive strength of the cap beam in psi, and $f_{y,b}$ is the yield capacity of the longitudinal dowel in psi.

C1.4.2.1 Dowel Embedment into Cap Beam

The headed reinforcing must extend into the cap beam for a length sufficient to fully develop the reinforcing bar while eliminating the potential for a conical pullout failure as illustrated in Figure C1.4.2.1.1. Equation 1.4.2.1.1a defines the required development length as specified in Article 12.6 of ACI 318 [ACI, 2011], while Equation 1.4.2.1.1b defines the required embedment depth to eliminate conical pullout failure as determined using the transfer mechanism shown in Figure C1.4.2.1.1. The embedment depth requirement in Equation 1.4.2.1c has

$L_e \geq \frac{0.016 * \psi * F_{y,b}}{\sqrt{f'_g}}$ (f'_g in psi) Equation 1.4.2.1a

$L_e \geq \sqrt{\frac{D^2}{4} + \frac{1.2F_{y,b}A_{st,b}}{6\pi\sqrt{f'_{c,cap}}}} - D/2$ ($f'_{c,cap}$ in psi) Equation 1.4.2.1b

$L_e \geq 3d_b + 0.5L_{db}$ Equation 1.4.2.1c

been included to ensure a minimum bonded length of $3d_b$ is included adjacent to the head on the end of the headed dowel as illustrated in Figure 1.4.1. This region of bonded reinforcing must be included to ensure adequate anchorage of the longitudinal reinforcing into the cap beam.

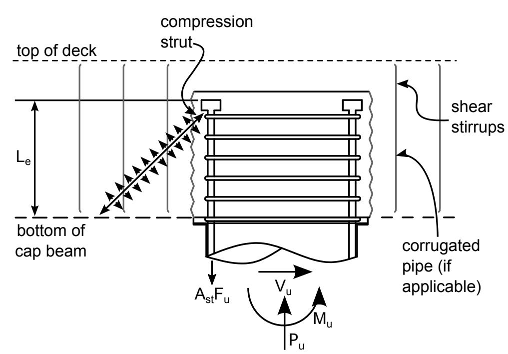

Figure C1.4.2.1.1 Dowel Transfer Mechanism

1.4.2.2 Dowel Embedment into CFST Column

Longitudinal reinforcing shall extend a distance $24d_b$ into the CFST column.

C1.4.2.2 Dowel Embedment into CFST Column

The required reinforcing embedment into the CFST column specified in Article 1.4.2.2 is based on research conducted on the pullout strength of reinforcing welded into CFSTs. Results suggest that the embedment can be decreased to as low as $16d_b$, however $24d_b$ is required to provide a reasonable factor of safety.

1.4.3 Dowel-to-Steel Tube Welds

Reinforcing bars shall be welded to the inside of the steel tube using flare bevel groove welds on both sides of the reinforcing bars as shown in Figure C1.4.3.1. The minimum length of the welds, L_w, shall be the maximum length calculated using Equation 1.4.3.1. All material strengths ($F_{y,bar}$ and F_{EXX}) are in ksi.

$$L_w = \frac{5.6 A_b F_{y,b}}{F_{EXX} d_b} \qquad \text{Equation 1.4.3.1a}$$

$$L_w = \frac{0.83 A_b F_{y,b}}{F_{y,st} t} \qquad \text{Equation 1.4.3.1b}$$

$$L_w = \frac{1.11 A_b F_{y,b}}{F_{u,st} t} \qquad \text{Equation 1.4.3.1c}$$

C1.4.3 Dowel-to-Steel Tube Welds

The weld lengths specified in Article 1.4.3 are calculated to develop the yield capacity of the reinforcing bars based on typical weld limit states for flare bevel groove welds. These equations are based on welding requirements for reinforcing bars specified in AWS 1.4, which defines the effective throat width to be $0.2d_b$ as illustrated in Figure C1.4.3.1. Equation 1.4.3.1a is based on failure of the weld metal, Equation 1.4.3.1b is based on yielding of the tube steel, and Equation 1.4.3.1c is based on rupture of the tube steel. Strength reduction factors specified according to the AISC Construction Manual have been included in Equation 1.4.3.1.

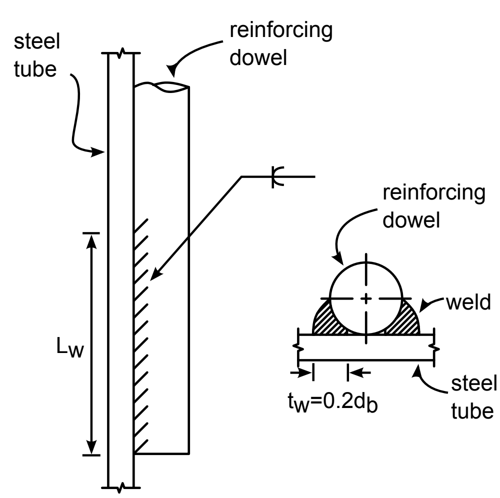

Figure C1.4.3.1 Flare Bevel Groove Weld

1.4.4 Debonded Dowels

Longitudinal column dowels shall be de-bonded from the surrounding concrete in the connection region according to the requirements in Section 1.4.4. The de-bonded region is denoted as L_{db} in Figure 1.4.4.1.

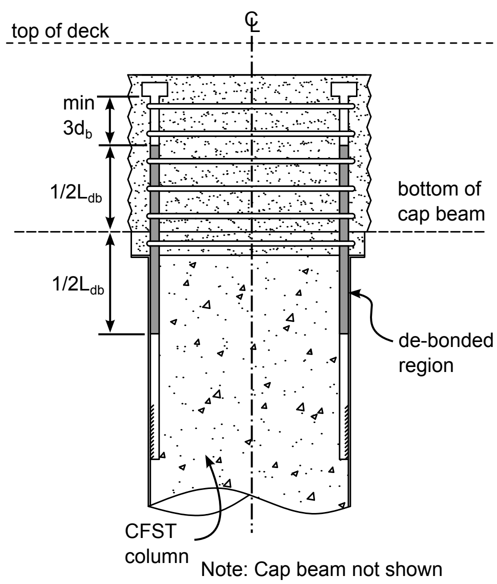

Figure 1.4.4.1 WD Debonding Details

C1.4.4 Debonded Dowels

Longitudinal reinforcing is de-bonded in the connection region with the intention of evenly distributing strain across the de-bonded length, thereby increasing the ductility of the connection.

1.4.4.1 Debonding Methods

The Engineer shall specify the de-bonding method on project plans on a project by project basis.

C1.4.4.1 Debonding Methods

Several de-bonding methods have been evaluated in previous research including encasing the bars in tight-fitting PVC pipe, or wrapping the bars with duct tape. Other methods may be considered so long as it has been shown that they adequately de-bond the reinforcing from the surrounding concrete.

1.4.4.1 Debonded Length

Longitudinal reinforcing shall be de-bonded from the surrounding concrete in the connection region as illustrated in Figure 1.4.4.1. The de-bonded length, L_{db}, shall be calculated according to Equation 1.4.4.2.1 or Equation 1.4.4.2.2 where θ is the target rotation for reinforcing bar fracture, and ϕ_s is the curvature of the connection at a steel strain limit of $0.7\epsilon_u$ as obtained from a moment curvature analysis. Half of the de-bonded length shall extend into the cap beam, and half of the de-bonded length shall extend through the soffit fill and into the CFST column as illustrated in Figure 1.4.1.

$$L_{db} = \frac{tan\theta(D-t-d_b/2)}{0.7\epsilon_u} \qquad \text{Equation 1.4.4.2.1}$$

$$L_{db} = \frac{\theta_u}{\phi_u} \qquad \text{Equation 1.4.4.2.2}$$

1.4.5 Transverse Column Reinforcing in Joint Region

Transverse reinforcing shall be included in the joint region in the form of spiral or discrete hoops as shown in Figure 1.4.1. The area and spacing of this reinforcing must conform to Equation 1.4.5.1. When discreet hoops are

C1.4.5 Transverse Column Reinforcing in Joint Region

Transverse reinforcing is placed around the reinforcing bars to increase confinement in the joint region especially through the depth of the soffit fill.

used, at least one hoop must be placed in the depth of the soffit fill.

1.4.6 Requirements for Bridge Layout and Cap Beam Design

1.4.6.1 Bridge Layout

The column shall be laid out between the longitudinal girders.

1.4.6.2 Cap Beam Reinforcing

(A) Flexural Reinforcing

Longitudinal flexural reinforcing shall be designed to resist $1.2M_p$ of the CFST column per requirements in the Caltrans SDC V. 1.8 [Caltrans, 2010]. Longitudinal flexural reinforcing shall be spaced uniformly across the width of the cap beam. Some longitudinal reinforcing in the bottom layer will be interrupted by the embedded corrugated pipe. The bottom layer of flexural reinforcing not interrupted by the corrugate pipe shall be designed to resist 1.2Mp of the CFST column. Interrupted bars shall still be included as shown in Figure 1.3.3.

(B) Vertical Stirrups

Vertical stirrups shall be included according to requirements in Article 7.4.4.2 in the Caltrans SDC [Caltrans, 2010].

(C) Horizontal Stirrups

Horizontal stirrups shall be included according to requirements in Article 7.4.4.2 in the Caltrans SDC [Caltrans, 2010].

1.4.6.3 Soffit Fill Depth

The soffit fill depth, L_s, shall be calculated according to Equation 1.4.6.1.1.

$$L_s \geq sin\left(\theta_u\right)\left(\frac{D}{2}+8t\right) \qquad \text{Equation 1.4.6.3.1}$$

C1.4.6.3 Soffit Fill Depth

The soffit fill depth requirement in Equation 1.4.6.1.1 ensures that the annular ring does not come into contact with the cap beam at the maximum expected drift, θ.

1.4.6.4 Requirements for Headed Reinforcing

Minimum cover shall be provided when headed reinforcing is anchored in the cap beam according to requirements in Article 1.4.6.4. These requirements are summarized in Figure 1.4.6.4.1.

1. The thickness of side cover around the head must be equal to or greater than the diameter of the head.
2. A minimum depth of $3d_h$ shall be included above the heads in the headed reinforcing where d_h is the diameter of the head.
3. Nominal amounts of longitudinal reinforcing (e.g. reinforcing steel in the plane orthogonal to the headed reinforcement) shall be placed above the head.

C1.4.6.4 Requirements for Headed Reinforcing

Unlike straight bar anchorage conditions, for which the deformations along the length of the bar provide progressive anchorage, in a headed bar the head itself provides most of the anchorage. Under tensile loading the head reacts and transfers the force through strutting action, as shown in Figure 1. Under compression, the headed bar transfers the force to the concrete through strutting action towards the base. In both conditions, four aspects of dimensioning are important: (1) sufficient concrete depth to limit the shear stresses along the compression strut, (2) sufficient cover, (3) horizontal (longitudinal) reinforcement to resist the horizontal component of the strut and (4) vertical (transverse) reinforcement to resist the vertical component of the strut.

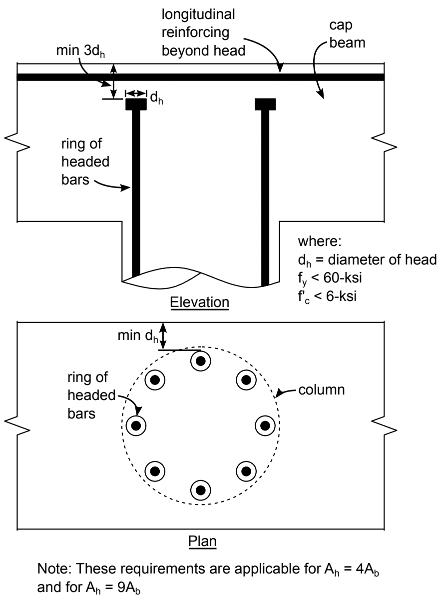

Figure 1.4.6.4.1 Cover Requirements for Headed Reinforcing

1.4.7 Construction Sequence

The welded dowel connection shall be constructed according to the sequence defined in Article 1.4.7 and illustrated in Figure 1.4.7.1C.

1. Cast foundation leaving a void for the steel tube using a corrugated pipe.

2. Place the steel pipe with annular ring welded to the bottom and longitudinal reinforcing and annular ring welded to the top.

3. Grout the steel tube into the foundation using fiber-reinforced grout.

4. Cast concrete fill.

5. For precast construction, place precast element on top of the CFST with a friction collar. The headed reinforcing should not come into contact with the top of the void in the cap beam. For CIP construction, build false work and cast cap beam around the CFST.

6. For precast construction, grout the welded reinforcing into the void in the cap beam.

C1.4.7 Construction Sequence

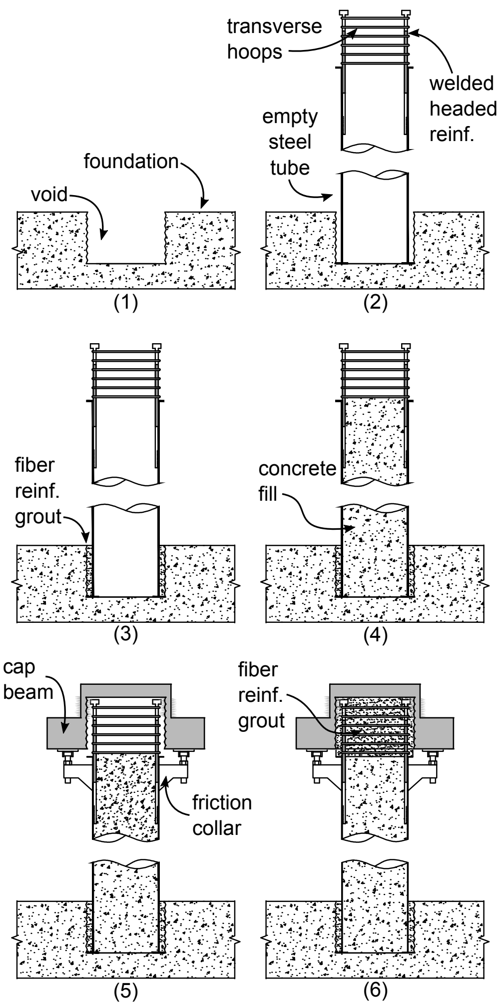

Figure 1.4.7.1C Construction Sequence for Welded Dowel Connection

1.5 Reinforced Concrete Connection

Reinforced concrete connections shall be designed according to requirements in Section 1.5.

1.5 Reinforced Concrete Connection

The reinforced concrete connection consists of a more traditional reinforced concrete dowel connection, as both transverse and longitudinal reinforcing extend from the CFST column into the cap beam. The strength and ductility of this connection type is controlled by the reinforcing ratio and moment arm of the longitudinal reinforcing. Note that construction of this connection using precast super-structure components requires use of a friction collar to temporarily support the cap beam.

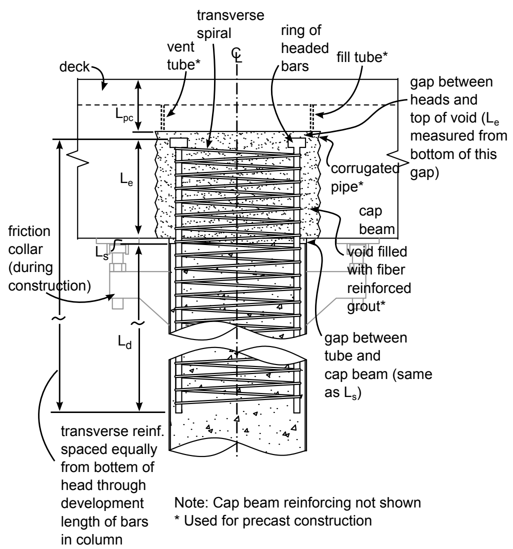

Figure 1.5.1 Reinforced Concrete Connection

1.5.1 Dowel Embedment into Column and Cap Beam

1.5.1.1 Dowel Embedment into Cap Beam

Longitudinal reinforcing shall extend into the cap beam as specified in Article 1.4.2.1.

1.5.1.2 Dowel Embedment into CFST Column

Longitudinal reinforcing shall extend a distance Ld into the CFST column according

C1.5.1.2 Dowel Embedment into CFST Column

The headed reinforcing must extend into the CFST column for a length sufficient to to Equation 1.5.2.2.1 where ψ_e is the reinforcing bar coating factor as defined in ACI 318 (1.0 for uncoated bars, and 1.2 for epoxy coated bars), $f'_{c,fill}$, is the compressive strength of the concrete fill in psi, and $f_{y,b}$ is the yield strength of the longitudinal dowels in psi.

$$L_d = \left(\frac{F_{y,b}\psi_e}{25\sqrt{f'_{cf}}}\right) d_b \qquad \text{Equation 1.5.1.1.1}$$

1.5.2 Transverse Reinforcing

Transverse reinforcing in the form of discrete hoops or spiral shall extend from the cap beam and into the column for a distance L_d as illustrated in Figure 1.5.1.

1.5.3 Requirements for Bridge Layout and Cap Beam Design

1.5.3.1 Bridge Layout

The column shall be laid out between the longitudinal girders.

1.5.3.2 Cap Beam Reinforcing

(A) Flexural Reinforcing

Longitudinal flexural reinforcing shall be designed to resist $1.2M_p$ of the CFST column per requirements in the Caltrans SDC V. 1.8 [Caltrans, 2010]. Longitudinal flexural reinforcing shall be spaced uniformly across the width of the cap beam. Some longitudinal

fully develop the reinforcing bar. Equation 1.5.2.21 defines the required development length as specified in Article 12.2 of ACI 318 [ACI, 2011]. Equation 1.5.2.2.1 is a simplified development length equation which pertains to geometries commonly found in reinforced concrete bridge columns. For uncommon geometries or reinforcing layouts, The Engineer shall reference Article 12.2 of ACI 318 [ACI, 2011].

reinforcing in the bottom layer will be interrupted by the embedded corrugated pipe. The bottom layer of flexural reinforcing not interrupted by the corrugate pipe shall be designed to resist $1.2M_p$ of the CFST column. Interrupted bars shall still be included as shown in Figure 1.3.3.

(B) Vertical Stirrups

Vertical stirrups shall be included according to requirements in Article 7.4.4.2 in the Caltrans SDC V. 1.8 [Caltrans, 2010].

(C) Horizontal Stirrups

Horizontal stirrups shall be included according to requirements in Article 7.4.4.2 in the Caltrans SDC V. 1.8 [Caltrans, 2010].

1.5.4 Requirements for Headed Reinforcing

Cover for headed reinforcing shall be included according to requirements in Article 1.4.6.2.

1.5.5 Construction Sequence

The reinforced concrete connection shall be constructed according to the sequence defined in Article 1.5.5 and illustrated in Figure 1.5.5.1C.

1. Cast foundation leaving a void for the steel tube using a corrugated pipe.

C1.5.5 Construction Sequence

2. Place the steel pipe with an annular ring welded to the bottom.

3. Grout the steel tube into the foundation using fiber-reinforced grout.

4. Temporarily support longitudinal reinforcing cage at the top of the column, and cast concrete fill.

5. For precast construction, place precast element on top of the CFST using a friction collar. The headed reinforcing should not come into contact with the top of the void in the cap beam. For CIP construction, build false work and cast cap beam around the CFST.

6. For precast construction, grout the longitudinal reinforcing cage into the cap beam using fiber-reinforced grout.

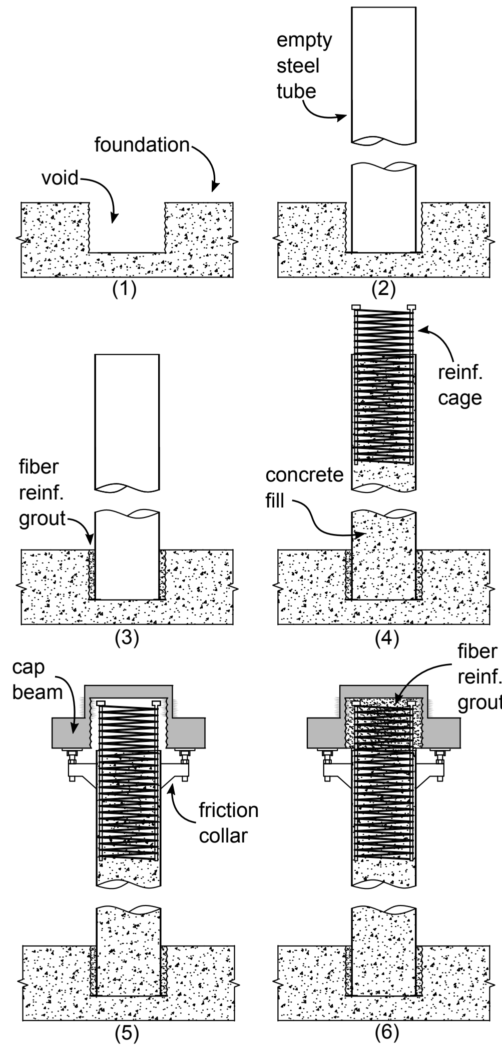

Figure 1.5.5.1C Reinforced Concrete Construction Sequence

Appendix D

STANDARD CONNECTION DRAWINGS

STANDARD CONCRETE FILLED TUBE CAP BEAM CONNECTIONS	
Designed By:	Max Stephens
Drawn By:	Max Stephens
Date:	24 October 2014
Page:	2/2

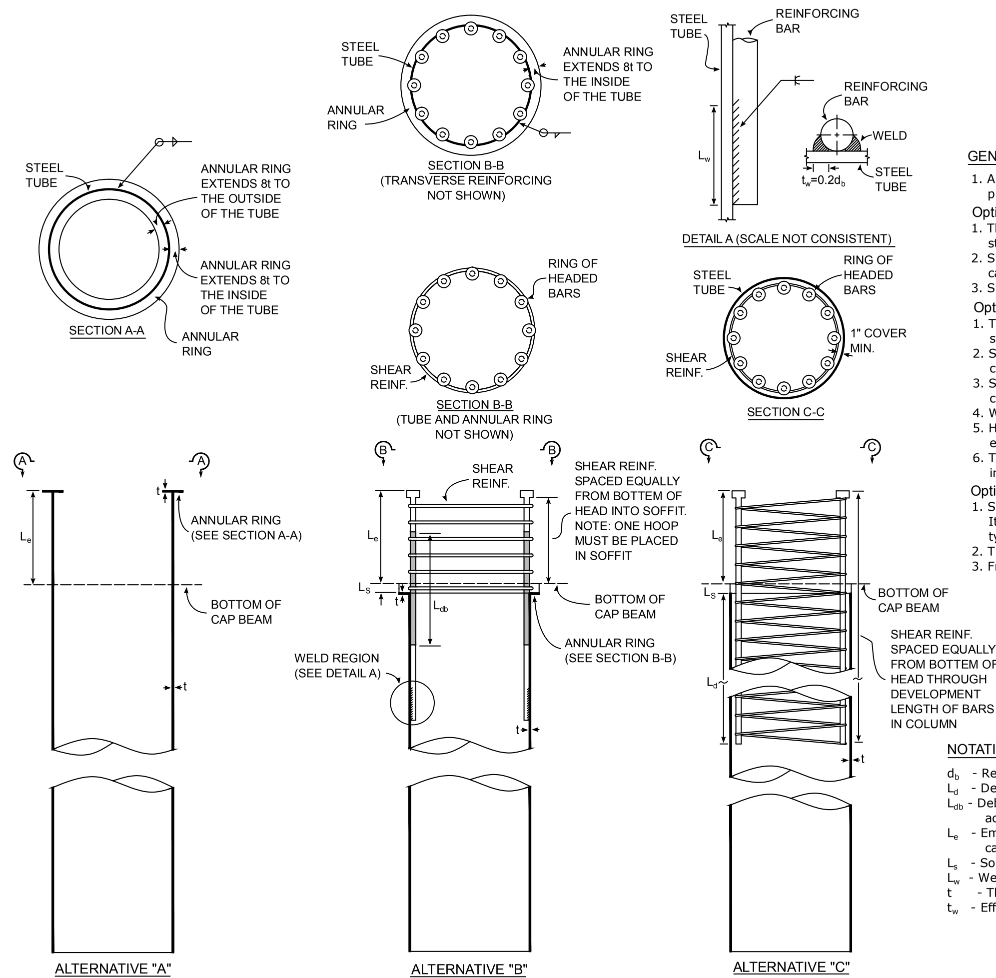

GENERAL NOTES:

1. All connections can be used with cast-in-place or precast cap components. See page 2 for standard precast cap beam requirements.

Option "A"
1. Thickness and strength of annular ring shall conform to the thickness and strength of steel tube.
2. Steel tube shall be welded to the annular ring using fillet welds designed to carry the full tensile capacity of the tube.
3. Strength and ductility of connection controlled by CFT component.

Option "B"
1. Thickness and strength of annular ring shall conform to the thickness and strength of steel tube.
2. Steel tube shall be welded to the annular ring using fillet welds designed to carry the full tensile capacity of the tube.
3. Strength and ductility controlled by longitudinal reinforcing which extends from CFT into cap beam.
4. Welded longitudinal bars must be placed with sufficient space to allow for welding.
5. Half of debonded length must extend into cap beam while half of the debonded length must extend into the CFT column.
6. Transverse reinforcing required to increase confinement in joint region. One hoop must be placed in the thickness of the soffit.

Option "C"
1. Strength and ductility controlled by longitudinal reinforcing which extends from CFT into cap beam. It is difficult to acheive the plastic moment strength of the composite column using this connection type due to the moment arm and reinforcing ratio of longitudinal reinforcing.
2. Transverse reinforcing included along the length of the longitudinal reinforcing.
3. Friction collar required if this connection type is used with precast cap beam element.

NOTATION AND DEFINITIONS:

- d_b - Reinforcing bar diameter
- L_d - Development length of reinforcing.
- L_{db} - Debonded length of reinforcing as calculated according to a moment curvature analysis.
- L_e - Embedment of steel into cap beam as calculated using EQ. xx.
- L_s - Soffit depth as calculated using EQ. xx.
- L_w - Weld length as calculated using EQ. xx.
- t - Thickness of steel tube
- t_w - Effective weld throat thickness

MATERIALS:

REINFORCED CONCRETE
f'_c = 6,000-psi
LOW SHRINKAGE ADMIXTURE REQUIRED IN CONCRETE CORE

CONNECTION REINFORCING
f_y = 60,000-psi
A706 REINFORCING REQUIRED

STEEL PIPE
Fy (minimum yield strength) = 45,000-psi
Fu(minimum tensile strength) = 60,000-psi
API GRADE STEEL PREFFERED

ANNULAR RING
ANNULAR RING SHALL HAVE SAME STRENGTH AS STEEL PIPE

Appendix E

GROUND MOTION CHARACTERISTICS

Table E.1: Ground Motion Characteristics

EQ Index	Event	Year	Magnitude	Station Name
1	Northridge	1994	6.7	Beverly Hills - 14145 Mulhol
2	Northridge	1994	6.7	Canyon Country - W Lost Cany
3	Northridge	1994	6.7	LA - Saturn St
4	Northridge	1994	6.7	Santa Monica City Hall
5	Northridge	1994	6.7	Beverly Hills - 12520 Mulhol
6	Duzce, Turkey	1999	7.1	Bolu
7	Hector Mine	1999	7.1	Hector
8	Imperial Valley	1979	6.5	Delta
9	Imperial Valley	1979	6.5	El Centro Array #11
10	Imperial Valley	1979	6.5	Calexico Fire Station
11	Imperial Valley	1979	6.5	SAHOP Casa Flores
12	Kobe, Japan	1995	6.9	Nishi-Akashi
13	Kobe, Japan	1995	6.9	Shin-Osaka
14	Kobe, Japan	1995	6.9	Kakogawa
15	Kobe, Japan	1995	6.9	KJMA
16	Kocaeli, Turkey	1999	7.5	Duzce
17	Kocaeli, Turkey	1999	7.5	Arcelik
18	Landers	1992	7.3	Yermo Fire Station
19	Landers	1992	7.3	Coolwater
20	Landers	1992	7.3	Joshua Tree
21	Loma Prieta	1989	6.9	Capitola
22	Loma Prieta	1989	6.9	Gilroy Array #3
23	Loma Prieta	1989	6.9	Oakland - Outer Harbor Wharf
24	Loma Prieta	1989	6.9	Hollister - South & Pine
25	Loma Prieta	1989	6.9	Hollister City Hall
26	Loma Prieta	1989	6.9	Hollister Diff. Array
27	Manjil, Iran	1990	7.4	Abbar
28	Superstition Hills	1987	6.5	El Centro Imp. Co. Cent
29	Superstition Hills	1987	6.5	Poe Road (temp)
30	Superstition Hills	1987	6.5	Westmorland Fire Sta
31	Cape Mendocino	1992	7.0	Rio Dell Overpass - FF
32	Chi-Chi, Taiwan	1999	7.6	CHY101
33	Chi-Chi, Taiwan	1999	7.6	TCU045
34	Chi-Chi, Taiwan	1999	7.6	TCU095
35	Chi-Chi, Taiwan	1999	7.6	TCU070
36	Chi-Chi, Taiwan	1999	7.6	WGK
37	Chi-Chi, Taiwan	1999	7.6	CHY006
38	San Fernando	1971	6.6	LA - Hollywood Stor FF
39	Friuli, Italy	1976	6.5	Tolmezzo

Appendix F

STEEL TUBE-TO-CONCRETE-FILL BOND EXPERIMENTS

To help characterize the composite nature of CFTs which utilize straight seam and spiral welded tubes, an ancillary experimental investigation was conducted. Of particular interest were the bond slip characteristics of two different tube types using a concrete fill both with and without a low shrinkage admixture.

Four bond-slip specimens were constructed to evaluate the bond-slip characteristics of CFTs with spiral weld and straight seam tubes. A full specimen matrix including tube type and material properties is summarized in Table F.1. Two CFT's with spiral welded and straight seam tubes were cast using concrete with a low shrinkage admixture, and two were cast with a concrete without a low shrinkage admixture. The specimens were cast with a 1-in. gap on the bottom to allow for push through of the concrete fill (as illustrated in Fig. F.1).

The specimens were instrumented using linear Duncan potentiometers, vibrating wire gages, and strain gages, and were tested under a 2.4-million lb capacity Universal testing machine. An overview of the instrumentation and test setup is illustrated in Fig. F.1.

The concrete core was loaded axially until a 1-in. displacement was recorded. The force-displacement behaviors of the specimens have been plotted in Fig. F.2. The addition of a low shrinkage admixture did not influence the bond-slip characteristics of the spiral welded tubes. This is because the primary bonding mechanism in this type of tube is mechanical; the spiral weld acts to force composite action between the concrete fill and steel tube. In contrast, the addition of low shrinkage admixture greatly improved the bond strength for straight seam tubes. This is because the primary bonding mechanism in this type of tube is chemical, and if the concrete shrinks away from the steel tube as it cures, a majority of the bond is lost.

Table F.1: Bond Slip Specimen Matrix

Specimen	Tube Type	D, in.	t, in.	D/t	Test Day f'_c, ksi	Concrete Admixture
SS-I	Straight Seam	20	0.25	80	7.95	Low Shrinkage
SW-I	Spiral Welded	24	0.25	96	7.95	None
SS-II	Straight Seam	20	0.25	80	7.53	Low Shrinkage
SW-II	Spiral Welded	20	0.25	80	7.53	None

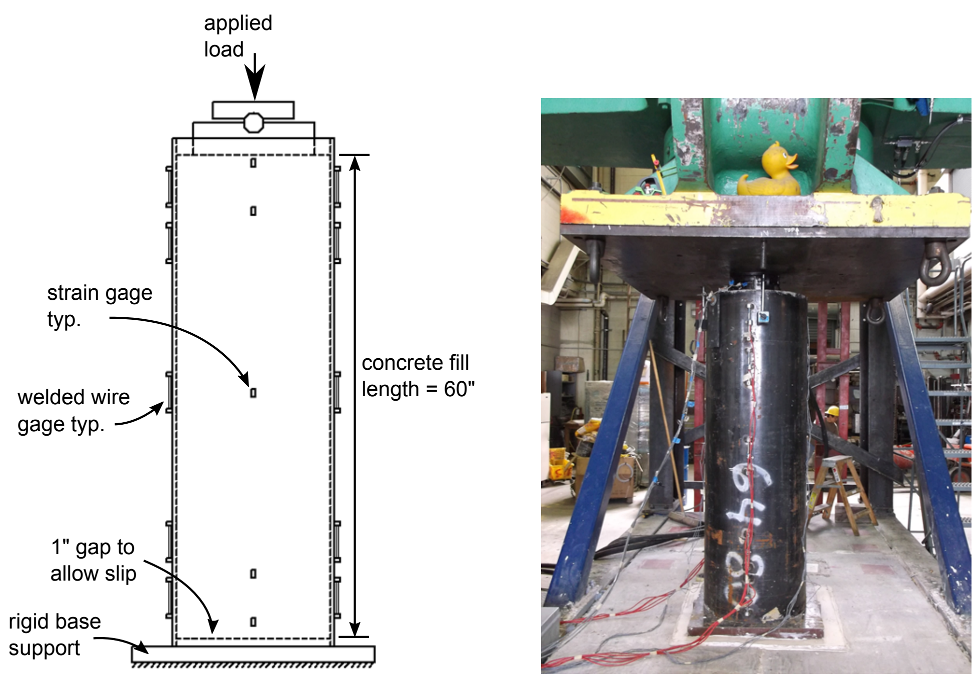

Figure F.1: Bond Slip Test Setup and Instrumentation

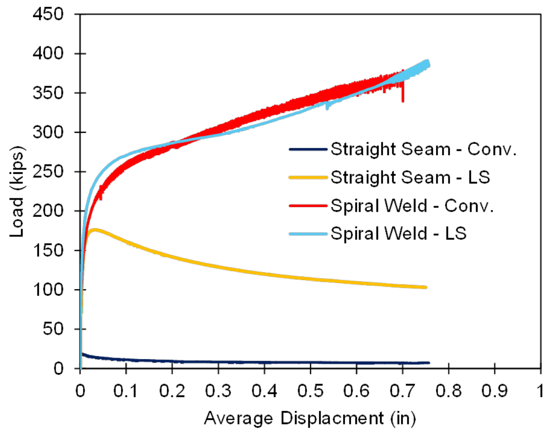

Figure F.2: Bond Slip Force-Displacement Behaviors